Prepared for:

Delft University of Technology

The longshore dimension in dune overwash modelling

Development, verification and validation of XBeach

MSc thesis

May 2008

Prepared for:

Delft University of Technology

The longshore dimension in dune overwash modelling

Development, verification and validation of XBeach

MSc thesis

Robert McCall

Supervisors:
Prof.dr.ir. M. Stive
Prof.dr.ir. J.A. Roelvink
Ir. J.S.M. van Thiel de Vries
Dr.ir. A.P. van Dongeren
Ir. D.J.R. Walstra
Dr.ir. P.J. Visser
Dr.ir. M. Zijlema

May 2008

WL | delft hydraulics

Client:	Delft University of Technology
Title:	The longshore dimension in dune overwash modelling

Abstract:

The primary objective of this thesis is to generate a 2DH-numerical model to simulate dune overwash. The first stage in this is achieved by modifying the program code of an existing overwash model in development, XBeach, to enable 2DH calculations. In the second stage the hydrodynamics of the model are verified using theoretical and laboratory and field tests. In the third stage the model is validated by simulating overwash and washover on Santa Rosa Island, Florida, during Hurricane Ivan. The secondary objective of this thesis is to evaluate the effect of longshore bathymetry variations on the patterns and amount of overwash using the newly developed XBeach model.

A numerical area model of part of Santa Rosa Island, Florida, is developed. The model is forced using Hurricane Ivan wave and surge conditions. The XBeach model shows five phases of morphology on the barrier island, leading from foredune erosion to breaching of the island. The model results are compared to high-resolution post-storm altimetry data. It is shown that although the XBeach model produces morphological features common to overwash conditions, the amount of erosion is an order greater than the measured erosion. Sensitivity studies are carried out to determine the influence of the hydraulic boundary conditions on the final erosion profile. It is found that the model is sensitive to total surge levels and surge level gradients across the island, but insensitive to wave heights. It is shown that under inundation overwash conditions the amount of erosion and patterns of deposition are almost entirely determined by longshore bathymetry features with length scales in the order of kilometres.

The primary recommendation given in this thesis is to develop and implement better sediment transport relations in XBeach and to account for effects of vegetation on the hydrodynamics and morphodynamics of the subaerial barrier island.

References:	

Ver	Author		Date	Remarks	Review		Approved by	
	Robert McCall							

Project number:	
Keywords:	XBeach, modelling, dune erosion, overwash, longshore variability
Number of pages:	120
Classification:	None
Status:	Final

Preface

This thesis concludes the Master of Science program at the Faculty of Civil Engineering and Geosciences at Delft University of Technology, The Netherlands. The thesis work was carried out at Deltares/Delft Hydraulics and USGS Center for Coastal and Watershed Studies, Saint Petersburg, Florida.

The devastating hurricane seasons in the USA of 2004 and 2005, have pointed towards the urgent need for accurate tools with which coastal flooding caused by extreme storms can be predicted. In order to address this need, the United States Army Corps of Engineers initiated the Morphos3D project. A collaboration of specialists at UNESCO-IHE, Delft University of Technology and Deltares, led by Professor Roelvink, was asked to participate by developing a process-based, time dependent numerical model to simulate nearshore hydrodynamics and dune morphodynamics. This numerical model is called XBeach.

This MSc thesis describes the development of the XBeach model to incorporate the longshore dimension in hydrodynamic and morphodynamic dune overwash modelling. The thesis describes the verification of the model through a series of hypothetical and experimental tests. This model is used to simulate overwash on Santa Rosa Island, Florida, during Hurricane Ivan. Finally the model is used to examine the effect of longshore space scales in the bathymetry on the amount and patterns of overwash.

I would like to thank all my supervisors for the opportunity to work with them on a fascinating project. I very much enjoyed working together with Jaap van Thiel de Vries, Ap van Dongeren and Dano Roelvink on the XBeach program code. Being able to directly contribute to the project gave a great amount of motivation. I would like to thank them in particular for their support and humor during the weeks in Delft and Saint Petersburg. Special thanks also go to Dirk-Jan Walstra, who made it possible for me to carry out my fieldwork in Florida.

Apart from my supervisors I would like to thank Jamie Lescinski at Deltares for her aid, especially during my first encounters with the various XBeach teething problems. Thank you to Dave Thompson and Nathaniel Plant and the other staff at USGS, Saint Petersburg for a wonderful stay in Florida.
I would never have been able to finish my work without the comments, support and distraction of my Deltares graduation colleagues John, Laura, Thomas, Noud, Claartje, Sam & Moos, Johan, Anton, Marieke, Gao, Renske and Thijs.
Special thanks go to my family for their support and to Joana for her interest, encouragement, support and patience.

Robert McCall,

Delft, May 2008

Summary

Overwash is the flow of water and sediment over the crest of a beach system when the runup level of waves or the water level exceeds the local beach or dune crest height. Severe overwash can lead to catastrophic flooding of highly populated coastal areas. It is a problem that affects low-lying areas across the world. Despite much attention from the scientific community, very few models exist that are able to correctly simulate the processes that occur during overwash.

The primary objective of this thesis is to generate a 2DH-numerical model to simulate dune overwash. The first stage in this is achieved by modifying the program code of an existing overwash model in development, XBeach, to enable 2DH calculations. In the second stage the hydrodynamics of the model are verified using theoretical and laboratory and field tests. In the third stage the model is validated by simulating overwash and washover on Santa Rosa Island, Florida, during Hurricane Ivan. The secondary objective of this thesis is to evaluate the effect of longshore bathymetry variations on the patterns and amount of overwash using the newly developed XBeach model.

As shown in Chapter 2, the hydrodynamics in very shallow water, and thus at the dune foot and in overwash, are dominated by variance in the infragravity wave band. The generation mechanisms and physics of infragravity waves are discussed. Chapter 2 also discusses current knowledge of the morphological processes related to dune erosion and overwash.

Chapter 3 treats the physics and numerical implementation of the XBeach model. XBeach is a process-based, time-dependent 2DH numerical model for the nearshore and coast. The model focuses on the generation and propagation of short-wave generated infragravity waves and currents. Morphology is taken into account by simple sediment transport relations and avalanching algorithms.

Various validation tests of the hydrodynamics in XBeach are discussed in Chapter 4 and Appendices C through V. It is shown that in general the hydrodynamics of the model function correctly. However some complications are discussed with respect to the generation of infragravity waves under irregular wave group forcing, the lateral boundary conditions and the grid dependency of the water level variance on the numerical grid size.

In Chapter 5 a numerical area model of part of Santa Rosa Island, Florida, is developed. The model is forced using Hurricane Ivan wave and surge conditions. These boundary conditions are provided by partially validated numerical models and are therefore uncertain. The XBeach model shows five phases of morphology on the barrier island, leading from foredune erosion to breaching of the island. The model results are compared to high-resolution post-storm altimetry data. It is shown that although the XBeach model produces morphological features common to overwash conditions, the amount of erosion is an order greater than the measured erosion.

Sensitivity studies are carried out to determine the influence of the hydraulic boundary conditions on the final erosion profile. It is found that the model is surprisingly insensitive to wave heights and surge level delays between the offshore boundary and back barrier bay. The influence of these parameters on the erosion may be lost in the general over prediction

of erosion on the barrier island. The model shows a large increase in erosion with greater surge levels and surge level gradients across the island. Interestingly, the model is relatively insensitive to a reduction in the equilibrium concentration coefficients. It is suggested that many sensitivity studies should be readdressed once the XBeach model is capable of more accurately reproducing the measured post-storm altimetry.

In Chapter 6 a study is made of the effect of longshore bathymetry smoothing scales on the patterns and amount of overwash. The Santa Rosa Island model is taken as a base case and the bathymetry is reduced in longshore detail from 10m longshore scales to 2000m longshore scales. It is shown that under inundation overwash conditions the amount of erosion and patterns of deposition are almost entirely determined by longshore bathymetry features with length scales in the order of kilometres. It is suggested that under such conditions, the amount of detail in the longshore direction in future numerical models may be reduced in order to decrease calculation time or to increase the longshore domain. It is found that the hydrodynamics in 1D-cross shore models respond differently to forcing than 2DH-models. It is therefore suggested that even in cases of relatively longshore uniform forcing and bathymetry, a 2DH model should still be used instead of a series of cross-shore profile models.

In Chapter 7 the main conclusions of this thesis are reiterated, as well as a discussion of several recommendations for future development and research. It is concluded that the primary objective is not fully fulfilled, as the model is not validated. The secondary objective is fulfilled under the assumption that the results of the simulations are qualitatively correct.

Contents

List of Figures
List of Symbols

1 Introduction 1
1.1 Background 1
1.2 Problem description 2
1.3 Objective 2
1.4 Methodology 2
1.5 Reader's guide 3

2 Literature study 4
2.1 Coastal terminology 4
2.2 Infragravity waves 5
2.2.1 Generation of infragravity waves 6
2.2.2 Bound infragravity wave shoaling 8
2.2.3 Infragravity wave reflection and dissipation 10
2.2.4 Nearshore infragravity wave energy 11
2.2.5 Modelling infragravity waves 12
2.3 Morphological processes 12
2.3.1 Swash regime 14
2.3.2 Collision regime 15
2.3.3 Overwash and inundation regimes 17

3 The XBeach model 26
3.1 Introduction 26
3.2 Model setup and governing equations 26
3.2.1 Short wave equations 27
3.2.2 Roller energy balance 28
3.2.3 Shallow water equations 29
3.2.4 Sediment transport 30
3.2.5 Bed level change 31
3.3 Numerical scheme 31
3.4 Boundary conditions 32
3.4.1 Short wave boundary conditions 33
3.4.2 Flow boundary conditions 34
3.4.3 Sediment transport and morphology boundary conditions 35

4 Validating the XBeach model 36
4.1 Introduction 36
4.2 Verification tests description 36

4.3 Results and conclusions 39
5 Santa Rosa Island case study 41
5.1 Introduction 41
5.2 Description of data 44
5.2.1 Bathymetry and altimetry data 44
5.2.2 Water level data 48
5.2.3 Wave data 52
5.3 Model setup 54
5.3.1 Grid setup 54
5.3.2 Boundary conditions 55
5.4 Base simulation results 56
5.4.1 Foredune erosion period (0-9h) 56
5.4.2 First overwash period (10-16h) 59
5.4.3 Second overwash period (17-22h) 61
5.4.4 First inundation period (23-32h) 63
5.4.5 Second inundation period (33-41h) 65
5.4.6 Comparison of post-storm results 68
5.5 Model sensitivity 70
5.5.1 Effect of a morphological acceleration factor 71
5.5.2 Effect of wave heights 73
5.5.3 Effect of water levels 74
5.5.4 Effect of sediment transport 79
5.5.5 Recommendations for further study 81
5.6 Conclusions 82
6 Longshore scale effects 83
6.1 Introduction 83
6.2 Model setup 83
6.3 Model results 85
6.4 Discussion 88
6.4.1 Washover fan location 88
6.4.2 Modelling large longshore domains 89
6.5 Conclusion 90
7 Conclusions and recommendations 92
7.1 Conclusions 92
7.2 Recommendations 93
8 References 96

List of Figures

Figure 1 Washover sediment covers large stretches of Dauphin Island, Alabama, after Hurricane Katrina. Several breaches are visible in the top of the photo. [Source: USGS] 1

Figure 2 Definition of nearshore areas [according to United States Army Corps of Engineers, 2002]. 5

Figure 3 Schematic representation of energy in ocean waves [from: Masselink and Hughes, 2003]. 6

Figure 4 According to the theory of Longuet-Higgins and Stewart, the water level (red line) under the highest waves (blue line) in a wave group is lower than that under the lowest waves between two wave groups 7

Figure 5 Calculated infragravity wave over a double barred profile, over one half of the period of the wave groups, T_g. Taken from [Symonds and Bowen, 1984; in: Fredsøe and Deigaard, 1992] 8

Figure 6 Definition of bound wave phase lag, as stated by Battjes *et al.* [2004]..... 10

Figure 7 An example of two cross shore velocity spectra from the outer and inner surf zone. Note the increase in the infragravity wave band in the inner surf zone [from Masselink and Hughes, 2003] 11

Figure 8 Schematic representation of short wave and infragravity wave amplitude in the nearshore under calm and storm conditions [modified from Holman, 1981] 12

Figure 9 Definition sketch of the parameters used to describe morphological response in the Storm Impact Scale system [taken from Sallenger, 2000].. 13

Figure 10 Dune erosion in the erosion profile model of Vellinga [taken from Vellinga, 1986] 16

Figure 11 Seven types of barrier island – dune system morphological response to overwash [taken from Donnelly, 2007] 19

Figure 12 Schematic representation of a washover fan, washover terrace and sheetwash [taken from Donnelly *et al.*, 2006] 20

Figure 13 Washover constricted in a beach access path on Ocracoke Island, North Carolina [taken from Donnelly *et al.*, 2006]..... 20

Figure 14 Five erosion stages in sand dike breaching [taken from Visser, 1998]..... 24

Figure 15 XBeach model orientation [taken from Roelvink *et al.*, 2007]..... 27

Figure 16 XBeach staggered grid [modified from Roelvink *et al.*, 2007] 27

Figure 17 Lateral wave energy boundaries: the wave group crest angle is found on the boundary and extended to the inner row. Wave energy is interpolated to the intersection of the inner row and the wave group crest. Wave energy is copied from the intersection to the originating boundary point. 34

Figure 18 Track of Hurricane Ivan, colour from blue to red denotes increasing hurricane intensity on the Saffir-Simpson scale [sources: NASA, National Hurricane Centre and Wikipedia] 41

Figure 19 Hurricane Ivan destroyed sections of the Pensacola Bay Bridge [source: AP] 42

Figure 20 Location of Santa Rosa Island relative to the landfall of Hurricane Ivan [image source: Google Earth] 43

Figure 21 Post-Ivan aerial view of Santa Rosa Island [source: USGS] 43

Figure 22 Santa Rosa Island and the study area [source: Google Earth] 44

Figure 23 Pre-Hurricane Ivan elevation data (top panel), post-storm elevation data (central panel) and erosion/deposition resulting from Hurricane Ivan (bottom panel). Images courtesy of Dave Thompson. 46

Figure 24 Pre-Hurricane Ivan LIDAR data overlaid on an aerial image of the study site [sources: USGS and Google Earth] 47

Figure 25 Elevation data extracted from the Coastal Relief Model [satellite image source: Google Earth] 47

Figure 26 Model location in July 2001(top panel) and 19 September 2004, three days after Hurricane Ivan (bottom panel). [Source: USGS] 48

Figure 27 Locations of NOAA tidal gauges and Hurricane Ivan landfall [image source: Google Earth] 49

Figure 28 Water elevation time series of the NOAA tidal gauge at Pensacola (top panel) and Panama Beach (bottom panel) during Hurricane Ivan. Measured water levels are shown in red, astronomical tide prediction in blue, the difference between measured and astronomical in green [source: NOAA Tides and Currents]. 50

Figure 29 The region of the Delft3D model (green box), the progress of the centre of Hurricane Ivan (yellow circles) and two example NOAA/AOML/HRD wind field grids. Image courtesy of Dave Thompson 51

Figure 30 Water level offshore of the study site according to the Delft3D-model 51

Figure 31 Water level offshore of the study site presented by Donnelly *et al.*[submitted]. 52

Figure 32 The region of the large SWAN model (purple box) and subsequent nested models (green and red boxes). Image courtesy of Dave Thompson. 53

Figure 33 Delft3D/SWAN-model output results for the study site: significant wave height (top panel), peak wave period (upper middle panel), mean wave direction (lower middle panel) and water level (bottom panel) 53

Figure 34 XBeach model domain 54

Figure 35 Initial bed elevation in the XBeach model 55

Figure 36 Input time series of offshore forcing for the base simulation 56

Figure 37 Initial bed level (left panel) and bed level after nine hours (right panel). Contour lines indicate -1m +MSL, 0m +MSL and +1m +MSL. Arrow indicates the start of an overwash throat. 57

Figure 38 Total erosion and deposition after nine hours 58

Figure 39 Snapshot of the water surface and bed level after nine hours. Note the start of the formation of an overwash throat between the foredunes at the western end of the model, which can also be seen in Figure 37. The lower panel shows the surge level at the time of the snapshot. 58

Figure 40 Bed level after nine hours (left panel) and after sixteen hours (right panel). Contour lines indicate -1m +MSL, 0m +MSL and +1m +MSL. 60

Figure 41 Total erosion and deposition after sixteen hours 60

Figure 42 Snapshot of the water surface and bed level after sixteen hours. The lower panel shows the surge level at the time of the snapshot. 61

Figure 43 Bed level after sixteen hours (left panel) and after twenty-two hours (right panel). Contour lines indicate -1m +MSL, 0m +MSL and +1m +MSL. 62

Figure 44 Total erosion and deposition after twenty-two hours 62

Figure 45 Snapshot of the water surface and bed level after twenty-two hours. The lower panel shows the surge level at the time of the snapshot 63

Figure 46 Bed level after twenty-two hours (left panel) and after thirty-two hours (right panel). Contour lines indicate -1m +MSL, 0m +MSL and +1m +MSL. 64

Figure 47 Total erosion and deposition after thirty-two hours 64

Figure 48 Snapshot of the water surface and bed level after thirty-two hours. The lower panel shows the surge level at the time of the snapshot 65

Figure 49 Bed level after thirty-two hours (left panel) and after forty-one hours (right panel). Contour lines indicate -1m +MSL, 0m +MSL and +1m +MSL. 66

Figure 50 Total erosion and deposition after fourty-one hours 66

Figure 51 Snapshot of the water surface and bed level after forty-one hours. The lower panel shows the surge level at the time of the snapshot. 67

Figure 52 Water surface after storm surge and final bed level 67

Figure 53 Comparison of post-storm bed level; available LIDAR data (left panel) and XBeach model data (right panel). 68

Figure 54 Comparison of post-storm erosion and deposition levels; available LIDAR data (left panel) and XBeach model data (right panel) 69

Figure 55 Relative error in the XBeach model. White indicates no error, red and blue indicate increasing errors in depositional and erosional zones respectively. 70

Figure 56 Measured post-storm bed elevation LIDAR data and the final bed elevation for three morphological acceleration factors 72

Figure 57 Measured post-storm erosion-deposition LIDAR data and the erosion-deposition data for three morphological acceleration factors 72
Figure 58 Measured post-storm bed elevation LIDAR data and the final bed elevation for the base simulation (morfac 10) and the simulation with reduced wave heights (morfac 10) 73
Figure 59 Measured erosion-deposition LIDAR data and the erosion-deposition data of the base simulation (morfac 10) and the simulation with reduced wave heights (morfac 10) 74
Figure 60 Imposed water level on the offshore and back barrier bay boundaries 75
Figure 61 Measured post-storm bed elevation LIDAR data and the final bed elevation for the base simulation (morfac 10) and the simulation with increased surge level (morfac 10) 76
Figure 62 Measured erosion-deposition LIDAR data and the erosion-deposition data of the base simulation (morfac 10) and the simulation with increased surge level (morfac 10) 76
Figure 63 Measured post-storm bed elevation LIDAR data and the final bed elevation for the base simulation (morfac 1) and the simulation with a large water level gradient (morfac 1) 77
Figure 64 Measured erosion-deposition LIDAR data and the erosion-deposition data of the base simulation (morfac 1) and the simulation with a large water level gradient (morfac 1) 77
Figure 65 Imposed water level on the offshore and back barrier bay boundaries 78
Figure 66 Measured post-storm bed elevation LIDAR data and the final bed elevation for the base simulation (morfac 10) and the simulation with a phase difference (morfac 10) 79
Figure 67 Measured erosion-deposition LIDAR data and the erosion-deposition data of the base simulation (morfac 10) and the simulation with a phase difference (morfac 10) 79
Figure 68 Measured post-storm bed elevation LIDAR data and the final bed elevation for the base simulation (morfac 10) and the simulation with lower equilibrium sediment concentration (morfac 10) 80
Figure 69 Measured erosion-deposition LIDAR data and the erosion-deposition data of the base simulation (morfac 10) and the simulation with lower equilibrium sediment concentration (morfac 10) 81
Figure 70 Initial bed profile (left panel) and a spectrum density-plot of the longshore elevation variance as a function of longshore length scale and cross shore position (right panel) 83
Figure 71 Initial bed elevation for five cases of longshore smoothing scale 85
Figure 72 Final erosion-deposition plots for all five longshore smoothing scales 86
Figure 73 Post-storm longshore smoothed LIDAR data (first and third rows) and post-storm longshore smoothed XBeach results (second and forth rows) 87

Figure 74 Relative error of the five longshore scaled simulations. White indicates no error, red and blue indicate increasing errors in depositional and erosional zones respectively. 88

Figure 75 Erosion-deposition plots for an XBeach simulation with 10 meter longshore grid size (left panel) and 100 meter grid size (right panel). Both simulations have the same input bed elevation with 2000 meter longshore smoothing scale. 89

Figure 76 Sedimentation and deposition in a series of 1D-models (left panel) and the coarse-grid 2DH-model 90

List of Symbols

Symbol	Unit	Description
A	$Jm^{-2}s^{-1}$	Wave action density
A	m	Wave amplitude
a	m	Wave amplitude
a_0	m	Wave amplitude in deep water
C	$m^3\ m^{-3}$	Depth average sediment concentration
C_{eq}	$m^3\ m^{-3}$	Depth average equilibrium sediment concentration
C_f	$m^{½}s^{-1}$	Chézy coefficient of bed roughness
c	ms^{-1}	Wave celerity
c_0	ms^{-1}	Wave celerity in deep water
c_g	ms^{-1}	Wave group velocity
c_{g_0}	ms^{-1}	Wave group velocity in deep water
D	Wm^{-3}	Wave energy dissipation
D_s	m^2s^{-1}	Sediment diffusion coefficient
E	Jm^{-2}	Wave energy per unit surface area
F	Wm^{-1}	Wave energy flux
F_x	Wm^{-1}	Cross shore component of wave energy flux
F_y	Wm^{-1}	Longshore component of wave energy flux
F_{w_x}	Nm^{-2}	Cross shore component of wave forcing
F_{w_y}	Nm^{-2}	Longshore component of wave forcing
g	ms^{-2}	Gravitational acceleration, constant 9.81 ms^{-2}
H	m	Wave height
H_{m0}	m	Significant wave height
$H_{\max}$	m	Maximum wave height
H_{rms}	m	Root mean square wave height

Symbol	Unit	Description
h	m	Water depth
K_s	-	Shoaling coefficient
K_r	-	Refraction coefficient
k	m^{-1}	Wave number, $2\pi L^{-1}$
L	m	Wave length
L_0	m	Wave length in deep water
n	-	Ratio between wave group velocity and wave celerity
p	Nm^{-2}	Water pressure
Q	m^3s^{-1}	Water discharge
Q_s	m^3s^{-1}	Sediment discharge
q	m^2s^{-1}	Discharge per unit width
q_s	m^2s^{-1}	Sediment discharge per unit width
R	Wm^{-2}	Rate of energy transfer per unit area from grouped short waves to forced long waves
S_x	m^2s^{-1}	Cross shore sediment transport rate
S_y	m^2s^{-1}	Longshore sediment transport rate
$S_{\alpha\beta}$	Nm^{-1}	Radiation stress in the direction of the axis α, on the vertical plain normal to the axis β
T	s	Wave period
T_g	s	Wave group period
T_p	s	Peak period
T_s	s	Sediment adaptation time
t	s	Time
u	ms^{-1}	Velocity x-direction
$u_{particle}$	ms^{-1}	Wave particle velocity in the wave direction
u_{rms}	ms^{-1}	Root-mean-square velocity
v	ms^{-1}	Velocity y-direction

Symbol	Unit	Description
$v_{particle}$	ms^{-1}	Wave particle velocity perpendicular to the wave direction
w	ms^{-1}	Sediment fall velocity
x	m	Horizontal axis coordinate, usually cross shore
x_w	m	Horizontal axis coordinate in the wave direction
y	m	Horizontal axis coordinate, usually longshore
y_w	m	Horizontal axis coordinate perpendicular to the wave direction
z	m	Vertical axis coordinate, positive upwards and zero at the mean water level
z_b	m	Bed level
α	-	Bed slope
ϕ	m^2s^{-1}	Velocity potential
φ	-	Wave phase
γ_b	-	Breaker coefficient
η	m	Water surface elevation
η_h	m^2s^{-1}	Horizontal eddy viscosity coefficient
θ	-	Wave angle, the angle between the wave crest normal and the inverse shore normal
θ_0	-	Wave angle in deep water
ρ	kgm^{-3}	Mass density of water
σ	s^{-1}	Intrinsic wave frequency
ω	s^{-1}	Absolute wave radian frequency, $2\pi T^{-1}$
ξ	-	Iribarren breaker parameter
ζ	m	Instantaneous water surface level above the short-wave or wave-group averaged water surface level

1 Introduction

1.1 Background

Low-lying coastal areas around the world are becoming increasingly populated as more and more people move from the interior to coastal cities and deltas. The chance of coastal flooding in these areas is increasing due to rising sea levels and the possibility of increased storm intensities related to global warming. The recent flooding caused by Cyclone Nargis in Myanmar has shown the devastating consequences of underestimating the effect of storms on low-lying coastal areas. Hurricane Katrina of 2005 proved that not only the Developing World is in drastic need of the ability to assess coastal vulnerability to extreme storms.

Approximately 20% the world's coastland is protected from the sea by natural sand dunes and barrier islands. Examples are the coast of much of the Netherlands and the United States Atlantic and Gulf Coasts. A primary cause of coastal flooding in these areas is dune overwash and breaching due to high surge levels and increased wave attack, see for instance Figure 1. Although these processes draw much attention from the scientific community, the capability to quantitatively predict and simulate overwash is only just beginning to emerge [Donnelly *et al.*, 2006].



Figure 1 Washover sediment covers large stretches of Dauphin Island, Alabama, after Hurricane Katrina. Several breaches are visible in the top of the photo. [Source: USGS]

1.2 Problem description

Various empirical, analytical and numerical models have been developed in the past to simulate dune erosion and dune overwash. Examples of models that have been used with varying levels of success are DUROSTA [Steetzel, 1993], UNIBEST-TC [Stive and Wind, 1986; Roelvink and Stive, 1989; Bosboom *et al.*, 2000] and SBeach [Larson and Kraus, 1989; Larson *et al.*, 1990]. Until now, all dune overwash models have been 1D- or 2DV-cross shore transect models. Such models assume uniformity in the longshore dimension and do therefore not incorporate longshore variations in either the hydraulic forcing, sediment transport or dune profile.

Field studies have shown that overwash is highly influenced by spatial variations in forcing and dune strength [e.g. Dolan and Hayden, 1981; Suter *et al.*, 1982; in Donnelly *et al.*, 2006]. This implies that in general overwash situations can not be assumed to be fully longshore-uniform. One of the most important future steps to be taken in dune overwash modelling is therefore the creation of a 2DH- or quasi 3D-model [Donnelly *et al.*, 2006].

1.3 Objective

The primary objective of this thesis is to create a numerical model that is capable of modelling dune overwash in a 2DH-environment. The secondary objective is to use the newly developed model to investigate the effects of longshore bathymetry variation scales on the patterns and amount of overwash.

1.4 Methodology

A new dune erosion and overwash model called XBeach [Roelvink *et al.*, 2007] has been developed at UNESCO-IHE, Delft University of Technology and Deltares/Delft Hydraulics with the possibility to include both the cross shore and longshore dimension. Initial studies have already shown that in a 1D cross-shore environment, XBeach accurately predicts dune erosion via its avalanching algorithm. This model will be used as a base for this thesis.

Three steps will be carried out to reach the primary objective. First, the existing XBeach program code is extended to ensure it is able to model hydrodynamics in a 2DH-environment. Although the program structure has been written to include the longshore dimension, no tests have yet been carried out in 2DH. It is therefore expected that certain changes may be needed to ensure the model runs correctly. Further development will include the introduction of boundary conditions that allow the model to be forced by realistic non-stationary and longshore-varying wave conditions.

In the second step, the 2DH-hydrodynamics in the XBeach model are verified by means of simple hypothetical models and field and laboratory experiments. During this second step problems may be encountered in the numerical model, leading to more code development. Thus step 1 and step 2 are closely related.

In the third step the model is validated by simulating wave overwash and washover on Santa Rosa Island, Florida, during Hurricane Ivan. Validation is determined by comparison of highly detailed pre- and post-storm altimetry data and the sedimentation and erosion patterns in the numerical model.

The secondary objective is to examine the effects of small-scale and large-scale elevation features on the patterns and amounts of overwash. This is reached by comparing simulated overwash patterns on Santa Rosa Island using varying initial bathymetries and altimetries. By applying increasing longshore smoothing scales on the initial bed profile of the Santa Rosa Island model, the effect of large-scale and small-scale elevation features on overwash can be examined.

1.5 Reader's guide

Chapter 2 gives a summary of current knowledge of overwash hydrodynamics, in particular infragravity waves. This chapter also discusses the morphodynamics of dunes and barrier islands during storms and our ability to model such morphodynamics. The XBeach model is described in Chapter 3 and the development of the model carried out during this thesis is discussed in Appendix B. The verification tests carried out to reach the primary objective are laid out in Chapter 4 and Appendix C through V. The third step of the primary objective, the validation of the XBeach model, is presented in Chapter 5. The secondary objective is discussed in Chapter 6. The main conclusions and recommendations of this thesis are given in Chapter 7

2 Literature study

The coastal zone is a complex environment in which hydrodynamic, aeolian, anthropomorphic and biological processes continually change the composition of the coast. In this chapter some of the hydrodynamic processes that are relevant to dune overwash are discussed, along with the morphological response to these processes. The chapter starts with a brief description of the terminology of the coast. Section 2.2 discusses the theoretical background behind infragravity waves, which is a major hydrodynamic component in overwash. Finally in section 2.3 the morphological responses of dune and barrier island systems are discussed. Simple linear wave theory is explained in Appendix A.

2.1 Coastal terminology

In this study references are made to a number of definitions describing areas of the coastal zone. The first, the *coastal zone*, is used to describe the transition zone between sea and land that is regularly affected by marine processes. This zone extends from the continental shelf landwards until the first topographic features that are not affected by storm surge and waves. The *coastline* or shoreline, see Figure 2, is the intersection of a certain water level and the land. This is often related to the foot of the dunes, in which case the coastline corresponds with the dominant storm surge level. The *coast* describes the section of the coastal zone landwards of the coastline. The *back barrier* is the area of the barrier island that lies landward of the primary seaward dunes. The *back barrier bay* is the waterbody separated and sheltered from the ocean or sea by a barrier island. The *beach* is the area seawards of the coastline that remains regularly subaerial, i.e. from the coastline to the low water mark. The area between the beach and the start of wave breaking is called the *nearshore*. Seawards of the nearshore is often called offshore. Wave breaking is often initiated on a breaker bar. Broken waves propagate through the nearshore in what is called the *surf zone* until they reach the subaerial beach. The area of the beach that lies between maximum wave runup and rundown is called the *swash zone*.

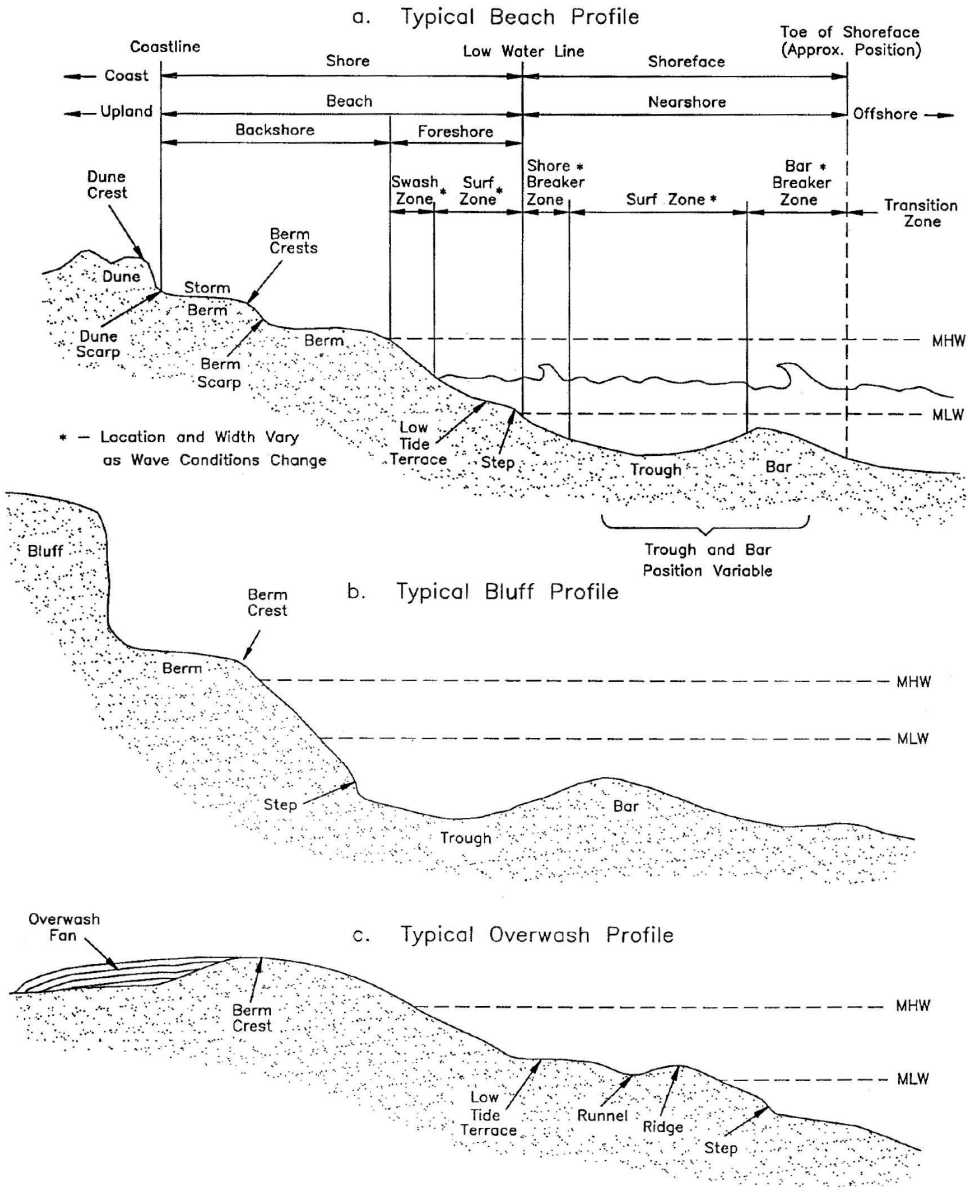


Figure 2 Definition of nearshore areas [according to United States Army Corps of Engineers, 2002].

2.2 Infragravity waves

Wave and current spectra in the surf zone often contain large amounts of energy at frequencies lower than the incident swell and wind waves [Masselink and Hughes, 2003]. Typically, the wave periods related to these lower frequencies range from approximately 20 seconds to several minutes. These wave motions are generally called infragravity waves, see Figure 3, but are sometimes also called *surf beat*. The term *infragravity wave* is used incorrectly for the phenomenon it describes, since it refers to a frequency band below that of gravity waves, whereas these waves are technically long period gravity waves [Battjes *et al.*, 2004]. However, in this document the term *infragravity wave* will be kept due to its wide-spread use in literature.

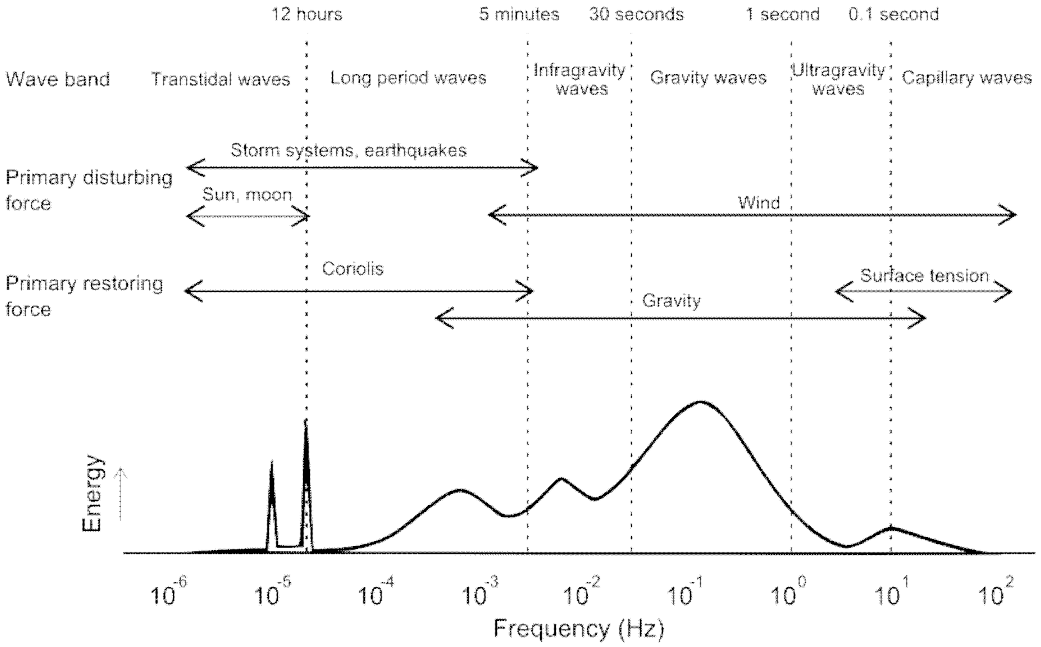


Figure 3 Schematic representation of energy in ocean waves [from: Masselink and Hughes, 2003].

Infragravity waves in shallow water were first described by Munk [1949] and Tucker [1950]. Although infragravity wave heights are small in deep water, infragravity wave run-up on beaches can be as much as several decimetres to one meter [Guza and Thornton, 1982, among others; in: Ruessink, 1998], but are generally in the order of 20-60% of the offshore wave height [Guza and Thornton, 1985; in: Masselink and Hughes, 2003]. Nearshore, the energy in the infragravity band is generally highly correlated to the short-wave energy band (typically 0.04 – 0.4 Hz), which indicates that the infragravity waves are locally driven, rather than arriving from remote sources [Guza and Thornton, 1982; Guza and Thornton, 1985 among others; in: Ruessink, 1998].

2.2.1 Generation of infragravity waves

Three theories have been developed to describe the existence of infragravity waves, namely [Ruessink, 1998]:

- Bound and released infragravity waves [Longuet-Higgins and Stewart, 1962b; 1964].
- The time-varying position of the breakpoint of the short-waves [Symonds *et al.*, 1982; Symonds and Bowen, 1984].
- The persistence of wave-groupiness into the surf zone [Foda and Mei, 1981; Watson and Peregrine, 1992; Schäffer, 1993].

The theory of Longuet-Higgins and Stewart is based on the concept of wave radiation stress. Longuet-Higgins and Stewart [1964] examine only the radiation stress S_{xx}, but in principle the theory can be applied to all radiation stresses. As wave groups travel across a stretch of water with a uniform, but shallow water depth relative to the wave group length, the water medium experiences variations in the wave radiation stress. In regions of high wave energy density, the radiation stress is greater than in regions of low wave energy density. The water experiences the radiation stress gradient as a force travelling at the velocity of the wave groups. It responds to the force by generating an opposing water surface gradient. In other

words, water is expelled from regions of high wave energy density towards regions of low wave energy density, thus creating a dip in the water level under the higher waves in the wave group, as can be seen in Figure 4. Longuet-Higgins and Stewart [1964] integrated the momentum and mass conversation equations for stationary longshore uniform situations with normally incident wave groups, without energy dissipation. They found that the instantaneous water surface level above the wave-group averaged water surface level could be written as:

$$\rho\zeta = -\frac{S_{xx}}{gh - c_g^2} + \text{constant} \tag{2.1}$$

In shallow water n approaches unity leading to the denominator in (2.1) becoming very small. In this case Longuet-Higgins and Stewart [1964] state:

$$c_g^2 \approx gh\left(1-\left(kh\right)^2\right)$$

And thus:

$$\zeta \approx -\frac{S_{xx}}{\rho\sigma^2 h^2} = -\frac{3ga^2}{2\sigma^2 h^2} \tag{2.2}$$

Supposing a minor variation in the water depth, but still no dissipation of wave energy, the amplitude of the water surface increases in decreasing water depths, since:

$$a^2 \propto h^{-0.5} \rightarrow \zeta \propto h^{-2.5} \tag{2.3}$$

Longuet-Higgins and Stewart [1964] speculate that the long waves bound to the wave groups are released when the incoming short-waves break in the surf zone and reflect off the shore.

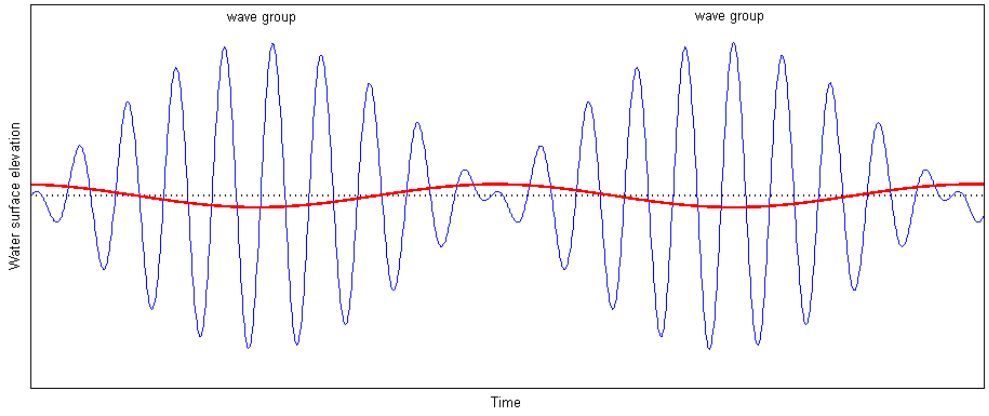


Figure 4 According to the theory of Longuet-Higgins and Stewart, the water level (red line) under the highest waves (blue line) in a wave group is lower than that under the lowest waves between two wave groups

The theory of the time varying position of the breakpoint is also explained using wave radiation stress. Incoming short-waves will break at different depths, depending on their wave height. The radiation stress gradient is negative to shoreward of the breakpoint and

positive to seaward. Symonds and Bowen [1984] state that varying radiation stress gradients due to incident wave groups leads to time-varying wave set-up and thus to long period waves, see Figure 5. List [1991; in: Watson and Peregrine, 1992] added to the theory by suggesting that modulations persist into non-saturated surf zones creating highly complex time-varying radiation stress fields.

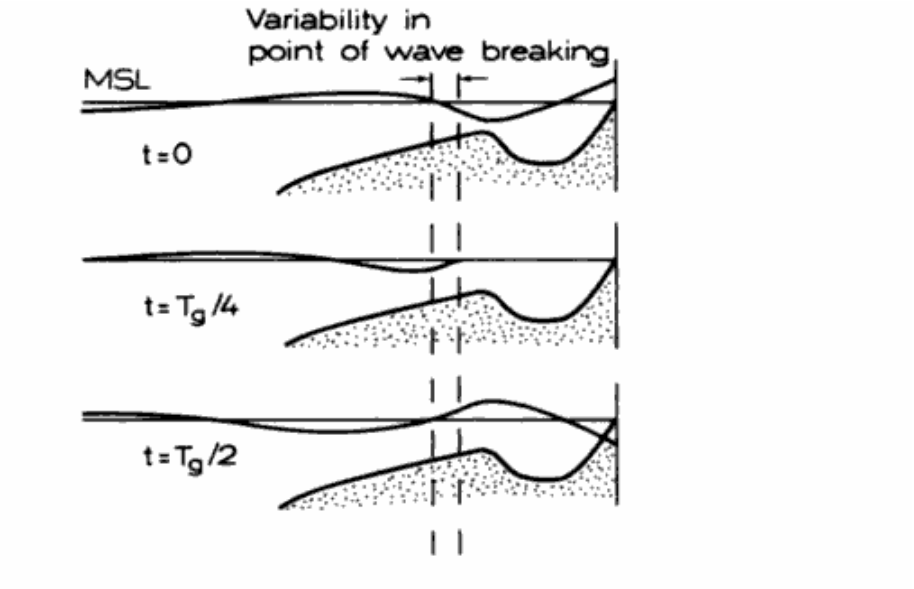


Figure 5 Calculated infragravity wave over a double barred profile, over one half of the period of the wave groups, T_g. Taken from [Symonds and Bowen, 1984; in: Fredsøe and Deigaard, 1992]

Watson and Peregrine [1992] used a short-wave resolving model to examine the generation of long waves in the surf zone. The short-wave resolving model allowed the creation and propagation of short-wave bores. They found that as sinusoidal wave groups enter the surf zone, the short-wave bore heights follow the same oscillating pattern as the wave heights in the wave group. They suggest that in the first half of the wave group, each successively larger wave pushes more water up the beach face. As the bore heights decrease in the second half of the wave group, water recedes down the beach slope to below the initial water surface level.

The amount of infragravity wave energy in the surf zone is known to increase with increasing swell energy [for instance: Okihiro *et al.*, 1993; Herbers *et al.*, 1995b; Aucan, 2004]. Battjes *et al.* [2004] show that the ratio between the amount of infragravity wave energy due to bound infragravity waves and due to a moving breakpoint depends on the steepness of the bed slope. For steep slopes, breakpoint generated infragravity waves are thought to be dominant. On mild-slopes wave group bound infragravity waves dominate. The infragravity wave energy due to the persistence of wave-groupiness into the surf zone is not discussed.

2.2.2 Bound infragravity wave shoaling

Bound infragravity waves shoal as they enter shallow water. However, the shoaling process is different to that of free long waves. Free long waves shoal according to Green's law:

$$\zeta \propto h^{-0.25}$$

Applying the shallow water limit depth relation in the theory of Longuet-Higgins and Stewart [1964] (2.3) to bound infragravity waves leads to a different wave heights:

$$\zeta \propto h^{-2.5}$$

As stated by various authors [e.g. Battjes *et al.*, 2004], numerical studies as well as observations [f.i. Elgar *et al.*, 1992] indicate that the rate of shoaling of bound infragravity waves is greater than that according to Green's law and less than that according to the equilibrium theory of Longuet-Higgins and Stewart. It should be noted however that Longuet-Higgins and Stewart state prior limited validity of their theory on sloping beds.

The shoaling rate of infragravity waves exceeding Green's law implies a transfer of energy to these waves as they shoal. Battjes *et al.* [2004] adopt the theory of Longuet-Higgins and Stewart to state that the energy is delivered primarily through gradients in radiation stresses. In stationary conditions, without dissipation, the energy balance of a 1-dimensional low-amplitude progressive long wave can be written as [Phillips, 1977; in Battjes *et al.*, 2004]:

$$\frac{dF}{dx} = R \equiv -\left\langle U \frac{dS_{xx}}{dx} \right\rangle$$

In the equation given above, the brackets denote phase averaging and the velocity refers to the depth average long-wave particle velocity.

Battjes *et al.* [2004] state that in constant water depth equation (2.1) applies and the stress gradient and particle velocity are out of phase by 90°. Thus the phase average energy transfer R is zero. For energy transfer to be possible, a phase lag must occur between the short wave envelope and the bound long wave elevation. The transfer due to a phase lag is described as:

$$R \cong \frac{1}{2} k_{lw} \hat{U} \hat{S}_{xx} \sin\left(\Delta\varphi\right) \tag{2.4}$$

In equation (2.4) the wave number refers to the long wave and the phase lag is defined as the lag of the bound wave minimum behind the maximum of the short wave envelope. The circumflexes denote amplitude.

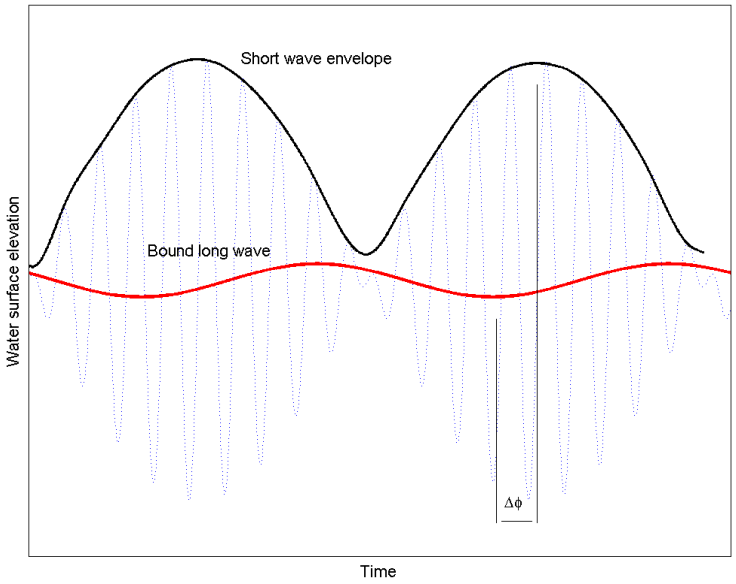


Figure 6 Definition of bound wave phase lag, as stated by Battjes *et al.* [2004]

Battjes *et al.* [2004] use high-resolution wave flume data to confirm the existence of the phase-lag between incident bound long waves and the short wave envelope in the shoaling zone. They find that the shoaling rate of the incident bound long waves varies between nearly that of free long waves (Green's law) for very low frequency bound waves, to nearly that of the equilibrium shallow water limit solution of Longuet-Higgins and Stewart [1964] for high frequency bound waves. The authors state that the shoaling of incident bound long waves is predicted quite accurately on the basis of the estimated rates of energy transfer.

2.2.3 Infragravity wave reflection and dissipation

Infragravity waves generated by incident short waves will partially dissipate in the surf zone and will partially reflect at the shore. Little is known about infragravity wave dissipation in the surf zone. It is suggested that infragravity wave energy dissipation is not inconsistent with quadratic bottom friction processes with additional contributions due to enhanced turbulence caused by wave breaking and swash processes [Henderson and Bowen, 2002; in: Battjes *et al.*, 2004]. The breaking of higher frequency infragravity waves due to the relative steepness of the bed slope is stated as another source of energy dissipation [Battjes *et al.*, 2004; van Dongeren *et al.*, 2006]. It has recently been suggested that infragravity waves transfer energy back to higher frequency waves in extremely shallow water depths [Thomson *et al.*, 2006].

Infragravity waves that are not dissipated, reflect at the shoreline. If the short-waves are normally incident to the shore, the free infragravity waves are likely to reflect away from the coast and escape the nearshore. These waves are called *leaky waves*. It is also possible for reflected infragravity waves to become trapped close to the shore by the bathymetry and refraction. These waves are called *edge waves*. Since a small difference in the angles of incidence of two obliquely incident wave groups combine to create a bound infragravity wave with a larger angle of incidence than either of the wave groups, it is expected that the infragravity field is directionally far broader than that of the incident short waves [Ruessink,

1998]. Therefore, it can also be expected that the majority of free infragravity waves will be trapped along the shore in case of gently sloping wide shore faces [Herbers *et al.*, 1995a; in: Ruessink, 1998]. This hypothesis is supported by field measurements at Imperial Beach, California and Babers Point, Hawaii [Okihiro *et al.*, 1992], where it was found that leaky waves and very high-mode edge waves contribute to less than 10% of infragravity energy at water depths of 8-13m.

2.2.4 Nearshore infragravity wave energy

Both laboratory data [van Thiel de Vries *et al.*, 2006] and in-situ measurements [Wright *et al.*, 1982, amongst others; Aucan *et al.*, 2008] show that infragravity energy dominates the wave energy spectrum in very shallow water and the swash zone, see Figure 7 for one example.

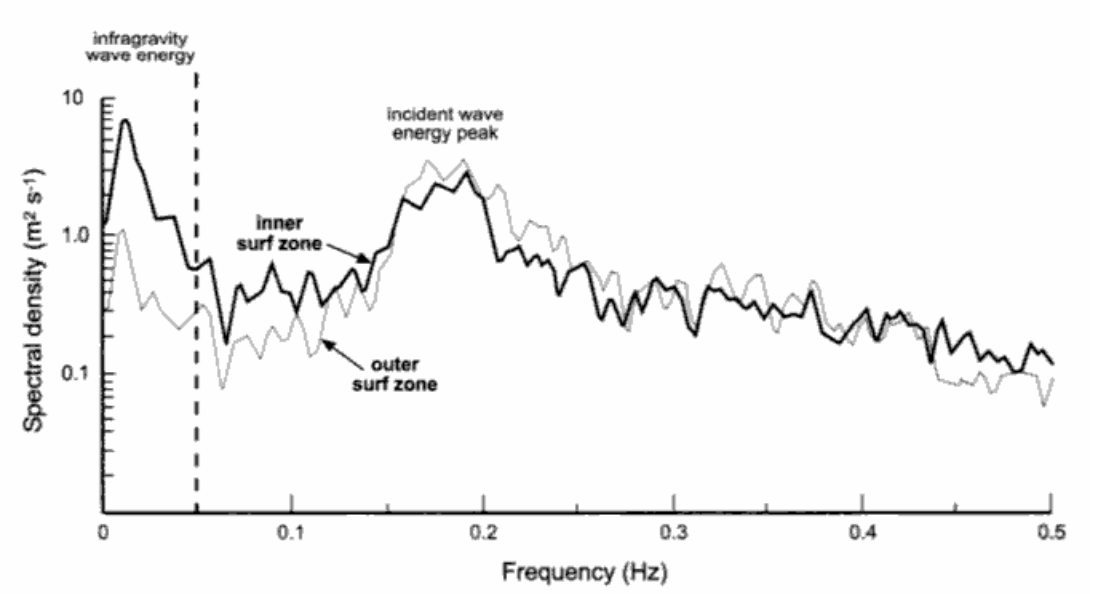


Figure 7 An example of two cross shore velocity spectra from the outer and inner surf zone. Note the increase in the infragravity wave band in the inner surf zone [from Masselink and Hughes, 2003]

This is can be explained by considering the incident short waves. As short waves approach shore, they start to break and eventually disappear in very shallow water. Infragravity waves on the other hand have longer wave lengths and are less steep than the incident short waves. Therefore infragravity waves are unlikely to break on the foreshore and lose energy. Thus energy in the infragravity wave band becomes relatively greater. Additionally, as stated in 2.2.2, energy is transferred from short waves to bound infragravity waves in the shoaling zone. The result of these processes is that the velocity and surface level amplitudes in very shallow water and the swash zone vary predominantly on the time scale of the incident infragravity waves. A schematic representation of the relative short wave and infragravity wave amplitudes in the cross shore is given in Figure 8.

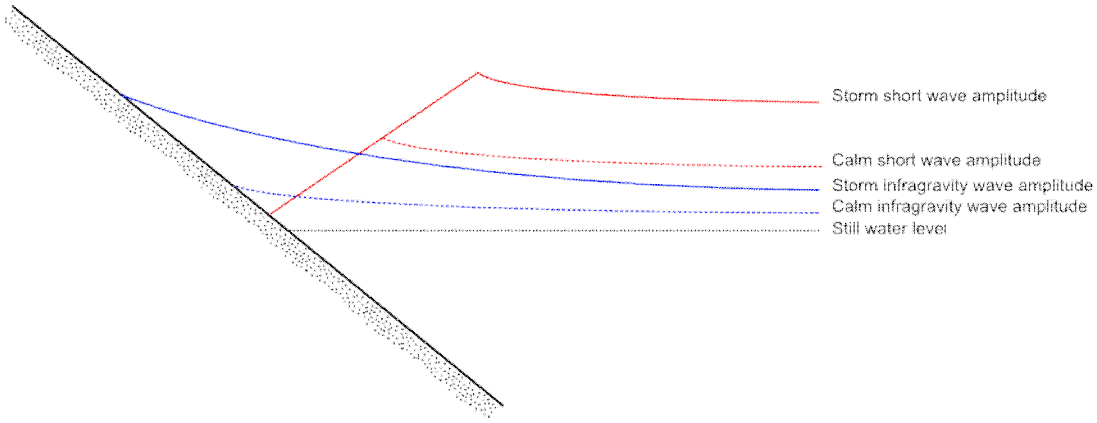


Figure 8 Schematic representation of short wave and infragravity wave amplitude in the nearshore under calm and storm conditions [modified from Holman, 1981]

Due to the dominance of energy in the infragravity frequency band in very shallow water and the swash zone, infragravity waves are important in wave overtopping and run-up on waves and dunes and dune erosion [Overton and Fischer, 1988; van Gent, 2001; in: Reniers *et al.*, 2006].

2.2.5 Modelling infragravity waves

Until recently, comparisons of computed infragravity conditions with field data have been limited [Reniers *et al.*, 2006]. List [1992] compared a one-dimensional model against field data measured at Duck, North Carolina in order to explain the release of bond long waves. Roelvink [1993b] developed a cross shore profile model that simulated the propagation of normally incident wave groups through the surf zone and their associated infragravity waves. The model was validated against several wave flume datasets. Reniers *et al.* [2002; in Reniers *et al.*, 2006] compared a one-dimensional spectral model to measurement data from the DELILAH field campaign and found good agreement for infragravity conditions. The DELILAH data was also used by Van Dongeren *et al.* [2003] to verify a two-dimensional non-linear infragravity wave model SHORECIRC [van Dongeren *et al.*, 1994; Svendsen *et al.*, 2002]. The model was found to be in good agreement in the infragravity frequency band. Van Thiel de Vries *et al.* [2006] compared the results of a modified version of Delft3D [WL | Delft Hydraulics, 2001] that included a surf beat routine, to field and wave flume measurement data. They found not only good spectral agreement, but also showed that water surface and velocity time series in shallow water could accurately be recreated using the model.

2.3 Morphological processes

Sallenger [2000] developed a Storm Impact Scale system with which to predict the morphological response of the subaerial part of barrier islands to storms. In this model the response is determined by four parameters. The hydrodynamic forcing is described by the maximum wave run-up level, R_{high}, and the wave run-down level, R_{low}. The dune profile is described using the height of the primary dunes, D_{high}, and the height of the base of the dune, D_{low}. A sketch of these parameters is given in Figure 9. Note that all four levels are set relative to a fixed vertical datum, lower than D_{low} and R_{low}, for instance MLLW.

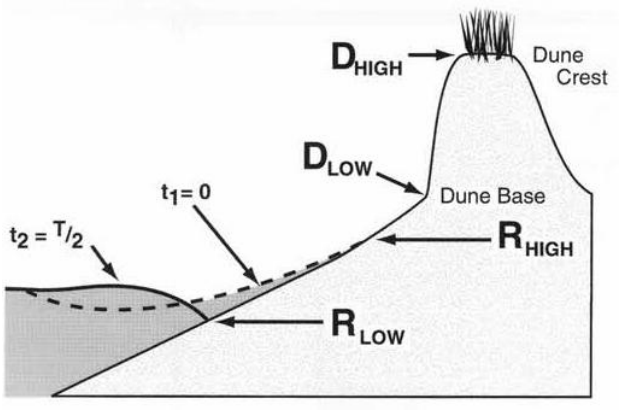


Figure 9 Definition sketch of the parameters used to describe morphological response in the Storm Impact Scale system [taken from Sallenger, 2000]

Sallenger states that four regimes exist which can be described by the relative values of the parameters given above. The first regime is called the *swash regime*. During this regime the movement of water is restricted to the foreshore and beach. This occurs if:

$$\frac{R_{high}}{D_{high}} < \frac{D_{low}}{D_{high}} \tag{2.5}$$

The second regime is called the *collision regime*. In this case the wave run-up collides with the base and face of the dune and dune erosion occurs. The conditions describing this regime are:

$$\frac{D_{low}}{D_{high}} \leq \frac{R_{high}}{D_{high}} < 1 \tag{2.6}$$

If hydrodynamic conditions grow stronger, wave run-up will eventually exceed the dune height. This regime is called the *overwash regime*. Water is able to flow landwards of the dunes, commonly causing features such as washover fans. This regime occurs if two conditions are met:

$$\frac{R_{high}}{D_{high}} \geq 1 \quad \text{and} \quad \frac{R_{low}}{D_{high}} < 1 \tag{2.7}$$

If the storm induced water level exceeds the height of the dunes, the entire system is submerged. The erosion processes on the dunes then become similar to surf zone processes. This regime is called the *inundation regime* and occurs if:

$$\frac{R_{low}}{D_{high}} \geq 1 \tag{2.8}$$

Although the Storm Impact Scale does not provide quantitative answers to many morphological problems, it does provide insight into the stages of dune system morphology

that occur during storms. For this reason, the following sections in this chapter will be based around the four regimes described above.

2.3.1 Swash regime

The swash regime represents relatively common low energy storm conditions. As stated by Sallenger [2000], such conditions lead to sediment being transported offshore from the foreshore and beach. Generally this sediment returns over a period of weeks to months when forcing conditions return to less energetic levels.

This process of erosion and return of sediment on the foreshore and beach has lead to the theory of an equilibrium beach profile. An equilibrium beach profile is defined as cross shore profile of constant shape that is reached after a long period of constant hydrodynamic forcing. The concept of equilibrium profiles under constant laboratory conditions was found valid by many researchers as long ago as 1939 [van de Graaff, 2006]. Recent work continues to support the theory in its application to natural beach faces [e.g. Yates *et al.*, 2008].

Van de Graaff [2006] lists a number of empirical beach profile formulae based on the theory of the equilibrium profile, some of which are described below.

Bruun [1954] developed one of the first predictive equations for the equilibrium beach profile. Based on measurement data of several Danish and Californian coasts, he presented a simple power law relating the water depth to the cross shore distance to the waterline:

$$h(x) = A_{sf} x^{\frac{2}{3}} \tag{2.9}$$

In the equation above, the constant A_{sf} represents a shape factor which is a function of the bed characteristics.

Dean [1977] suggested that natural beach slopes tend toward uniform and equilibrium wave energy dissipation across the surf zone:

$$\frac{1}{h}\frac{\partial\left(Ec_g\right)}{\partial x} = -D_{eq} \tag{2.10}$$

It can be shown that under regular wave forcing and constant breaker index, Dean's law has the same two-thirds power curve as Bruun's equation.

Vellinga [1986] developed an erosion profile similar to the equilibrium profiles of Bruun and Dean. Using laboratory data and historical data of the 1953 storm in the Netherlands, Vellinga proposed a formula for the shape of an erosion profile:

$$h(x) = 0.70\left(\frac{H_0}{L_0}\right)^{0.17} w^{0.44} x^{0.78} \tag{2.11}$$

The erosion profile as presented in the equation above is not an equilibrium profile, but a post-storm profile. Since time is not included in the equation, it does not take into account the duration of the storm. Despite this and certain other limitations, the erosion profile method has been used to calculate the safety of Dutch dunes.

In order to accurately predict time-dependent morphology, much research has been carried out in the field of nearshore and foreshore sediment transport. This has led to the development of several sediment transport formulations for the cross shore, mainly based on the energy dissipation concept, e.g. Kriebel and Dean (1985), and the energetics approach, e.g. Bagnold (1962), Bailard and Inman (1981) [in van de Graaff, 2006]. All of these sediment transport formulae have varying success in representing reality.

Recently, research of sediment transport in the swash zone has increased. Sediment transport in the swash zone has remained difficult to predict because of the complex hydrodynamic conditions in the swash zone (infiltration, asymmetrical uprush and downrush) and the difficulty in making in-situ measurements. Some attempts have been made to introduce new sediment transport formulae for the swash zone based on measurement campaigns [e.g. Puleo *et al.*, 2000; Larson *et al.*, 2004b]. Baldock *et al* [2007] use a probabilistic approach to model morphological bed level change in the swash zone. Despite the prominence of infragravity energy in the swash zone, many theories do not explicitly include infragravity wave movement.

2.3.2 Collision regime

The collision regime is mostly associated with dune erosion. Wave run-up reaches the base and face of the dune and transports sediment offshore and alongshore. According to Sallenger [2000], sediment transported in this way does generally not return to the original location and thus net dune erosion occurs. Other authors suggest that dune erosion is at least partially compensated by aeolian processes redistributing sediment from washover fans and beach face to the dunes [Leatherman and Zaremba, 1987, among others].

Larson *et al*. [2004a] state that there are essentially two types of analytical dune erosion models, namely those based on the equilibrium profile theory and those based on the wave impact approach.

The equilibrium dune erosion models use the theory of the equilibrium beach profiles described in section 2.3.1 and extend the formula to include the dune face and crest. Bruun [1962] applied his former theory of equilibrium beach profiles [Bruun, 1954] to estimate shoreline retreat as a function of sea level rise. The assumption was made that the equilibrium profile would translate shoreward and upward due to sea level rise in such a manner that sediment is conserved in the cross shore profile. This has come to be known as Bruun's law.

The work carried out by Vellinga [1986] included dune erosion as well as beach profile change due to storms, see and can also be considered to be an equilibrium-type model. A earlier relation set up by Vellinga was used by Van de Graaff [1986] to develop a probabilistic design method for dunes on the Dutch coast.

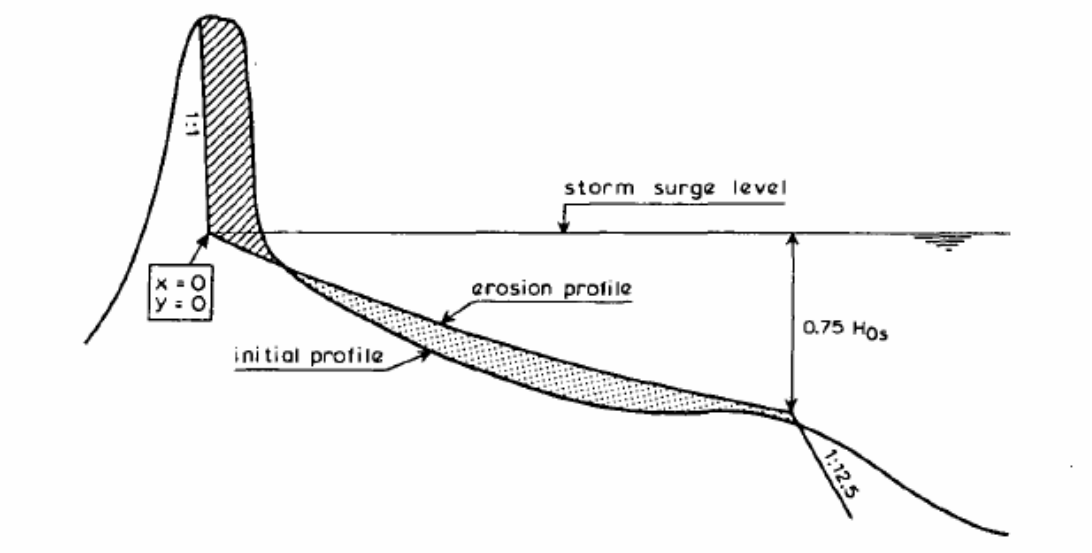


Figure 10 Dune erosion in the erosion profile model of Vellinga [taken from Vellinga, 1986]

Kriebel and Dean [1985] developed a time-dependent model to predict dune retreat based on the equilibrium wave dissipation theory of Dean [1977]. The model was verified using various idealized cases of dune erosion during Hurricane Eloise. By assuming sediment transport rates in the cross shore are a linear function of the difference between the current wave energy dissipation rate and the equilibrium rate, they found an exponential retreat of the dune over time:

$$x_{dune}(t) = x_{dune,equilibrium}\left(1-\exp\left(\frac{-t}{T_{dune}}\right)\right) \tag{2.12}$$

They showed that the morphological time scales related to the equilibrium profile of the beach and dune retreat were significantly larger than the time scales of storms. Thus dune retreat is less than would be predicted according to the equilibrium equation.

Larson *et al*. [Larson and Kraus, 1989; Larson *et al.*, 1990] developed a numerical model called SBEACH that is able to simulate beach face and dune erosion during storms. The model has been verified against wave tank and field data. In the model different sections of the nearshore and beach are handled using separate empirical equilibrium equations. Time dependency is found through exponential decay. Dune erosion is handled by allowing steep dune slopes to avalanche to a stable angle known as the residual angle after shearing [Allen, 1970; in Larson and Kraus, 1989].

Other authors have also applied the exponential retreat rate decay to models. Larson *et al*. [2004a] suggest that such relations could theoretically be applied to all equilibrium-based models to make the results sensitive to storm duration.

An alternative to the equilibrium-based models is the wave impact model [Fischer and Overton, 1984; Nishi and Kraus, 1996; in Larson *et al.*, 2004a]. In this model, a relationship is assumed between the frequency and force of wave impacts on a dune face, and the dune erosion. These models have been verified against wave flume data and have shown that a linear relationship between the summation of calculated swash forces over selected time

intervals and eroded volumes could predict the measured evolution of the dune erosion [Larson *et al.*, 2004a].

Larson *et al*. [2004a] developed a model using the wave impact theory. They suggested that the weight of the eroded sediment and force of the wave bores hitting the dune face are linearly related:

$$\Delta W_{sed} = cF_{bore} \tag{2.13}$$

The force of the bores was determined by:

$$F_{bore} = m_{bore}\frac{du_{bore}}{dt} \tag{2.14}$$

In which the mass of the bore is found from geometrical relations, the velocity of the bore is found from ballistics theory and the time period is assumed to be the wave period of the incident waves. The model was tested against laboratory and field data and was found to reproduce the measurements relatively well. However in order to achieve this, empirical coefficients for the sediment transport had to be tuned differently, leading to a large spread in the values of these coefficients between cases. The overall practicality of this model has therefore yet to be proven.

A third type of model not discussed by Larson *et al*. [2004a] is listed by Tuan [2007]. The author refers to such models as physically-based models. Such models are defined by the fact that they attempt to accurately model all the physical processes involved, without assumptions modifying the physics of the processes. The basic formulation used in cross shore evolution models of this type is:

$$S_x(x,t) = \int_{z=z_{bed}}^{\eta} u(x,t,z)c(x,t,z)dz \tag{2.15}$$

In most models equation (2.15) is reduced to a simpler form, usually approximating cross shore sediment transport rate by means of a time averaged sediment transport rate. Some available models of this type are DUROSTA [Steetzel, 1993], UNIBEST-TC [Stive and Wind, 1986; Roelvink and Stive, 1989; Bosboom *et al.*, 2000] and XBeach [Roelvink *et al.*, 2007]. A interesting, but little verified, hybrid model of the equilibrium theory and process modelling is described by Leont'yev [1996].

2.3.3 Overwash and inundation regimes

Sallenger [2000] associates the overwash and inundation regimes with large depositions of sediment from the beach face and dunes on the back barrier. Transport of sediment can take place over large distances. An example is given of the remnant of an eroded spit found a kilometer landwards of the original position after Hurricane Andrew. Although the forcing conditions differ distinctively between the overwash and inundation regimes, the morphological response of the barrier system has a less clear distinction. For this reason

these two regimes are discussed together in this section. In the extensive review of the current state of knowledge on overwash given by Donnelly *et al*. [2006], the authors refer to the overwash regime as *runup overwash* and the inundation regime as *inundation overwash*.

Donnelly *et al*. [2007] analyzed over 110 pre- and post-storm prototype cross shore overwash profiles. They came to the conclusion that the barrier island – dune system has seven types of morphological response to runup and inundation overwash, see Figure 11. In order of increasing severity, these are:

- Crest accumulation. This is thought to occur when wave runup just reaches the crest of the dune. Due to friction and percolation the flow of water stops and sediment is deposited on the top of the dune. Later work by Donnelly [2007] shows that crest accumulation only occurs under low surge level conditions.
- Landward translation of dunes/berms. Donnelly *et al*.[2007] state that the landward translation of dunes is difficult to explain. The authors hypothesize that the translation may be caused by a period of dune lowering, followed by crest accumulation during less severe conditions, thereby restoring the dune height to its original value. Donnelly [2007] suggests that dune translation occurs in the case of wide-crested dunes or systems with multiple dunes. Additionally low runup levels are required.
- Dune lowering. In this case sediment is transported from the seaward side of the crest landward. Thus the height of the dune is lowered and the height of the back barrier is increased.
- Dune destruction. If dune lowering continues until there is no discernable dune remaining after the storm, the response is called dune destruction. It is thought that dune destruction occurs more frequently on narrow dunes and dunes of small initial volume [Donnelly, 2007]. Sediment is transported from the dune to the back barrier, where it is deposited due to lateral flow expansion and friction and percolation losses. It is suggested by Donnelly *et al*.[2007] that dune lowering and dune destruction occur under runup overwash conditions.
- Barrier accretion. In this case sediment is eroded from the foreshore and deposited on the back barrier. As the deposits do not reach the back barrier bay, the barrier island becomes narrower and increases in height. Additionally, the back slope becomes steeper.
- Barrier rollover. If sediment is transported from the nearshore across the island and deposited in the back barrier bay, the entire barrier island translates landward. It is thought that the processes involved in barrier rollover are different to those involved in dune translation [Donnelly *et al.*, 2007].
- Barrier disintegration. If hydraulic conditions are severe enough, sediment is eroded from the barrier island and deposited subaqueously in the back barrier bay or offshore. Breaching may occur as a result of continued erosion. A example of barrier disintegration is the Chandeleur Islands after Hurricane Katrina [e.g. Sallenger *et al.*, 2008].

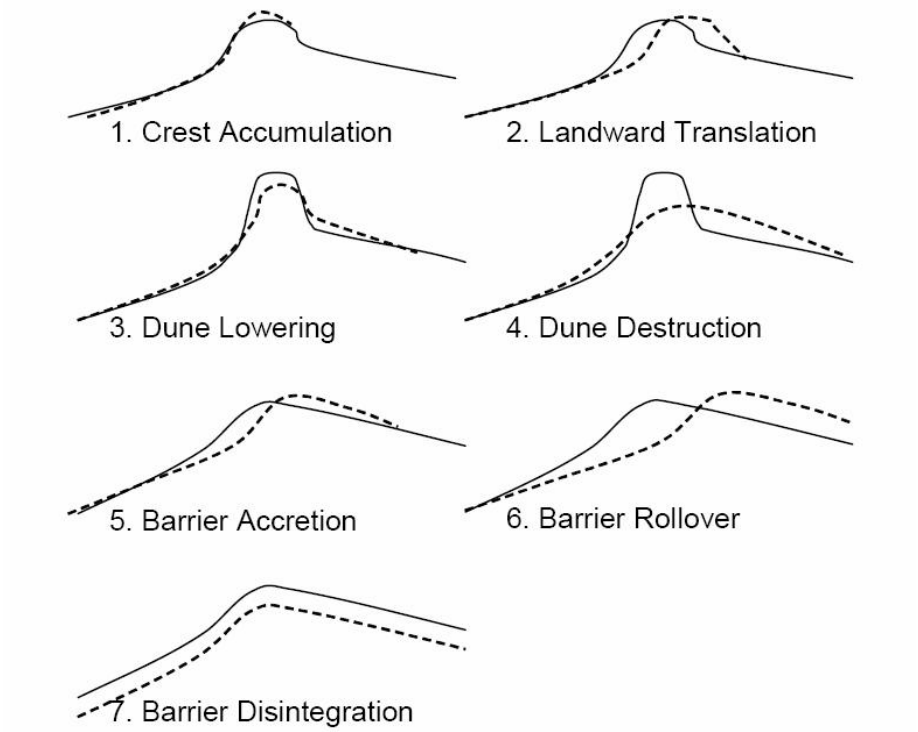


Figure 11 Seven types of barrier island – dune system morphological response to overwash [taken from Donnelly, 2007]

On coastlines with varying dune heights, overwash generally exploits existing gaps in the foredunes and old overwash locations [Donnelly *et al.*, 2006]. It has been suggested that on low coasts without dunes, overwash locations may be determined by hydraulic forcing variations, e.g. zero mode edge waves or standing waves between two capes [Orford and Carter, 1982; in Donnelly *et al.*, 2006].

At a single overwash location water is funneled through the gap in the foredunes. This point is referred to as the throat of the overwash. The velocity of the overwashing water drops due to friction and percolation as it spreads laterally on the back barrier. Sediment transported in the overwash event, the *washover*, is deposited on the back barrier in a fan-like pattern. The morphological features created by this sediment are called *washover fans*, see Figure 12. Washover fans may become constricted due to the topography of the back barrier. In this case the overwash fan may channel far inland, before spreading laterally, see Figure 13. If the longshore distance between overwash throats is limited, or if the lateral spreading of the overwashing water is particularly large, washover fans may merge to become *washover terraces*. Washover terraces may also form on uniform, low-lying islands and beaches [Donnelly *et al.*, 2006]. In the case of inundation overwash, water flow is not constricted to channels and instead covers the entire back barrier. This type of flow is called *sheetwash* and leaves sheetwash deposits across the entire back barrier.

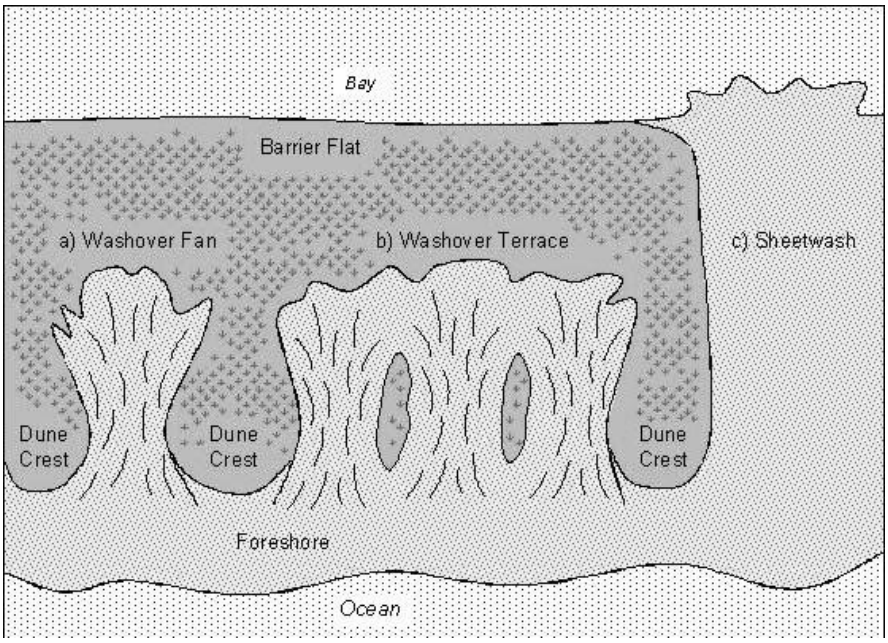


Figure 12 Schematic representation of a washover fan, washover terrace and sheetwash [taken from Donnelly *et al.*, 2006]



Figure 13 Washover constricted in a beach access path on Ocracoke Island, North Carolina [taken from Donnelly *et al.*, 2006]

Modeling washover

One of the first attempts to quantitatively model overwash was carried out by Cleary and Hosier [1979; in Donnelly *et al.*, 2006]. In this study, a high negative correlation was found between the vegetation in cross shore transects and the history of overtopping. Using this information, the authors were able to produce overwash susceptibility rankings for areas along the North Carolina coast. More recently, newer models have been developed to determine the likelihood and magnitude of overwash based on cross shore data, for instance the Storm Impact Scale of Sallenger [2000].

The models described above give order of magnitude insight into overwash processes. In order to model actual profile change during overwash, more detailed modeling is required. Describing sediment transport during overwash is an essential part of this.

Williams [1978; in Donnelly *et al.*, 2006] presented two formulae to describe washover volumes due to runup overwash in terms of the excess runup height ΔR (the theoretical runup height less the height of the dune crest or approximately R_{high} - D_{high}) and the incoming wave period T.

$$Q_s = \frac{K_1}{T}\left(\Delta R\right)^{\alpha}$$
$$Q_s = \frac{K_2}{T}\Delta R \cdot e^{-K_3 \Delta R} \qquad (2.16)$$

In equation (2.16) K values are proportionality constants. The two formulae were compared to laboratory data and were both found to calculate order-of-magnitude overwash volumes. Neither formula consistently produced better results.

Kobayashi *et al*. [1996] carried out a wave flume experiment examining wave overtopping and runup overwash on a dune profile. Overtopping water and sediment volumes caused by incoming irregular waves were collected in a stilling basin. It was found that nearly all sediment transport took place as bed load. A linear relation was found between the average overtopping water volume and sediment volume without voids:

$$Q_s = 0.0389Q \qquad (2.17)$$

This relation was used successfully by Tanaka *et al*. [2002] to calculate the order of magnitude of washover in the Gamo Lagoon, Japan.

Nguyen *et al.* [2006] modified the earlier work of Williams and others to produce a new empirical runup overwash transport formulation:

$$Q_s = 0.0011\frac{D_{high}}{R}\frac{t_D}{T}\Delta R^2 \qquad (2.18)$$

In equation (2.18), t_D is the overwash duration and R is the runup height. The relation was validated against ten field measurements. In most cases the sediment transport rate was within a factor of two of the observed transport.

Tuan *et al.* [2006b] developed a modifed UNIBEST-TC numerical model, which included wave overwash based on their earlier work [Tuan *et al.*, 2006d]. An upwind numerical scheme was used to solve the hydrodynamics of the overwashing water. The morphology of the back barrier was calculated using an empirical relation between the width and depth of the washover channel and fan. The results compared satisfactorily to laboratory data.

Baldock *et al.* [2005] compared a numerical swash hydrodynamic model to a wave flume model of a truncated beach. They found good agreement between measured and calculated overwash volumes. Using a Shields model for bedload transport and the modelled velocity field, the authors succeeded in modelling runup sediment washover volumes relatively well. At this stage it is not known how well the model will perform in prototype cases [Donnelly *et al.*, 2006].

According to Donnelly *et al.* [2006] the only model that has successfully predicted 1D profile change during runup overwash in prototype conditions is SBeach [Larson and Kraus, 1989; Larson *et al.*, 1990]. Formulations have been added to SBeach to represent sediment transport in the swash zone, the dune crest and the back slope of the dune. Swash zone transport is determined by the uprushing bore velocity, u_{bore}, and bore period, T, the duration of submergence, t_0, and the difference between the beach slope, $\beta_{foreshore}$, and the equilibrium beach slope, $\beta_{equilibrium}$ [in Donnelly *et al.*, 2006]:

$$q_{s,swash} = K_c \frac{u_{bore}^3}{g}\left(\tan\beta_{foreshore} - \tan\beta_{equilibrium}\right)\frac{t_0}{T} \tag{2.19}$$

Following the work of Kobayashi *et al.* [1996], the washover sediment on the dune crest is assumed to be linearly related to the average overwash volume per wave:

$$q_{s,crest} = K_B q_{crest} = K_B 2\sqrt{\frac{2g}{R}}\left(R - D_{high}\right)^2 \tag{2.20}$$

The transport rate on the landward slope of the dune is related to the velocity cubed, and linear lateral spreading of the flow on the back slope is assumed:

$$q_{s,backslope} = \frac{q_{s,crest}}{1 - \frac{\mu_{spreading} x}{B_{throat}}} \tag{2.21}$$

In equation (2.21) x refers to the cross shore distance from the crest of the dune (negative in landward direction), μ is a spreading coefficient and B_{throat} is the width of the overwash throat. An analytical solution to almost identical formulations was given by Larson *et al.* [2005].

Little work has been carried out to model washover caused by inundation overwash. At this stage it is unclear if specific inundation models are required or if for instance high velocity sediment transport formulations used in river engineering will suffice. Donnelly *et al.* [2006] do describe the work of Pirrello [1992], which focusses specifically on inundation overwash. However, they state that the laboratory experiments in the work of Pirrello were insufficient to fully verify the assumptions made in the model.

Breaching

In case of extreme forcing, enough sediment can be eroded from a dune row or barrier island to form a channel that remains below sea level after the storm event. This process is called breaching and can be considered to be a special case of overwash. Breaching of dune systems can lead to catastrophic flooding in low-lying areas behind the dunes. According to Kraus [2003], there are three causes of natural barrier island breaching: runup or inundation overwash, elevated water levels in the back barrier bay causing liquifaction and piping, and the narrowing of the barrier island due to a reduction in longshore sediment supply.

Tuan [2007] discusses a number of models set up to simulate breaching caused by overwash, but states that they are generally limited in their applicability and accuracy due to the current incomplete knowledge of the morphological processes involved in breaching. The breach models reviewed by Tuan can be divided into four types: empirical, analytical, parametric and numerical models. A number of these breach models will be discussed in the following sections.

Kraus [2003] developed an analytical model to describe the incipient breaching of coastal barriers. The model assumes an idealized breach shape and that the breach will reach an equilibrium depth and width if forcing conditions do not change. By solving coupled solutions for the development of the breach depth and width, it is shown that the breach growth follows an exponential behaviour with a characteristic time scale. This time scale is determined by the ratio of the equilibrium breach volume and the representative maximum sediment transport rate through the breach. Kraus goes on to show that seven variables control the idealized breach growth: the initial breach width and depth, the equilibrium breach width and depth, the width of the barrier island and the representative maximum sediment transport at the sides and bottom of the breach. The analytical model was compared to observations of the 1980 breach at Moriches Inlet, New York and was found to reproduce the general qualitative and quantitative features of barrier island breaching. The drawback of this model is that the equilibrium breach size must be known prior to simulation.

Visser [1998] developed a parametric model to describe breach growth in sand dikes. The term parametric is used in this sense to describe a model that imposes assumptions about the breach evolution [Tuan, 2007]. Visser describes five stages in sand dike breaching based on observations of various laboratory experiments and a prototype-scale field test. His model assumes that a small initial breach exists at the top of the dike at the start of the simulation. In stage I, see Figure 14, the overwashing water erodes a channel on the back slope of the dike until a critical channel slope is reached at $t=t_1$. The width and depth of the initial breach remain constant. In stage II, the erosion channel maintains its critical slope, but moves seaward until it reaches the front of the dike at $t=t_2$. In stage III, the breach growth

accelerates as the widening and deepening of the breach allows for more sediment transport. The flow characteristics change from highly supercritical for $t \leq t_2$, to transcritical at $t=t_3$. At the end of stage III the dike is fully breached. The further growth of the breach depends on certain geometrical and material properties of the dike, such as the presence of a toe construction or a relatively inerodable foreland and the resistance of the base of the dike to erosion. In the case of natural sand dikes on sand beds, the breach will continue to widen and deepen in stage IV. During this stage the flow through the breach becomes subcritical. In stage V the breach growth in vertical direction stops, but the breach continues to widen until an equilibrium width is found at $t=t_5$.

In order to simulate breach growth, Visser [1998] developed a numerical cross shore profile model called BRES. In BRES, separate formulations are used to calculate hydrodynamic and morphological conditions in each of the five stages of breaching. The numerical model was verified using a field test and laboratory data. Good agreement was found between the measurements and the model prediction for the increase in breach width.

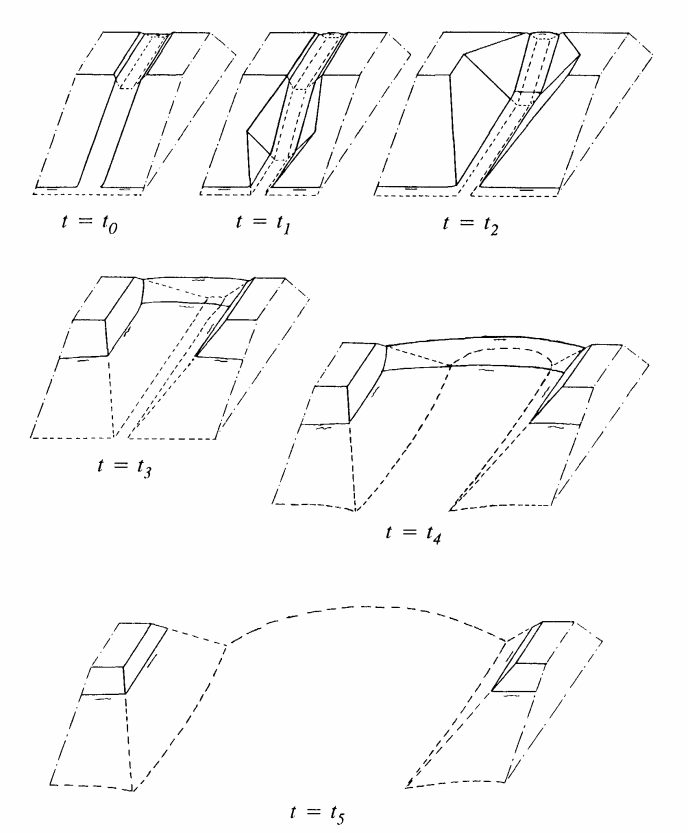


Figure 14 Five erosion stages in sand dike breaching [taken from Visser, 1998]

Tuan [2007] and Tuan *et al*. [2006a; 2006c] developed a profile-based numerical model to simulate sand barrier breaching due to overflow. An important development in the model was the introduction of a source term for the back barrier hydraulic jump in order to accurately model the hydraulic jump-induced scour hole. Sediment transport in the breach is calculated using the transport relations of Van Rijn [1984a; 1984b]. An empirical relation was used to describe the ration between the width and depth of the back barrier erosion channel. The numerical model was validated against laboratory data, a field experiment and post-typhoon field observations. The model was shown to be capable of simulating the time-

dependent development of sand barrier breaches under arbitrary hydraulic conditions, without the prior definition of morphological evolutionary stages.

Roelvink *et al*. [2003] simulated breaching using Delft3D. The model was validated using the laboratory and field measurements of Visser [1998] and was subsequently applied to model breaching along the coast of Long Island, New York. Effects of short wave and infragravity wave swash were included by the addition of a higher harmonic component on the offshore water level boundary condition. The study showed that Delft3D remains numerically stable under breaching conditions and that the breaching process is qualitatively and quantitatively well represented.

3 The XBeach model

3.1 Introduction

After the devastating hurricane seasons of 2004 and 2005 in the USA, the United States Army Corps of Engineers (USACE) received funding for the MORPHOS-3D project. MORPHOS-3D aims to bring together models and data in order to predict the effects of large storms and hurricanes. The project will attempt to predict all aspects of hurricanes, from wind fields, to wave and surge generation, to coastal erosion and flooding. XBeach is being developed within the MORPHOS-3D framework. The purpose of XBeach is to model nearshore hydrodynamics and morphodynamics in a time-dependent, process-based manner. Once completed, XBeach will be able to predict nearshore waves and currents, dune erosion, overwash and breaching of barrier islands and dunes. XBeach is designed to incorporate infragravity wave hydraulics. It will be the first program to model these processes in a 2DH environment. The model, which is public-domain, is being developed by IHE-UNESCO, Delft University of Technology, Deltares and the University of Miami. XBeach is written in Fortran 90/95.

3.2 Model setup and governing equations

The information in this section is a brief summary of the XBeach Annual Report and Model Description [Roelvink *et al.*, 2007].

XBeach uses a coordinate system in which the x-axis is oriented towards the coast, approximately perpendicular to the shoreline, see Figure 15. The model uses a staggered grid, in which conservative quantities (water level, bed level, etc.) are calculated in cell centres and fluxes (velocities, sediment transport, radiation stress gradients, etc.) are calculated in cell interfaces, see Figure 16. XBeach allows the grid size to vary in cross shore and longshore direction.

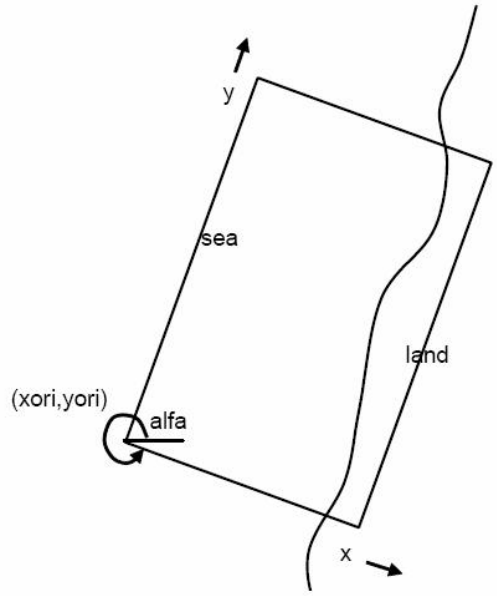


Figure 15 XBeach model orientation [taken from Roelvink *et al.*, 2007]

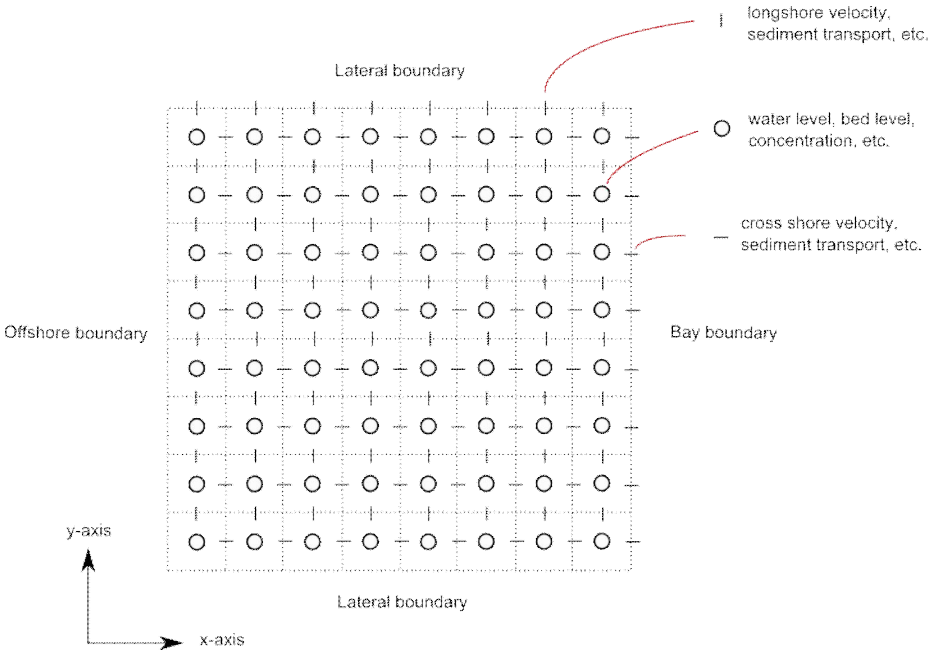


Figure 16 XBeach staggered grid [modified from Roelvink *et al.*, 2007]

3.2.1 Short wave equations

XBeach solves the time-dependent short wave action balance on the scale of wave groups. The equation set is similar to that used in the second generation HISWA model [Holthuijsen *et al.*, 1989]. The directional distribution of the short wave action density is taken into account in the model, but the frequency distribution is reduced to a single representative peak frequency. The wave action balance is given as follows:

$$\frac{\partial A}{\partial t}+\frac{\partial c_x A}{\partial x}+\frac{\partial c_y A}{\partial y}+\frac{\partial c_\theta A}{\partial \theta}=-\frac{D}{\sigma} \tag{3.1}$$

Wave action is determined as:

$$A(x,y,\theta)=\frac{E(x,y,\theta)}{\sigma(x,y)}$$

The x- and y-velocities in equation (3.1) represent the summation of the respective components of the group velocity and background current, if wave current interaction is included. The velocity in directional space takes into account refraction due to bottom and currents. XBeach does not calculate wave diffraction and does not include source terms for waves generated by wind.

Wave breaking is modelled according to Baldock *et al.* [1998], or Roelvink [1993a]. Preference is made for Roelvink in the case of irregular waves and Baldock *et al.* for regular waves. Both models produce a value for the dissipation that is used in equation (3.1).

From the spatial distribution of wave energy, radiation stresses and wave forcing is calculated:

$$\begin{aligned} F_{w_x} &= -\left(\frac{\partial S_{xx}}{\partial x}+\frac{\partial S_{xy}}{\partial y}\right) \\ F_{w_y} &= -\left(\frac{\partial S_{yy}}{\partial y}+\frac{\partial S_{yx}}{\partial x}\right) \end{aligned} \tag{3.2}$$

3.2.2 Roller energy balance

A roller energy balance in included in XBeach in order to model energy from breaking waves. Dissipation of short wave energy is used as a source term in the roller energy balance. As with the short wave action balance, directional distribution of the roller energy is resolved, but frequency distribution is not:

$$\frac{\partial E_{roller}}{\partial t}+\frac{\partial c_x E_{roller}}{\partial x}+\frac{\partial c_y E_{roller}}{\partial y}+\frac{\partial c_\theta E_{roller}}{\partial \theta}=-D_{roller}+D_{waves} \tag{3.3}$$

The x- and y-velocities in equation (3.3) represent the summation of the respective components of the roller celerity and background current, where roller celerity is found from linear wave theory. The velocity in directional space takes into account refraction due to bottom and currents.

Roller energy dissipation is calculated according to Deigaard [1993], using roller induced surface shear stress expressed by Svendsen [1984].

Roller induced shear stresses are calculated from the spatial distribution of roller energy:

$$\begin{aligned} S_{xx,roller} &= \int \cos^2(\theta) E_{roller} d\theta \\ S_{yy,roller} &= \int \sin^2(\theta) E_{roller} d\theta \\ S_{xy,roller} &= \int \sin(\theta)\cos(\theta) E_{roller} d\theta \\ S_{yx,roller} &= \int \sin(\theta)\cos(\theta) E_{roller} d\theta \end{aligned} \tag{3.4}$$

The radiation stresses in equation (3.4) are added to the wave induced radiation stresses before the wave forcing is calculated.

3.2.3 Shallow water equations

XBeach solves the momentum and mass balance equations on a staggered grid: momentum balance is solved in cell interfaces, mass balance in cell centres. To include wave-induced mass fluxes and return flows in shallow water, XBeach uses the Generalized Lagrangian Mean formulation to solve the shallow water momentum equations [Andrews and McIntyre, 1978; Walstra *et al.*, 2000]. In the GLM-method Lagrangian, Eulerian and Stokes velocities are related as follows:

$$\begin{aligned} u^L &= u^E + u^S \\ v^L &= v^E + v^S \end{aligned} \tag{3.5}$$

Stokes velocities are calculated from the wave and roller energy:

$$\begin{aligned} u^S &= \frac{\left(E_{waves} + 2E_{roller}\right)\cos(\theta)}{c\rho h} \\ v^S &= \frac{\left(E_{waves} + 2E_{roller}\right)\sin(\theta)}{c\rho h} \end{aligned} \tag{3.6}$$

The GLM-shallow water equations, without Coriolis forcing, are given as follows:

$$\begin{aligned} &\frac{\partial u^L}{\partial t} + u^L \frac{\partial u^L}{\partial x} + v^L \frac{\partial u^L}{\partial y} - \eta_h \left(\frac{\partial^2 u^L}{\partial x^2} + \frac{\partial^2 u^L}{\partial y^2} \right) = \\ &\qquad - g\frac{\partial \eta}{\partial x} - g\frac{u^E \left|u^E\right|}{C_f^2 h} + \frac{F_{w_x}}{\rho h} + \frac{F_{wind_x}}{\rho h} \end{aligned} \tag{3.7}$$

$$\begin{aligned} &\frac{\partial v^L}{\partial t} + v^L \frac{\partial v^L}{\partial y} + u^L \frac{\partial v^L}{\partial x} - \eta_h \left(\frac{\partial^2 v^L}{\partial y^2} + \frac{\partial^2 v^L}{\partial x^2} \right) = \\ &\qquad - g\frac{\partial \eta}{\partial y} - g\frac{v^E \left|v^E\right|}{C_f^2 h} + \frac{F_{w_y}}{\rho h} + \frac{F_{wind_y}}{\rho h} \end{aligned} \tag{3.8}$$

$$\frac{\partial \eta}{\partial t} + \frac{\partial u^L h}{\partial x} + \frac{\partial v^L h}{\partial y} = 0 \tag{3.9}$$

The horizontal eddy viscosity coefficient in the surf zone is assumed to be related to wave breaking and thus the roller energy dissipation [Battjes, 1975; Reniers *et al.*, 2004]. This roller contribution is added to a global value for the horizontal eddy viscosity:

$$\eta_h = \eta_{h0} + h\left(\frac{D_{roller}}{\rho}\right)^{\frac{1}{3}} \tag{3.10}$$

At this stage it is unclear if equation (3.10) is physically correct as the first term on the right-hand side may be superfluous in combination with the second term.

3.2.4 Sediment transport

XBeach uses a depth-averaged advection-diffusion scheme to transport sediment [Galapatti, 1983]:

$$\frac{\partial hC}{\partial t} + \frac{\partial hCu^E}{\partial x} + \frac{\partial hCv^E}{\partial y} + \frac{\partial}{\partial x}\left(D_s h \frac{\partial C}{\partial x}\right) + \frac{\partial}{\partial y}\left(D_s h \frac{\partial C}{\partial y}\right) = \frac{hC_{eq} - hC}{T_s} \tag{3.11}$$

In equation (3.11) the adaptation time T_s is approximated with the local water depth and sediment fall velocity.

The equilibrium concentration is calculated using the Soulsby-Van Rijn formulation [Soulsby, 1997]:

$$C_{eq} = \frac{A_{sb} + A_{ss}}{h}\left(\left(\left|u^E\right|^2 + 0.018\frac{u_{rms}^2}{C_d}\right)^{0.5} - u_{cr}\right)^{2.4}\left(1 - \alpha_b m\right) \tag{3.12}$$

In equation (3.12) A_{sb} and A_{ss} are bed load and suspended load coefficients and are functions of the local water depth, grain size and relative density of the sediment. The drag coefficient C_d is due to flow velocity only. In order to set sediment in motion, the combined Eulerian velocity and orbital velocity must exceed a threshold velocity u_{cr}. The last term in equation (3.12) introduces bed slope effects. This has not yet been implemented in XBeach.

Note that sediment transport due to short wave asymmetry is not included in XBeach. Methods exist to include this effect, averaged over wave group periods, such as that described by Reniers *et al.* [2004]. This may be included in later versions of XBeach.

3.2.5 Bed level change

XBeach uses sediment transport gradients to make bed level updates. Sediment transport rates are calculated as:

$$\begin{aligned} S_x &= hCu^E - D_s h\frac{\partial C}{\partial x} - f_{slope}\left|u^L\right| h\frac{\partial z_b}{\partial x} \\ S_y &= hCv^E - D_s h\frac{\partial C}{\partial y} - f_{slope}\left|v^L\right| h\frac{\partial z_b}{\partial y} \end{aligned} \tag{3.13}$$

In equation (3.13) f_{slope} is a slope correction coefficient, the value is determined by the user.

Bed level change due to sediment transport rate gradients is calculated as follows:

$$\frac{\partial z_b}{\partial t} + \frac{f_{mor}}{(1-p)}\left(\frac{\partial S_x}{\partial x} + \frac{\partial S_y}{\partial y}\right) = 0 \tag{3.14}$$

in which p is porosity and f_{mor} is a morphological acceleration factor.

In order to simulate dune slumping during storm conditions and the movement of sediment from the dry regime to the wet regime, XBeach uses an avalanching algorithm. Avalanching occurs if the bed slope near the waterline exceeds a user-set critical value for wet or dry points:

$$\left|\frac{\partial z_b}{\partial x}\right| > m_{cr} \quad , \quad \left|\frac{\partial z_b}{\partial y}\right| > m_{cr} \tag{3.15}$$

Bed level change in cross shore direction is then calculated by:

$$\begin{aligned} \Delta z_b &= \left(\left|\frac{\partial z_b}{\partial x}\right| - m_{cr}\right)\Delta x \quad , \quad \frac{\partial z_b}{\partial x} > 0 \\ \Delta z_b &= -\left(\left|\frac{\partial z_b}{\partial x}\right| - m_{cr}\right)\Delta x \quad , \quad \frac{\partial z_b}{\partial x} < 0 \end{aligned} \tag{3.16}$$

Similar equations are used to calculate bed level change in longshore direction. Morphological acceleration is taken into account by iterating f_{mor} times through the algorithm. To ensure large shockwaves are not generated, slumping is limited to a maximum value per second.

3.3 Numerical scheme

XBeach must be able to handle many complex hydrodynamic situations, including supercritical flow, hydraulic jumps and long wave bores. Therefore a very robust numerical

scheme is required. An explicit scheme is used to minimize numerical diffusion and to allow easy insight into the code for future programmers.

Wave action and roller energy is solved using First Order Upwind spatial and Euler Explicit time integration.

$$\begin{aligned}\frac{\partial c^n A^n}{\partial x}(i,j,k) &= \frac{c^n_{i,j,k}A^n_{i,j,k} - c^n_{i-1,j,k}A^n_{i-1,j,k}}{x_{i,j} - x_{i-1,j}} \quad , \; c^n_{i,j,k} > 0 \\ \frac{\partial c^n A^n}{\partial x}(i,j,k) &= \frac{c^n_{i+1,j,k}A^n_{i+1,j,k} - c^n_{i,j,k}A^n_{i,j,k}}{x_{i+1,j} - x_{i,j}} \quad , \; c^n_{i,j,k} < 0\end{aligned} \tag{3.17}$$

$$\frac{A^{n+1}_{i,j,k} - A^n_{i,j,k}}{\Delta t} = -\left[\frac{\partial c^n_x A^n}{\partial x}\right]_{i,j,k} - \left[\frac{\partial c^n_y A^n}{\partial y}\right]_{i,j,k} - \left[\frac{\partial c^n_\theta A^n}{\partial \theta}\right]_{i,j,k} - \left[\frac{D}{\sigma}\right]_{i,j,k} \tag{3.18}$$

Equation (3.17) shows an example of the Upwind wave action scheme for propagation along the x-axis, in which c represents the cross shore component of the wave group velocity. Similar equations are used for propagation in longshore and directional space. These values are used in equation (3.18) in which Euler Explicit time integration takes place. XBeach allows the user to prescribe stationary wave conditions on the offshore boundary. In this case the wave action and roller energy balances are not integrated in time, but are iterated until the equilibria across the model domain are found.

For the GLM-shallow water equations, a momentum conservative method is applied following Stelling and Duinmeijer [2003]. This method improves long wave run-up and back wash on the beach face, while still retaining a simple first order approach [Roelvink *et al.*, 2007]. Spatial and temporal integration are First Order Upwind and Euler Explicit respectively. First order accuracy is accepted as there is a need for small spatial and temporal steps to represent the strong gradients in the nearshore and swash zone [Roelvink *et al.*, 2007].

The sediment concentration advection-diffusion scheme is solved using First Order Upwind and Euler Explicit integration.

3.4 Boundary conditions

Boundary conditions are required to inform the interior of the numerical model about the world outside the model. Boundary conditions ensure that the model produces only one out of an infinite set of possible answer. Because of the strong influence of boundary conditions on the result of the model, it is essential to have properly defined boundaries. The boundary conditions used in XBeach are described in the following sections.

3.4.1 Short wave boundary conditions

Offshore boundary

In XBeach short wave forcing only occurs on the offshore boundary. XBeach allows various methods of short wave forcing, but only those used in this thesis will be described.

The most simple short wave offshore boundary condition is the stationary wave condition, or monochromatic short waves. In this case incoming wave energy is uniform in longshore direction and does not vary in time. Since there is no variation in short wave energy, no bound infragravity waves are generated. The short wave energy at the offshore boundary is given as:

$$E_{boundary}(\theta) = \frac{1}{8}\rho g H_{rms}^2 \cos^m(\theta - \theta_{mean}) \tag{3.19}$$

In this case the user specifies the incoming short wave height and period, the mean wave direction and the coefficient of directional spreading m.

In XBeach it is also possible to force the offshore boundary with regular wave groups, or bichromatic waves, c.f. Appendix A. In this case the incoming short wave energy varies periodically in time and can be non-uniform in longshore direction. The offshore short wave energy is specified by:

$$E_{boundary}(\theta) = \frac{1}{8}\rho g H_{rms}^2 \cos^m(\theta - \theta_{mean}) \cdot \frac{1}{2}\left[1 + \cos\left(2\pi\left(\frac{t}{T_{long}} - \frac{y}{L_{long}}\right)\right)\right] \tag{3.20}$$

$$L_{long} = \frac{c_g T_{long}}{\sin(\theta)}$$

In this case the user additionally specifies the period of the regular wave groups T_{long}. Wave energy varies in longshore direction with the period of the longshore component of the incoming wave groups.

The most complex wave boundary condition module used in XBeach was developed as part of this thesis. The module allows the generation of spatially, directionally and temporally varying irregular wave groups, based on an input wave spectrum. The module is based on earlier work [van Dongeren *et al.*, 2003] used in combination with the SHORECIRC model [van Dongeren *et al.*, 1994]. This module is explained in greater detail in Appendix B and Appendix Y.

Lateral boundaries

As described by Roelvink *et al.* [2007] two wave energy boundaries exist along the lateral boundaries. In the case of stationary waves, it is assumed that the longshore wave energy gradient is zero across the lateral boundaries and a simple Neumann boundary condition is applied to the wave energy.

In the case of non-stationary waves it is assumed that the wave energy gradient along the crest of the wave group is zero. The local mean wave direction is used to determine the angle of the crest of the wave group on the boundary. The wave energy on the lateral boundary is then found by interpolation of the wave energy of the inner row, see Figure 17.

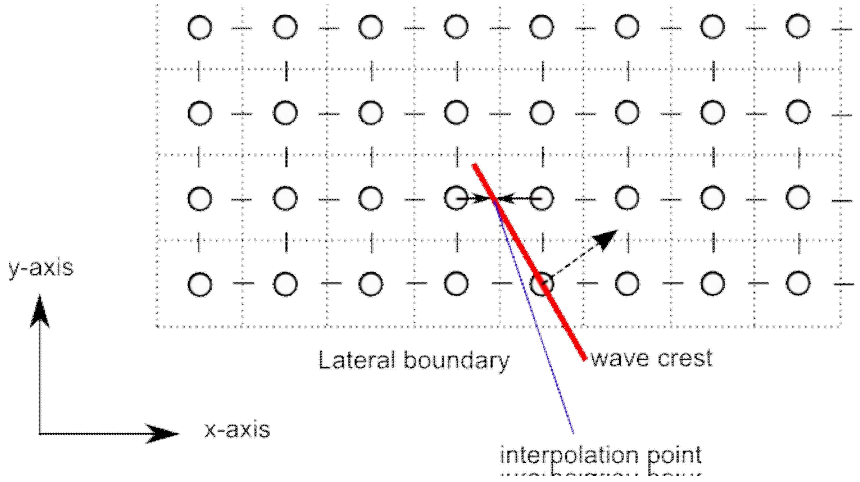


Figure 17 Lateral wave energy boundaries: the wave group crest angle is found on the boundary and extended to the inner row. Wave energy is interpolated to the intersection of the inner row and the wave group crest. Wave energy is copied from the intersection to the originating boundary point.

Back bay boundary

At the back bay boundary, wave energy is allowed to propagate freely out of the model domain. As in general there is no propagation of wave energy in the negative x-direction, the back boundary has no influence on the results of the model. No special treatment is required for the wave energy on the back bay boundary.

Theta space boundaries

As the wave action balance spans directional space as well as x- and y- space, boundary conditions are required on the boundaries of theta (directional) space. At this stage only simple boundary conditions have been implemented in XBeach, allowing wave energy to propagate out of theta space, but not to enter theta space from outside. To prevent wave energy leakage out of the model, it is essential to ensure the model theta domain is large enough to encompass all wave directions.

3.4.2 Flow boundary conditions

Offshore boundary

In XBeach the absorbing-generating boundary condition of Van Dongeren and Svendsen [1997] is applied on the offshore boundary. This boundary condition is based on the Method of Characteristics and allows outgoing long waves to pass through the boundary with

minimal reflection, irrespective of the angle of the long wave. At the same time the boundary can be used to generate long waves which propagate into the model. In the case of incident regular wave groups, the boundary uses the equilibrium theory of Longuet-Higgins and Stewart [1962b] to calculate the related incident bound long wave. In the case of irregular incident wave groups, the bound long waves are generated using the theory of Herbers *et al.* [1994], see Appendix B.

Lateral boundaries

By default XBeach uses normal Neumann boundary conditions for the flow on the lateral boundaries. The assumption is made that no longshore gradients exist in the water level and longshore and cross shore flow across the lateral boundaries. This is valid in the case of normally incident wave groups and longshore uniform bathymetry. However, it has been found that the Neumann assumption also works acceptably in more complex cases with oblique wave groups and quasi-longshore uniform bathymetry [Roelvink *et al.*, 2007]. XBeach allows the user to select wall boundaries instead of Neumann boundaries at the lateral edges, for instance to model wave flume or wave tank tests. No wall friction is taken into account.

Back bay boundary

By default XBeach uses the absorbing boundary condition of Van Dongeren and Svendsen [1997] on the back bay boundary. This allows the propagation of long waves out of the model with minimal reflection. Note that no long waves are generated at this boundary. XBeach also allows the user to select a wall boundary at the back bay boundary.

3.4.3 Sediment transport and morphology boundary conditions

In XBeach sediment concentration gradients across all four boundaries are assumed to be zero. Therefore Neumann conditions are applied to all boundaries. Bed levels are copied across the lateral boundaries. Bed level change is not calculated at the offshore and back bay boundary, but sediment transport can propagate freely through both.

4 Validating the XBeach model

4.1 Introduction

A series of tests is set up to evaluate the 2DH hydrodynamics in XBeach. The tests are designed to progressively increase the complexity of the numerical model by varying the hydrodynamic forcing conditions and the model bathymetry. Verification of the model takes place by comparison with hydrodynamic theory in the more simple cases and measurement data in the most complex cases.

4.2 Verification tests description

A detailed description of each validation test can be found in Appendix C through Appendix V. This section will briefly describe the set-up of the verification tests and the reasoning behind each test. A short summary of each test is given in Table 1.

Table 1 Summary of verification tests.

Test name	Wave forcing	Bathymetry	Surge	Appendix
Test 0	none	longshore uniform	non-stationary	C
Test 1	stationary, normally incident	longshore uniform	stationary	D
Test 1g	stationary, normally incident	longshore uniform	stationary	E
Test 2	stationary, obliquely incident	longshore uniform	stationary	F
Test 3	stationary, normally incident	longshore non-uniform	stationary	G
Test 3g	stationary, normally incident	longshore non-uniform	stationary	H
Test 3s	stationary, normally incident	longshore non-uniform	non-stationary	I
Test 4	bichromatic wave groups, normally incident	longshore uniform	stationary	J
Test 5	bichromatic wave groups, normally incident	longshore non-uniform	stationary	K

Test 6	bichromatic wave groups, obliquely incident	longshore non-uniform	stationary	L
Test 6g	bichromatic wave groups, obliquely incident	longshore non-uniform	stationary	M
Test 6s	bichromatic wave groups, obliquely incident	longshore non-uniform	non-stationary	N
Test 7	irregular wave groups, normally incident	longshore uniform	stationary	O
Test 8	irregular wave groups, obliquely incident	longshore non-uniform	stationary	P
Test 8s	irregular wave groups, obliquely incident	longshore non-uniform	non-stationary	Q
Test 9	stationary, normally incident	longshore non-uniform	stationary	R
Test 10	irregular wave groups, normally incident	longshore non-uniform	stationary	S
Test 11	irregular wave groups, obliquely incident	longshore non-uniform	non-stationary	T
Test 12	irregular wave groups, obliquely incident	one dimensional	stationary	U
Test 13	irregular wave groups, obliquely incident	longshore non-uniform	stationary	V

In Test 0 a time-varying surge level is imposed on the model boundaries. No short waves or infragravity waves are imposed or generated in the model. This test verifies whether the surge level boundary conditions work and whether XBeach is capable of handling basic hydrodynamic calculations in 2DH-mode.

In Test 1 normally incident stationary waves are in introduced to the model. This model tests whether the short-wave propagation scheme works correctly over a longshore uniform bathymetry. Results can be compared with linear wave theory. Test 1g is a variation on Test 1 in which the influence of the numerical grid size is examined.

Test 2 introduces obliquely incident short waves to the model. This introduces wave-generated longshore currents and refraction. Verification takes place by comparing results to linear wave theory.

In Test 3 the longshore uniform bathymetry is replaced by a non-uniform bathymetry containing a bar in the nearshore. The test introduces breaking over the bar and the associated wave set-up and set down around the bar. The wave-generated currents that occur around the bar are compared to hydrodynamic theory. Test 3g is a variation of Test 3 that examines the effects of the numerical grid size on the wave generated current around the

bar. Test 3s introduces simultaneous wave and surge forcing on the offshore boundary and focuses on the ability of XBeach to handle combined forcing.

Non-stationary short waves are introduced in Test 4. In this test regular sinusoidal bichromatic wave groups are imposed on the offshore boundary. The short wave energy time series on the boundary is calculated using equation (3.20). The incoming bound long wave flux is calculated using the theory of Longuet-Higgins and Stewart [1962b; 1964]. The model bathymetry is kept uniform in longshore direction in this simulation. Results of the simulation are compared to the theory of Longuet-Higgins and Stewart.

Test 5 increases the model complexity by introducing a longshore non-uniform bathymetry. This test is designed to evaluate whether long waves propagate correctly over non-uniform bathymetry in 2DH-simulations. Comparisons can be made with the results of Test 3.

In Test 6 obliquely incident regular wave groups are introduced. The purpose of this test is to check the stability of the regular wave group generating boundary condition and to examine in better detail the oblique propagation of long waves across the numerical grid. Test 6g is similar to Test 6, but examines the effect of numerical grid spacing on the long wave propagation in the longshore direction. Test 6s examines the stability of the model under simultaneous surge and regular wave group forcing.

Test 7 introduces irregular wave group forcing using the method developed during this thesis and described in Appendix B and Appendix Y. The offshore boundary is forced using a JONSWAP short wave spectrum. The purpose of the simulation is to test whether the offshore wave boundary condition is able to generate the correct wave forcing. Furthermore, the ability of XBeach to handle irregular wave groups and bound and free infragravity waves travelling in independent directions is evaluated. Since the hydrodynamic forcing has become increasingly complex, the results cannot be easily verified. Comparisons are made between the expected and modelled time-averaged wave and current statistics.

In Test 8 irregular wave groups are forced on a longshore non-uniform bathymetry. In all relevant aspects this test represents prototype conditions. Verification takes place by examining the time-average wave and current statistics. Test 8s adds surge level forcing to the set-up of Test 8.

In Test 9 and Test 10 two wave basin tests [Berkhoff, 1982; Berkhoff *et al.*, 1982] are simulated in order to quantitatively verify the short wave propagation in XBeach. The dataset provided by the Berkhoff experiments is commonly used to verify numerical wave refraction/diffraction models. Test 9 uses stationary wave forcing. In Test 10 irregular wave groups are created using a measured short-wave spectrum.

In Test 11 the hydrodynamics at Duck, North Carolina are simulated during the DELILAH measurement campaign. Detailed bathymetric surveys and hydrodynamic measurement data along a cross shore transect make it possible to verify the hydrodynamics in XBeach under prototype conditions.

Very limited data are available to verify 2DH-overwash modelling. Therefore two simple overwash simulations are set up to examine whether XBeach can handle wave overwash conditions. In Test 12 a one-dimensional simulation is carried out to gain some insight into

the processes in the model. In Test 13 a two-dimensional model is examined. The results are checked on stability and the physical plausibility of the results. No comparisons are made with measured or theoretical data.

4.3 Results and conclusions

The results and individual conclusions of all the verification tests can be found in Appendix C through Appendix V. In this section the main conclusions will be reiterated.

Test 1 to Test 3 show that in general the short wave propagation scheme works very well. In the models, shoaling and refraction along a longshore uniform bathymetry match linear wave theory. The longshore current generated by obliquely incident short waves is in the order of estimates using other numerical approximations. The short wave propagation does not fare as well in Test 9 and Test 10. The error between the observed and calculated wave heights around and behind the shoal in the wave basin is in the order of 30% - 40%. In front and on top of the shoal, the results are better. Given the limitations of the wave propagation model, i.e. no diffraction, this is still considered a reasonable result.

Bound infragravity waves generated by bichromatic regular wave groups using the theory of Longuet-Higgins and Stewart [1962b; 1964] propagate realistically through the model domain. As shown in Test 4 to Test 6, incoming infragravity waves reflect at the shoreline and produce a standing wave pattern with clear nodes and antinodes. The time-averaged hydrodynamic conditions correspond well with the expected conditions.

The tests involving irregular wave groups and associated bound long waves show that the time-averaged short wave conditions and current velocities are correct. However, as shown in Test 7, the principal variance in the short wave energy levels is not in the infragravity band as would be expected. Instead, the majority of the variance is found in the very low frequency band with periods in the order of 100 to 500 seconds. As shown in Test 11, the principal variance of the water surface elevation is also found in the very low frequency band. The infragravity wave height calculated in the XBeach model of Duck is less than the measurements by a factor of two. Some explanations for this error are given in Appendix T.

Test 12 and 13 showed that XBeach is stable under overwash conditions, even in simulations with morphological change. The results showed a marked difference between the amount of overwash in the one-dimensional model and the two-dimensional model. It is suggested that this difference is caused by the difference in the hydrodynamics between the two models. In the one-dimensional model the hydrodynamics are entirely longshore uniform, whereas in the two-dimensional model the hydrodynamics may vary in longshore direction. This allows overwashing water to fan out in the longshore direction rather than be confined as in the one-dimensional case. This difference illustrates one of the limitations of modelling overwash in one-dimensional models.

In the sensitivity studies of the numerical grid size it is shown that the short wave propagation scheme is very insensitive to grid size variables. In most cases the long wave propagation remains constant on all three numerical grids. However, in the case of non-stationary wave forcing, the variance of the water surface elevation and therefore possibly

the energy in the infragravity frequency band differs by as much as 30% in certain locations between simulations on different grids.

Tests with normally incident wave forcing show a tendency for the lateral boundaries to pump water in or out of the model domain. The most likely cause for this is that the lateral boundary condition formulations are weak. Without strong longshore signals, for instance a longshore current, the lateral boundaries overreact to erroneous internal signals. These boundary effects become less prominent under irregular wave group forcing. It is therefore expected that under prototype conditions these boundary effects will not adversely affect the model computations.

In conclusion it can be stated that the hydrodynamics of the 2DH-XBeach model are sufficiently well modelled. One area that still requires some development is the generation of infragravity waves under irregular wave group forcing. The model is assumed capable of qualitatively modelling complex prototype situations.

5 Santa Rosa Island case study

The XBeach model has been verified in Chapter 4. In this chapter, the model will be validated against a field case. This case study was done at the Centre for Coastal and Watershed Studies of the United States Geological Survey (USGS) in Saint Petersburg, Florida. The case study was carried out in close cooperation with Nathaniel Plant and Dave Thompson, of USGS.

5.1 Introduction

The Gulf Coast of the United States is routinely hit by hurricanes. Since 1900, forty major hurricanes have crossed the area between Texas and the Florida Panhandle. The 2004 hurricane season was particularly devastating for the United States Gulf Coast, with 15 named storms in total. Estimates show that over 3000 people lost their lives and roughly $50 billion in damages occurred in North America. In the 2004 season, five hurricanes reached the Florida coast: Hurricane Bonnie, Charley, Frances, Ivan and Jeanne. Of these five, Hurricane Ivan was the largest, ranking as the tenth most powerful Atlantic storm on record. Hurricane Ivan made landfall at 06:50 UTC on 16 September just east of Mobile Bay, Alabama, as a category 3 hurricane on the Saffir-Simpson scale [National Hurricane Center, 2008], for reference see the storm track of Hurricane Ivan in Figure 18. The damage to properties and infrastructure, see Figure 19, caused by Hurricane Ivan is estimated at $14.6 billion [National Hurricane Center, 2008].

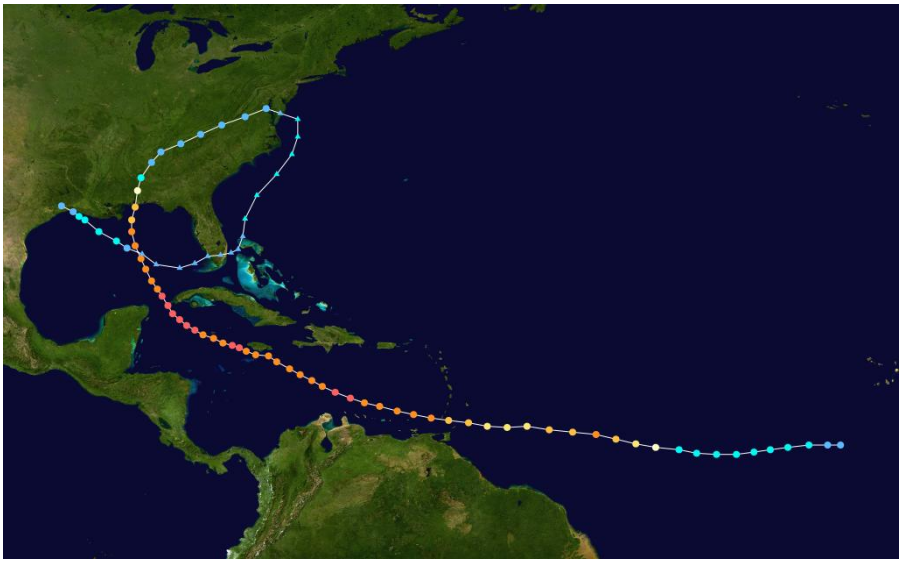


Figure 18 Track of Hurricane Ivan, colour from blue to red denotes increasing hurricane intensity on the Saffir-Simpson scale [sources: NASA, National Hurricane Centre and Wikipedia]



Figure 19 Hurricane Ivan destroyed sections of the Pensacola Bay Bridge [source: AP]

The area selected for study is part of Santa Rosa Island. Santa Rosa Island is a wave dominated, narrow barrier island between the Gulf of Mexico and the Santa Rosa Sound on the Northern Florida Panhandle. The island is aligned approximately east-west and has a length of roughly 85 kilometres. The width of the island varies between 150 to 500 meters, see Figure 20 and Figure 22. The island has three communities, Pensacola Beach, Navarre Beach and Fort Walton Beach. Large parts of the island belong to the US National Parks Service and are part of the Gulf Islands National Seashore. Dune development varies across the island. Regions of high, established dunes exist as well as regions of semi-continuous foredunes and low non-continuous foredunes [Donnelly *et al.*, submitted]. The tides around Santa Rosa Island are predominantly diurnal, with an average tidal range of 0.43m. Average offshore significant wave heights in summer and winter are 0.8m and 1.2m respectively [Donnelly *et al.*, submitted].

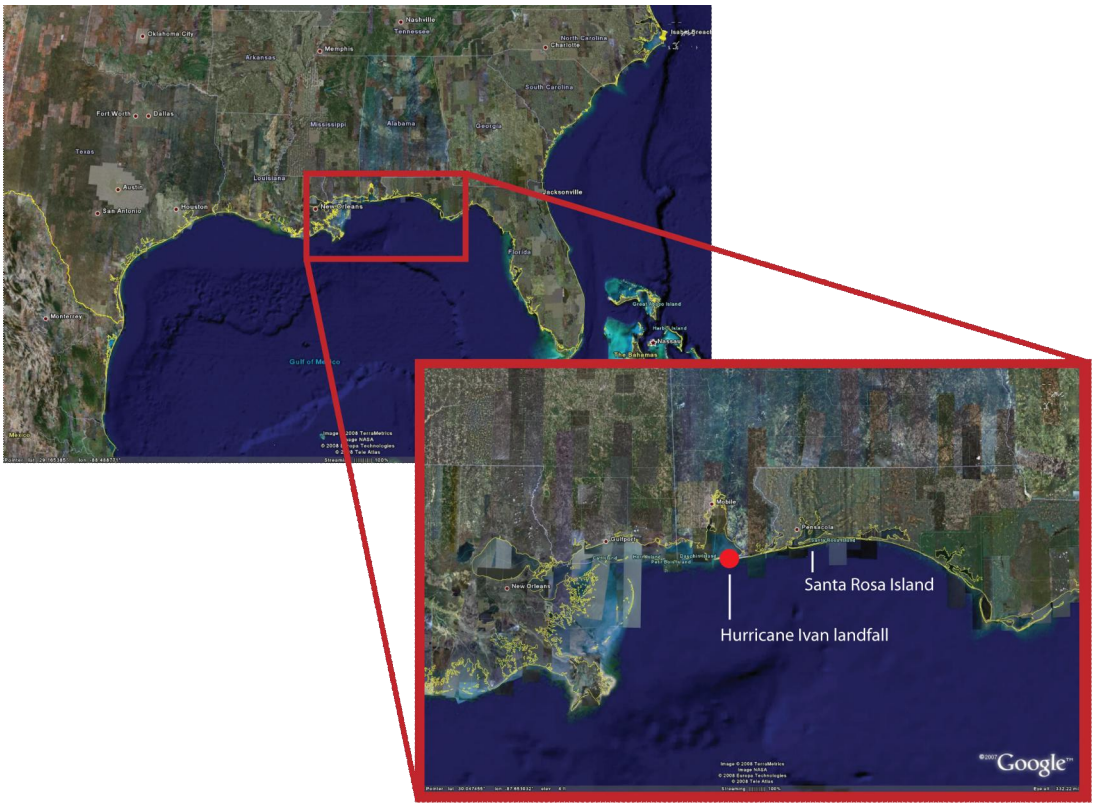


Figure 20 Location of Santa Rosa Island relative to the landfall of Hurricane Ivan [image source: Google Earth]

During Hurricane Ivan, large stretches of Santa Rosa Island were overwashed, see Figure 21. Most of the overwash occurred as sheetwash, but some confined runup overwash occurred on the eastern end of the island. The island was breached at the narrowest point on its western tip, which was approximately 50 kilometres from the location of Hurricane Ivan landfall [Donnelly *et al.*, submitted].



Figure 21 Post-Ivan aerial view of Santa Rosa Island [source: USGS]

The specific site of this study is a one kilometer stretch of coast in the Gulf Islands National Seashore between Pensacola Beach and Navarre Beach, see Figure 22. Note that the images in Figure 22 were taken after Hurricane Ivan.

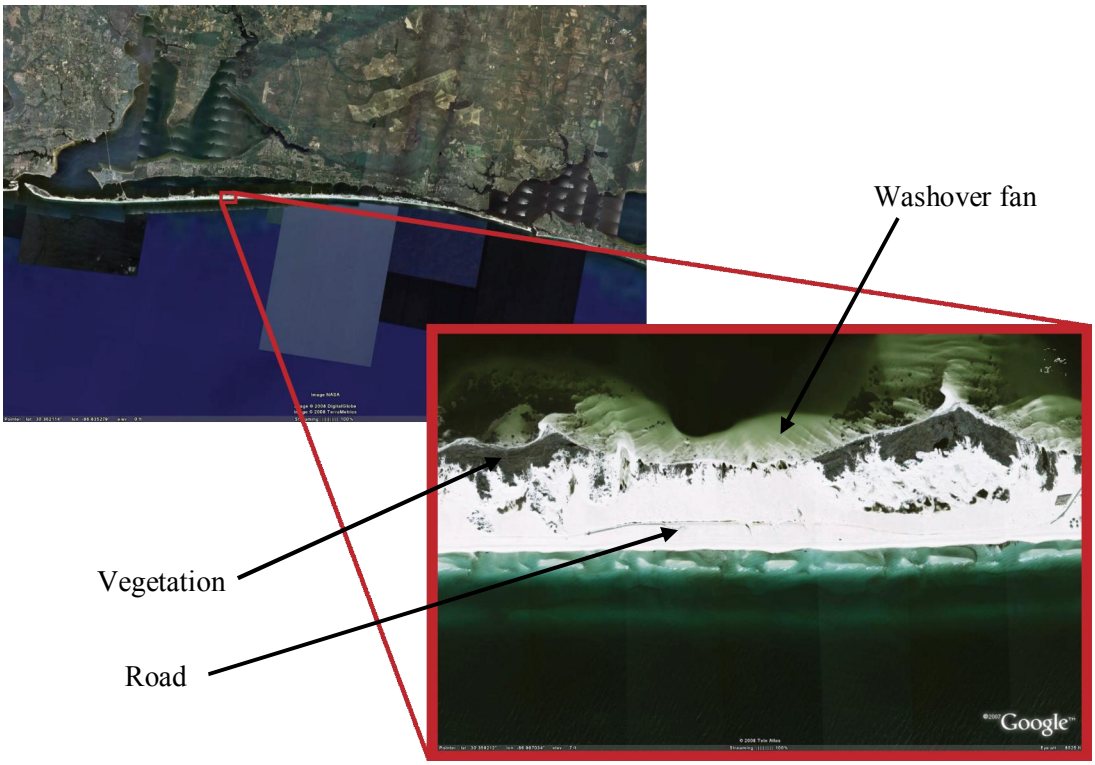


Figure 22 Santa Rosa Island and the study area [source: Google Earth]

The area shows clear signs of dune erosion and overwashing. A clearly developed washover fan can be seen on the bay side of the barrier island.

Due to the current limitations of XBeach in modelling vegetation and hard structures, a site was required with minimal amounts of vegetation and hard covering. The selected site has little vegetation, although pre-storm vegetation may have been more abundant. The area also has no hard features except for the road. At this stage it is assumed that the road was covered by sand in the early stages of the storm and thus will not influence the model results to a great extent.

5.2 Description of data

5.2.1 Bathymetry and altimetry data

In order to study changes along the coast caused by hurricanes, the United States Army Corps of Engineers (USACE), the National Aeronautics and Space Administration (NASA) and USGS set up a spatially high resolution measurement campaign to collect pre- and post-storm bathymetry and altimetry along the entire United States coast. The measurement system used to collect data in this campaign is airborne LIDAR, or LIght Detection And Ranging. LIDAR is a remote sensing technology whereby a laser pulse is fired at the ground and the reflection is measured. This is used to create highly detailed digital elevation maps.

As a partner in the LIDAR measurement campaign, USGS has access to LIDAR data of Santa Rosa Island collected on 15 May 2004 and 19 September 2004, respectively four months prior to Hurricane Ivan landfall and three days after landfall. The 15 May 2004 data are used to create the initial elevation in the XBeach model.

The LIDAR data available to this project are pre-processed by USACE to remove spurious measurements. Further pre-processing by USGS presents reliable digital elevation data at a spatial resolution of approximately one meter. The vertical accuracy of the processed LIDAR data is approximately 20 cm.

The LIDAR measurements prior to Hurricane Ivan span most of the width of Santa Rosa Island and much of the foreshore, see Figure 24. Post Hurricane Ivan LIDAR data are less complete than the pre-storm data. Only one swath was made in order to quickly assess the state of the dunes and barrier island. Much of the bay side of the island was not surveyed, along with the foreshore on the Gulf side, see Figure 23 (central panel). Analysis of the pre- and post-storm data shows patterns of erosion and deposition shown in Figure 23 (bottom panel).

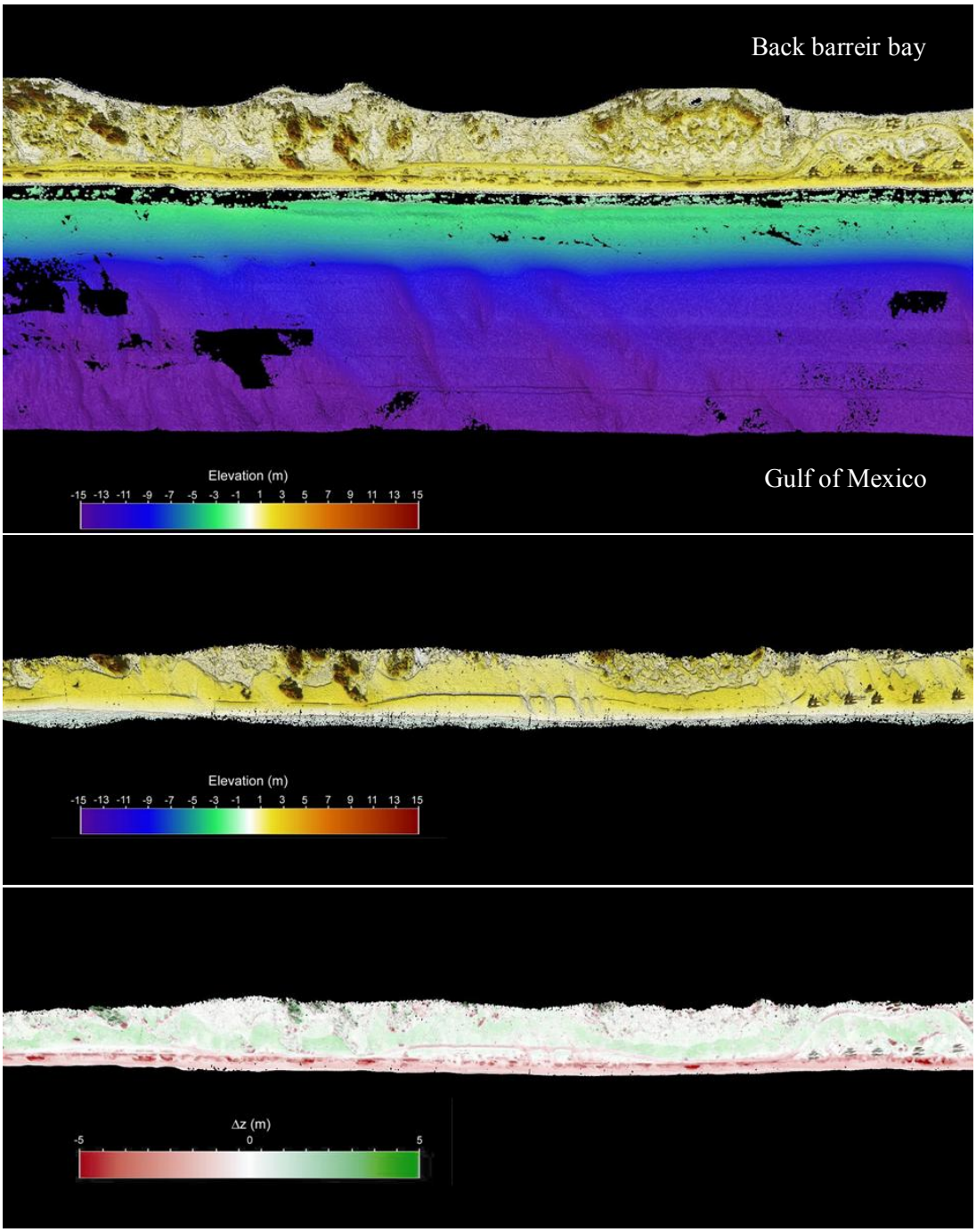


Figure 23 Pre-Hurricane Ivan elevation data (top panel), post-storm elevation data (central panel) and erosion/deposition resulting from Hurricane Ivan (bottom panel). Images courtesy of Dave Thompson.

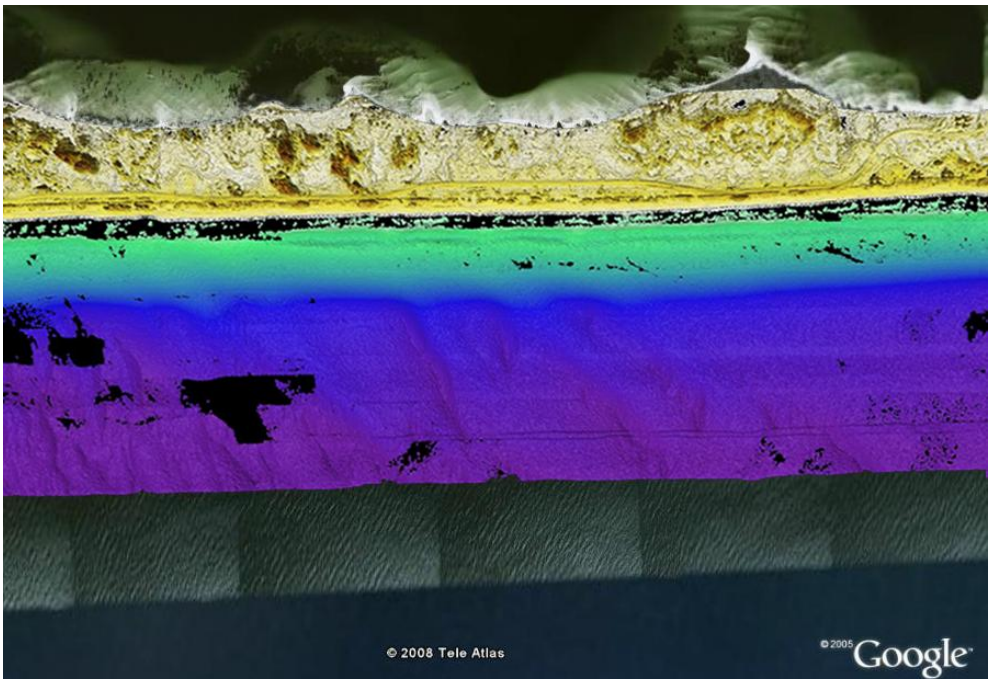


Figure 24 Pre-Hurricane Ivan LIDAR data overlaid on an aerial image of the study site [sources: USGS and Google Earth]

In order to set up an XBeach model including the back bay area, the NGDC Coastal Relief Model is used [Divins and Metzger, 2008]. This model provides digital elevation data of the United States Continental Shelf with a spatial resolution of three arc-seconds, roughly 90 meters. A section of the Coastal Relief Model around the study area is shown in Figure 25. These data are assumed to be less accurate than the LIDAR data as the dataset used in the creation of the Coastal Relief Model includes hydrographic surveys carried out as long ago as the 19th century. It is unclear how old the dataset is that was used for the bathymetric model of the region of interest. The data in the Coastal Relief Model are pre-Hurricane Ivan and can therefore not be used to analyse the post-storm XBeach results.

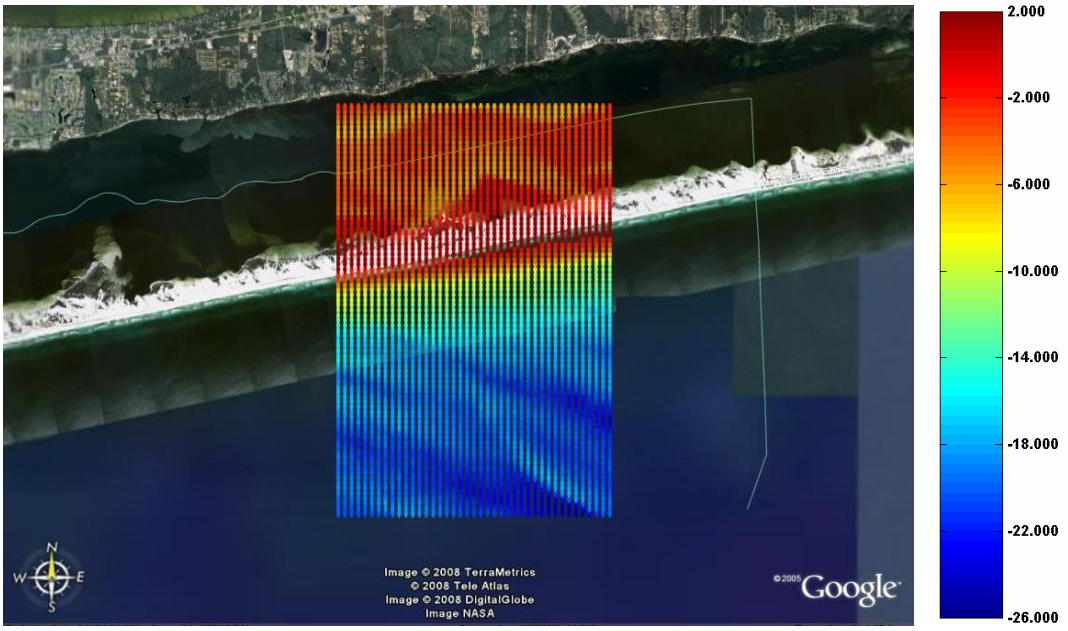


Figure 25 Elevation data extracted from the Coastal Relief Model [satellite image source: Google Earth]

Further qualitative information about the elevation and composition of the study area can be extracted from aerial photographs taken before and after Hurricane Ivan, see Figure 26.

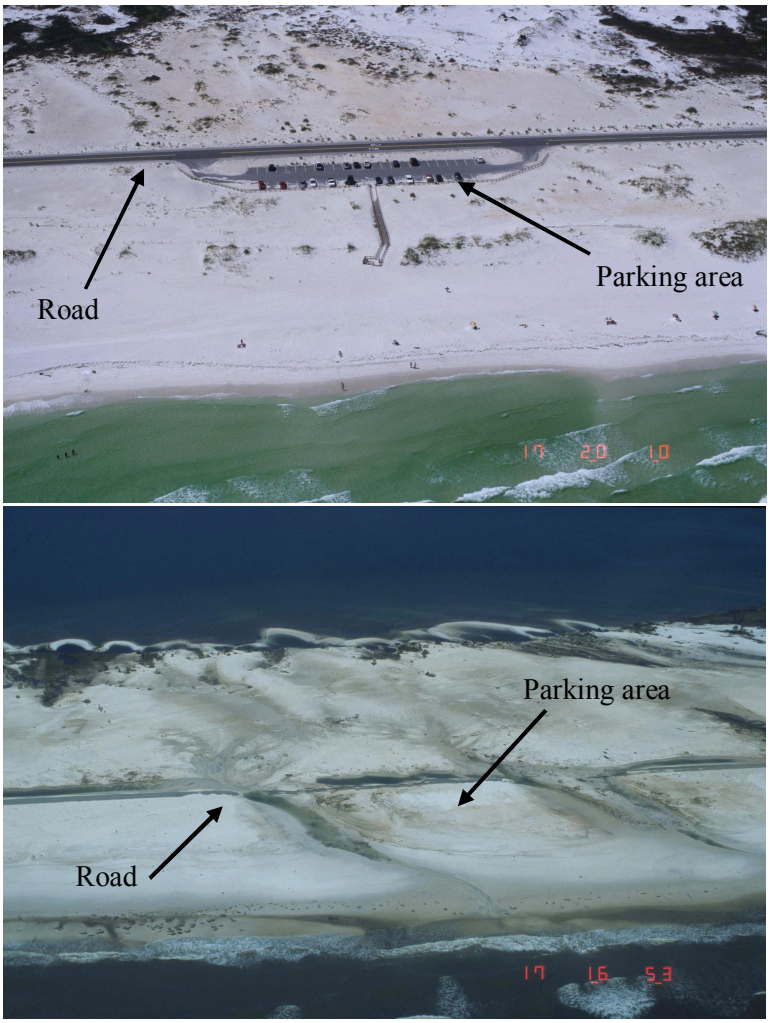


Figure 26 Model location in July 2001(top panel) and 19 September 2004, three days after Hurricane Ivan (bottom panel). [Source: USGS]

5.2.2 Water level data

The National Oceanic and Atmospheric Administration (NOAA) has two tidal gauge stations near Santa Rosa Island that were measuring during Hurricane Ivan. The tidal gauge nearest the study site is the gauge at Pensacola, see Figure 27, and is located within Pensacola Bay behind Santa Rosa Island. The tidal gauge at Panama Beach is located directly on the Gulf of Mexico, but is over 100 kilometres from the study site. The measured water level and NOAA-predicted water level records for the two gauges during Hurricane Ivan are shown in Figure 28. Note that the tidal gauge in Pensacola stopped recording approximately two hours before Hurricane Ivan made landfall.

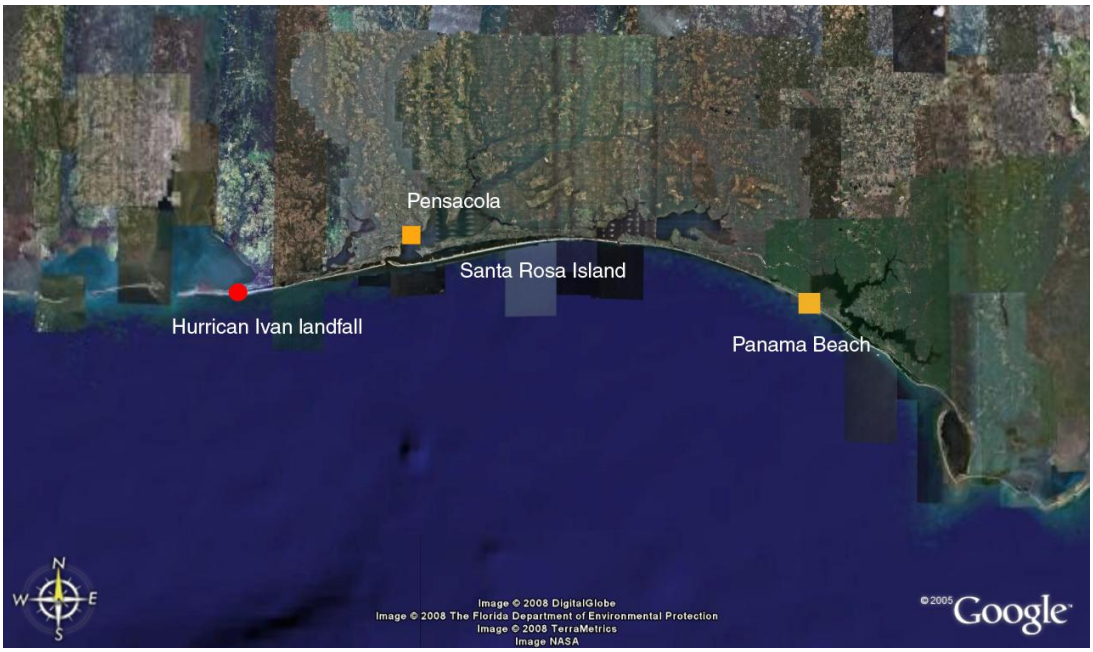


Figure 27 Locations of NOAA tidal gauges and Hurricane Ivan landfall [image source: Google Earth]

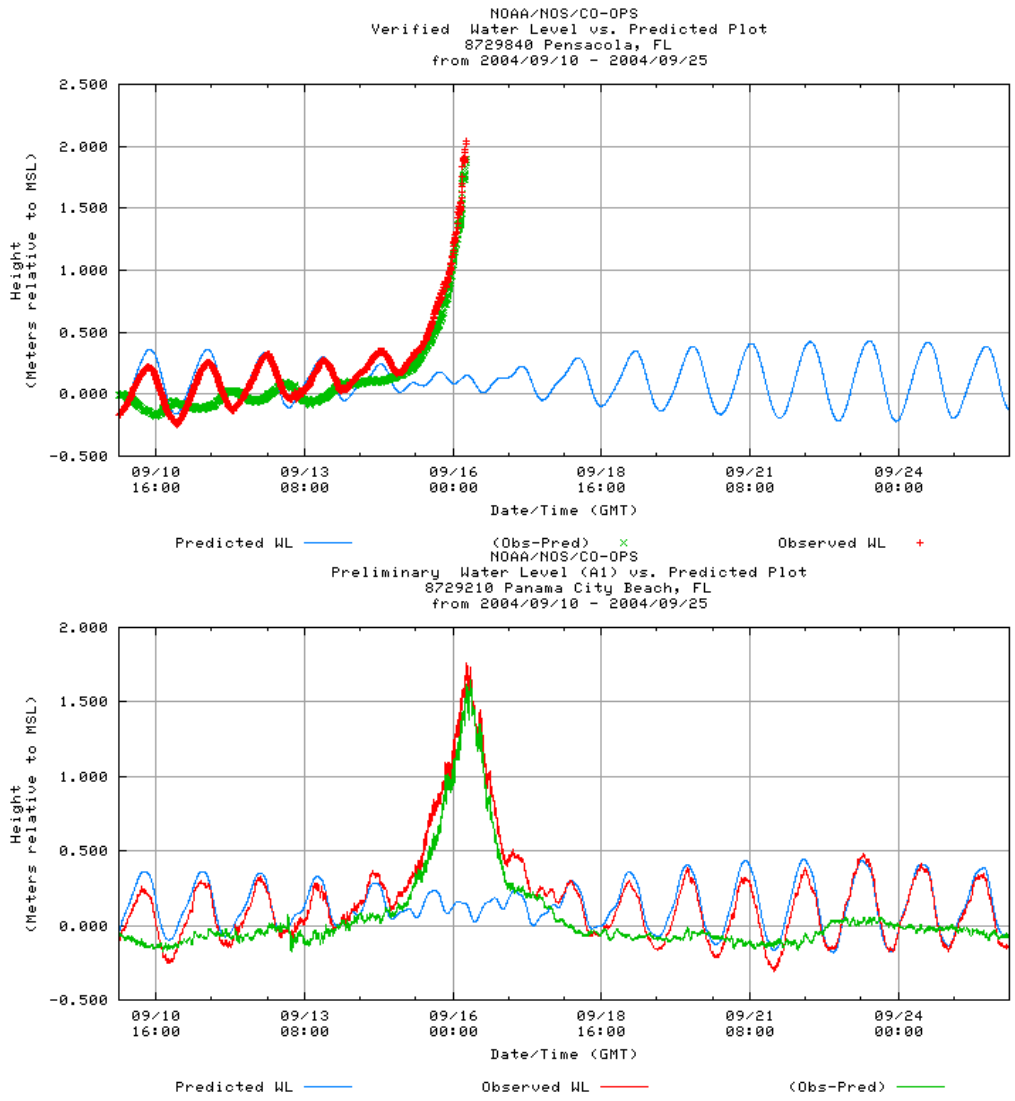


Figure 28 Water elevation time series of the NOAA tidal gauge at Pensacola (top panel) and Panama Beach (bottom panel) during Hurricane Ivan. Measured water levels are shown in red, astronomical tide prediction in blue, the difference between measured and astronomical in green [source: NOAA Tides and Currents].

The water levels measured by these two and other gauges further from the storm are used to calibrate a Delft3D-FLOW numerical model of Hurricane Ivan [Thompson, unpublished]. The model was forced using three hourly wind field datasets provided by NOAA Hurricane Research Division of AOML and NOAA National Climatic Data Center and the dominant tidal constituents.

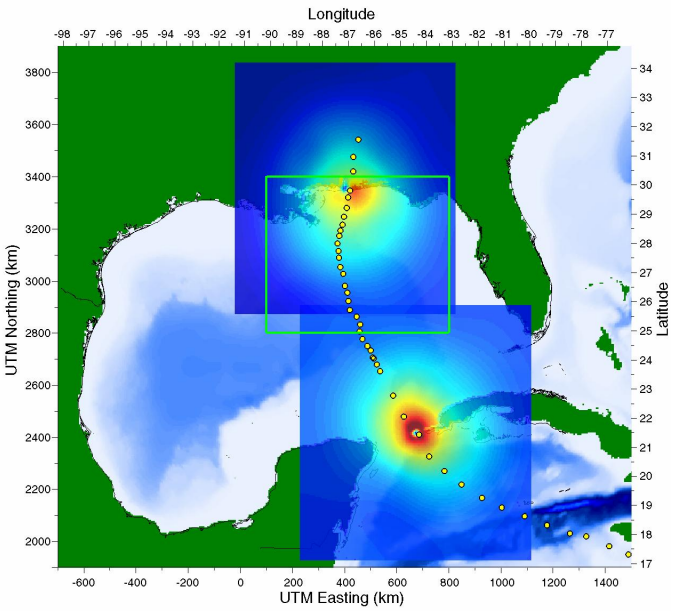


Figure 29 The region of the Delft3D model (green box), the progress of the centre of Hurricane Ivan (yellow circles) and two example NOAA/AOML/HRD wind field grids. Image courtesy of Dave Thompson

The hourly Delft3D-model results for the water level offshore of the study site are shown in Figure 30. It is should be noted that the Delft3D model was unable to match the peak surge levels at Panama Beach and thus may be underestimating the surge level at the study site by as much as two meters. Additionally, the spatial resolution of the model was two by two kilometres and was therefore not large enough to resolve Santa Rosa Island.



Figure 30 Water level offshore of the study site according to the Delft3D-model

Donnelly *et al.*[submitted] looked at morphological response of Santa Rosa Island after Hurricane Ivan. In this article the authors extract water level data for the Gulf of Mexico side and back barrier bay from the ADCIRC-model results of Chen *et al.* [submitted]. The water level data of a location near to the study location are shown in Figure 31.

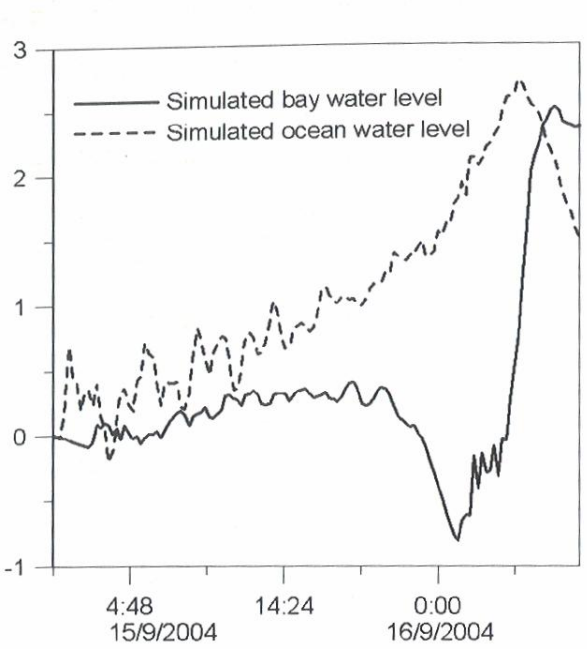


Figure 31 Water level offshore of the study site presented by Donnelly *et al.*[submitted].

It is uncertain how the model data presented by Donnelly *et al.* were acquired. It is unknown if the water levels refer to locations in the nearshore and contain wave setup, or are offshore water levels. The water level presented by Donnelly *et al.* at the bay side of the Pensacola Bay inlet exceeds the maximum measured water level by the Pensacola tide gauge by one meter. At this stage, it is assumed that the surge level presented in Figure 31 may exceed the levels required as boundary conditions for the XBeach model.

5.2.3 Wave data

No nearshore or shallow water in-situ wave measurements exist for the study area of this model during Hurricane Ivan. However as Hurricane Ivan approached land, several NOAA wave buoys measured wave heights in deep water. These buoy data were used to calibrate a SWAN numerical wave model [Thompson, unpublished]. One-way interaction from the Delft3D-FLOW model to the SWAN model was used to provide water depths. Wind fields were generated from the same datasets as those used in the Delft3D-model. The SWAN-model domain extended over 1000 kilometres with a grid resolution of four kilometres. Subsequent nested models reduced the model domain and increased the spatial resolution to one kilometre, see Figure 32.

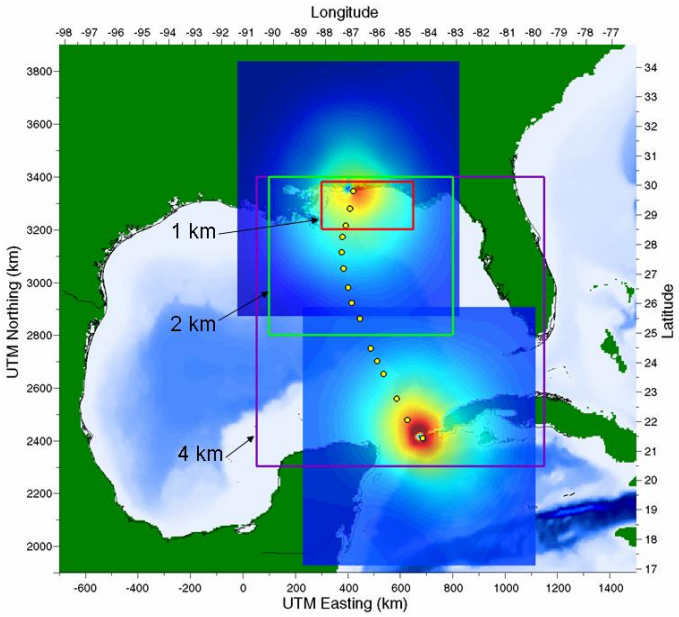


Figure 32 The region of the large SWAN model (purple box) and subsequent nested models (green and red boxes). Image courtesy of Dave Thompson.

The hourly SWAN-model results for the significant wave height, peak period and mean wave direction offshore as well as the water level at the study site are shown in Figure 33.

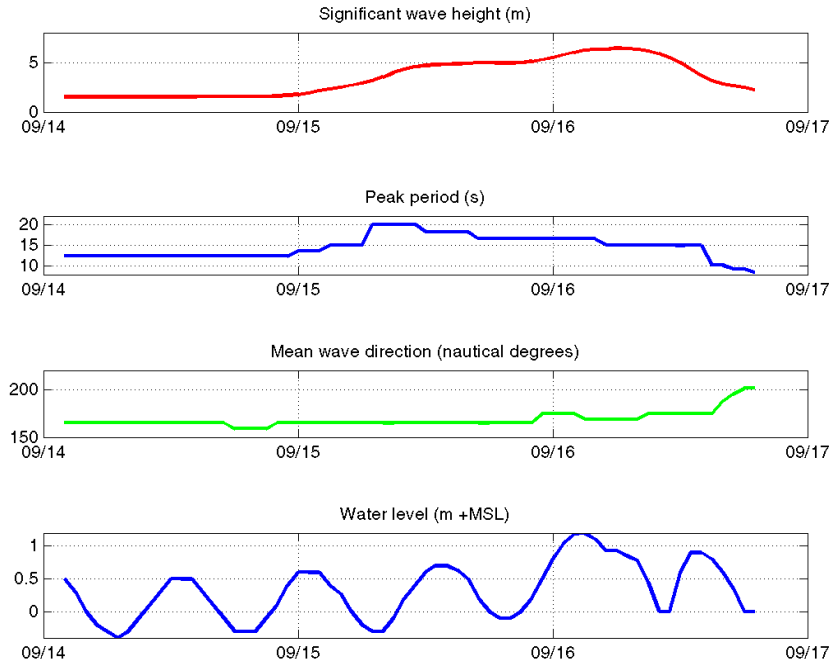


Figure 33 Delft3D/SWAN-model output results for the study site: significant wave height (top panel), peak wave period (upper middle panel), mean wave direction (lower middle panel) and water level (bottom panel)

5.3 Model setup

5.3.1 Grid setup

A section of the study site is chosen to be modelled using XBeach. The model domain is shown in Figure 34 and is one kilometre wide and roughly two-and-a-half kilometres long. It contains an area that was entirely overwashed (western end) and an area that remained relatively intact (eastern end). The model domain also contains a prominent washover fan.

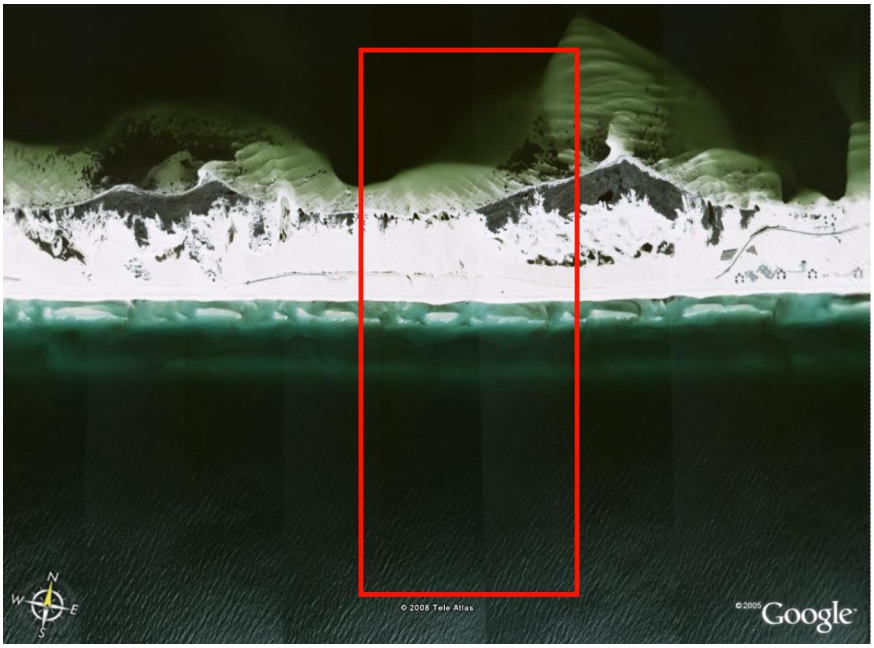


Figure 34 XBeach model domain

To create a bed level grid for XBeach, the pre-storm LIDAR and Coastal Relief Model data are combined and missing points are interpolated. The data are smoothed in cross shore and longshore direction according to a method developed by Plant *et al*. [2002]. A smoothing scale of ten meters in the longshore direction and five meters in the cross shore direction is selected, thereby removing features with smaller length scales. The initial elevation of the XBeach model is shown in Figure 35.

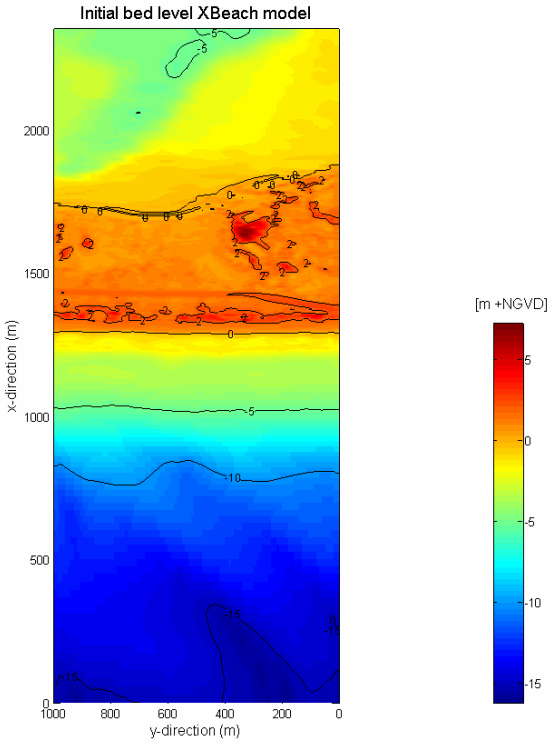


Figure 35 Initial bed elevation in the XBeach model

The calculation grid has uniform 10 meter longshore spacing and a variable spacing in cross shore direction. The variable cross shore spacing allows the nearshore and onshore regions to be modelled in high resolution, while simultaneously letting the resolution to drop in the offshore region. This allows a combination of fast and detailed modelling of the region of interest.

5.3.2 Boundary conditions

Given the number of uncertainties in the offshore forcing conditions, it is difficult to specify one hydraulic boundary condition that can be used to correctly model the system. Therefore one base simulation is carried out, described in detail in section 5.4. In section 5.5 other simulations are described using modified boundary conditions.

In the base simulation the Delft3D/SWAN model results are used as input data for the water level and incident short waves. The water level on both sides of the barrier island is assumed to be equal. Short waves are generated using a parameterised JONSWAP spectrum input, based on the SWAN model results. The simulation starts at 00:00 September 15 at the time of high tide and the start of increasing wave heights, see Figure 33 and Figure 36. The simulation ends 18:00 September 16, after the high tide following Hurricane Ivan landfall. The hydraulic boundary conditions are updated hourly in the XBeach model.

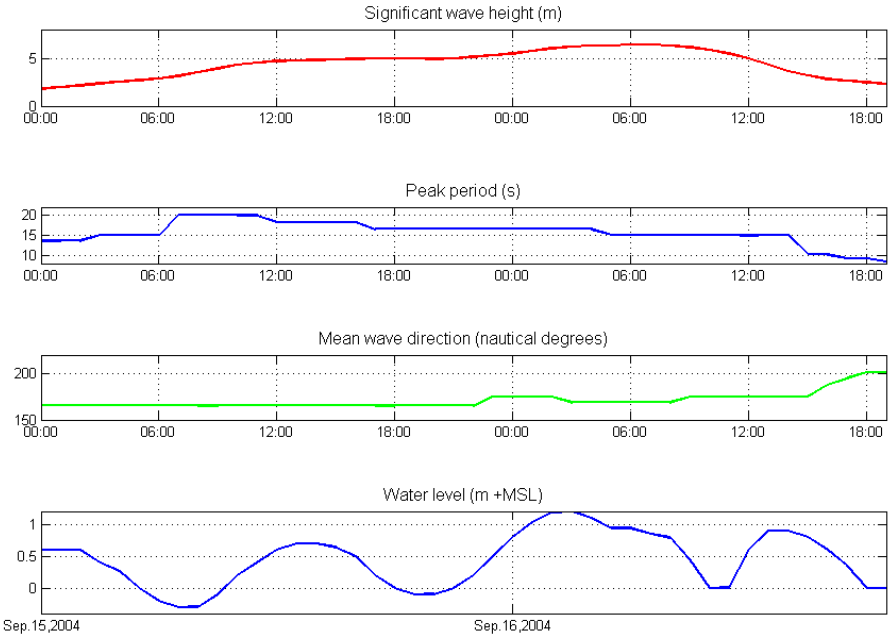


Figure 36 Input time series of offshore forcing for the base simulation

All flow, wave, sediment and morphological parameter values used in the model are listed in Appendix AA.

5.4 Base simulation results

The simulation can be divided into five periods, based on the morphological change of the barrier island in the XBeach model. These periods are discussed in the following sections.

5.4.1 Foredune erosion period (0-9h)

For the first nine hours of the simulation, the barrier island is essentially in the collision regime, with a transformation to an overwash regime in the ninth hour. The water level is not yet higher than normal levels, but the significant wave height of 2-4 meters is in the order of average storm conditions.

Following the method of Sallenger [2000], we determine the dominant value of R_{high} during this period. It should be noted however that the Storm Impact Scale was not developed to predict intra-storm changes and therefore cannot strictly be used in this sense, see section 5.4.6.

$$R_{high} = R_{2\%} + \eta_{SWL} \approx H_0 \left(0.83\xi + 0.20\right) + \eta_{SWL} \tag{5.1}$$

In which $R_{2\%}$ is the representative wave runup. With a bed slope of between 0.013 and 0.020 and offshore wave heights and periods of 2-4 meters and 15 seconds respectively, the maximum R_{high} is approximately 1.2m to 1.5m +MSL. The majority of the foredunes are higher than this level. Thus according to the Storm Impact Scale the system is in the collision regime.

In the XBeach model, the period is characterised by a slow erosion of the seaward slopes of the foredunes and a landward migration of the mean water line. The eroded foredune sediment is principally deposited in the nearshore, making the foreshore slope more gentle, see Figure 37.

At the end of the first period, the system starts to change to an overwash regime. Several overwash throats start to appear in the gaps between the foredunes, the most prominent of which can start to be seen at the western end of the island in Figure 37 (arrow right panel). The total amount of erosion and deposition after nine hours is shown in Figure 38. Figure 39 shows a snapshot of the water surface level after nine hours of simulation. The overwash can be seen in several locations along the island.

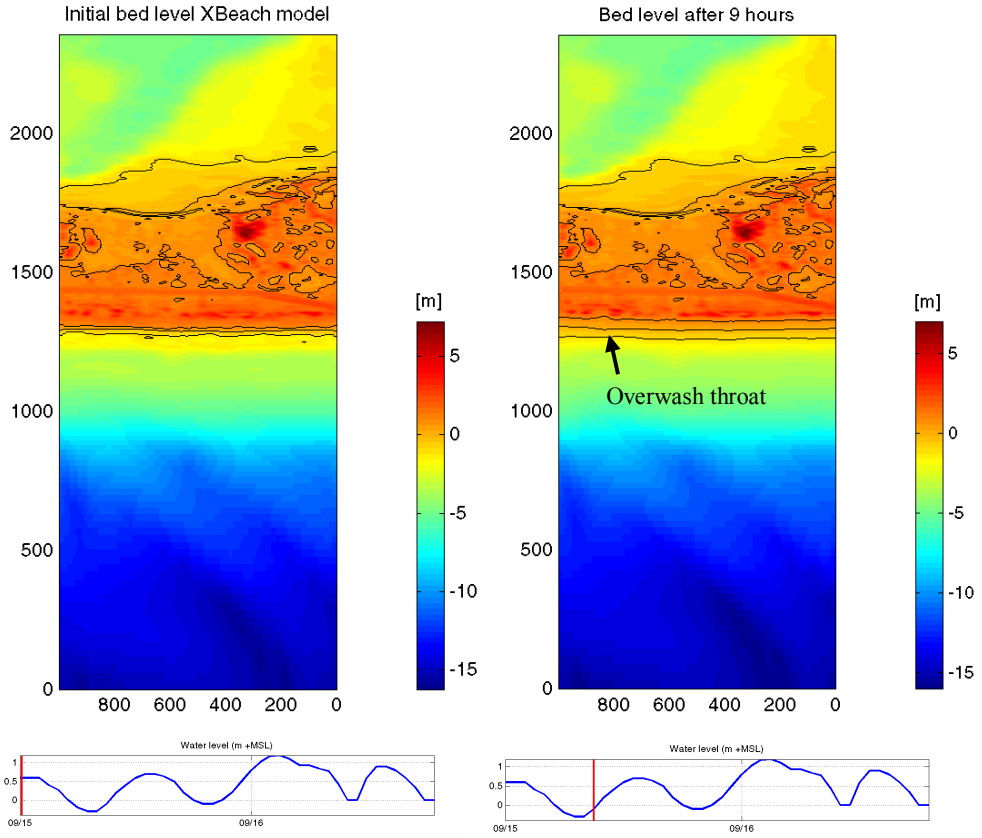


Figure 37 Initial bed level (left panel) and bed level after nine hours (right panel). Contour lines indicate -1m +MSL, 0m +MSL and +1m +MSL. Arrow indicates the start of an overwash throat.

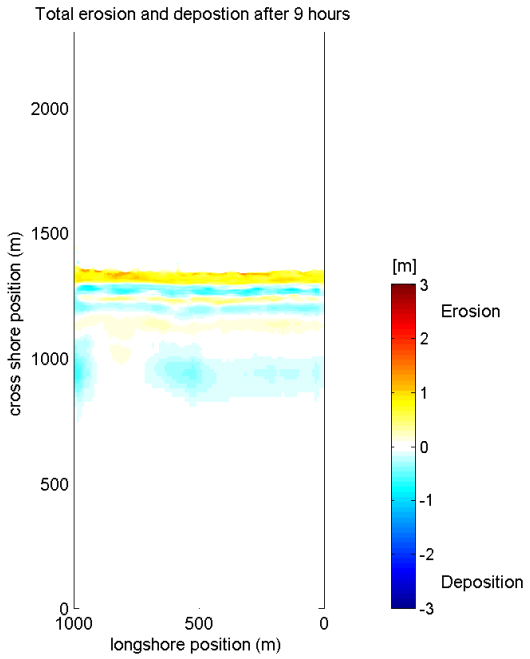


Figure 38 Total erosion and deposition after nine hours

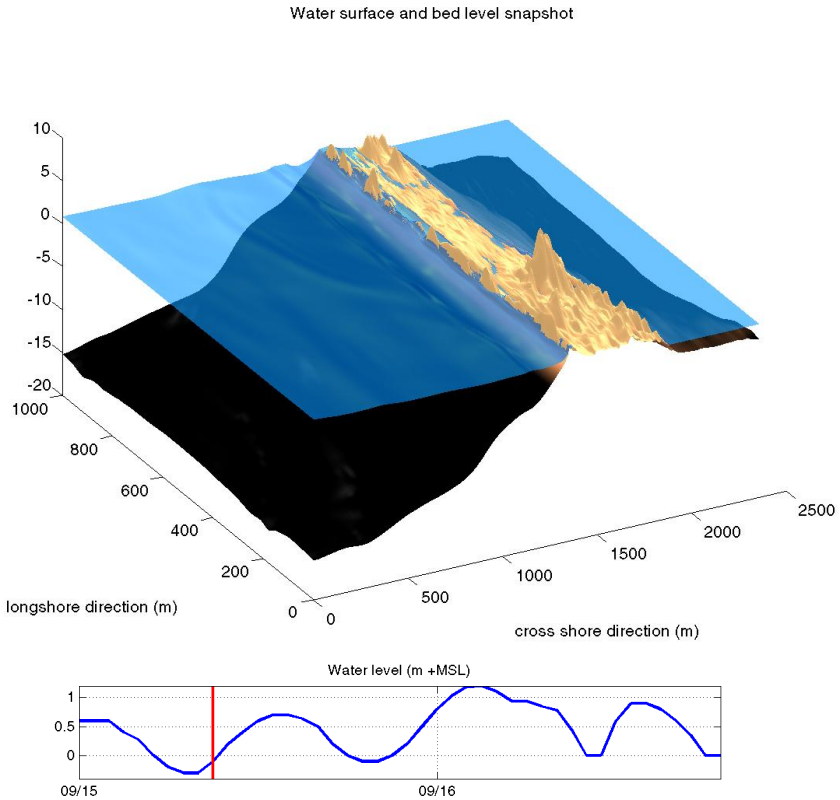


Figure 39 Snapshot of the water surface and bed level after nine hours. Note the start of the formation of an overwash throat between the foredunes at the western end of the model, which can also be seen in Figure 37. The lower panel shows the surge level at the time of the snapshot.

5.4.2 First overwash period (10-16h)

At the start of the tenth hour of the simulation until the sixteenth, the barrier island system changes to a strong overwash regime. The dominant value of R_{low} during this period is [Sallenger, 2000]:

$$R_{low} = R_{high} - S_{2\%} \approx H_0\left(-0.02\xi + 0.14\right) + \eta_{SWL} \tag{5.2}$$

In which $S_{2\%}$ is the representative swash amplitude. With offshore wave heights and periods of 5 meters and 16-20 seconds respectively, the Iribarren number lies between 0.11 and 0.20. R_{high} then becomes 2.0m +MSL and R_{low} is in the order of 0.6m +MSL during high tide. Most of the foredunes are above R_{low} but below R_{high} because of the erosion in the previous period.

Two main morphological changes occur during this period. The first is the development of. three distinctive overwash throats, as can be seen in Figure 40 (right panel), which create a washover terrace on the back bay side of the island. The second large morphological change is the lowering and destruction of the foredunes. The total amount of erosion and deposition after sixteen hours is shown in Figure 41.

The volume of water overtopping the island is quite considerable, as can be seen in Figure 42. Only the relatively high back barrier dunes in the eastern end of the model domain remain above water.

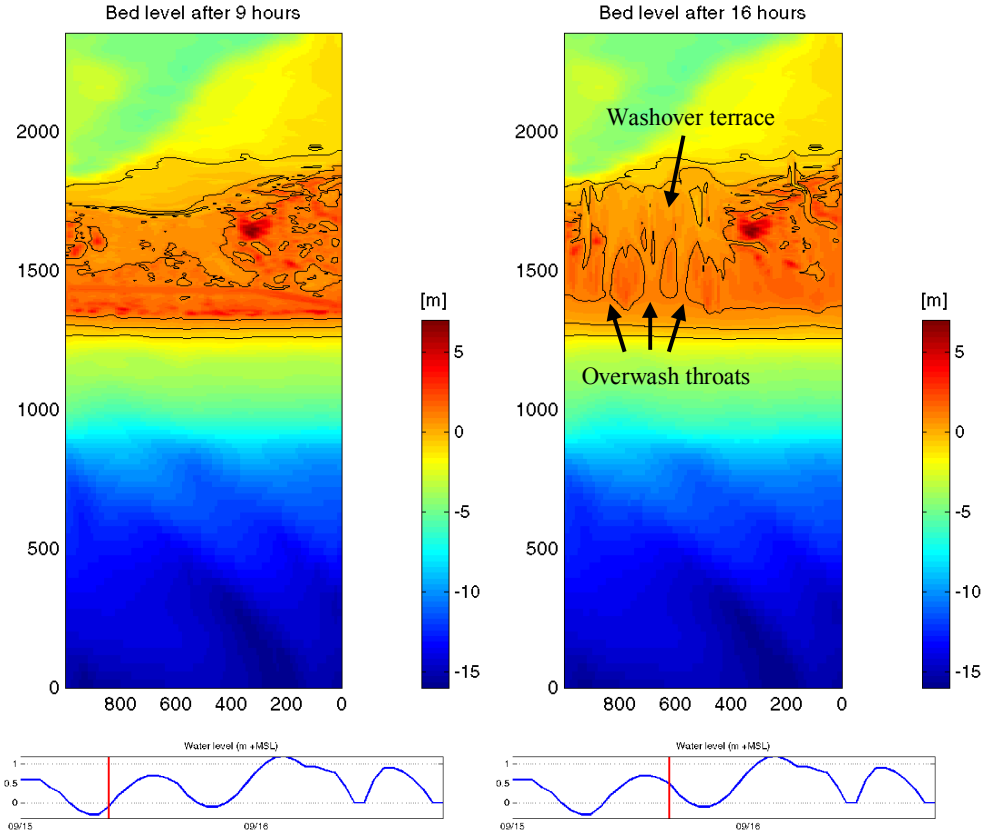


Figure 40 Bed level after nine hours (left panel) and after sixteen hours (right panel). Contour lines indicate -1m +MSL, 0m +MSL and +1m +MSL.

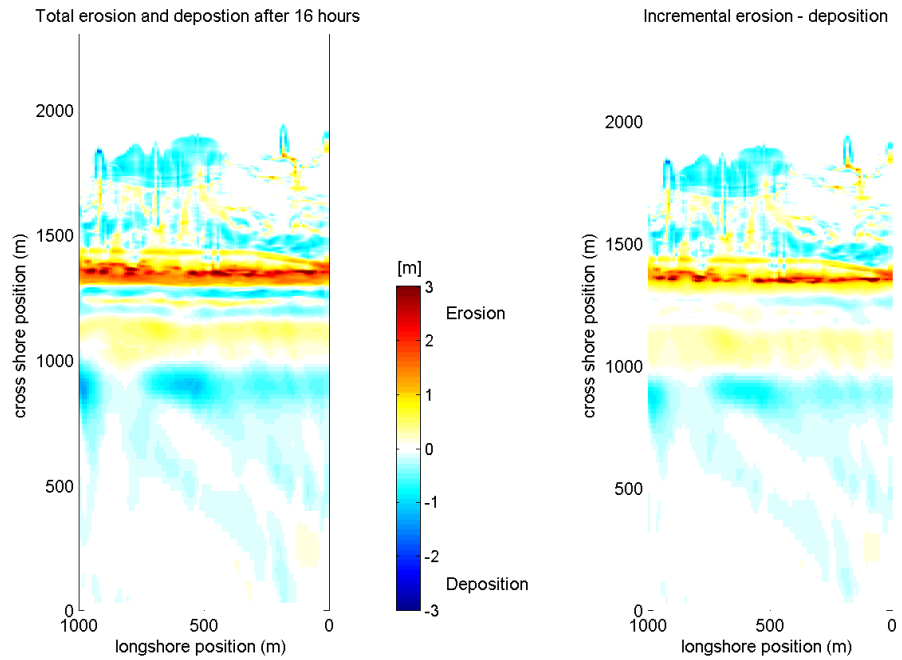


Figure 41 Total erosion and deposition after sixteen hours (left panel) and incremental erosion and deposition between nine hours and sixteen hours (right panel)

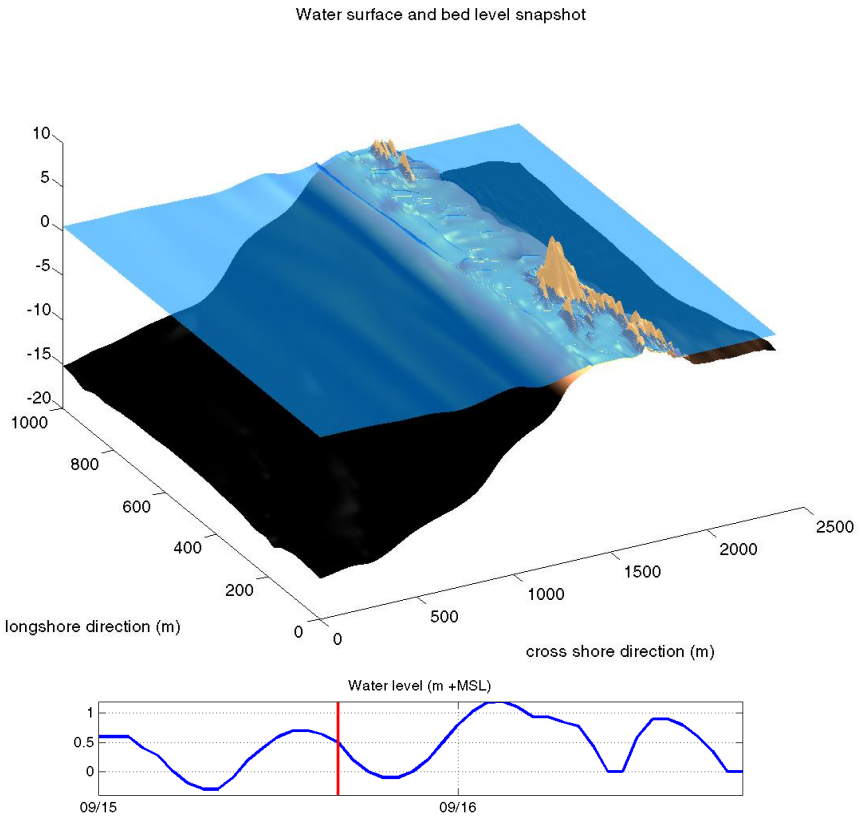


Figure 42 Snapshot of the water surface and bed level after sixteen hours. The lower panel shows the surge level at the time of the snapshot.

5.4.3 Second overwash period (17-22h)

The period until the twenty-second hour of the simulation is characterised by almost zero morphological change. The water level drops to lower levels than in the previous period while the wave forcing remains at the same level. The result is that the total hydraulic forcing on the barrier island lessens. The barrier island system remains in the overwash regime as R_{high} is still above the height of the remains of the foredunes. Large volumes of water still overwash the island, see Figure 45 and Figure 44. However, in this period no new morphological features are developed and the existing features do not expand, see Figure 43. The only change is a slight reduction in the slope of the beach and nearshore, as the beach tries to reach an equilibrium slope. The back barrier system appears to reach a new equilibrium.

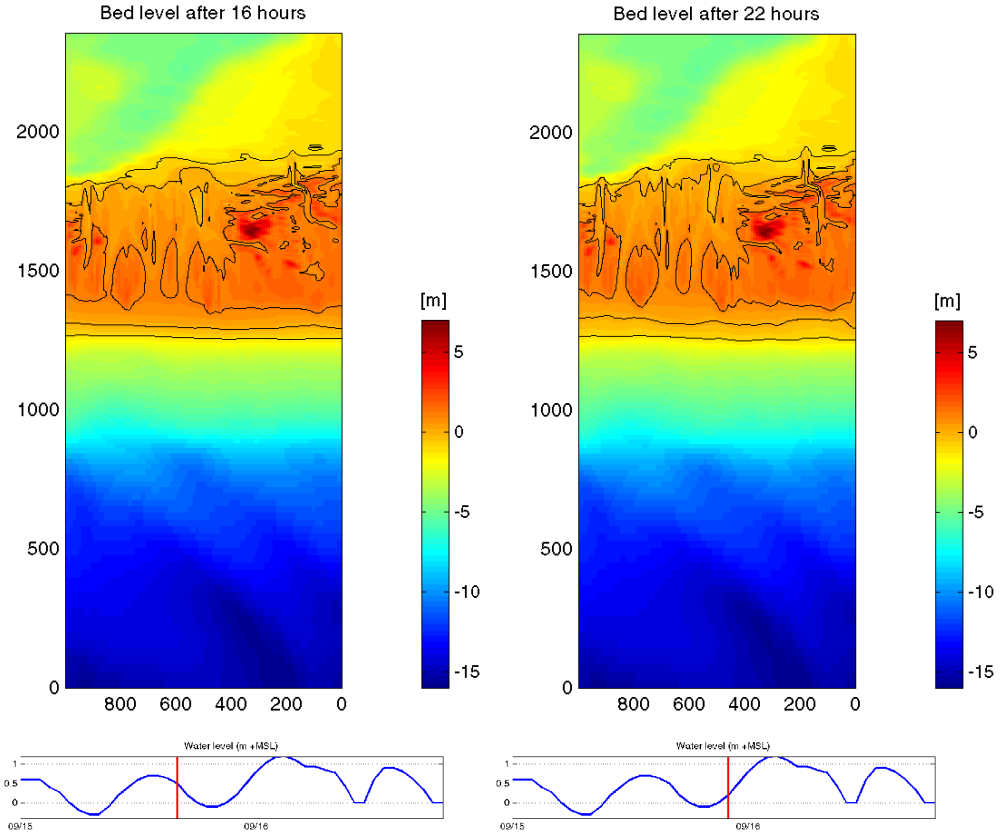


Figure 43 Bed level after sixteen hours (left panel) and after twenty-two hours (right panel). Contour lines indicate -1m +MSL, 0m +MSL and +1m +MSL.

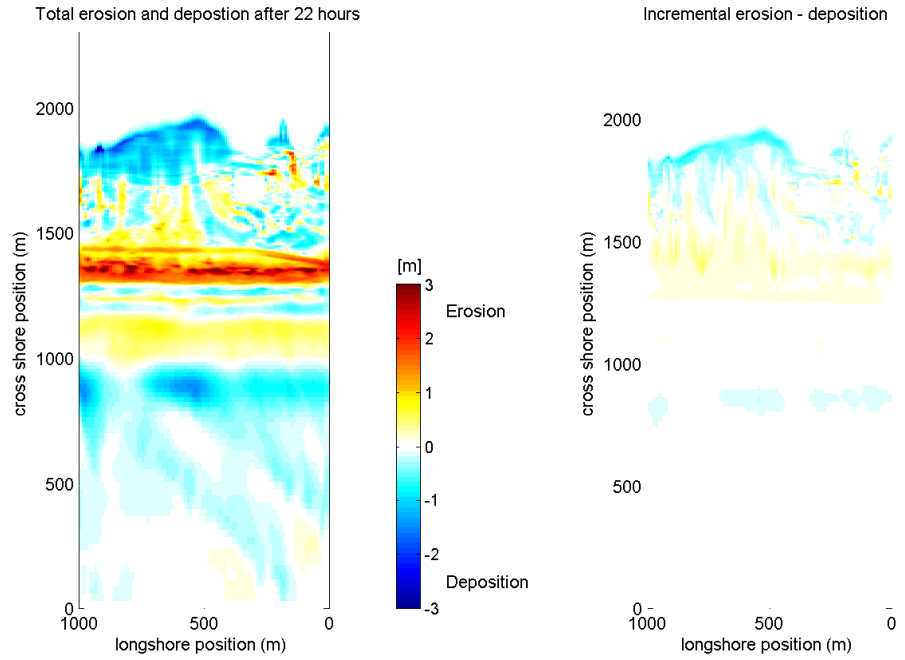


Figure 44 Total erosion and deposition after twenty-two hours (left panel) and incremental erosion and deposition between sixteen hours and twenty-two hours (right panel)

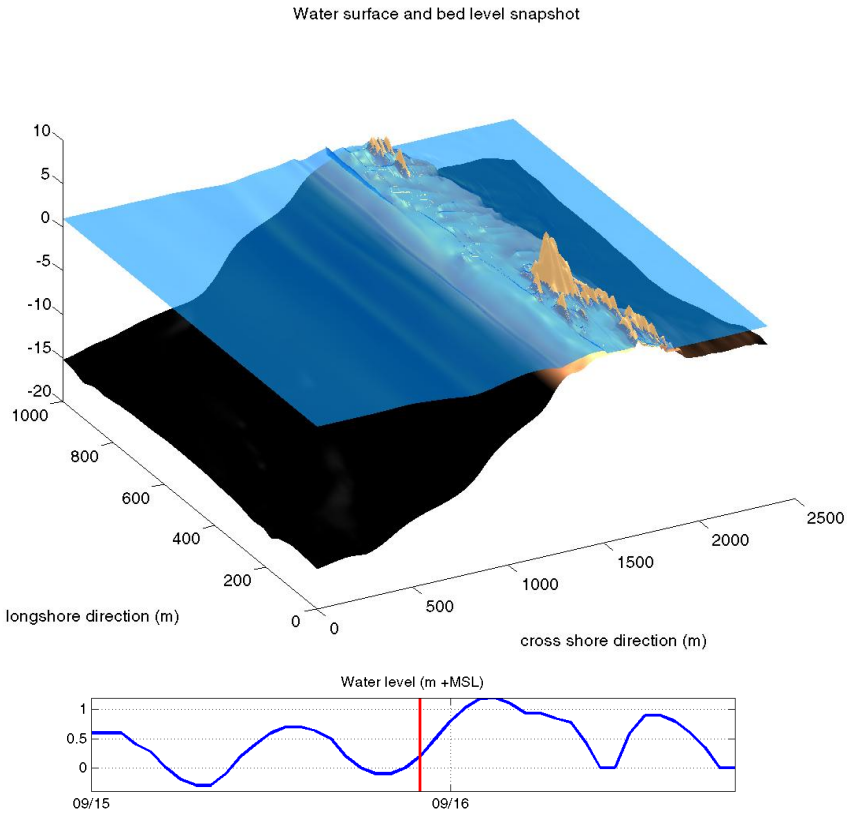


Figure 45 Snapshot of the water surface and bed level after twenty-two hours. The lower panel shows the surge level at the time of the snapshot.

5.4.4 First inundation period (23-32h)

As the peak of the storm approaches land, the wave heights gradually increase towards their maximum level. Simultaneously the storm surge raises water levels above the height of many parts of the island. From the twenty-second hour onwards this leads to a great amount of morphological change. During this period the barrier island system is in the inundation regime. The R_{low} values vary between 1.2m +MSL at the start of the period to roughly 2.2m +MSL at the peak of the storm. Only the highest dunes on the eastern side of the model domain remain above the level of the inundation, see Figure 48.

In this period there is a clear development of a washover fan or washover delta in the back barrier bay, see Figure 46 and Figure 47. Large amounts of sediment are transported over 200 meters into the Santa Rosa Sound. The sediment for the washover fan is removed from large areas of the barrier island. All small to medium sizes features on the island are eroded, leaving behind an almost smooth landscape. The majority of the area in the model domain is only barely above mean sea level.

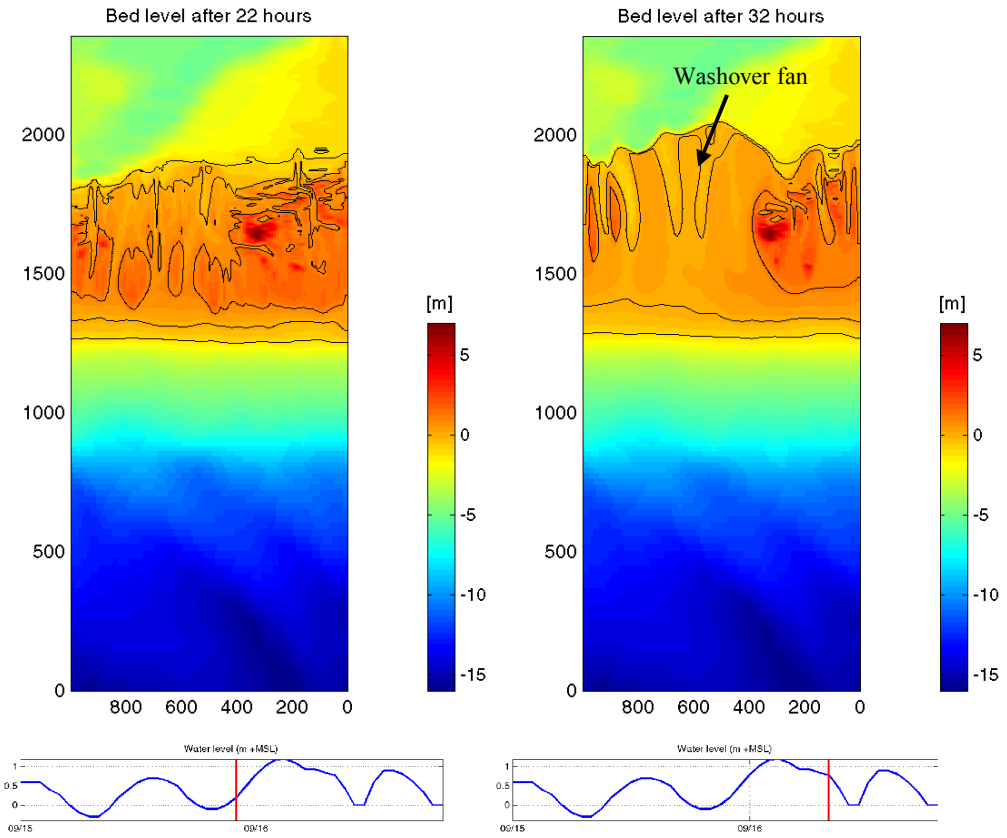


Figure 46 Bed level after twenty-two hours (left panel) and after thirty-two hours (right panel). Contour lines indicate -1m +MSL, 0m +MSL and +1m +MSL.

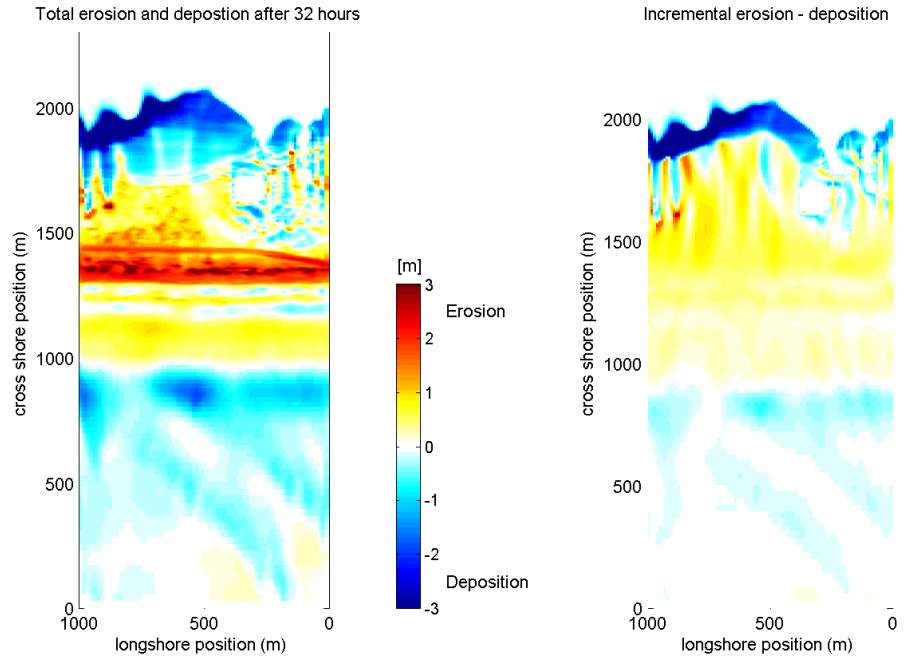


Figure 47 Total erosion and deposition after thirty-two hours (left panel) and incremental erosion and deposition between twenty-two hours and thirty-two hours (right panel)

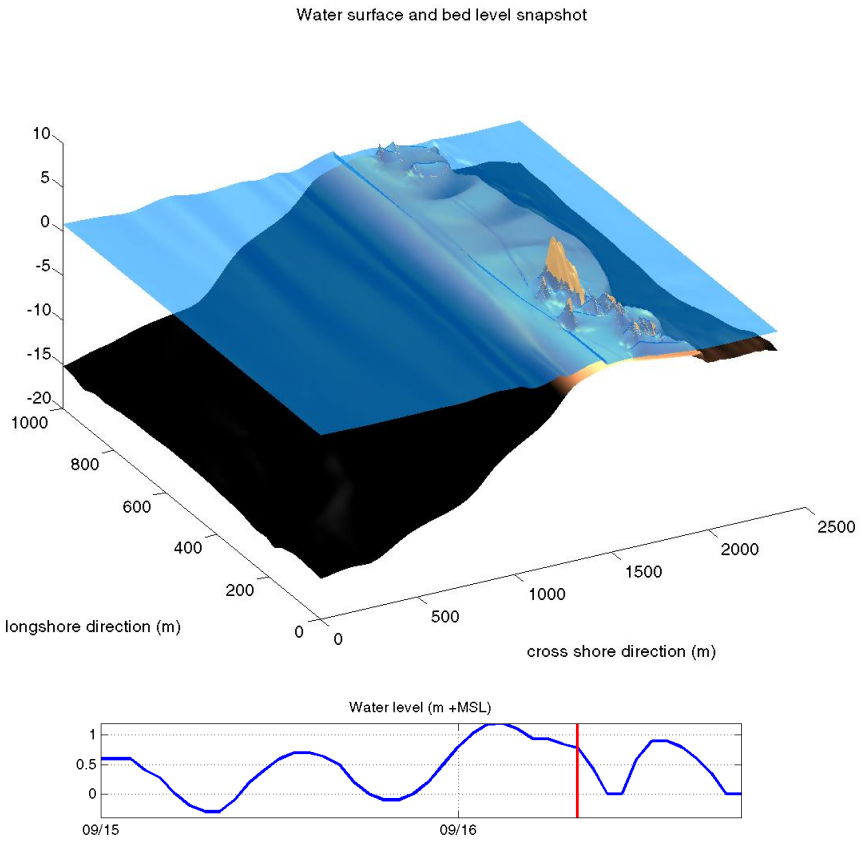


Figure 48 Snapshot of the water surface and bed level after thirty-two hours. The lower panel shows the surge level at the time of the snapshot.

5.4.5 Second inundation period (33-41h)

In the period from the thirty-second hour onwards, the barrier island system is still mostly in the inundation regime as the greater part of the island is only just above mean sea level, see Figure 51. However, once the peak of the storm has passed, the morphological changes start to slow down.

Figure 49 shows the bed level at the start and end of the fifth period. The main morphological feature, the washover fan and delta, remains fairly much the same over the nine hour period, see also Figure 50. Some of the sediment in the centre of the washover fan is deposited further into the back barrier bay. The washover fan retains very steep slopes at its edges, a phenomenon that has been reported by post-storm USGS surveys [Thompson and Sallenger, personal correspondence].

The main morphological change is the development of a breach across the island on the western side of the washover fan. As can be seen in Figure 52, the breach remains open when water levels reach mean sea level.

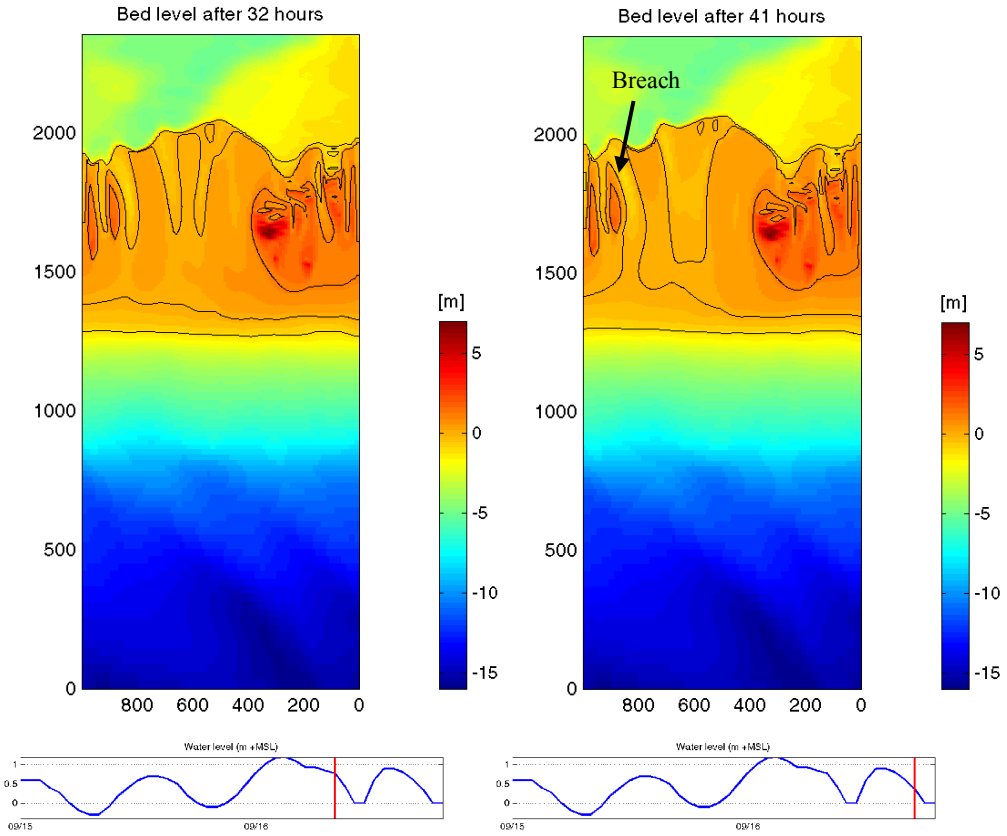


Figure 49 Bed level after thirty-two hours (left panel) and after forty-one hours (right panel). Contour lines indicate -1m +MSL, 0m +MSL and +1m +MSL.

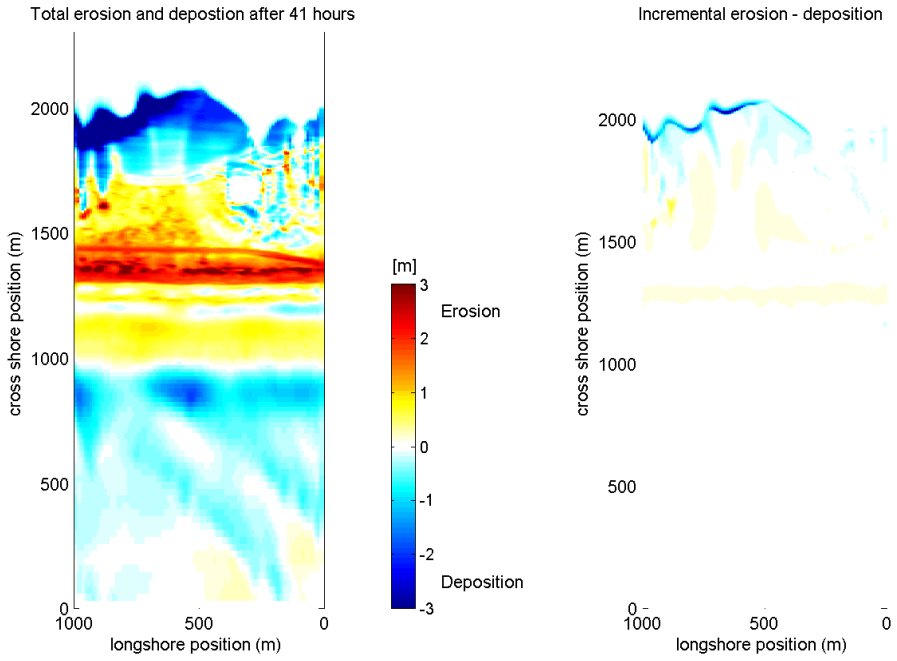


Figure 50 Total erosion and deposition after fourty-one hours (left panel) and incremental erosion and deposition between thirty-two hours and fourty-one hours (right panel)

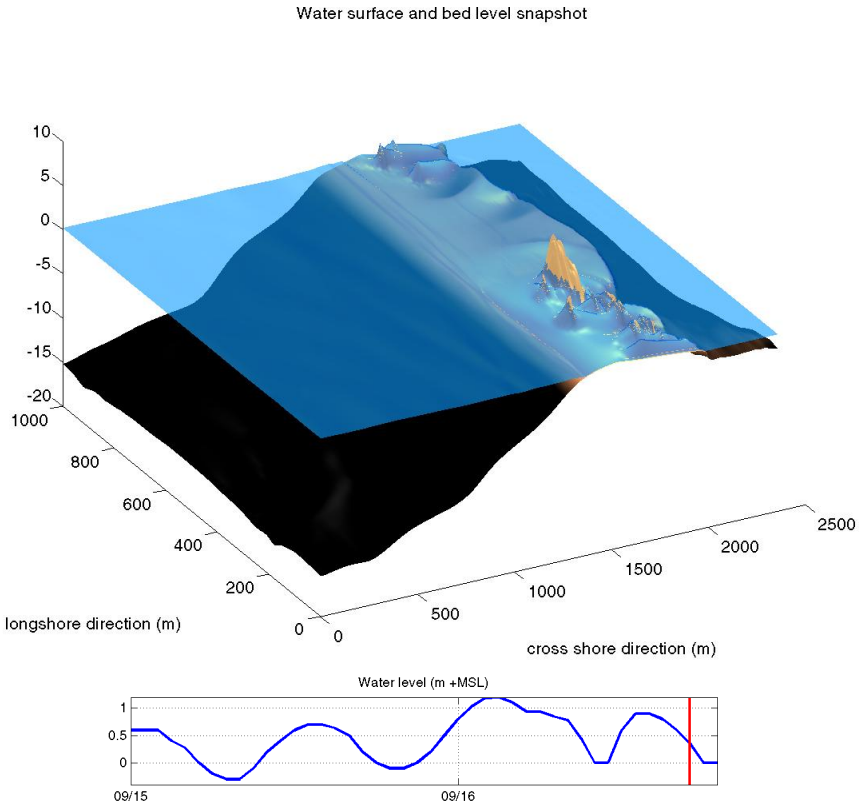


Figure 51 Snapshot of the water surface and bed level after forty-one hours. The lower panel shows the surge level at the time of the snapshot.

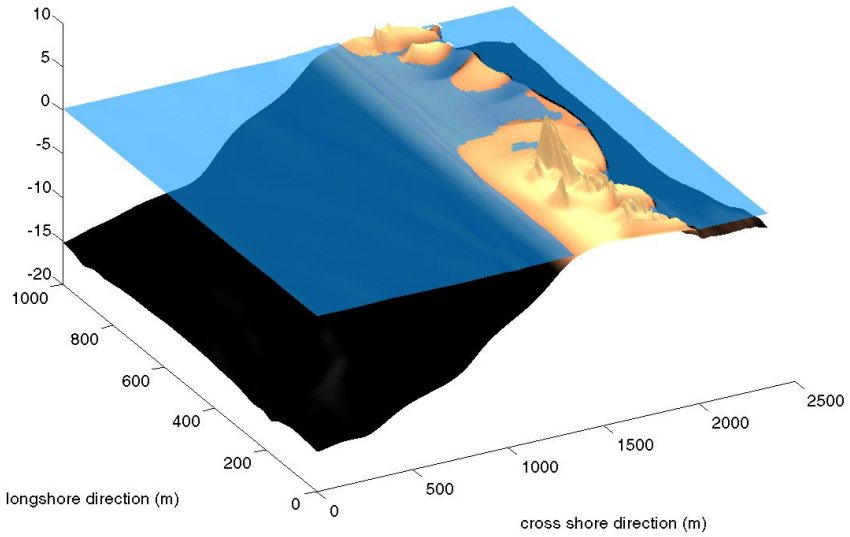


Figure 52 Water surface after storm surge and final bed level

5.4.6 Comparison of post-storm results

In the previous sections the Storm Impact Scale was used to indicate in what morphological state the barrier island system is in during the storm. However, the Storm Impact Scale was not designed to predict intra-storm morphology. In its intended form, the dune height parameters are determined from the pre-storm profile and the wave parameters from the wave conditions during the peak of the storm. Using this approach it is found that R_{high} is roughly 3.1m +MSL and R_{low} is 2.2m +MSL. An examination of the initial elevation in Figure 35 reveals that D_{high} is at least 2.0m +MSL. According to the Storm Impact Scale, the island is certainly in the overwash regime and possibly in the inundation regime. This differs from the results of XBeach, which show clear inundation regime-type hydrodynamics and morphodynamics.

In order to compare the XBeach results in a more quantitative manner, the post-storm XBeach bed level elevation is compared to the measured LIDAR elevation. Unfortunately, the post-storm LIDAR data only covers parts of the barrier island, and none of the nearshore and back barrier bay. The XBeach and LIDAR bed elevation data are shown in Figure 53.

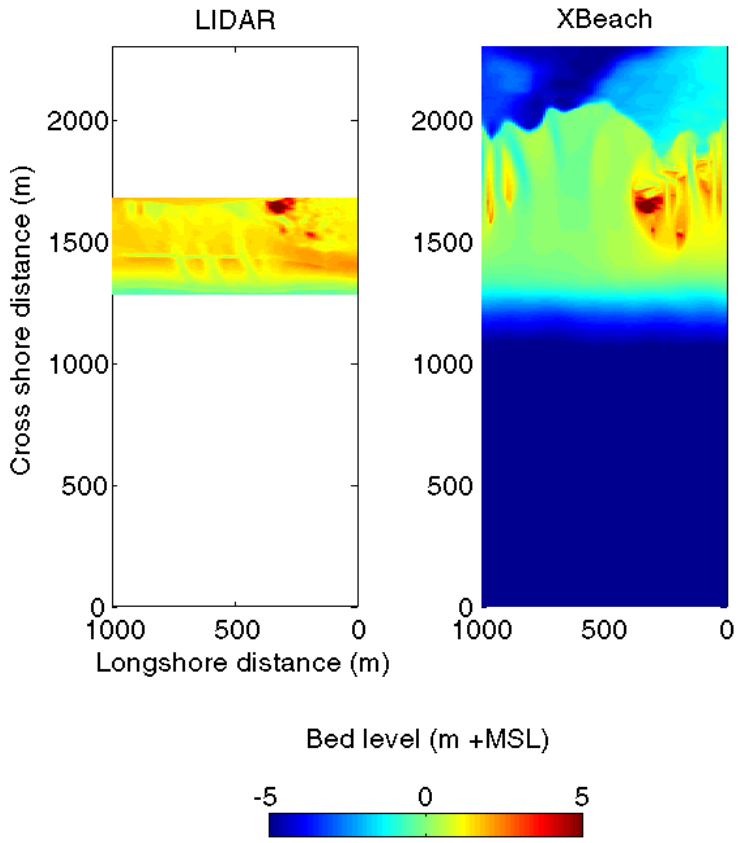


Figure 53 Comparison of post-storm bed level; available LIDAR data (left panel) and XBeach model data (right panel).

Two things stand out in Figure 53. The first is that the bed level in the XBeach model is almost without exception lower than the LIDAR elevation. The second is that the LIDAR data show far more elevation variation than the XBeach results. It also appears from the

LIDAR data that the washover fan was less developed than in the XBeach results, although back barrier bay LIDAR data would be required to verify this.

In general it appears as though the XBeach model has eroded too much sediment from the island and deposited too much in the back barrier bay. To examine this more closely, the storm-integrated erosion and deposition (pre-storm minus post-storm elevation) levels are analysed. These erosion-deposition plots are shown in Figure 54.

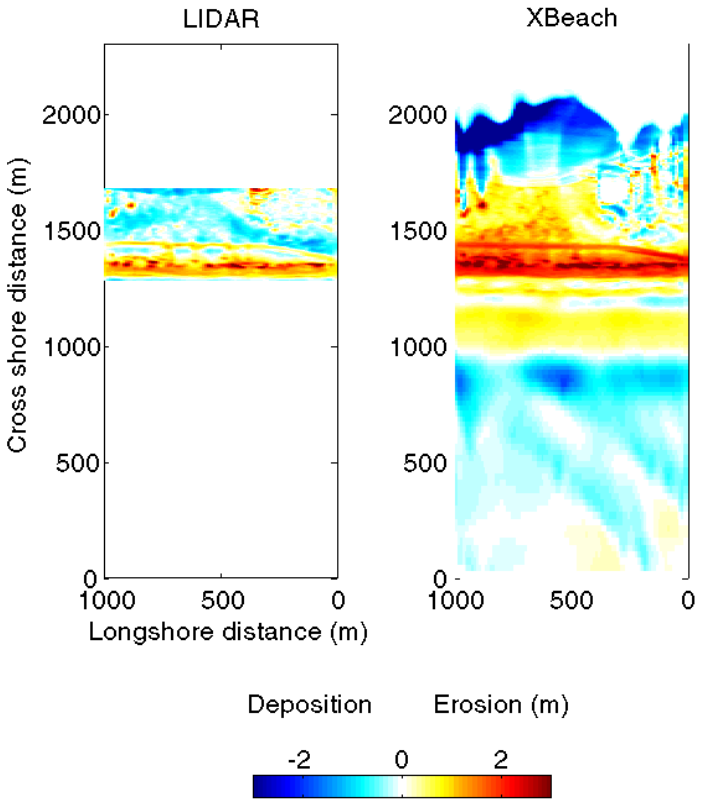


Figure 54 Comparison of post-storm erosion and deposition levels; available LIDAR data (left panel) and XBeach model data (right panel).

Figure 54 shows clearly that the amount of erosion over the island is greatly overestimated by the XBeach model. Compared to the LIDAR data, the foredunes erode very strongly by the XBeach model. More importantly, the XBeach model predicts erosion on the back barrier, whereas the LIDAR data show almost one meter of deposition. Interestingly, this back bay deposition fan in the LIDAR data and the erosion fan in the XBeach results have very much the same shape. This may indicate that the right kind of flow is taking place over the back barrier, but that the sediment transport is being incorrectly calculated.

To quantify the error in the final bed elevation, the relative error is examined. In this case the relative error is defined as the error in the final bed level compared to the total change in reality, assuming that the LIDAR data represent reality:

$$\text{relative error} = \frac{\left| z_{bed,final,LIDAR} - z_{bed,final,XBeach} \right|}{z_{bed,final,LIDAR} - z_{bed,initial,LIDAR}} \tag{5.3}$$

Thus, negative relative errors refer to areas where in reality erosion occurred and positive relative errors to areas where deposition occurred. Errors greater than 1 or less than -1 indicate failure of the model. The relative error of the XBeach model in the areas where post-storm LIDAR data are available is shown in Figure 55.

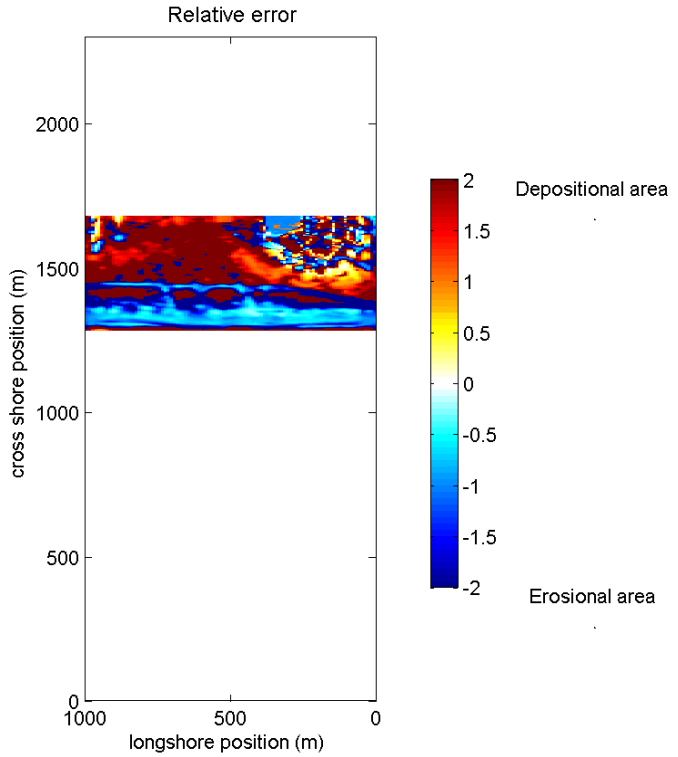


Figure 55 Relative error in the XBeach model. White indicates no error, red and blue indicate increasing errors in depositional and erosional zones respectively.

It can be concluded from the base simulation that the XBeach model develops morphology that is common in overwash and inundation cases, such as washover fans, overwash throats and breaches. However, in the base model the magnitude of erosion and deposition is somewhat greater than in reality. In general the XBeach model tends to predict erosional areas more accurately than depositional areas.

5.5 Model sensitivity

The boundary condition input data for the base simulation are likely to be incorrect. Especially the surge level data from the Delft3D model are likely to be too low, considering the water levels measured in Pensacola and Panama Beach. The significant wave heights calculated by the SWAN model for the Santa Rosa Island model are in the same order as the results of other validated SWAN hurricane models. However, since no measurement data of wave heights in the nearshore of Santa Rosa are available, they may still be considered uncertain. In order to analyse the influence of uncertain boundary conditions on the model results, several sensitivity studies are carried out.

5.5.1 Effect of a morphological acceleration factor

To decrease calculation time during the sensitivity studies, it is preferable to incorporate a morphological acceleration factor. However, no information or guidelines are available about the use of morphological acceleration in XBeach.

The assumption that allows morphological acceleration in morphological models is that the morphology reacts on a very slow time scale compared to the hydrodynamic time scale. In most models, morphological acceleration is achieved by splitting the time domain into several sections during which the forcing conditions remain relatively constant. The morphological change occurring during part of a time section is considered representative for the entire section. Thus a multiplication of the morphological change during part of the time section is applied to that time section. This process is repeated for the following time section.

In the case of the Santa Rosa Island simulation, this method is impractical. The forcing conditions during the storm are highly instationary. It is therefore very difficult to reduce the forcing time series to a set of stationary conditions without making each time section impractically short. The dangers of using short wave forcing time series are for instance discussed in Appendix Y. The solution applied to the XBeach model is to simulate the entire hydrodynamic time series, but to compact the entire duration of the storm by the morphological acceleration factor. For instance, in the case of a morphological acceleration factor of ten, the total hydrodynamic time simulated was just 4.2 hours instead of 42 hours. The number of wave groups generated in this period is therefore also reduced by a factor of 10. However, the rise and fall of surge levels is accelerated by a factor of ten in this approach, leading to further complications that may influence the results of the model. Although the morphological acceleration method applied here may lead to errors, the benefit of being able to quickly explore the effect of parameter space on the model results makes it appealing. Further research into the morphological time scales in cross shore and longshore storm morphodynamics is needed to support the theoretical justification of applying a morphological acceleration factor.

In order to compare the effect of the morphological acceleration factor on the XBeach model results, the base simulation is carried out again with a morphological acceleration factor of 5 and of 10. The final bed elevation of all three models are shown in Figure 56. The erosion-deposition plot for the same models is show in Figure 57

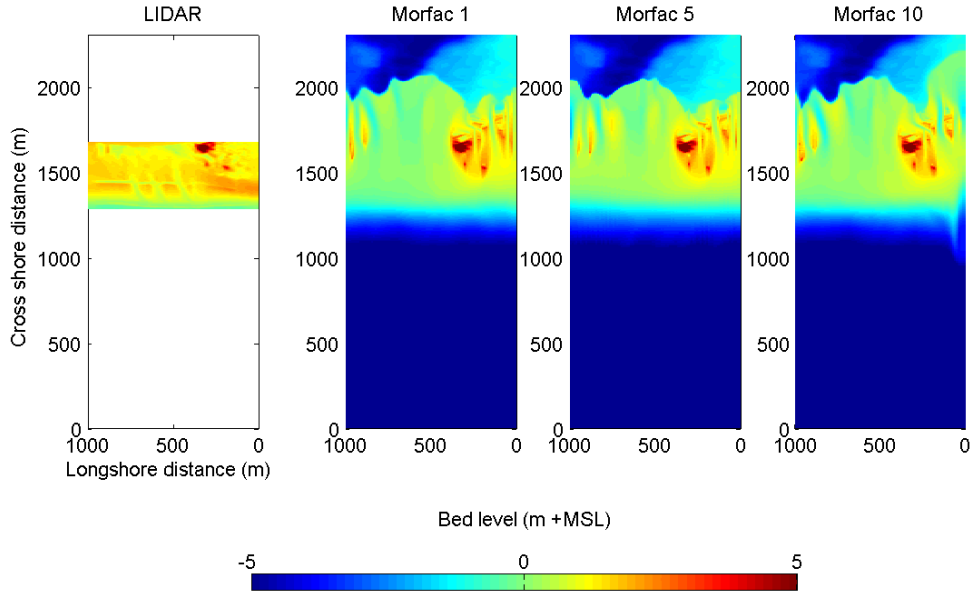


Figure 56 Measured post-storm bed elevation LIDAR data and the final bed elevation for three morphological acceleration factors

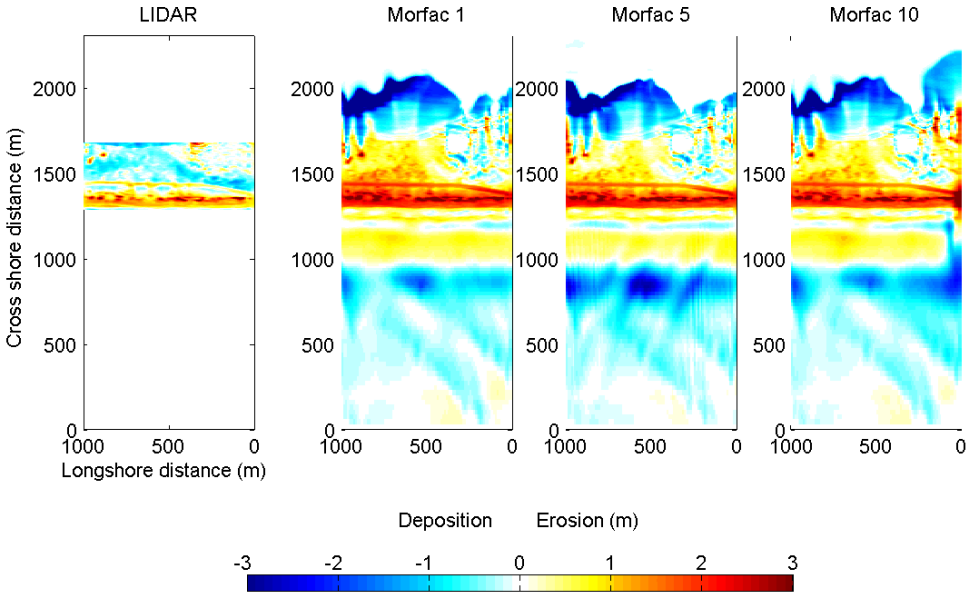


Figure 57 Measured post-storm erosion-deposition LIDAR data and the erosion-deposition data for three morphological acceleration factors

As can be seen in Figure 56 and Figure 57, the morphological acceleration factor has little influence on the final XBeach results. The erosion-deposition results of the simulation with an acceleration of 5 appear to even improve on the results of the base simulation. In the simulation with an acceleration factor of 10, there appears to be boundary-related issues on the eastern end.

The differences between the three XBeach results are and order of magnitude smaller than the difference between any of the simulations and the LIDAR data. It can therefore be

concluded that in order to explore parameter space, it is acceptable to increase the morphological acceleration factor.

5.5.2 Effect of wave heights

In an attempt to understand if the excess erosion in the XBeach model is caused by an overestimation of the incoming waves, the significant wave height on the offshore boundary is reduced by 25%. The maximum significant wave height during the peak of the storm is then 5.1 meters. Other wave parameters are kept the same, along with the surge levels. The final bed elevation of this simulation compared to the base simulation is shown in Figure 58. The erosion-deposition plot of the same is shown in Figure 59.

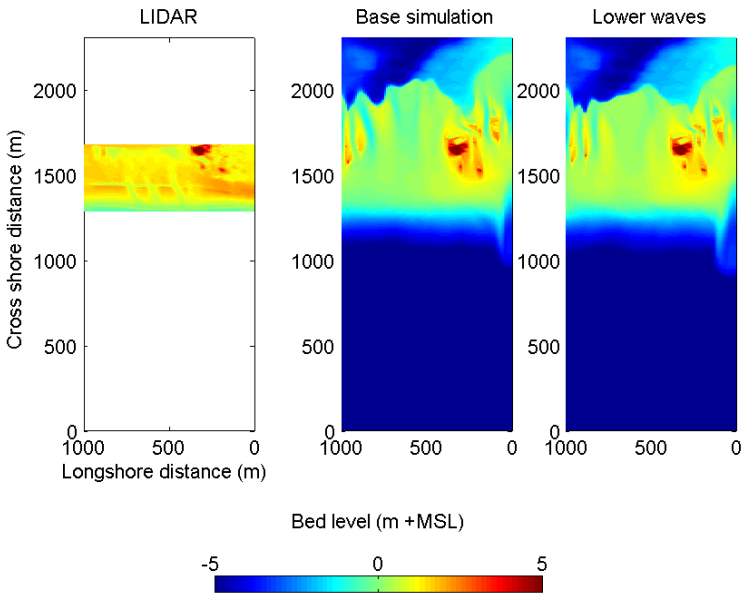


Figure 58 Measured post-storm bed elevation LIDAR data and the final bed elevation for the base simulation (morfac 10) and the simulation with reduced wave heights (morfac 10)

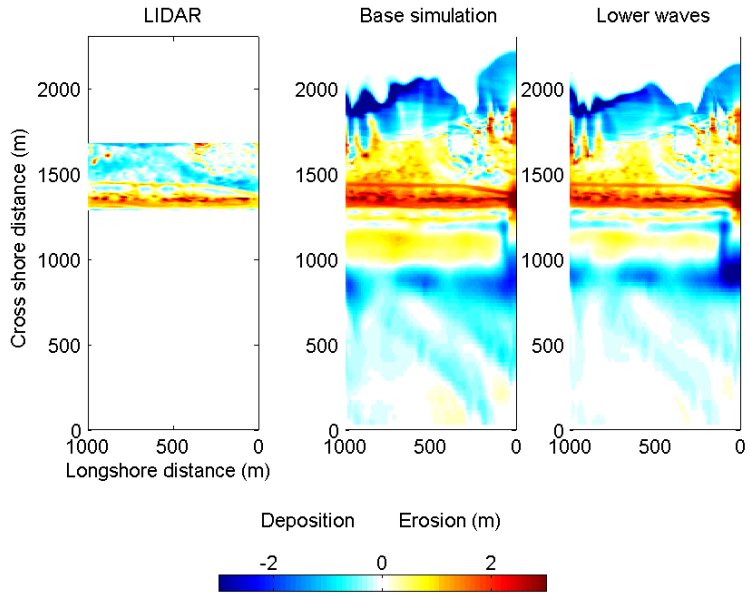


Figure 59 Measured erosion-deposition LIDAR data and the erosion-deposition data of the base simulation (morfac 10) and the simulation with reduced wave heights (morfac 10)

The results show that despite a large reduction in the incoming wave energy, the general erosion and deposition patterns do not change that much. In general, erosion of the foredunes and back barrier is less than in the base simulation, but the difference is insignificant compared to the difference to the post-storm LIDAR data.

5.5.3 Effect of water levels

The second important uncertainty in the Santa Rosa island model is the water level on either side of the barrier island. In the base simulation, the water level was assumed equal on both sides of the island and the peak surge level was very possibly underestimated. It is assumed that lower surge levels and zero water level gradient across the island will lead to less erosion than high surge levels and strong gradients. Therefore carrying out simulations with higher water levels and gradients is likely to lead to worse XBeach predictions. However, the results may still lead to insight into physical processes.

As mentioned in section 5.2.2, Donnelly *et al.*[submitted] used the water level data of the ADCIRC-model of Chen *et al.* [submitted] to analyse dune morphology. Since the water level data used in the base simulation are unlikely to be accurate, it would be interesting to study the effects on the XBeach results using elements of the ADCIRC-model water level data of Chen *et al*. The water levels of the ADCIRC-model differ in three ways from the water levels used in the base simulation. Firstly, the peak water level is far greater than the water level according to the Delft3D simulation. Secondly, the peak water level in the back barrier bay is lower than the peak on the offshore side of the island. Thirdly, there is a clear phase lag between the water levels on the offshore side and the back barrier bay.

In order to run a new simulation with the ADCIRC-model water levels, the water level time series would have to be extrapolated in the period after the storm, leading to further model

uncertainties. Until further information is available, more insight may be gained by analysing the effects of all three differences in water level on the base simulation separately.

Higher peak surge

To study the effect of a higher surge level during the peak of the storm, the imposed water levels on the offshore and back barrier bay boundaries are increased equally during the peak of the storm. The surge level in the period between low water before and after the storm is linearly increased until the maximum surge level is 2.0m +MSL, see Figure 60. The wave boundary conditions are kept the same as in the base simulation.

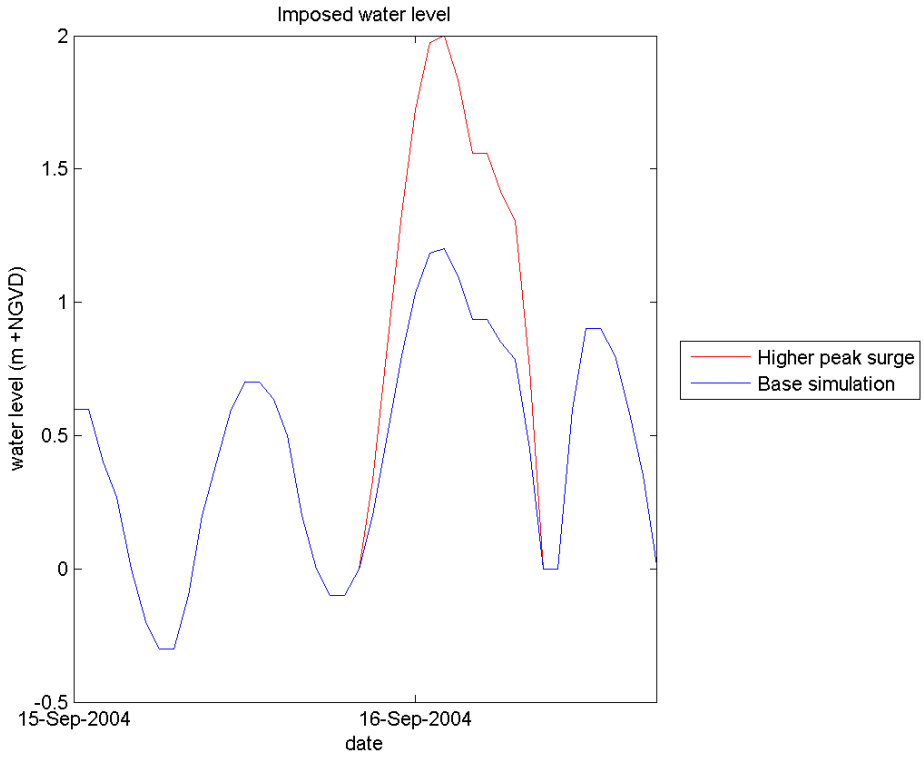


Figure 60 Imposed water level on the offshore and back barrier bay boundaries

The effect on the increased surge on the final bed elevation, see Figure 61, and on the erosion-deposition, see Figure 62, is quite significant. The increased surge level not only leads to slightly more erosion, but the deposition of sediment is no longer restricted to the washover fan and delta. Instead, deposition occurs evenly along the entire back barrier bay.

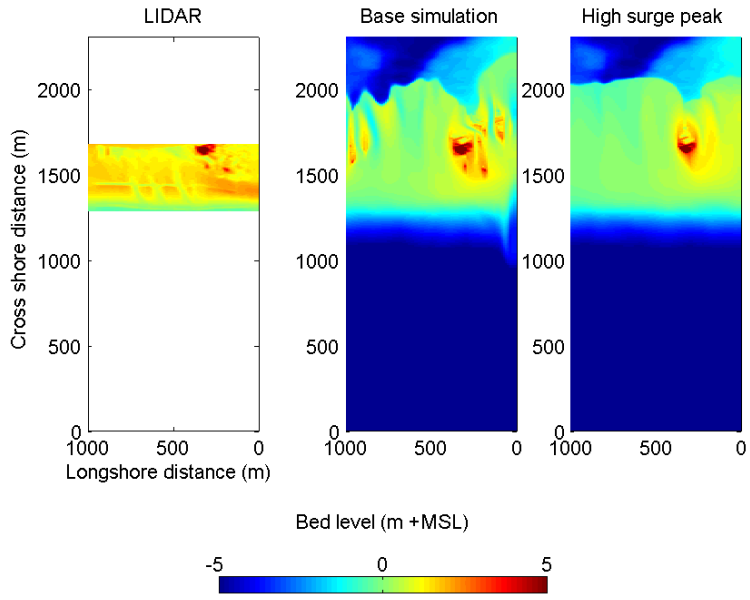


Figure 61 Measured post-storm bed elevation LIDAR data and the final bed elevation for the base simulation (morfac 10) and the simulation with increased surge level (morfac 10)

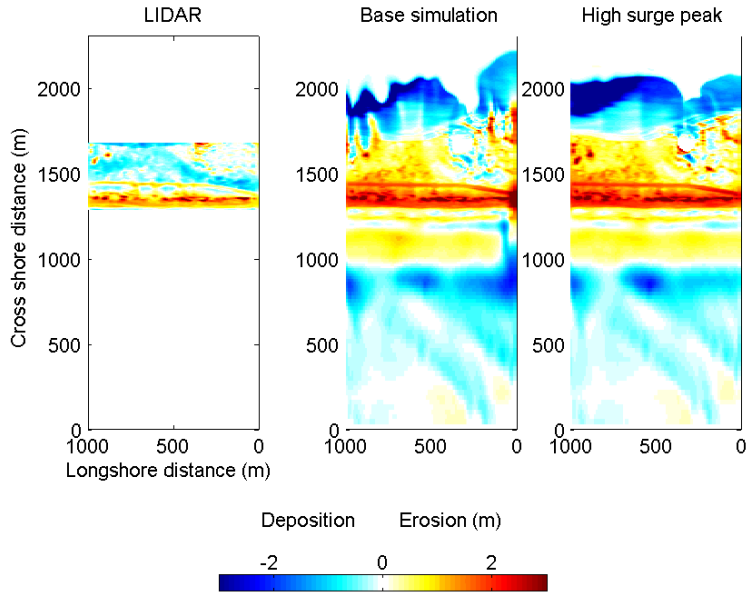


Figure 62 Measured erosion-deposition LIDAR data and the erosion-deposition data of the base simulation (morfac 10) and the simulation with increased surge level (morfac 10)

Water level gradient across the barrier island

In the ADCIRC-model data of Chen *et al.*, the peak water level on the seaward side of the island is higher than the peak water level on the bay side of the island. Essentially this leads to a water level gradient across the island. In order to study the effects of a water level gradient, the imposed water level on the back barrier bay boundary is set to 0m +MSL for

the entire time series. The water level on the offshore boundary is kept the same as in the base simulation, as are the wave boundary conditions.

The water level gradient over the island has an important impact on the morphology of the island. The effect is very different than the effect of a higher overall surge level, see Figure 63 and Figure 64.

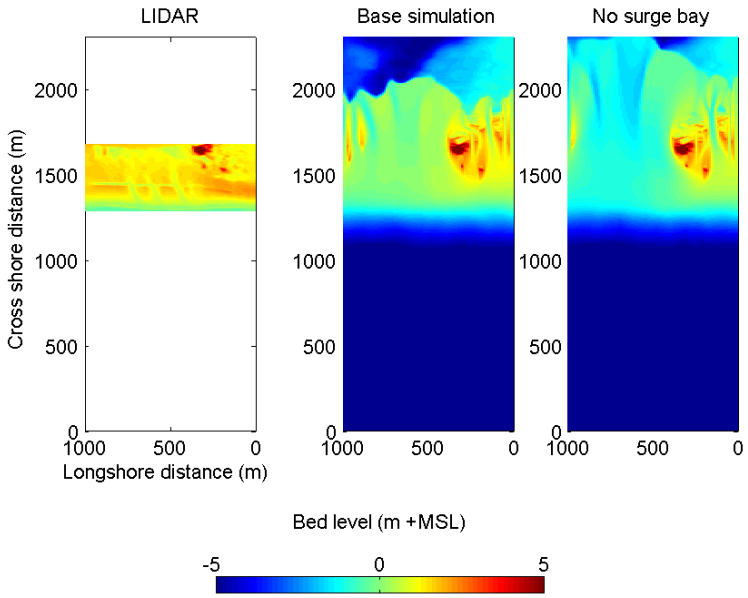


Figure 63 Measured post-storm bed elevation LIDAR data and the final bed elevation for the base simulation (morfac 1) and the simulation with a large water level gradient (morfac 1)

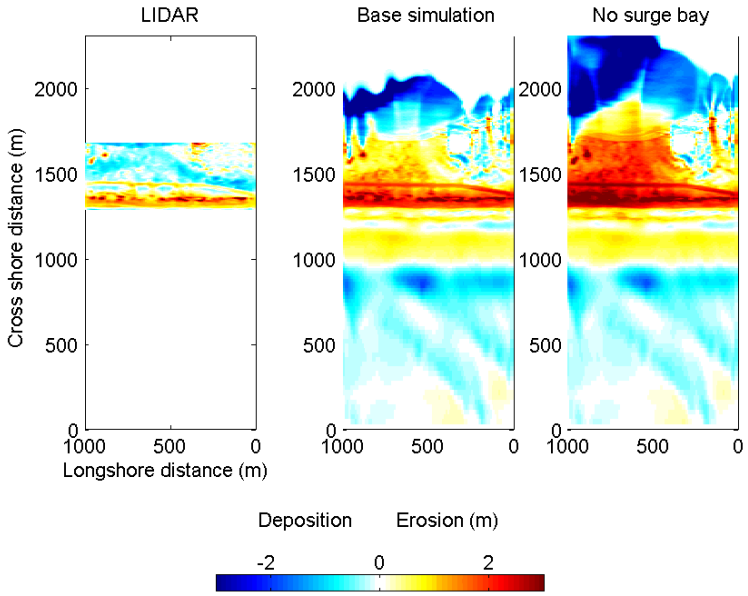


Figure 64 Measured erosion-deposition LIDAR data and the erosion-deposition data of the base simulation (morfac 1) and the simulation with a large water level gradient (morfac 1)

The results show substantially more erosion than in the base case and the higher peak surge simulation. The increase erosion takes place across the entire breadth of the island in

roughly the funnel between the larger back barrier dunes on the eastern edge of the model domain and just outside the western edge of the domain. Erosion in this area is so great that the island breaches. The simulation shows that deposition is confined to a limited area, which could be described as a washover delta. However, unlike in the base case and the case of an increased peak surge, the washover remains entirely below mean sea level.

Phase lag between water levels

To study the effect of a phase lag between the water level in the Gulf of Mexico and the back barrier bay, a third simulation is run. In this simulation the water level on the offshore boundary is kept the same as in the base simulation. The water level on the back barrier bay boundary is copied from the offshore boundary with a one hour delay, see Figure 65. This delay is based on the approximate travel time of a free shallow water wave from the Pensacola Inlet to the location of the model domain. The offshore wave conditions are kept the same as in the base simulation.

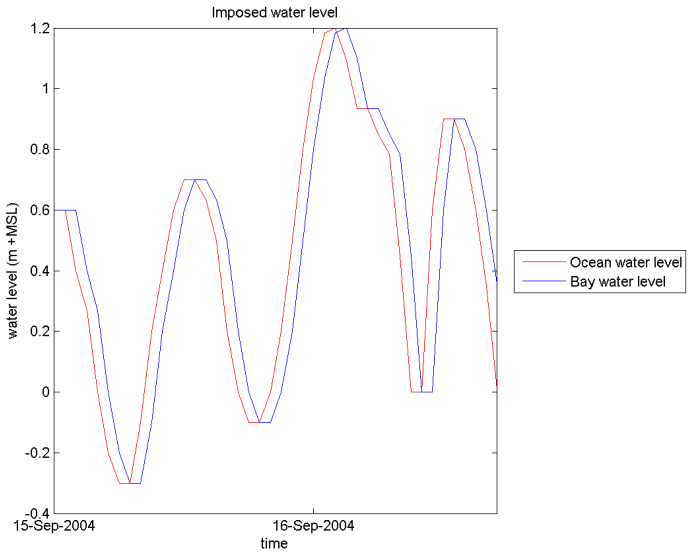


Figure 65 Imposed water level on the offshore and back barrier bay boundaries

The effect of this phase shift is essentially varying water level gradients across the island. Especially after the peak of the storm, when large parts of the island have been eroded, the backwash from the back barrier bay to the open ocean may lead to new morphodynamic behaviour. However, as can be seen in Figure 66 and Figure 67, this is not the case. The net effect of a one-hour phase lag is almost negligible in the final results of the XBeach simulations.

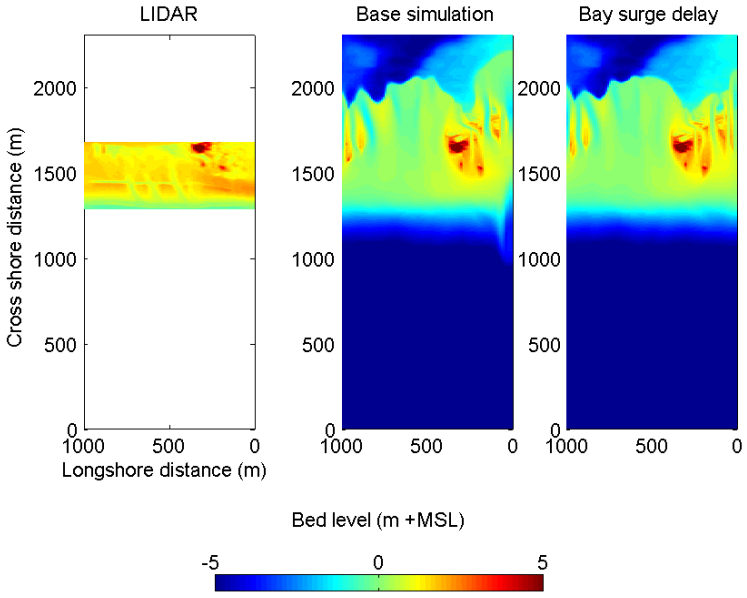


Figure 66 Measured post-storm bed elevation LIDAR data and the final bed elevation for the base simulation (morfac 10) and the simulation with a phase difference (morfac 10)

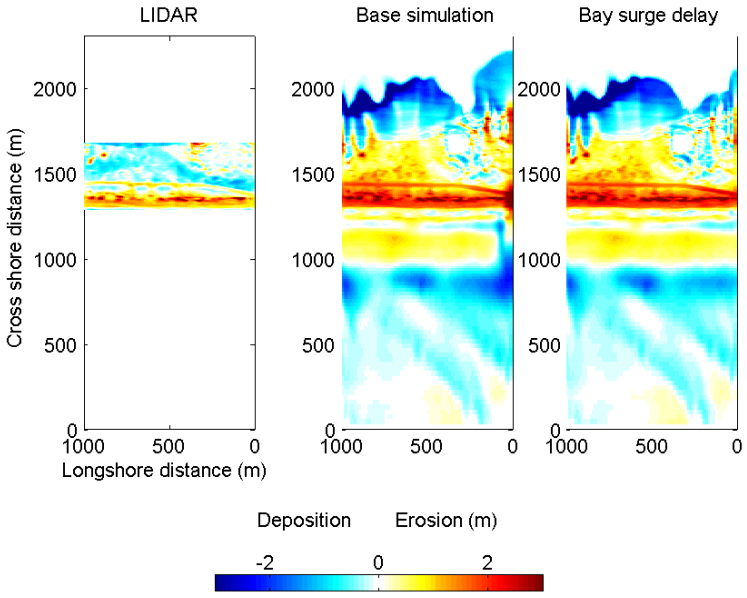


Figure 67 Measured erosion-deposition LIDAR data and the erosion-deposition data of the base simulation (morfac 10) and the simulation with a phase difference (morfac 10)

5.5.4 Effect of sediment transport

This study has almost entirely focussed on the hydrodynamics of overwash and the associated morphological changes. Almost no attention has been given to the influence of the sediment transport parameters in the calculation of bed level changes. In order to gain some insight into the effect of the sediment transport scheme on the morphology of the

barrier island in the XBeach simulations, the formulation for the equilibrium concentration, see also section 3.2.4 and equation (3.12), is modified from:

$$C_{eq} = \frac{A_{sb} + A_{ss}}{h}\left(\left(\left|u^E\right|^2 + 0.018\frac{u_{rms}}{C_d}\right)^{0.5} - u_{cr}\right)^{2.4} \tag{5.4}$$

to:

$$C_{eq,new} = \frac{1}{2}C_{eq} \tag{5.5}$$

By halving the equilibrium concentration, sediment will be eroded less quickly from the foredunes and will settle faster on the back barrier. The results for this simulation can be seen in Figure 68 and Figure 69.

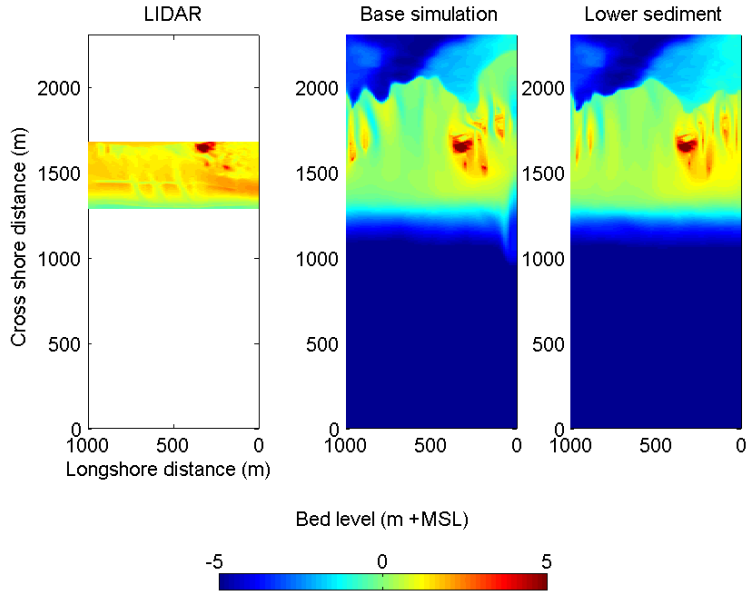


Figure 68 Measured post-storm bed elevation LIDAR data and the final bed elevation for the base simulation (morfac 10) and the simulation with lower equilibrium sediment concentration (morfac 10)

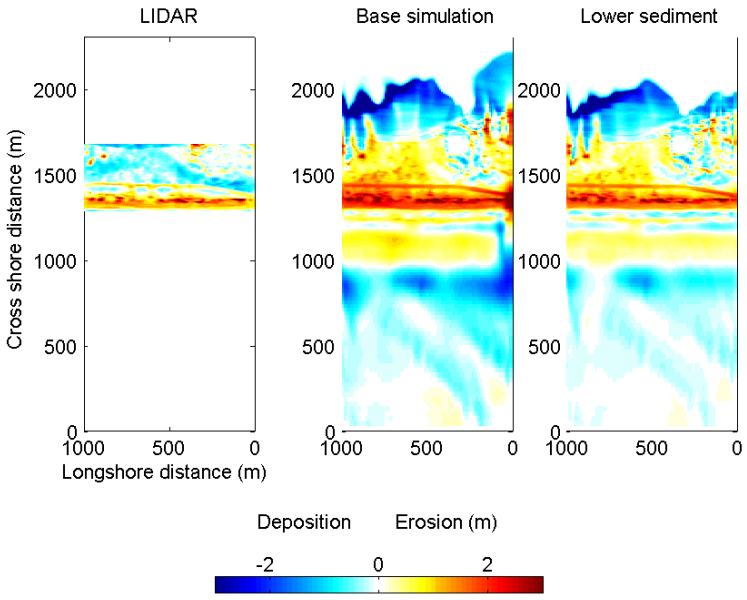


Figure 69 Measured erosion-deposition LIDAR data and the erosion-deposition data of the base simulation (morfac 10) and the simulation with lower equilibrium sediment concentration (morfac 10)

Halving the equilibrium sediment concentration has surprisingly little effect on the final results. As can be seen in Figure 69, the amount of erosion on the back barrier is reduced a little, but not enough to turn it into a deposition zone. The final elevation of the barrier island appears to be little affected by the change in equilibrium sediment concentration and does certainly not present the same variability as seen in the LIDAR data.

5.5.5 Recommendations for further study

The sensitivity study has shown the effect of those parameters that are expected to have the greatest influence on the sedimentation and erosion patterns. Several external and internal parameters however remain to be examined.

Several recent studies [e.g. Steetzel, 2002; Coeveld and de Vroeg, 2004] have shown that an increase in the incident peak period leads to greater dune erosion. This parameter could be explored in its relation to overwash and related washover.

As the duration of the storm on the coast of Santa Rosa Island is relatively well documented, this variable was not varied. However, in an academic sense it is very interesting to determine if longer storm durations lead to greater amounts of erosion, or that the barrier island reaches a storm erosion profile and does not respond to further forcing.

The short wave forcing on the offshore boundary was determined from parameterized SWAN-output. The output did not contain information about the amount of directional spreading of the short waves. This parameter is known to affect the amount of energy in the bound infragravity wave band. Further studies should study the effects of narrow and wide directional wave spectra on the patterns and amount of overwash.

In the current XBeach model, the surface of the barrier island is given the same bed roughness as the seafloor. It is expected however, that vegetation and percolation on the barrier island will lead to reduced flow velocities. In subsequent studies, attention should be paid to the effect of the roughness coefficient on the subaerial barrier on the washover volumes.

In the sensitivity studies, no analysis was made of the effect of internal model parameters. In future research the effect of the critical slope angles used in the avalanching algorithm should be examined as this controls to a great extent the speed at which the foredunes erode. The effect of avalanching can also be examined by repeating the base simulation without the avalanching algorithm.

5.6 Conclusions

Through a series of academic test cases based on a real scenario, XBeach has shown it is able to model complex hydrodynamics associated with dune overwash and inundation. The model also appears to be able to reproduce morphological features associated with such hydrodynamics. However, the magnitude of erosion in the simulations on Santa Rosa Island is an order greater than the measured erosion.

By means of a sensitivity study, it is shown that the XBeach model reacts significantly to the imposed global surge level and the water level gradient across the island. Since the boundary conditions imposed on the base simulation are likely to be underestimates of the true surge conditions, this sensitivity cannot be used to explain the large erosion rate in the model.

By means of a limited sensitivity study, the XBeach model is shown to relatively insensitive to the sediment transport function, although more attention should be given to examining this statement further.

In this study sensitivity analyses were principally carried out using the external forcing parameters, wave height and surge. Further attention must be spent on varying internal parameters, such as the critical bed slope in the avalanching mechanism.

6 Longshore scale effects

6.1 Introduction

The secondary objective of this thesis is to determine the effect of the longshore variation of dune and barrier island elevation on the patterns and amount of overwash. In Chapter 5 a model was set up of part of Santa Rosa Island during Hurricane Ivan. In this model, the LIDAR/Coastal Relief Model elevation data were smoothed in longshore and cross shore direction, using the method of Plant *et al.*[2002]. The longshore smoothing scale was set at 10 meters, allowing very small features to be resolved in the model. In this chapter, two questions are posed. First, what is the effect of the small scale features on the overwash during Hurricane Ivan compared to the effect of the large scale features? Second, is it possible to set up overwash models with less detailed elevation data than the LIDAR data and still expect to find the same simulated overwash patterns? Theoretically it may even be possibly that the XBeach model performs better if the model input is less detailed [Plant *et al.*, 2008].

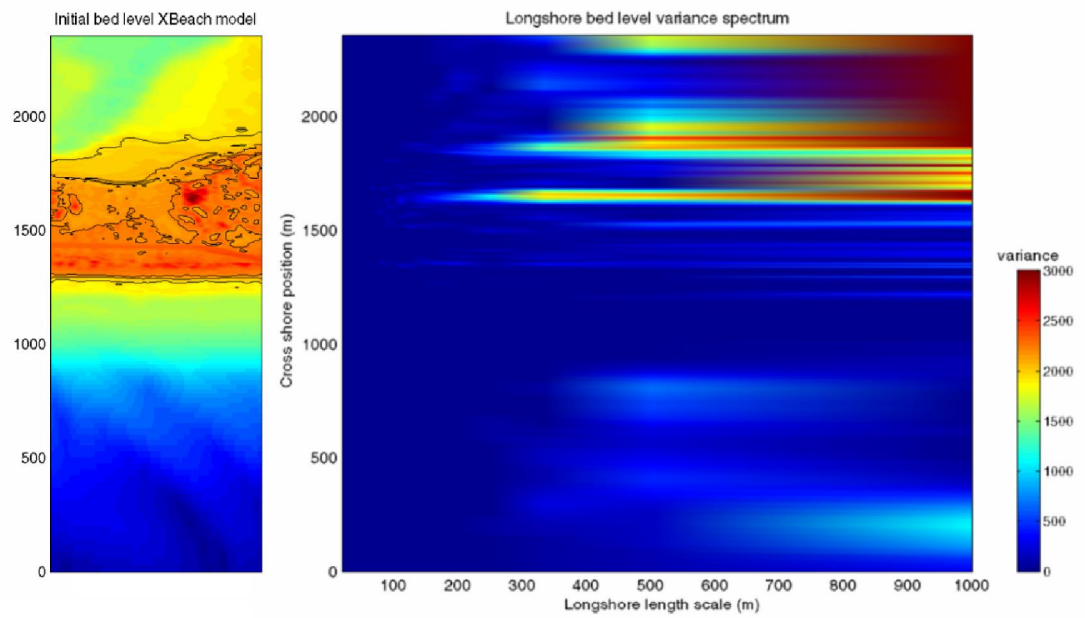


Figure 70 Initial bed profile (left panel) and a spectrum density-plot of the longshore elevation variance as a function of longshore length scale and cross shore position (right panel)

6.2 Model setup

An analysis is first made of the presence of longshore variation in the initial bed level of the Santa Rosa Island model. Figure 70 shows a spectral plot of the variance in the bed level elevation as a function of longshore wave length and cross shore position, obtained by Fourier transformation of longshore transects. The greatest longshore variance is located in

the back barrier bay at length scales of over 900 meters. This corresponds with the spacing of large scale structures on the back of the barrier island, see for instance Figure 22. The subaerial part of the barrier island contains a larger spread of spectral variance. On the back barrier, length scales in the range between 300 and 1000 meters contribute equally to the elevation pattern. The foredunes also appear to be dominated by length scales in the range of 100 to 1000 meters, although the contribution of the foredunes to the total longshore variance is limited. Finally, it should be noted that the Fourier transform took place on the smoothed LIDAR data and will therefore by definition not contain variance below 10 meter length scales.

It is expected that despite the fact that the majority of the longshore variance is located in long length scales, shorter length scales may play an important role due to non-linearities. One example of this is the influence of bed slopes, which is related to the longshore variance via the inverse of the length scale.

To evaluate the effect of longshore variance in the XBeach model, five model runs are set up using increasing longshore smoothing scales. The base simulation has the same 10-meter longshore smoothing scale as in the original Santa Rosa Island model. The remaining 4 models use initial elevation data based on a 100 meter, 250 meter, 500 meter and 2000 meter longshore smoothing scale of the LIDAR/Coastal Relief Model data respectively. These first two longshore smoothing scales correspond with the start of variance in the foredunes (100m) and back barrier (250m). With the 500 meter longshore smoothing scale significant features in the subaerial barrier island are removed. The 2000 meter longshore smoothing scale leads to a quasi-longshore uniform topography. In all cases the cross shore smoothing scale is kept at 5 meters, the same value as in the original Santa Rosa Island model. The initial bed elevation for all five models are shown in Figure 71.

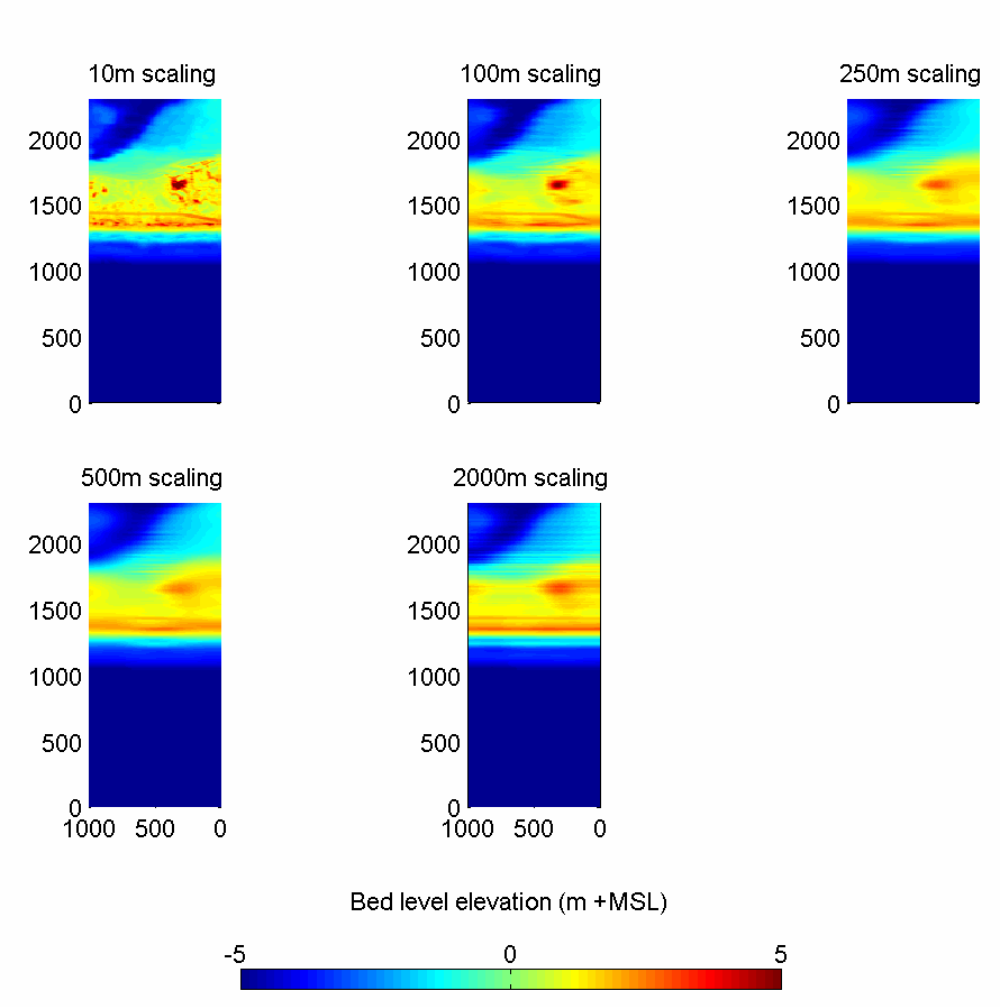


Figure 71 Initial bed elevation for five cases of longshore smoothing scale

To ensure that the hydrodynamics are not changed by to the numerical grid size, the longshore grid size is set at 10 meters for all simulations.

To shorten the calculation time of the simulations, only 10 hours around the peak of Hurricane Ivan are modelled. In this period wave and surge conditions are kept constant, based on the average levels during the 10-hour period. The exact same boundary conditions between simulations are guaranteed by reusing the boundary condition files of the first simulation, see Appendix Y. Calculation time is further shortened by applying a morphological acceleration factor of five.

6.3 Model results

The erosion-deposition plots of all five simulations are shown in Figure 72. All five simulations show remarkable similarities.

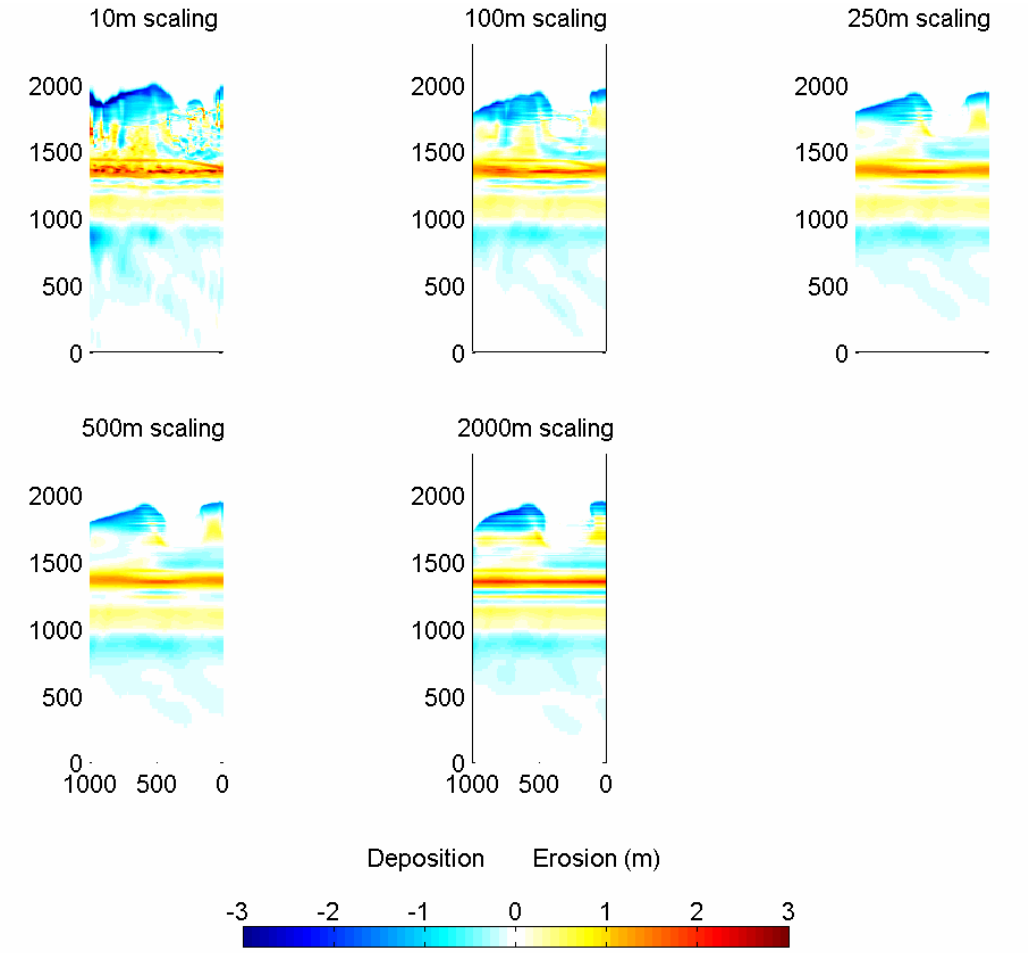


Figure 72 Final erosion-deposition plots for all five longshore smoothing scales

The main morphological feature in the simulation, the washover fan, reappears in all five simulations in the same location and is approximately the same size. The erosion of the foredunes is in the same order of magnitude in all simulations and all simulations predict a deposition layer in front of the high back barrier dunes on the eastern end on the model domain.

Other smaller-scale features are not represented in all simulations. The erosional fan behind the foredunes at the location of the washover fan does not appear in the simulations with a longshore smoothing scale of 500 or 2000 meters and is highly underdeveloped in the 250 meter case. Instead this areas undergoes zero change of a slight deposition in the higher longshore smoothing scale simulations. Surprisingly, the erosion of the road behind the foredunes is not well represented in the simulations with smoothing scales of 250 meters and up. As can be seen in Figure 71, the road is visible in all the initial bed profiles. The cross shore smoothing was kept intentionally constant to resolve such features.

Although only part on Hurricane Ivan was simulated, the post-storm LIDAR data are compared to the results of the XBeach simulations. In order to do this, the post-storm LIDAR data are first longshore-smoothed in the same manner as the initial elevation data were. A comparison between the final XBeach results and the smoothed, measured LIDAR data is given in Figure 73.

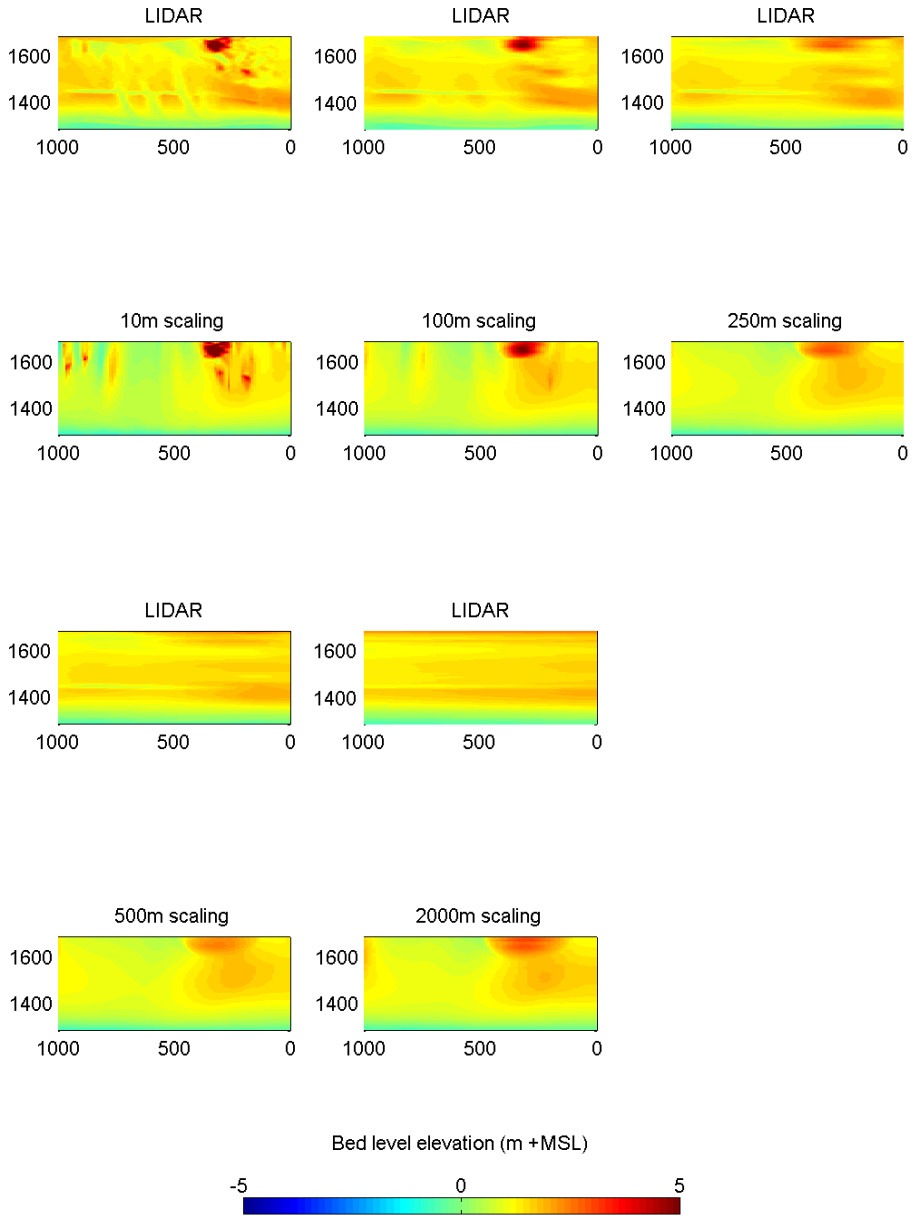


Figure 73 Post-storm longshore smoothed LIDAR data (first and third rows) and post-storm longshore smoothed XBeach results (second and forth rows)

It should be noted that the final XBeach results of the five simulations are unlikely to match the LIDAR results given the inaccuracies discussed in Chapter 5 and the fact that the storm is simulated in a highly schematic manner.

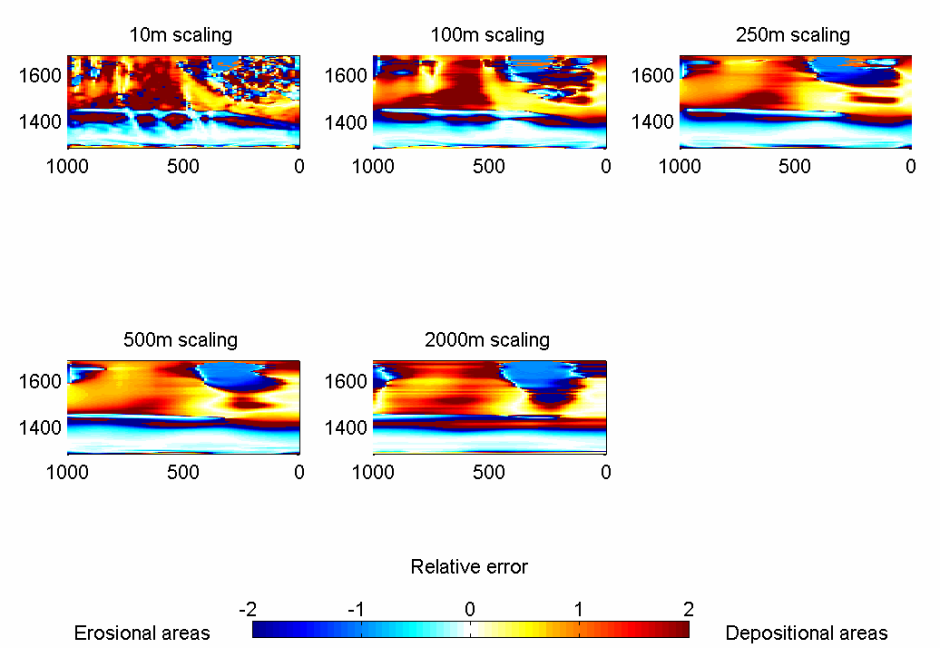


Figure 74 Relative error of the five longshore scaled simulations. White indicates no error, red and blue indicate increasing errors in depositional and erosional zones respectively.

Figure 74 shows the relative error as defined in equation (5.3). It can be seen in this figure that no longshore smoothing scale fares particularly better than any other. Therefore it can be concluded that at this stage XBeach is equally inaccurate whatever the longshore smoothing scale.

6.4 Discussion

6.4.1 Washover fan location

In literature the location of washover fans is generally related to gaps in the foredunes and variations in their height. However, as can be seen in Figure 71, in the simulations with the highest longshore smoothing scales, the foredune height variation is minimal or non-existent. Therefore the location of the washover fan is unlikely to be caused by variations in the foredunes.

The only features remaining in the highest longshore smoothing scales are the high back barrier dunes. It is suggested that the variation in height of these back barrier dunes determines the location of the washover fan under these forcing conditions. Overwashing water is likely to become channelled between such high features before reaching the back barrier bay, thus first eroding the lower section of the back barrier and eventually depositing sediment in the back barrier bay.

The size of the washover fan also appears to be independent of the longshore smoothing scale. This may be because the sediment used for the creation of the washover fan comes from the foredunes. As in all simulations the foredunes are entirely destroyed, the available sediment is similar in all cases.

It should be noted that the results obtained in the five longshore smoothing simulations follow a period in which the island is inundated. In such extreme conditions it can be argued that the variation in foredune height plays an insignificant role. In order to examine the effect of the back barrier dunes and foredunes on the location of washover fans more thoroughly, similar simulations should be carried out under less extreme forcing conditions. Careful attention should also be given to the results of sensitivity study in section 5.5.3, in which it is shown that at higher levels of inundation, the washover fan disappears entirely.

6.4.2 Modelling large longshore domains

The apparent insensitivity of the XBeach model to longshore length scales in reproducing large scale morphological features offers the possibility to model large stretches of coast using coarse longshore data. In order to make this computationally feasible, it is necessary to reduce the number of calculation grid points. It is suggested that the most efficient way to do this is to increase the longshore grid spacing. It is expected that the calculation time decreases at least linearly with the increase in longshore grid size.

To determine if it is still possible to model the main morphological features on a coarse longshore calculation grid, a new simulation is set up. In this simulation the longshore calculation grid spacing is set at 100 meters. The initial bed elevation is taken from the 2000 meter longshore smoothing scale simulation and interpolated to the new calculation points. The erosion-deposition plot of the coarse simulation is shown in Figure 75.

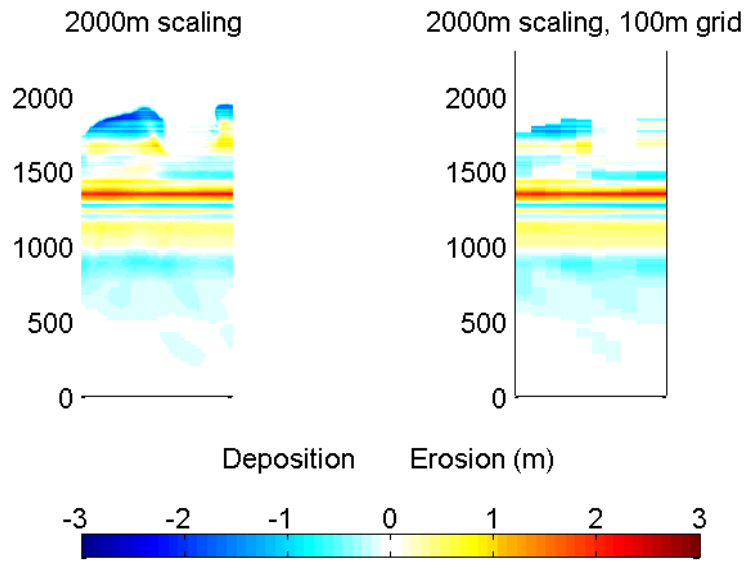


Figure 75 Erosion-deposition plots for an XBeach simulation with 10 meter longshore grid size (left panel) and 100 meter grid size (right panel). Both simulations have the same input bed elevation with 2000 meter longshore smoothing scale.

Figure 75 shows clear similarities between the simulation on the fine calculation grid and the coarse calculation gird. It is suggested that for many applications in coastal management

and coastal engineering the dominant morphological features are represented adequately in the coarse model.

Since the model results appear to be unaffected by longshore bathymetry smoothing scales, it would seem possible to model the Santa Rosa domain in a series of one-dimensional models. In order to examine possible differences between 1D- and 2DH-modelling, a series of one-dimensional models is set up along the 20 cross shore transects in the coarse-grid 2DH-model. The results of the combined 1D-models and the coarse-grid 2DH model are shown together in Figure 76. Although the two figures are remarkably similar, there are several differences. The first difference is the shape of the washover fan. In the 1D-models the fan is short and distinctly symmetrical. The second and more striking difference is the amount of erosion of the foredunes. As discussed earlier in Appendix V, the hydrodynamics in 1D-models is restricted by the numerical boundaries of the model. In the case of high water levels, this leads to more overwash and therefore more erosion. It is concluded that the limited calculation-time benefits of the 1D-models do not outweigh the error in the hydraulic forcing.

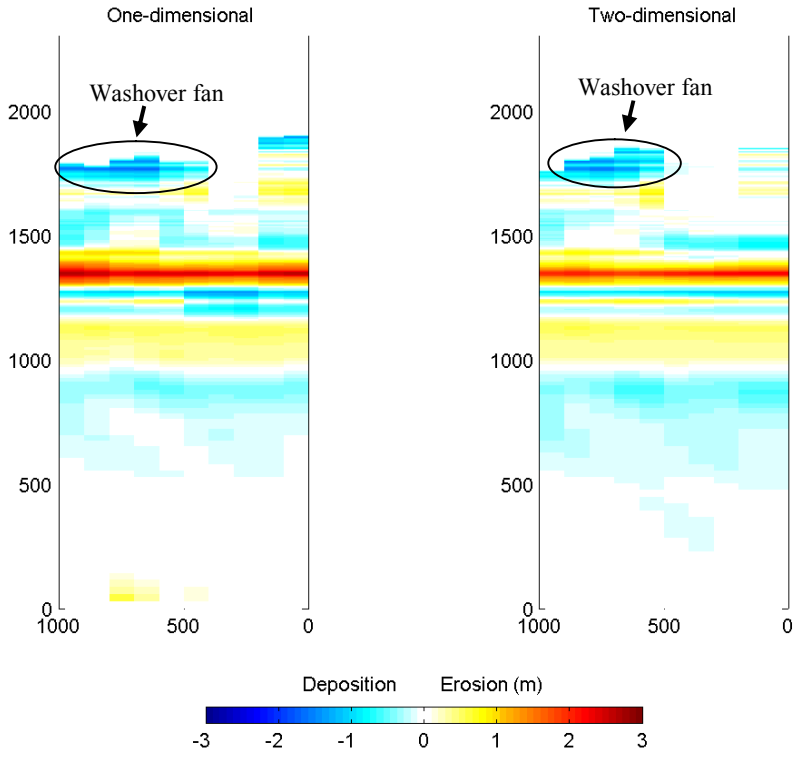


Figure 76 Sedimentation and deposition in a series of 1D-models (left panel) and the coarse-grid 2DH-model

6.5 Conclusion

The erosion-deposition patterns shown in Figure 72 clearly show that even if the XBeach model is given limited longshore data, it may be able to reproduce the major morphological features, such as foredune erosion and washover fans. It has been shown that small

longshore scale features do not play an important role in the location and magnitude of large scale morphological structures. It should be noted however that this may only be the case in inundation regimes, as discussed in section 6.4. Detailed features, such as washover throats and channels will still be relatively well reproduced if the longshore smoothing scale is less than or equal to the length scale at which longshore variation starts in the foredune region, in this case 100 meters.

7 Conclusions and recommendations

7.1 Conclusions

The primary objective of this thesis is to create a numerical model that is capable of modelling dune and barrier island overwash in a 2DH environment. The results of the Santa Rosa Island validation test shows that although major steps forward have been taken, XBeach is not yet ready to be used in field cases, other than as a research tool.

The verification tests have shown that the hydrodynamics in XBeach have generally been successfully adapted to function in a 2DH environment. The model has been shown to correctly predict short wave propagation over irregular longshore bathymetry. The generation of wave-driven currents in cross shore and longshore direction has been verified. Comparisons with measured data at Duck, North Carolina show that the model is capable of accurately predicting these hydrodynamics in prototype conditions.

Infragravity wave energy has not been validated in the XBeach model. As described in Chapter 4 and Appendix T, the most likely reason for the failure of XBeach to accurately model the infragravity wave heights is an error in the offshore boundary conditions or the implementation of incorrect wave group velocity of the short waves. It is therefore expected that with the removal of this error the model will become more accurate in the infragravity frequency band. However since it is assumed that dune erosion and overwash is primarily a function of nearshore infragravity wave heights, the reliability of the entire model cannot be guaranteed at this stage.

The Santa Rosa Island validation test shows that XBeach is capable of modelling complex morphological structures that are common during overwash conditions. The model can be said to be qualitatively correct. The amount of morphological change in the XBeach model however, is an order too great and therefore the model is not validated.

Sensitivity studies showed that the amount of erosion on the barrier island is almost independent of the amount of morphological acceleration. It is put forward that this independence may be due to the fact that in the model an equilibrium bed level is reached before the end of the simulation in all cases. This may not be the case if the speed of erosion is reduced in the model.

The amount of erosion and deposition is highly affected by the water level gradient and associated velocities across the island. Increasing surge levels and therefore depth of water over the barrier island increase the amount of erosion.

Erosion and deposition on the barrier island is affected relatively little by the incoming short wave energy and the surge level lag between the offshore and back barrier bay. It should be noted however that this might be due to the overall exaggerated amount of erosion in the base simulation. The model showed little sensitivity to variation of the equilibrium sediment concentration.

The secondary objective of this thesis is to examine the effect of longshore variation in the bathymetry on overwash patterns. Since the Santa Rosa Island model did not validate XBeach, no strong conclusions can be made with respect to this issue. However, since it is assumed that the model is qualitatively correct, several qualitative conclusions can be drawn.

The location and magnitude of washover fans appear to be independent of the amount of small-scale longshore smoothing in inundation overwash cases. The location appears to be determined by the longshore length scales of the back barrier dunes, which are in the order of 2-5 kilometres. The size of washover fans appears to be determined by the amount of foredune erosion. In inundation overwash cases, the amount of foredune erosion is comparable for all longshore smoothing scales, thus leading to similar-sized washover fans.

Since inundation washover is not greatly affected by small longshore scales in the bathymetry, it is possible for certain applications to decrease the numerical detail in longshore direction to improve the computation time. It has been shown that the size and location of the washover fan and fore dune erosion is well reproduced by increasing the numerical grid size in longshore direction to 100 meters.

A comparison is made between the erosion-deposition results of a 2DH-model with those of several 1D cross shore XBeach models. It is shown that although the 1D-models are in qualitative agreement with the 2DH-model, the amount of erosion is somewhat larger. It can be concluded that under equal modelling conditions, the hydrodynamics in a 2DH-model react differently to those in 1D-models.

7.2 Recommendations

The tests with XBeach have shown that there is still much room for improvement, especially with respect to the morphological development. In this section some suggestions are made with respect to the further development, verification and validation of XBeach.

One of the first issues that must be resolved is the error in the bound infragravity wave energy in the case of irregular wave group forcing. Without being able to correctly model the hydrodynamic forcing at the dune foot in prototype conditions, the model will never be validated. Currently errors in the offshore infragravity wave generation routine and wave group propagation velocity are being examined.

An important development required to model barrier island overwash is the inclusion of relations to represent the effect of vegetation on hydrodynamics and sediment transport. The effect of vegetation on the pick-up of sediment is currently being incorporated in XBeach by the inclusion of multiple sediment layers. Using this method a top layer can be specified which is more difficult to erode. Vegetation also affects flow across the back barrier. In future developments this resistance to flow should be incorporated.

Sediment transport is generally more poorly simulated by numerical models than the hydrodynamics. This error is often minimized by the careful selection of sediment transport

formulations. Testing XBeach with other sediment transport formulae may lead to more accurate results.

Until now the avalanching algorithm in XBeach has proved to be successful despite its limited physical basis. In order to model other soil types than loose sand, a more detailed avalanching algorithm will be necessary. It is suggested that the implementation of simple geotechnical relations may help improve the performance of the model in for instance cohesive soils.

In the current version of XBeach short-wave asymmetry is not taken into account. Under mild wave conditions, wave asymmetry moves sediment landwards. Although this effect is generally minor under storm conditions, inclusion of wave asymmetry may improve model accuracy in the nearshore.

At this stage the computation time of large 2DH simulations in XBeach is too great to be used in forecast studies. The Santa Rosa Island simulations for instance have a calculation to simulation time ratio of 2 to 1. Additionally, due to the way the XBeach code is written, large 2DH simulations require very large amounts of computer memory to run. It is therefore recommended to parallelize the program code to allow one simulation to be carried out on multiple processors to reduce calculation time, or to allow a simulation to be carried out in parts on one processor to reduce the demands on the computer memory. At this stage a trial is being carried out to develop XBeach using Open MPI.

In order to continue verification of the hydraulics of XBeach a more comprehensive study must be carried out on the effects of the numerical grid size on the variance of the water surface elevation. This would ideally be combined with further verification of the infragravity wave heights using large-scale measurement campaign data, for instance DELILAH data.

In order to validate the model the Santa Rosa Island model can be used if new information regarding the wave and surge boundary conditions is available. At this stage, the uncertainty in the model forcing makes full validation impossible. It is recommended that several other locations along Santa Rosa Island or elsewhere with different hydraulic forcing and different morphological regimes be modelled. It is suggested that at least one area is modelled in which only dune erosion took place, one area in which the barrier island was breached and one area in which vegetation is thought to have played an important role. All models should preferably be forced by measured time series of surge and wave conditions.

As stated in the conclusions, the results of the longshore variability study can only be examined in a qualitative sense. This study should therefore be repeated as soon as XBeach has been fully validated in order to strengthen the conclusions drawn in this preliminary study.

Apart from repeating the simulations carried out in Chapter 6, several similar simulations should be carried out in which respectively less and more overwash took place. It is suggested that the longshore variability plays a minor role in the patterns and amount of washover since the hydraulic forcing is too great to be affected by the small-scale variations. Simulations in which only dune erosion or in which large-scale inundation takes place can confirm or deny this hypothesis.

From a practical and academic sense it may be interesting to study the effects of the variation in longshore forcing on the amount and patterns of washover. Such a study could take place by filtering the offshore boundary conditions in the longshore direction.

8 References

Allen, J.R., **1970**. Avalanching of Granular Solids on Dune and Similar Slopes. *Journal of Geology*, vol. 78(3): 326-351.

Andrews, D.G. and McIntyre, M.E., **1978**. An exact theory of nonlinear waves on a Lagrangian-mean flow. *Journal of Fluid Mechanics*, vol. 89(4): 609-646.

Aucan, J., **2004**, Notes on infragravity waves, http://www.soest.hawaii.edu/jaucan/infra/

Aucan, J., Pequignet, A.C., Vetter, O.J., Becker, J.M. and Merrifield, M.A., **2008**. Wave transformation and setup across Ipan Reef, Guam during tropical storm Man-Yi, Ocean Sciences Conference, Orlando.

Baldock, T.E., Holmes, P., Bunker, S. and Van Weert, P., **1998**. Cross-shore hydrodynamics within an unsaturated surf zone. *Coastal Engineering*, vol. 34: 173-196.

Baldock, T.E., Hughes, M.G., Day, K. and Louys, J., **2005**. Swash overtopping and sediment overwash on a truncated beach. *Coastal Engineering*, vol. 52(2005): 633-645.

Baldock, T.E., Kim Son, P., Manoonvoravong, P., Barnes, M.P. and Alsina, J.M., **2007**. Probabilistic-deterministic modelling of swash zone morphology, Coastal Sediments. ASCE, New Orleans.

Battjes, J.A., **1974**. Surf similarity, Proc. of 14th International Conference on Coastal Engineering, Copenhagen, pp. 467-479.

Battjes, J.A., **1975**. Modelling of turbulence in the surfzone, Symposium on Modeling Techniques. Am. Soc. of Civ. Eng., San Francisco.

Battjes, J.A., **2001**. Korte golven. Delft University of Technology, Delft.

Battjes, J.A., Bakkenes, H.J., Janssen, T.T. and Van Dongeren, A.R., **2004**. Shoaling of subharmonic gravity waves. *Journal of Geophysical Research*, vol. 109(C02009): 1-15.

Berkhoff, J.C.W., **1982**. Refraction and diffraction of water waves, Delft Hydraulics, Delft.

Berkhoff, J.C.W., Booij, N. and Radder, A.C., **1982**. Verification of numerical wave propagation models for simple harmonic linear water waves. *Coastal Engineering*, vol. 6: 255-279.

Bosboom, J., Aarninkhof, S.G.J., Reniers, A., Roelvink, J.A. and Walstra, D.J.R., **2000**. UNIBEST-TC 2.0 - Overview of model formulations, Rep, H2305.42, Delft Hydraulics, Delft.

Bruun, P.F., **1954**. Coast erosion and the development of beach profiles. U.S. Army Corps of Engineers Beach Erosion Board Technical Memo Number 44.

Bruun, P.F., **1962**. Sea level rise as a cause of shore erosion. *Journal of Waterways and Harbors Division*, vol. 88(1): 117-130.

Chen, Q.J., Wang, L., Douglass, S.L. and Zhao, H., **submitted**. Wave forces on bridge decks under hurricane conditions. Coastal Engineering.

Cleary, W.J. and Hosier, P.E., **1979**. Geomorphology, washover history and inlet zonation: Cape Lookout, N.c. to Bird Island, N.C. In: S.P. Leatherman (Editor), Barrier Islands, from the Gulf of St. Lawrence to the Gulf of Mexico. Academic Press, New York, pp. 237-271.

Coeveld, E.M. and de Vroeg, J.H., **2004**. Modelonderzoek duinafslag, Meetverslag kleinschalige gidsproeven, WL | Delft Hydraulics, Delft.

Dean, R.G., **1977**. Equilibrium beach profiles: U.S. Atlantic and Gulf coasts. Dept. of Civil Engineering and College of Marine Studies, University of Delaware, Newark.

Deigaard, R., **1993**. A note on the three-dimensional shear stress distribution in a surf zone. *Coastal Engineering*, vol. 20: 157-171.

Divins, D.L. and Metzger, D., **2008**, NGDC Coastal Relief Model,

Dolan, R. and Hayden, B., **1981**. Storms and shoreline configuration. *Journal of Sedimentary Petrology*, vol. 51(3): 737-744.

Donnelly, C., **2007**. Morphologic Change by Overwash: Establishing and Evaluating Predictors, Proc. of International Coastal Symposium. Journal of Coastal Research, Gold Coast, Australia, pp. 520-526.

Donnelly, C., Kraus, N. and Larson, M., **2006**. State of Knowledge on Measurement and Modeling of Coastal Overwash. *Journal of Coastal Research*, vol. 22(4): 965-991.

Donnelly, C., Matias, A. and Chen, Q.J., **submitted**. Back Barrier Processes during Overwash. Marine Geology.

Donnelly, C., Wamsley, T.V., Kraus, N., Larson, M. and Hanson, H., **2007**. Morphological Classification of Coastal Overwash, Proc. of 30th International Coastal Engineering Conference. World Scientific Press.

Elgar, S., Herbers, T.H.C., Okihiro, M., Oltman-Shay, J. and Guza, R.T., **1992**. Observations of Infragravity Waves. *Journal of Geophysical Research*, vol. 97(C10): 15573-15577.

Fischer, J.S. and Overton, M.F., **1984**. Numerical model for dune erosion due to wave uprush, Proc. of 19th Coastal Engineering Conference. ASCE, Houston, pp. 1553-1558.

Foda, M.A. and Mei, C.C., **1981**. Nonlinear excitation of long-trapped waves by a group of short swells. *Journal of Fluid Mechanics*, vol. 111: 319-345.

Fredsøe, J. and Deigaard, R., **1992**. Mechanics of Coastal Sediment Transport. World Scientific.

Galapatti, R., **1983**. A depth integrated model for suspended transport. Report 83-7, Communications on Hydraulics. Department of Civil Engineering, Delft University of Technology.

Guza, R.T. and Thornton, E.B., **1982**. Swash oscillations on a natural beach. *Journal of Geophysical Research*, vol. 87: 483-491.

Guza, R.T. and Thornton, E.B., **1985**. Observations of surf beat. *Journal of Geophysical Research*, vol. 90(C4): 3161-3172.

Henderson, S.M. and Bowen, A.J., **2002**. Observation of surf beat forcing and dissipation. *Journal of Geophysical Research*, vol. 107.

Herbers, T.H.C., Elgar, S. and Guza, R.T., **1994**. Infragravity-Frequency (0.005–0.05 Hz) Motions on the Shelf. Part I: Forced Waves. *Journal of Physical Oceanography*, vol. 24(5): 917-927.

Herbers, T.H.C., Elgar, S. and Guza, R.T., **1995a**. Generation and propagation of infragravity waves. *Journal of Geophysical Research*, vol. 100(C12): 24863-24872.

Herbers, T.H.C., Elgar, S., Guza, R.T. and O'Reilly, W.C., **1995b**. Infragravity-Frequency (0.005–0.05 Hz) Motions on the Shelf. Part II: Free Waves. *Journal of Physical Oceanography*, vol. 25(6): 1063-1079.

Holman, R.A., **1981**. Infragravity energy in the surfzone. *Journal of Geophysical Research*, vol. 86(C7): 6442-6450.

Holthuijsen, L.H., Booij, N. and Herbers, T.H.C., **1989**. A Prediction Model for Stationary, Short-crested Waves in Shallow Water with Ambient Currents. *Coastal Engineering*, vol. 13: 23-54.

Iribarren, C.R. and Nogales, C., **1949**. Protection des ports., Proc. of XVIIth Int. Nav. Congress, Lisbon.

Kobayashi, N., Tega, Y. and Hancock, M.W., **1996**. Wave reflection and overwash of dunes. *Journal of Waterway, Port, Coastal and Ocean Engineering*, vol. 122(3): 150-153.

Kraus, N., **2003**. Analytical model of incipient breaching of coastal barriers. *Coastal Engineering Journal*, vol. 45(4): 511-531.

Kriebel, D.L. and Dean, R.G., **1985**. Numerical simulation of time-dependent beach and dune erosion. *Coastal Engineering*, vol. 9: 221-245.

Lamb, H., **1945**. Hydrodynamics. Dover Publication, New York.

Larson, M., Donnelly, C. and Hanson, H., **2005**. Analytical modeling of dune response due to wave impact and overwash.
Larson, M., Erikson, L. and Hanson, H., **2004a**. An analytical model to predict dune erosion due to wave impact. *Coastal Engineering*, vol. 51(8-9): 675-696.
Larson, M. and Kraus, N., **1989**. SBEACH: Numerical model for simulating storm-induced beach change, Report 1: Empirical foundation and model development, Technical Report. CERC-89-9. US Army Engineer Waterways Experiment Station, Vicksburg, MS.
Larson, M., Kraus, N. and Byrnes, M.R., **1990**. SBEACH: Numerical model for simulating storm-induced beach change, Report 2: Numerical formulation and model tests, Technical Report. CERC-89-9. US Army Engineer Waterways Experiment Station, Vicksburg, MS.
Larson, M., Kubota, S. and Erikson, L., **2004b**. Swash-zone sediment transport and foreshore evolution: field experiments and mathematical modeling. *Marine Geology*, vol. 212: 61-79.
Leatherman, S.P. and Zaremba, R.E., **1987**. Overwash and aeolian processes on a U.S. Northeast coast barrier. *Sedimentary Geology*, vol. 52: 183-206.
Leont'yev, I.O., **1996**. Numerical modelling of beach erosion during storm event. *Coastal Engineering*, vol. 29: 187-200.
List, J.H., **1991**. Wave groupiness variations in the nearshore. *Coastal Engineering*, vol. 15: 475-496.
List, J.H., **1992**. A model for the generation of two dimensional surf beat. *Journal of Geophysical Research*, vol. 97: 5623-5635.
Longuet-Higgins, M.S. and Stewart, R.W., **1962a**. Radiation stress and mass transport in gravity waves. *Journal of Fluid Mechanics*, vol. 13: 481-504.
Longuet-Higgins, M.S. and Stewart, R.W., **1962b**. Radiation stress and mass transport in gravity waves, with applications to 'surf-beats'. *Journal of Fluid Mechanics*, vol. 13: 175-189.
Longuet-Higgins, M.S. and Stewart, R.W., **1963**. A note on wave set-up. *Journal of Marine Research*, vol. 21: 4-10.
Longuet-Higgins, M.S. and Stewart, R.W., **1964**. Radiation stresses in water waves: A physical discussion. *Deep Sea Research*, vol. 11: 529-562.
Masselink, G. and Hughes, M.G., **2003**. Introduction to Coastal Processes and Geomorphology. Oxford University Press US, 354 pp.
Miles, M.D. and Funke, E.R., **1989**. A comparison of methods for synthesis of directional seas. *J. Offshore Mech. Polar Eng.*, vol. 111: 43-48.
Munk, W.H., **1949**. Surf Beat. *EOS, Transactions American Geophysical Union*, vol. 30: 849-854.
National Hurricane Center, **2008**, Tropical Cyclone Report, Hurricane Ivan
Nguyen, X.T., Donnelly, C. and Larson, M., **2006**. A new empirical formula for coastal overwash volume, Proc. of Vietnam-Japan Estuary Workshop 2006, Hanoi.
Nishi, R. and Kraus, N., **1996**. Mechanism and calculation of sand dune erosion by storms, Proc. of 25th Coastal Engineering Conference. ASCE, Orlando, pp. 3034-3047.
Okihiro, M., Guza, R.T. and Seymour, R.J., **1992**. Bound infragravity waves. *Journal of Geophysical Research*, vol. 98(C7): 11453-11469.
Okihiro, M., Guza, R.T. and Seymour, R.J., **1993**. Excitation of seiche observed in a small harbor. *Journal of Geophysical Research*, vol. 98(C10): 18201-18212.
Orford, J.D. and Carter, R.W.G., **1982**. Crestal overtop and washover sedimentation on a fringing sandy gravel barrier coast, Carnsore Point, Southeast Ireland. *Journal of Sedimentary Petrology*, vol. 52(1): 265-278.
Overton, M.F. and Fischer, J.S., **1988**. Simulation of modeling dune erosion, Proc. of 21st International Conference on Coastal Engineering. American Society of Civil Engineers, New York, pp. 1857– 1867.

Phillips, O.M., **1977**. The Dynamics of the Upper Ocean. Cambridge University Press, New York.

Pirrello, M.A., **1992**. The Role of Wave and Current Forcing in the Process of Barrier Island Overwash, University of Florida, Gainesville, Florida, 117 pp.

Plant, N.G. *et al.*, **2008**. Filtering effects of a nearshore process model.

Plant, N.G., Holland, K.T. and Puleo, J.A., **2002**. Analysis of the scale of errors in nearshore bathymetric data. *Marine Geology*, vol. 191: 71-86.

Puleo, J.A., Beach, R.A., Holman, R.A. and Allen, J.S., **2000**. Swash zone sediment suspension and transport and the importance of bore-generated turbulence. *Journal of Geophysical Research*, vol. 105(C7): 17021-17044.

Reniers, A., MacMahan, J.H., Thornton, E.B. and Stanton, T.P., **2006**. Modelling infragravity motions on a rip-channel beach. *Coastal Engineering*, vol. 53(2-3): 209-222.

Reniers, A., Roelvink, J.A. and Thornton, E.B., **2004**. Morphodynamic modeling of an embayed beach under wave group forcing. *Journal of Geophysical Research*, vol. 109(C01030).

Reniers, A., Van Dongeren, A.R., Battjes, J.A. and Thornton, E.B., **2002**. Linear modeling of infragravity waves during Delilah. *Journal of Geophysical Research*, vol. 109: 3137.

Roelvink, J.A., **1993a**. Dissipation in random wave groups incident on a beach. *Coastal Engineering*, vol. 19: 127-150.

Roelvink, J.A., **1993b**. Surf beat and its effect on cross-shore profiles, Delft University of Technology, Delft.

Roelvink, J.A. *et al.*, **2007**. XBeach Annual Report and Model Description.

Roelvink, J.A. and Stive, M.J.F., **1989**. Bar-generating criss-shore flow mechanisms on a beach. *Journal of Geophysical Research*, vol. 94(C4): 4785-4800.

Roelvink, J.A., van Kessel, T., Alfageme, S. and Canizares, R., **2003**. Modelling of barrier island response to storms, Proc. of Coastal Sediments, Clearwater Beach, Florida.

Ruessink, B.G., **1998**. Infragravity waves in a dissipative multiple bar system, Universiteit Utrecht, Utrecht, 245 pp.

Sallenger, A.H., **2000**. Storm Impact Scale for Barrier Islands. *Journal of Coastal Research*, vol. 16(3): 890-895.

Sallenger, A.H., Wright, C.W. and Howd, P., **2008**. Continued Barrier Island Deterioration following Hurricane Katrina, Ocean Sciences Conference, Orlando.

Schäffer, H.A., **1993**. Infragravity wave induced by short-wave groups. *Journal of Fluid Mechanics*, vol. 247: 551-588.

Soulsby, R., **1997**. Dynamics of marine sands. Thomas Telford Publications, London.

Steetzel, H., **2002**. Effect van zwaardere golfcondities op duinenkust. Verkenning effect grotere golfhoogte en langere golfperiode op mate duinafslag en veiligheid duinenkust, Alkyon, Emmeloord.

Steetzel, H.J., **1993**. Cross-shore transport during storm surges. Delft Hydraulics Communication, Rep. No. 476, Delft.

Stelling, G.S. and Booij, N., **1999**. Computational modelling flow and transport. Delft University of Technology, Delft.

Stelling, G.S. and Duinmeijer, S.P.A., **2003**. A staggered conservative scheme for every Froude number in rapidly varied shallow water flows. *International Journal for Numerical Methods in Fluids*, vol. 43(12): 1329-1354.

Stewart, R.H., **2007**. Introduction to Physical Oceanography. Texas A & M University.

Stive, M.J.F. and Wind, H.G., **1986**. Cross-shore mean flow in the surfzone. *Coastal Engineering*, vol. 10: 325-340.

Suter, J.R., Nummedal, D., Maynard, A.K. and Kemp, P., **1982**. A process-reponse model for hurricane washovers, Proc. of 18th Coastal Engineering Conference, Capetown, pp. 1459-1789.

Svendsen, I.A., **1984**. Wave heights and set-up in a surf zone. *Coastal Engineering*, vol. 8: 303-329.

Svendsen, I.A., Haas, K. and Zhao, H., **2002**. Quasi-3D Nearshore Circulation Model SHORECIRC. University of Delaware, Newark.

Symonds, G. and Bowen, A.J., **1984**. Interactions of nearshore bars with incoming waves groups. *Journal of Geophysical Research*, vol. 89: 1953-1959.

Symonds, G., Huntley, D.A. and Bowen, A.J., **1982**. Two-dimensional surf beat. Long wave generation by a varying breakpoint. *Journal of Geophysical Research*, vol. 80: 492-498.

Tanaka, H., Nagasawa, T. and Suntoyo, **2002**. Sediment intrusion into Gamo Lagoon by wave overtopping, Proc. of 28th International Conference on Coastal Engineering, Cardiff, pp. 823-835.

Thompson, D.M., **unpublished**. Delft3D model of waves and surge along Florida Panhandle and Alabama coast during Hurricane Ivan

Thomson, J., Elgar, S., Raubenheimer, B., Herbers, T.H.C. and Guza, R.T., **2006**. Tidal modulation of infragravity waves via nonlinear energy losses in the surfzone. *Geophys. Res. Lett.*, vol. 33: L05601.

Tuan, T.Q., **2007**. Seasonal breaching of coastal barriers, Delft University of Technology, Delft.

Tuan, T.Q., Stive, M.J.F. and Visser, P.J., **2006a**. Breaching vulnerability of coastal barriers under the effects of tropical cyclones: a model study of the Hue lagoon-Vietnam, Proc. of 2nd International Estuary Coast Conference, Guangzhou, China.

Tuan, T.Q., Verhagen, H.J., Visser, P. and Stive, M.J.F., **2006b**. Numerical modelling of wave overwash on low-crested sand barriers, Proc. of 30th Coastal Engineering Conference. World Scientific, San Diego.

Tuan, T.Q., Verhagen, H.J. and Visser, P.J., **2006c**. Advances in one-dimensional breach modelling of coastal sand barriers, Proc. of 3rd International Scour Erosion Conference. CURNET, pp. 649-658.

Tuan, T.Q., Verhagen, H.J., Visser, P.J. and Stive, M.J.F., **2006d**. Wave overwash at low-crested beach barriers. *Coastal Engineering Journal*, vol. 48(4): 371-393.

Tucker, M.J., **1950**. Surfbeats: sea waves of 1 to 5 minutes period, Proc. of Royal Society London. Series A 202, pp. 565-573.

United States Army Corps of Engineers, **1990**, DELILAH measurement database, ftp://frf.usace.army.mil/pub/delilah/

United States Army Corps of Engineers, **2002**. Coastal Engineering Manual. U.S. Army Corps of Engineers.

van de Graaff, J., **1986**. Probabilistic design of dunes: an example from The Netherlands. *Coastal Engineering*, vol. 9: 479--500.

van de Graaff, J., **2006**. Coastal morphology and coastal protection. Delft University of Technology, Delft.

van Dongeren, A.R., Battjes, J.A., Janssen, T.T., Steenhauer, K. and Reniers, A., **2006**. Shoaling and shoreline dissipation of low-frequency waves. *Journal of Geophysical Research*, vol. 112(C2): C02011.1-C02011.15.

van Dongeren, A.R., Reniers, A. and Battjes, J.A., **2003**. Numerical modeling of infragravity waves response during DELILAH. *Journal of Geophysical Research*, vol. 108(C9): 3288.

van Dongeren, A.R., Sancho, F.E., Svendsen, I.A. and Putrevu, U., **1994**. SHORECIRC: A quasi 3-D nearshore model, 24th International Conference on Coastal Engineering. Am. Soc. of Civ. Eng., Kobe.

van Dongeren, A.R. and Svendsen, I.A., **1997**. Absorbing-Generating Boundary Condition for Shallow Water Models. *Journal of Waterway, Port, Coastal and Ocean Engineering*, vol. 123(6): 303-313.

van Gent, M.R.A., **2001**. Wave runup on dikes with shallow foreshores. *Journal of Waterway, Port, Coastal and Ocean Engineering*, vol. 127(5): 254-262.

van Rijn, L.C., **1984a**. Sediment transport, part I: bed load transport. *Journal of Hydraulic Engineering*, vol. 110: 1431-1456.

van Rijn, L.C., **1984b**. Sediment transport, part II: suspended load transport. *Journal of Hydraulic Engineering*, vol. 110: 1631-1641.

van Thiel de Vries, J.S.M., van de Graaff, J., Raubenheimer, B., Reniers, A. and Stive, M.J.F., **2006**. Modeling inner surf hydrodynamics during storm surges. In: J. Mckee Smith, Proc. of 30th International Conference on Coastal Engineering. World Scientific Pub. Co. Inc. , San Diego.

Vellinga, P., **1986**. Beach and Dune Erosion during Storm Surges, Delft University of Technology, Delft.

Visser, P.J., **1998**. Breach Growth in Sand-Dikes, Delft University of Technology, Delft.

Walstra, D.J.R., Roelvink, J.A. and Groeneweg, J., **2000**. Calculation of wave driven currents in a 3D mean flow model, Proc. of Coastal Engineering 2000, Sydney, pp. 1050-1063.

Watson, G. and Peregrine, D.H., **1992**. Low frequency waves in the surf zone, Proc. of 23rd Int. Conf. on Coastal Eng. ASCE, pp. 818-831.

Whitham, G.B., **1974**. Linear and Nonlinear Waves. Wiley, New York.

Williams, P.J., **1978**. Laboratory Development of a Predictive Relationship for Washover Volume on Barrier Island Coastlines, University of Delaware, Newark, 141 pp.

WL | Delft Hydraulics, **2001**. User Manual Delft3D-FLOW, Delft.

Wright, L.D., Guza, R.T. and Short, A.D., **1982**. Dynamics of a high-energy dissipative surf zone. *Marine Geology*, vol. 45: 41-62.

Yates, M.L., Guza, R.T., Seymour, R.J. and O'Reilly, W.C., **2008**. Seasonal beach changes and equilibrium concepts, Ocean Sciences Conference, Orlando.

Prepared for:

Delft University of Technology

The longshore dimension in dune overwash modelling

Development, verification and validation of XBeach

Appendices

May 2008

Prepared for:

Delft University of Technology

The longshore dimension in dune overwash modelling

Development, verification and validation of XBeach

Appendices

Robert McCall

Supervisors:
Prof.dr.ir. M. Stive
Prof.dr.ir. J.A. Roelvink
Ir. J.S.M. van Thiel de Vries
Dr.ir. A.P. van Dongeren
Ir. D.J.R. Walstra
Dr.ir. P.J. Visser
Dr.ir. M. Zijlema

May 2008

WL | delft hydraulics

Client:	Delft University of Technology
Title:	The longshore dimension in dune overwash modelling

Abstract:

This document contains the appendices relating to the MSc-thesis entitled "*The longshore dimension in dune overwash modelling. Development, verification and validation of XBeach*".

References:

Ver	Author		Date	Remarks	Review		Approved by	
	Robert McCall							

Project number:	
Keywords:	XBeach, modelling, dune erosion, overwash, longshore variability
Number of pages:	155
Classification:	None
Status:	Final

Contents

1 Introduction 1

Appendices

A Linear wave theory 2
A.1 Wave groups 2
A.2 Wave energy and wave energy flux 4
A.3 Shoaling 5
A.4 Refraction 7
A.5 Wave breaking 8
A.6 Radiation stress 9
B Changes implemented in XBeach 11
B.1 Irregular wave group forcing 11
B.2 Automatic time step 15
B.3 Short wave numerical dissipation 16
B.4 Lateral boundaries 21
B.5 Miscellaneous 23
C Test 0 24
C.1 Model description 24
C.2 Results 24
C.3 Conclusions 27
D Test 1 28
D.1 Model description 28
D.2 Results 28
D.3 Conclusions 34
E Test 1g 35
E.1 Model description 35
E.2 Results 35
E.3 Conclusions 38
F Test 2 39
F.1 Model description 39
F.2 Results 39
F.3 Conclusions 45

G Test 3 46
G.1 Model description 46
G.2 Results 46
G.3 Conclusions 49
H Test 3g 51
H.1 Model description 51
H.2 Results 51
H.3 Instabilities 55
H.4 Conclusions 56
I Test 3s 57
I.1 Model description 57
I.2 Results 57
I.3 Conclusions 58
J Test 4 59
J.1 Model description 59
J.2 Results 59
J.3 Conclusions 63
K Test 5 64
K.1 Model description 64
K.2 Results 64
K.3 Conclusions 68
L Test 6 69
L.1 Model description 69
L.2 Results 69
L.3 Conclusions 73
M Test 6g 74
M.1 Model description 74
M.2 Results 74
M.3 Conclusions 78
N Test 6s 79
N.1 Model description 79
N.2 Results 79
N.3 Conclusions 81
O Test 7 82
O.1 Model description 82
O.2 Results 82

O.3 Conclusions 89
P Test 8 90
P.1 Model description 90
P.2 Results 90
P.3 Conclusions 93
Q Test 8s 94
Q.1 Model description 94
Q.2 Results 94
Q.3 Conclusions 94
R Test 9 95
R.1 Model description 95
R.2 Results 97
R.3 Conclusions 100
S Test 10 101
S.1 Model description 101
S.2 Results 102
S.3 Conclusions 103
T Test 11 104
T.1 Model description 104
T.2 Results 106
T.3 Conclusions 112
T.3.1 Insufficient infragravity wave energy generated on the boundary 113
T.3.2 Internal infragravity wave issues 114
T.3.3 Discussion 114
U Test 12 116
U.1 Model description 116
U.2 Results 116
U.3 Conclusions 119
V Test 13 120
V.1 Model description 120
V.2 Results 120
V.3 Conclusions 122
W Semi-analytical linear wave model 123
X Bathymetry data 127
X.1 Longshore uniform bathymetry 127
X.2 Longshore non-uniform bathymetry 127

X.3 Irregular non-uniform bathymetry 128
Y User guide spectrum-based boundary conditions 130
Y.1 Spectrum-based non-stationary wave boundary conditions 130
Y.2 Use of JONSWAP spectrum 131
Y.3 Use of SWAN spectrum 132
Y.4 Use of formatted variance density spectrum 135
Y.5 Reusing existing boundary condition files 136
Y.6 Use of time-varying spectra 137
Y.7 Examples 137
Y.8 Theory 139
Y.9 Explanation of input/output 139
Y.10 Params.txt file 140
Z Numerical dissipation wave action balance 144
AA Input parameters of the Santa Rosa Island model 146

I Introduction

This document contains the appendices relating to the MSc-thesis entitled "*The longshore dimension in dune overwash modelling. Development, verification and validation of XBeach*".

A Linear wave theory

The dynamics of free surface waves in a constant medium can be described in a 2DV-context using the Laplace equation:

$$\frac{\partial^2\phi}{\partial x^2}+\frac{\partial^2\phi}{\partial z^2}=0 \tag{A.1}$$

It is assumed that the bed is impermeable and that therefore the vertical flow at the bed is zero:

$$\frac{\partial\phi}{\partial z}=0 \tag{A.2}$$

The velocity potential at the surface is bound by continuity of mass and momentum relations:

$$\begin{aligned}&\frac{\partial\phi}{\partial z}-\frac{\partial\eta}{\partial t}-\frac{\partial\phi}{\partial x}\frac{\partial\eta}{\partial x}=0\\&\frac{\partial\phi}{\partial t}+g\eta+\frac{1}{2}|\vec{u}|^2=0\end{aligned} \tag{A.3}$$

In linear (Airy) wave theory it is assumed that the wave amplitude is small in relation to the water depth and the wave length. Under such conditions the non-linear terms in equation (A.3) are relatively small and can be discarded. Although linear wave theory is strictly not valid in shallow water, many hydrodynamic processes in the nearshore can still be described relatively well with the use of linear wave theory. This appendix discusses a number of concepts related to linear wave theory.

A.1 Wave groups

When two wave trains with different wave periods and wave lengths exist at the same time in a waterbody, they will form a single set of resultant waves. Where the waves are in phase, the amplitudes the wave components complement each other to form a resultant amplitude, which is greater than the amplitude of either of the individual wave trains. Where the waves are out of phase, the resultant amplitude is lower than the individual amplitudes. In this manner the two wave trains lose their individual identity and form a series of wave groups, separated by regions of low waves, see Figure 1

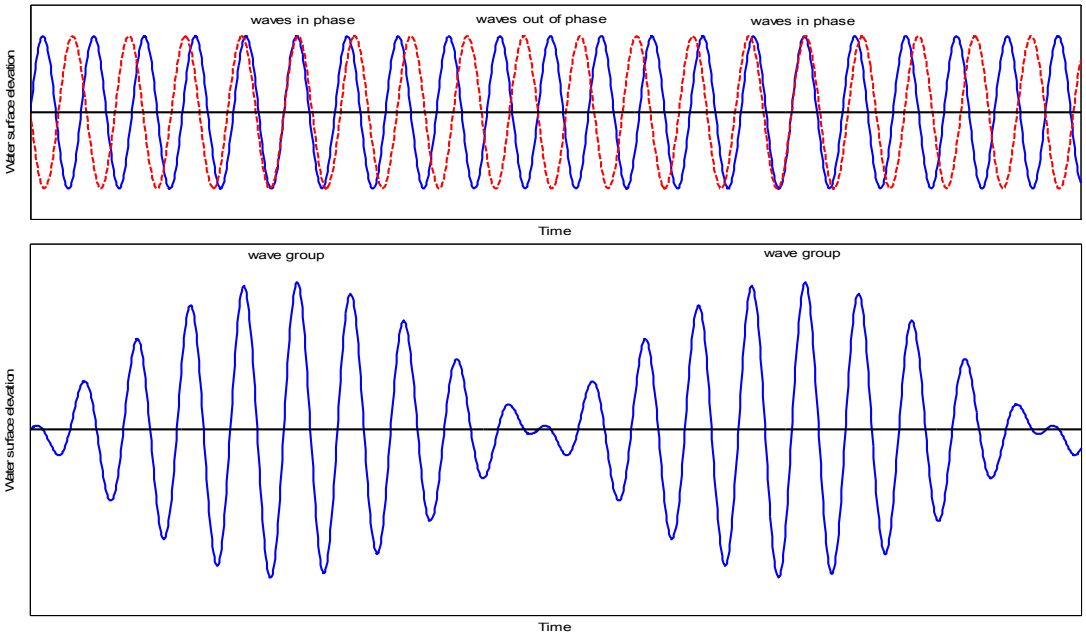


Figure 1 Two wave trains with different wave lengths (upper plate) merge to form wave groups (lower plate). [Adapted from: Masselink and Hughes, 2003].

The individual wave trains travel at their own velocity. The resultant wave groups do not travel at the same speed as the components. Instead, the velocity of the wave groups is determined by the properties of the composing wave trains. This wave group velocity is given as:

$$c_g = \frac{\omega_1 - \omega_2}{k_1 - k_2}$$

where the subscripts 1 and 2 refer to the first and second wave train respectively. More generally, group velocity can be written as [Whitham, 1974; in: Stewart, 2007]:

$$c_g = \frac{\partial \omega}{\partial k} \tag{A.4}$$

In which the wave frequency can be determined using the dispersion relation for free surface gravity waves [Lamb, 1945 in; Stewart, 2007]:

$$\omega^2 = gk \tanh\left(kh\right) \tag{A.5}$$

Therefore:

$$c_g = \frac{1}{2}\left(1 + \frac{kh}{\sinh\left(2kh\right)}\right)c \tag{A.6}$$

The wave group velocity as a function of the water depth is shown in Figure 2 for various incident wave periods. The figure shows that as waves approach the shore, there is an initial

region in which the wave group velocity increases. After this point, which is wave period dependent, the wave group velocity quickly decreases.

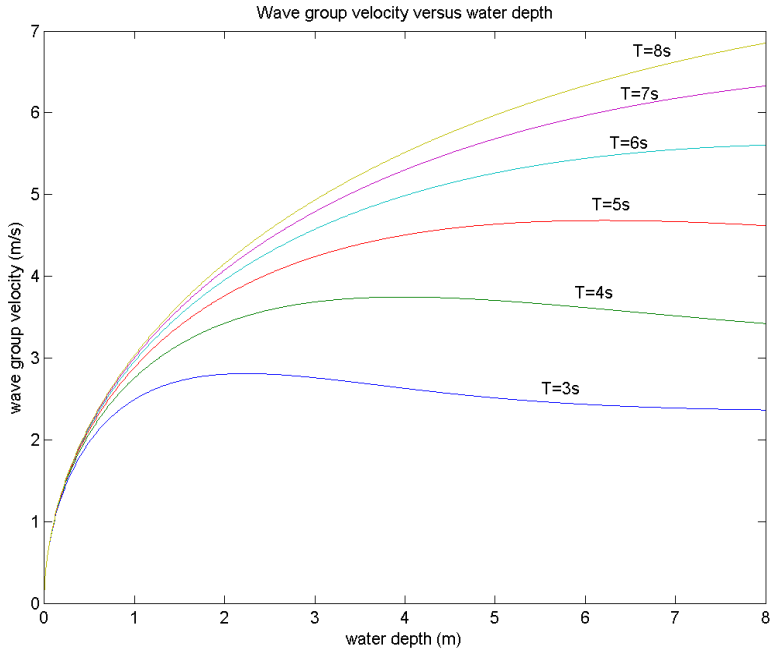


Figure 2 Wave group velocity as a function of water depth for a varying wave periods

A.2 Wave energy and wave energy flux

Wave energy can be seen to be the summation of the potential energy in a wave and the kinetic energy in a wave [from: Battjes, 2001]:

$$E \equiv E_p + E_k \tag{A.7}$$

The formal definitions for the time-average potential and kinetic energy are:

$$E_p \equiv \frac{1}{2}\rho g\overline{\eta^2}$$

$$E_k \equiv \overline{\int_{-h}^{\eta} \frac{1}{2}\rho q^2 dz}$$

Assuming sinusoidal free surface gravity waves and using the dispersion relation (A.5), the equations for the potential and kinetic energy can be written as:

$$E_p = \frac{1}{4}\rho g a^2$$

$$E_k = \frac{1}{4}\rho g a^2$$

Thus the total wave energy is:

$$E = \frac{1}{2}\rho g a^2 = \frac{1}{8}\rho g H^2 \tag{A.8}$$

The average energy transfer in the wave direction per unit of time, per unit of wave breadth, or wave energy flux, is defined as:

$$F \equiv \overline{\int_{-h}^{\eta}\left(p + \rho g z + \frac{1}{2}\rho q^2\right) u dz}$$

In linear wave theory the third term between the brackets can be disregarded along with the contribution of the integral between $z = 0$ and $z = \eta$. Thus the wave energy flux can be calculated using [Battjes, 2001]:

$$F = \left(\frac{1}{2}\rho g a^2\right)\left(\frac{1}{2} + \frac{kh}{\sinh(2kh)}\right)\left(\frac{\omega}{k}\right) \tag{A.9}$$

if we state:

$$n = \frac{1}{2} + \frac{kh}{\sinh(2kh)}$$

then (A.9) can be written as:

$$F = Enc \tag{A.10}$$

Furthermore, as we can also write:

$$n = \frac{c_g}{c}$$

then (A.10) becomes:

$$F = Ec_g \tag{A.11}$$

A.3 Shoaling

Wave period and frequency are invariant due to continuity relations. Therefore the only free variables in equation (A.5) are the water depth and the wave number. In changing water depths, the dispersion relation consequently dictates that the wave length must vary. This relation between the local water depth and the wave length can be described as [from: Battjes, 2001]:

$$\frac{\mathrm{L}}{\mathrm{L}_0} = \tanh\left(\frac{2\pi h}{L}\right) \tag{A.12}$$

with

$$L_0 = \frac{gT^2}{2\pi}$$

As wave celerity is equal to wave length over wave period and the wave period remains constant, it can also be stated that:

$$\frac{c}{c_0} = \tanh\left(\frac{2\pi h}{L}\right) \tag{A.13}$$

From (A.12) and (A.13) it can be concluded that the wave length and wave celerity decrease in decreasing water depth.

Assuming shore normal waves, longshore uniform bathymetry and that there is no energy loss due to dissipation, it can be stated that the wave energy flux must remain constant in cross shore direction:

$$\frac{dF}{dx} = \frac{d}{dx}\left(Ec_g\right) = 0$$

Which means that:

$$\frac{E}{E_0} = \frac{c_{g_0}}{c_g}$$

And therefore:

$$\frac{a}{a_0} = \sqrt{\frac{c_{g_0}}{c_g}} = K_s \tag{A.14}$$

Equation (A.14) shows that as the wave group velocity decreases in respect to the deep water wave group velocity, the amplitude of the wave group increases. As shown in Figure 2, wave group velocity decreases in shallow water, thereby causing the wave height to increase.

A.4 Refraction

Refraction is a process that occurs when waves encounter a slope that is not parallel to the wave crests. As wave crests approach this slope, parts of the wave crests that are in shallow waters travel slower than those in deep water, due to shoaling. The difference in wave celerity along the wave crest causes the wave crest to rotate towards the shallow area, see Figure 3. The change in angle along the line of travel of the waves can be described using the following relation [from: Battjes, 2001]:

$$\frac{d\theta}{ds} = \frac{1}{c}\frac{\partial c}{\partial b} \tag{A.15}$$

In which s is the direction in the line of travel of the waves and b is the direction along the wave crest. In the case of longshore uniform bathymetry, (A.15) can be written as Snell's law:

$$\frac{d}{ds}\left(\frac{\sin\theta}{c}\right) = 0$$

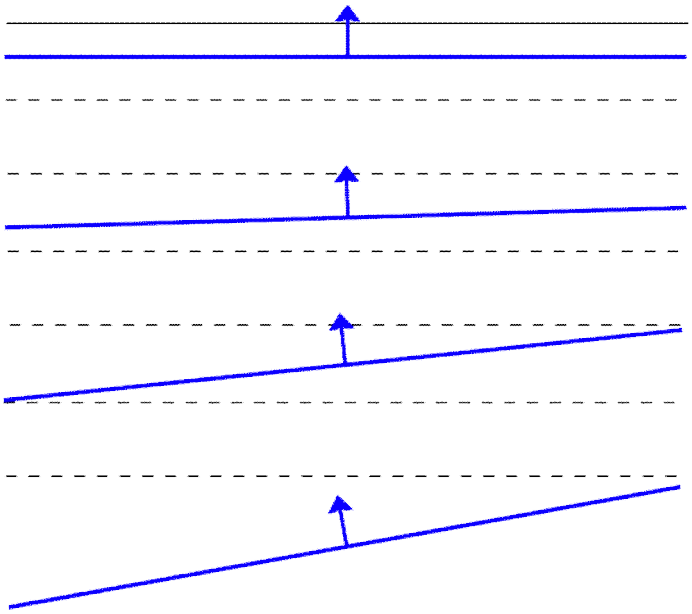


Figure 3 Oblique wave crests refract as they approach shore

Since the ratio between $\sin\theta$ and c remains constant along a wave crest, the local wave angle can be written as a function of the wave angel at another point, for instance in deep water:

$$\sin\theta = \frac{c}{c_0}\sin\theta_0 \tag{A.16}$$

With the assumption of no longshore change in the longshore component of the wave energy flux and no energy loss due to dissipation, it can be stated that:

$$Ec_g \cos\theta = \text{constant}$$

Thus:

$$\frac{a}{a_0} = \sqrt{\frac{c_{g_0}}{c_g}} \sqrt{\frac{\cos\theta_0}{\cos\theta}} = K_s K_r \tag{A.17}$$

This formulation combines the contributions of shoaling and refraction. Note that in shallow water K_s is less than unity, but K_r is greater than unity.

A.5 Wave breaking

Wave breaking is a process that occurs as waves enter very shallow water, or when waves become too steep. The process is associated with large amounts of wave energy dissipation. In order to fully explain wave breaking it is necessary to study particle motions within waves. In this case however, a simple model for wave breaking is discussed.

Wave celerity is related to water depth; the greater the water depth, the greater the wave celerity. As the water depth under the wave crest is greater than the water depth under the wave trough, the wave celerity of the crest is greater than that of the trough.
As waves move into shallow water, their height increases, as shown in (A.14) and (A.17). The height difference relative to the mean water depth becomes greater as waves move into shallow water. At a certain point, the celerity difference is so great, that the crest will try to overtake the trough in front. This is the point at which wave breaking occurs. It is generally thought that the wave crest and wave trough continue forwards in the form of a shock-wave or roller. Much wave energy is dissipated into heat and turbulence in this process, leading to lower wave heights.

In linear wave theory two standard conditions are required for wave breaking. The first condition is related to the wave steepness. From theoretical considerations, the limiting steepness is found to be [from: van de Graaff, 2006]:

$$\left[\frac{H}{L}\right]_{\max} = \frac{1}{7}\tanh\left(\frac{2\pi h}{L}\right) \tag{A.18}$$

In deep water this occurs if the crest angle is roughly 120°.

The second condition for wave breaking is the ratio between the wave height and the local water depth [from: van de Graaff, 2006]:

$$\frac{H_{\max}}{h} = \gamma_b \tag{A.19}$$

In most cases the breaker coefficient on the right of (A.19) is set at 0.6 – 0.7 in the case of regular waves. In the case of irregular waves, the breaker coefficient is in the order of 0.5 – 0.6 [from: van de Graaff, 2006].

The relations given in (A.18) and (A.19) are derived for a flat horizontal bed. In reality, the bed will be sloping, which will lead to different breaker conditions. This is taken into account by the Iribarren parameter [Iribarren and Nogales, 1949; in: van de Graaff, 2006]:

$$\xi = \frac{\tan\alpha}{\sqrt{\frac{H_0}{L_0}}} \tag{A.20}$$

Different values of the Iribarren parameter correspond to different types of breaking waves, as described well by Battjes [1974]. Breaking occurs if:

$$\xi < \frac{4}{\sqrt{\pi}}$$

A.6 Radiation stress

The radiation stress theory was originally posed in a series of papers by Longuet-Higgins and Stewart [1962a; 1963; 1964]. The theory describes how propagating waves exert a force on vertical surfaces. The formal definition of radiation stress is: the contribution of waves to the horizontal flux of horizontal momentum per unit of width, measured in a vertical plain from the bed to water surface and averaged over a whole number of wave periods [Battjes, 2001].
As stated by the second law of Newton, temporal momentum flux is equivalent to force. Thus the momentary force on a vertical plain with unit width from bed to water surface is [from: van de Graaff, 2006]:

$$\text{Force} = \int_{-h}^{\eta} \left(p + \rho u_{particle}^2 \right) dz$$

Using the formal definition stated above, the radiation stress in the wave direction on a plain perpendicular to the wave direction is [from: Battjes, 2001]:

$$S_{x_w x_w} = \overline{\int_{-h}^{\eta} \left(p + \rho u_{particle}^2 \right) dz} - \int_{-h}^{0} \left(\rho g z \right) dz \tag{A.21}$$

The formulation above (A.21) contains a component caused by varying pressure and a component caused by the orbital velocity. In short, the pressure contribution is due to the fact that the momentary pressure under a wave crest minus the hydrostatic pressure is greater than the hydrostatic pressure minus the momentary pressure under a wave trough. The resultant pressure over a wave period is therefore positive. The contribution due to the orbital velocity can be explained by examining a vertical plain. As a wave crest passes through this plain from left to right, the right side of the plain experiences an increase in momentum as mass is added with a positive velocity. As the wave trough passes the plain, the right side loses mass with negative velocity and thus loses negative momentum. As the

total momentum is conserved, the momentum on the right side of the plain must increase. Longuet-Higgins and Stewart [1964] combined both components:

$$S_{x_w x_w} = \left(\frac{1}{2} + \frac{2kh}{\sinh(2kh)} \right) E = \left(2n - \frac{1}{2} \right) E \tag{A.22}$$

Expressions similar to (A.21) can be set up to describe the other radiation stress tensors, taking into account the correct orbital velocity directions and pressure contributions:

$$\begin{aligned} S_{y_w y_w} &= \overline{\int_{-h}^{\eta} \left(p + \rho v_{particle}^2 \right) dz} - \int_{-h}^{0} (\rho g z) dz \\ S_{x_w y_w} &= \overline{\int_{-h}^{\eta} \left(\rho u_{particle} v_{particle} \right) dz} \\ S_{y_w x_w} &= \overline{\int_{-h}^{\eta} \left(\rho v_{particle} u_{particle} \right) dz} \end{aligned} \tag{A.23}$$

The radiation stresses described in (A.21) and (A.23) can be converted to stresses in a coordinate system with an arbitrary rotation with respect to the wave direction. This allows the radiation stresses to be calculated in directions relative to the shore [in: Battjes, 2001]:

$$\begin{aligned} S_{xx} &= \left(n - \frac{1}{2} + n\cos^2(\theta) \right) E \\ S_{xy} &= \left(n\cos(\theta)\sin(\theta) \right) E \\ S_{yx} &= \left(n\sin(\theta)\cos(\theta) \right) E \\ S_{yy} &= \left(n - \frac{1}{2} + n\sin^2(\theta) \right) E \end{aligned} \tag{A.24}$$

B Changes implemented in XBeach

At the start of this thesis work, XBeach had been programmed to work as a 2DH-model. However, at that stage testing had only been carried out in 1D-mode. Many changes had taken place in the code that had been configured to work in 1D-mode, but not in 2DH. The majority of the work on the XBeach code done during this thesis work consisted of minor changes and debugging to allow the model to run properly in 2DH-mode. In the following sections some of the larger changes made during this thesis work are discussed.

B.1 Irregular wave group forcing

In order for XBeach to simulate storms, it is essential to be able to specify spatially, temporally and directionally varying wave conditions. As part of this thesis work a wave boundary module was developed with the ability to generate random short wave energy packets and associated bound long waves, based on an input wave spectrum. The module generates short wave energy values for every directional bin at every offshore boundary grid point at every time step, as well as infragravity water flux values at every offshore boundary grid point at every time step. The module is based on work carried out by Van Dongeren *et al* [2003]. The theory behind the module is explained in this section.

In order to create a time series of wave energy along the offshore boundary, the input spectrum is assumed to be composed of K single summation wave components [Miles and Funke, 1989; in van Dongeren *et al.*, 2003] in the range around the spectral peak where the energy density is greater than 8% of the peak energy density. Each wave component has a specific frequency, phase, amplitude and direction. Summed together the wave components create a time series of the sea surface at the offshore boundary:

$$\eta(0,y,t)=\sum_{i=1}^{K} B_i \cos\left(k_i \sin\left(\theta_i\right) y - 2\pi f_i t + \varphi_i\right) \tag{B.1}$$

In equation (B.1) B_i represents the amplitude of each wave component.

In order to determine the specific properties of the wave components, the frequencies of all K components are distributed uniformly in the range around the spectral peak. This choice leads to a frequency resolution which is dependent on K. Each wave component is given a wave phase using the random phase model. The direction of each wave component is determined randomly using the Cumulative Distribution Function of the wave direction of the input spectrum, see Figure 4. At this stage the directional CDF is based on integration across all frequencies. In the case of strong frequency-directional correlation, it may be advisable to use frequency dependent CDFs instead.

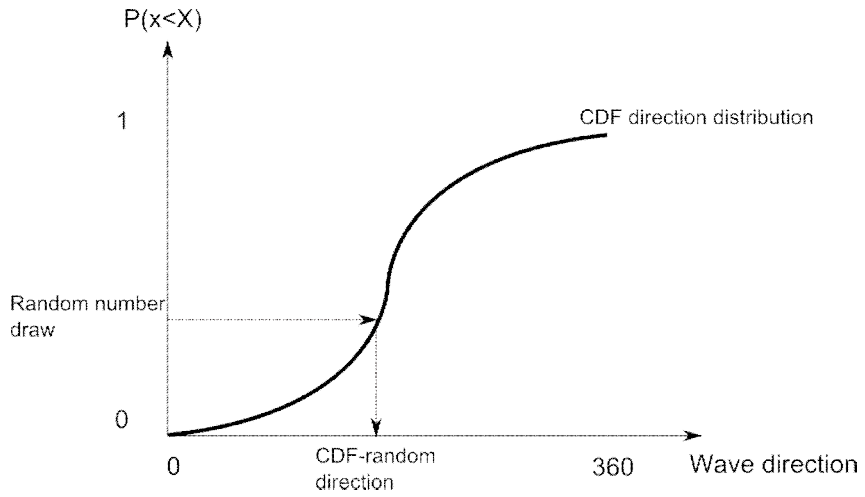


Figure 4 Random wave angles are chosen using a random number generator and the cumulative distribution function of the directional spreading of the input spectrum

Once the frequency and direction of each wave component has been selected, the amplitude B_i can be calculated by two dimensional interpolation across the 2D-input wave variance spectrum. A linear correction is made to the amplitudes of the wave components to ensure the integrated wave variance of the K components is the same as that of the input spectrum. The wave number k_i is determined using the dispersion relation, given the mean still water depth at the offshore boundary.

Equation (B.1) can now be used to generate a time series of the sea surface elevation at the offshore boundary. The envelope of the sea surface time series can be calculated using a Hilbert transform, the amplitude of which being a measure for the wave energy:

$$E_{\theta_i}(y,t) = \frac{1}{2}\rho g A_{\theta_i}(y,t) \tag{B.2}$$

The directional wave energy time series is outputted at every offshore grid point at every desired point in time to a boundary condition file. This file is read by the main XBeach program.

The mass flux due to bound infragravity waves at the offshore boundary is calculated according to the expressions developed by Herbers *et al.* [1994]. It is stated that bound infragravity waves are generated by the interaction of two wave components with different frequencies. The frequency of the bound infragravity wave is given as:

$$f_3 = f_2 - f_1 \tag{B.3}$$

In the equation above, the subscripts on the right hand side refer to the indices of interacting short wave pairs. In order to ensure positive interaction frequencies, indices should be ordered according to increasing frequency of the short wave components. It should be noted that two interacting wave components contribute to only one infragravity wave frequency. However, one infragravity wave frequency may be forced by many different wave component interactions.

Similarly, other properties of the bound infragravity wave can be deduced from the associated properties of the short wave components. The bound wave number, wave group velocity and wave phase are given as:

$$k_3 \equiv \left|\vec{k_1} - \vec{k_2}\right| = \sqrt{k_1^2 + k_2^2 - 2k_1 k_2 \cos(\theta_3)} \tag{B.4}$$

$$c_{g3} = \frac{2\pi f_3}{k_3} \tag{B.5}$$

$$\varphi_3 = \varphi_2 - \varphi_1 + \pi \tag{B.6}$$

Note that equation (B.6) is based on the assumption that the short wave groups and bound long waves are in equilibrium, and therefore are 180° out of phase. The angle of the bound long wave can be found using the following relation:

$$\theta_3 = \arctan\left(\frac{k_2 \sin\theta_2 - k_1 \sin\theta_1}{k_2 \cos\theta_2 - k_1 \cos\theta_1}\right) \tag{B.7}$$

The energy related to a bound infragravity wave with a specific frequency is given as [van Dongeren *et al.*, 2003]:

$$\begin{aligned} E_3(f_3) = 2\int_{\Delta f}^{\infty}\int_0^{2\pi}\int_0^{2\pi} & D^2\left(f + f_3, -f, \left|\theta_1 - \theta_2\right| + \pi\right) \\ & \cdot E\left(f + f_3, \theta_1\right) E\left(f, \theta_2\right) d\theta_2 d\theta_1 df \end{aligned} \tag{B.8}$$

Where in equation (B.8) the first term behind the triple integral is the interaction coefficient as defined by Herbers *et al.*[1994]. This interaction coefficient is determined through a perturbation expansion of the Bernouilli equation, details in original publication. In the wave boundary condition module a modification of the interaction coefficient is implemented to convert the output to surface level elevation instead of bed level pressure [Van Dongeren, private correspondence]:

$$D_{surface} = D_{bed} \frac{\cosh(k_3 h)}{\cosh(k_1 h)\cosh(k_2 h)} \tag{B.9}$$

The amplitude of each bound wave can be found from the bound wave energy [van Dongeren *et al.*, 2003]:

$$A_3 = \sqrt{2E_3 df} \tag{B.10}$$

Where in equation (B.10) *df* refers to the frequency resolution of the short waves, i.e. the frequency step used to generate all *K* frequency components around the peak of the short wave spectrum.

A time series for the cross shore water flux across the offshore boundary at the origin of the XBeach computational axis is generated by means of an Inverse Fourier Transform:

$$q_x(0,t) = IFFT\left[\sum_{i=1}^{K} \frac{A_{3,i}}{2} e^{-i\varphi_{3,i}} c_{g3,i} \cos\theta_{3,i}\right] \tag{B.11}$$

Phase-shift is calculated along the y-axis by adding the longshore distance to the next grid point and the longshore wave number components:

$$q_x(y,t) = IFFT\left[\sum_{i=1}^{K} \frac{A_{3,i}}{2} e^{-i\varphi_{3,i}} c_{g3,i} \cos\theta_{3,i} e^{-ik_{y3,i}y}\right] \tag{B.12}$$

The cross shore flux is outputted at every offshore grid point at every desired point in time to a boundary condition file. This file is read by the main XBeach program.

The boundary condition module in XBeach has been designed to recognise various input spectrum formats. The most simple method is to describe the wave spectrum using several JONSWAP parameters. The module creates a symmetrical 2D-wave variance spectrum from the data before proceeding to calculate the wave energy envelope and cross shore flux. The module has also been programmed to recognise SWAN 2D spectrum output files. The module is able to convert the SWAN output data to the XBeach model coordinates.
The module has been designed to be able to recalculate wave boundary conditions during a computation. It is therefore possible to specify varying wave conditions during a storm simulation, thereby allowing a more realistic hydrodynamic forcing. A complete user guide for this module is given in Appendix Y. Figure 5 shows an example output of a simulation using the wave module.

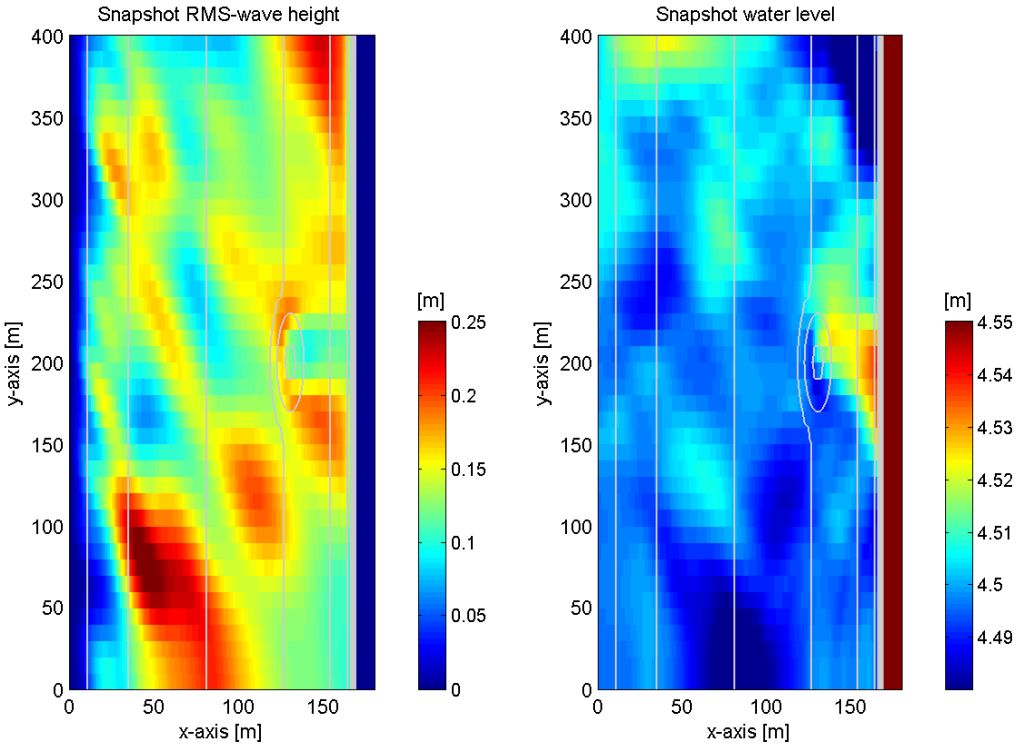


Figure 5 Examples of irregular wave groups (left panel) and associated bound and reflected infragravity waves (right panel) generated with the wave boundary condition explained in this section

B.2 Automatic time step

The numerical schemes used to solve the long wave and short wave propagation are first order explicit in time and therefore set limitations to the numerical time step in order to remain stable. However, the use of excessively small time steps leads to long calculation times and increased numerical diffusion. It is therefore sensible to find the largest time step for which the model is still stable. This is done in the automatic time step generator routine.

In the first order explicit scheme, numerical stability is guaranteed if information cannot travel more than the entire distance between grid points in one time step. In the case of long wave propagation, the velocity of information is:

$$\vec{c}_{\text{information}} = \pm\sqrt{gh} + \vec{u}_{local} \tag{B.13}$$

In other words, the velocity of information is determined by the local water depth and the local water velocity vector. The maximum information velocity vector is found by taking both RHS-components of equation (B.13) in the same direction. This vector is shown in Figure 6 from the perspective of a cross-shore velocity point.

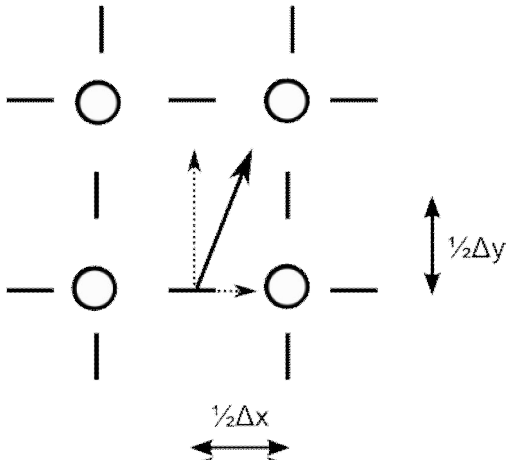


Figure 6 Information velocity vector and its cross shore and longshore components in a cross-shore velocity point

To ensure stability the distance covered by *x*-component of the information velocity vector in one time step may not exceed half the grid size in cross shore direction, see Figure 6. A similar condition exists for the *y*-component. Thus the maximum allowable time step can be found by dividing half the local grid size by the local *x*- or *y*-component of the maximum information velocity vector.

Stability in *x*- and *y*-direction in the short wave propagation scheme is guaranteed if the conditions for the long wave scheme are met, because the group velocity of short waves is always less than, or equal, to the long wave celerity. However, since the short wave propagation also takes place in theta-space, a third time step condition must be set up to ensure stability in theta-space. This condition states that short wave information may not travel more than one grid step in theta-space in one time step. The short wave propagation velocity used to calculate the time step is calculated internally in the short wave propagation routine. Generally the long wave propagation criteria are dominant over the theta-space criterion.

The time step used in the numerical model can be adjusted by the user by varying the CFL-coefficient:

$$\Delta t_{used} = \mathrm{CFL} \cdot \Delta t_{max,stable} \tag{B.14}$$

Theoretically the model should remain stable if the CFL-coefficient is chosen equal to or less than one. However, it has been found that in certain simulations the model becomes unstable at CFL-coefficient values as low as 0.7. It is unclear at this moment how these instabilities occur.

B.3 Short wave numerical dissipation

During the verification tests of XBeach it was shown that under stationary wave forcing, short wave heights across the model domain were decaying or increasing in time. This

change was great enough to show substantial differences in wave height and secondary parameters between the end results of simulations carried out with seemingly similar inputs.

Various parameters were examined in order to determine the cause of the short wave energy decay. To this end a number of simulations were run with varying parameters and physical processes. All simulations were carried out on the same model bathymetry. The wave forcing remained the same in all simulations. Normally incident stationary wave conditions were selected due to the ease with which comparisons can be made between the model results and theory. The simulations were carried out on a regularly spaced grid.

In order to ensure that the wave decay was not due to the implementation of physical wave dissipation, a simulation was set up in which dissipation was removed from the wave action balance. The wave height decay rate calculated in this simulation along the centre cross shore transect is show in Figure 7. It is clear from the figure that the situation is not stationary. This shows that the non-stationarity of the short wave heights is not due to the dissipation term.

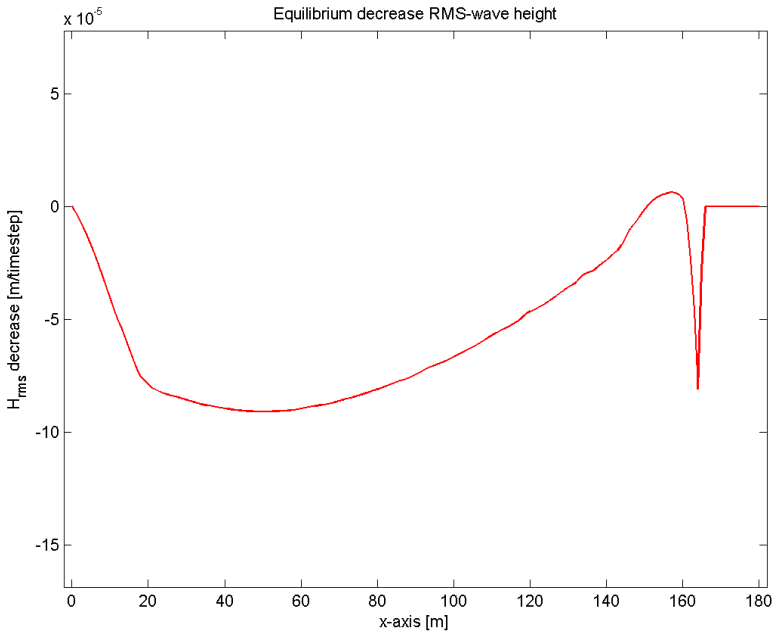


Figure 7 Short wave decay rate (wave height decrease per second) along the centre cross shore transect in the case of zero physical dissipation

A possible explanation for the wave height decay was that short wave energy was leaking across the theta boundaries of the model. In order to test this hypothesis two new simulations were set up. The first simulation contained only one grid cell in theta space, ranging from -90° to +90°. The second contained 9 grid cells in theta space, each 20°, in total also spanning -90° to +90°. It was shown that the two outer cells in the second simulation contained no energy during the entire calculation. In the second simulation it is therefore impossible for any wave energy to leak out across the theta boundaries.
The energy decay rate along the centre cross shore transect for both simulations is show in Figure 8. The results show that there is minimal difference between the two simulations. Energy leakage across the theta boundaries is not the cause of the wave height decay.

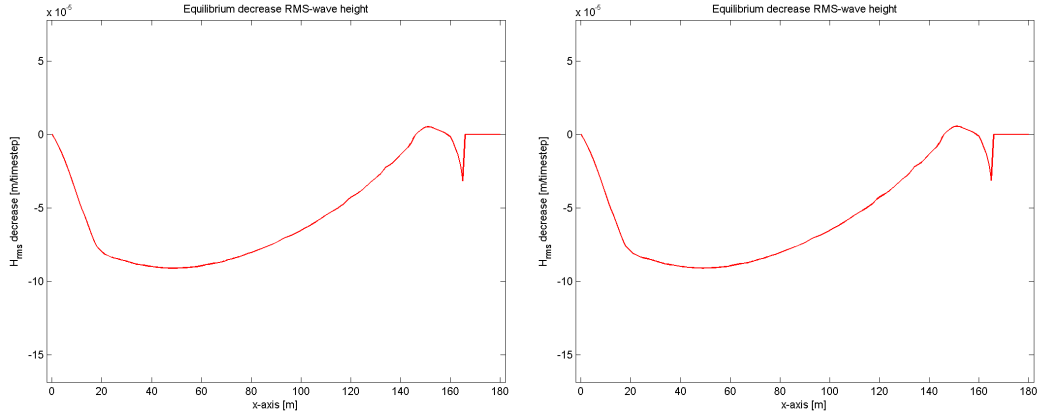


Figure 8 Short wave decay rate along the centre cross shore transect in the case of one theta grid cell (left panel), and in the case of nine theta grid cells (right panel).

Another source of wave energy decay is the numerical diffusion inherent in the numerical scheme. Numerical diffusion is dependent on spatial and temporal grid step sizes. To examine the effect of the time step on the decay of short wave heights, two simulations were set up with different CFL-conditions. The first simulation was run with a Courant number of 0.1, the second with a Courant number of 0.8. The wave height decay along the centre cross shore transect for both simulations is shown in Figure 9.

The results show a strong dependence on the CFL-condition. Since the grid size is the same in both models, the Courant number difference relates almost linearly to the time step size difference between the two simulations. As a first order approximation, the time steps in the first simulation are 8 times smaller than those of the second simulation. This shows that the wave height decay is inversely related to the time step size, or positively related to the number of time steps per second.

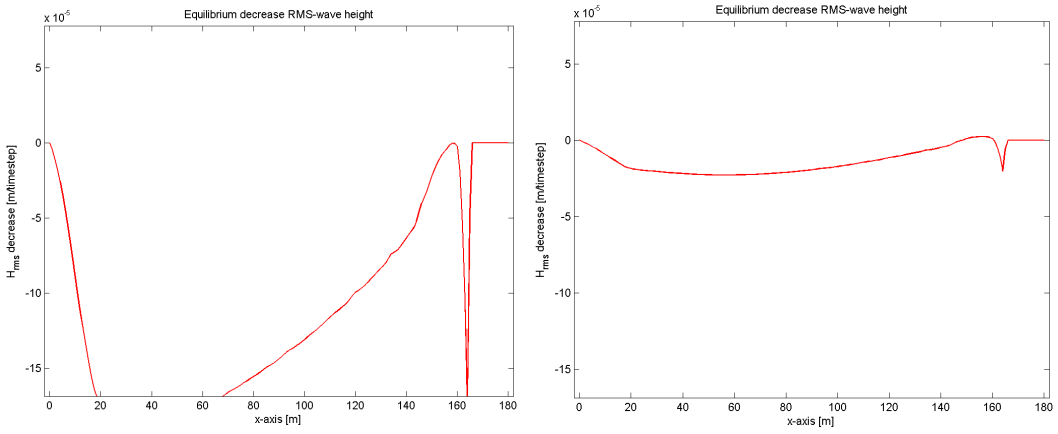


Figure 9 Short wave decay rate along the centre cross shore transect with Courant number 0.1 (left panel), and with Courant number 0.8 (right panel).

The effect of the spatial grid step size were studied in a series of subsequent tests. Figure 10 shows the change in the short wave height over time for two simulations with different spatial grid sizes in two locations along the central cross shore transect. The results appear to show a strong inverse relationship between the spatial grid step size and the rate of wave decay. However, this may be because of different time stepping conditions related to the difference in spatial grid step size.

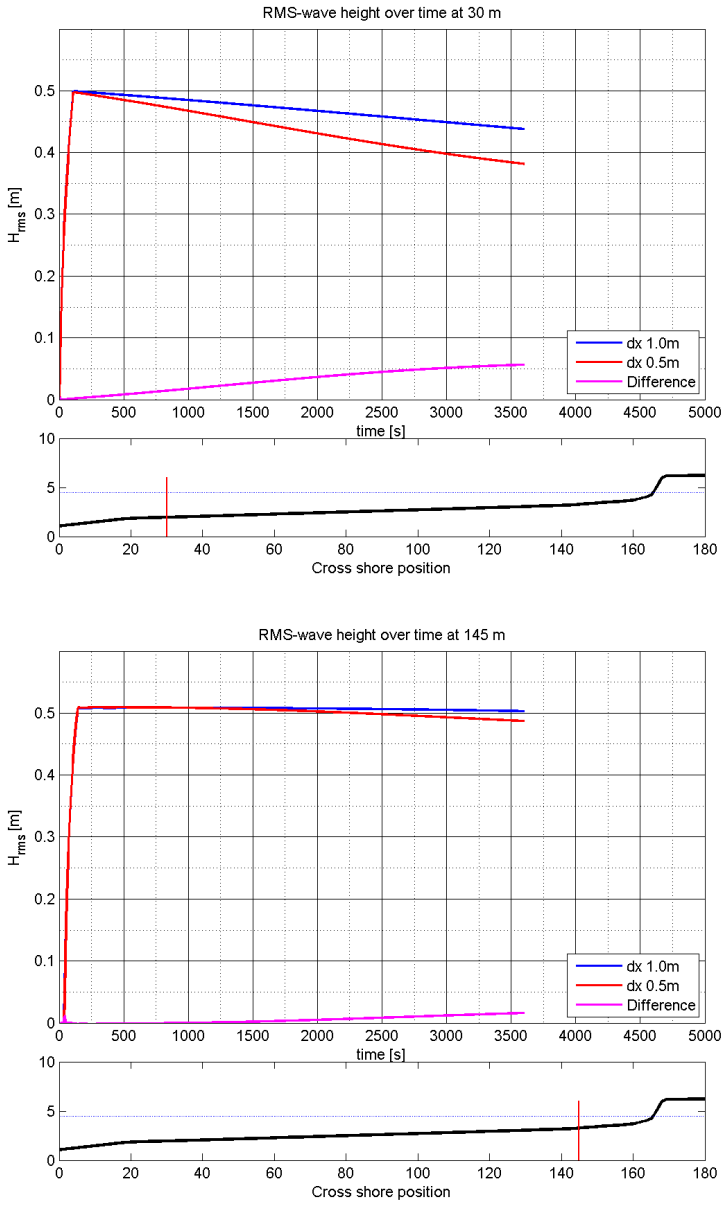


Figure 10 Short wave height over time for two grid sizes at two cross shore locations

To overcome the dependency of the temporal step size on the spatial step size, XBeach was modified to accept constant time steps. Using this modification, four simulations were carried out with different spatial and temporal grid step sizes. The change in the short wave height over time for one point in the shoaling zone in all four simulations is given in Figure 11.

It is clear from the results of the final four simulations that the spatial grid size steps play a negligible roll in the wave decay. The temporal steps on the other hand seem to determine almost entirely the short wave height decay.

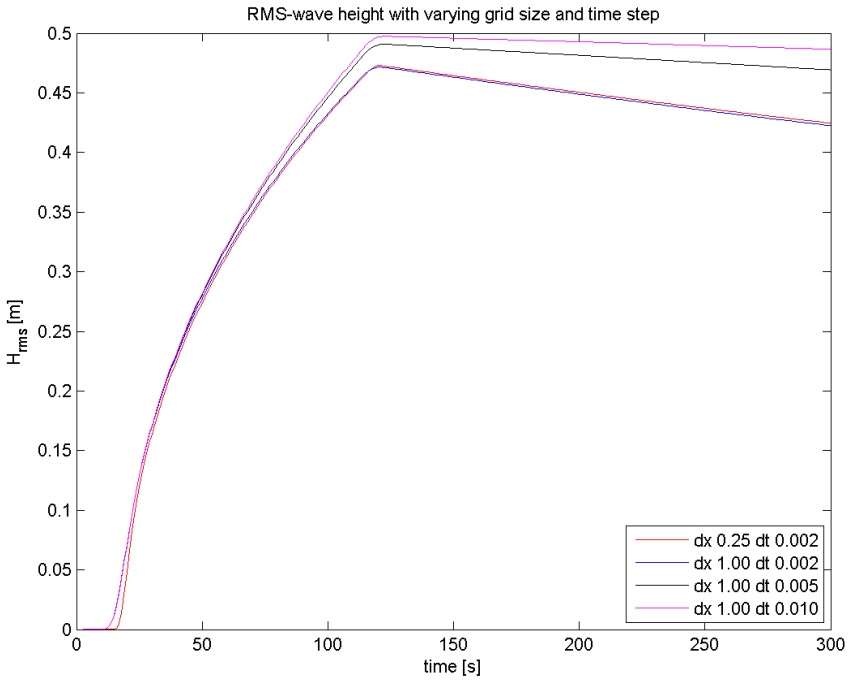


Figure 11 Change in short wave height over time according to four simulations with different spatial and temporal grid step sizes

In order to understand how the spatial and temporal step sizes effect the numerical diffusion, a simplified one-dimensional expression for the wave action balance is examined. It is shown in Appendix Z that the numerical dissipation coefficient for this simplified equation can be written as:

$$K = -\frac{1}{2} c_g \left(c_g \Delta t - \Delta x \right) \tag{B.15}$$

Equation (B.15) shows that the numerical dissipation should increase as the time step size increases. In the results shown above, the opposite is the case. Therefore it is unlikely that numerical diffusion is responsible for the short wave height decay. This hypothesis is supported by further tests using the Warming and Beam scheme for the wave action balance. This scheme which is Second Order Upwind in space and Lax-Wendroff in time, should minimize numerical dissipation. The tests showed no discernable improvement due to the higher order scheme.

A debugging routine lead to the source of the wave height decay. In the original code the wave dispersion relation had been linearized for speed. The linearization was calibrated for water depths and waves likely to be used in XBeach. This routine calculates the wave number from the wave frequency with a very small error due to the linearization. In the original XBeach version this was not a great problem as the wave frequency remained constant during the simulation. Therefore the error in the wave number remained constant.
With the introduction of wave-current interaction in XBeach, it became necessary to recalculate the relative wave frequency from the updated wave number. The updated wave frequency now contained an error due to the error in the original wave number. This error was fed back into the dispersion relation, leading to ever greater errors. This mechanism is

positively related to the number of dispersion relation calculations per simulation, and thus inversely related to the time step size.

To address the issue of short wave height decay, the dispersion relation algorithm was replaced by an iteration scheme using the following relation:

$$L = L_0 \tanh\left(\frac{2\pi h}{L}\right) \tag{B.16}$$

Fast convergence is found by using the results of the previous time step as the initial guess and using a Golden Ratio weighting scheme. The error in the wave number calculation can now be set to a very small and known value. Tests showed that an error of less than 10^{-5}m per time step lead to no visible wave height decay over an hour-long simulation. The total additional calculation time due to the iteration scheme was found to be 8% compared to the old linear dispersion relation scheme. The accuracy of the scheme and resulting short wave heights increased enormously. Figure 12 shows the short wave height change for one point in the shoaling zone using the old and new dispersion relation.

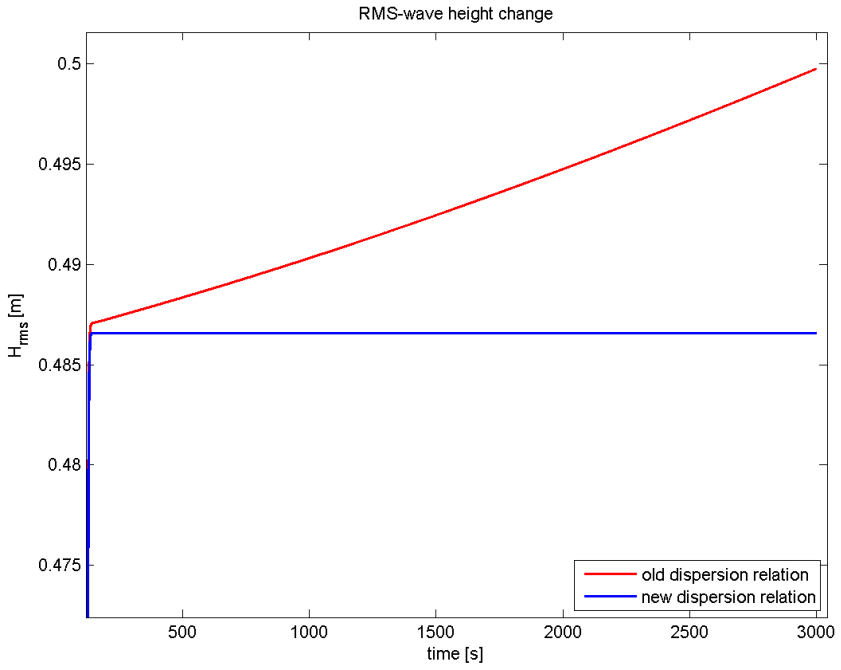


Figure 12 Short wave height over time for one point in the shoaling zone. The figure shows results using the original dispersion relation and the new iterative dispersion relation.

B.4 Lateral boundaries

The lateral flow boundaries in XBeach have to handle very complex hydrodynamic conditions. Typically there may be a wave induced longshore current, shore trapped edge waves, reflected leaky waves and a tidal current. The wave induced longshore current may be unstable and shear in the balance of forcing and friction. These processes do often not correspond to the zero longshore gradient assumption made in the case of Neumann

boundary conditions. During the development of XBeach from a 1D to a 2DH-model, these boundaries have been the cause of many instabilities.

The basic set-up of the lateral Neumann flow boundaries is shown in Figure 13. Longshore uniformity in hydrodynamic conditions is assumed across the lateral boundary. This assumption allows the water level and cross shore velocity to be copied across the lateral boundary to the edge row. With this information the longshore velocity can be calculated in the normal manner.

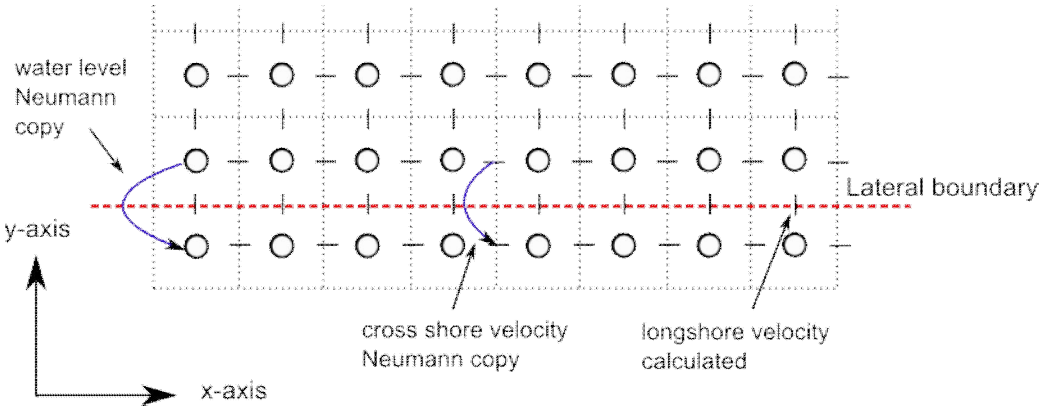


Figure 13 Basic structure of lateral Neumann flow boundaries

With this configuration, simulations would only remain stable for short periods of time in the case of normally incident, or nearly normally incident waves. With the presence of a strong wave generated longshore current, simulations would remain stable. Various solutions were tested for this problem, including the creation of special boundary conditions for the longshore advection term in the longshore momentum equation. These solutions improved stability, but the model was still prone to creating large inflows across the lateral boundaries.

By means of detailed code debugging, it was found that the cause of instabilities was a mismatch between wave forcing on the lateral boundaries and the water surface gradient across the boundary. The dominant terms in the longshore momentum equation across the model are:

$$\frac{\partial v^L}{\partial t} = -g\frac{\partial \eta}{\partial y} + \frac{F_{w_y}}{\rho h} \tag{B.17}$$

It was found that on the lateral boundaries the wave forcing was very large and that it could only be balanced by acceleration of the flow, since the water surface gradient is set to zero across the boundary.
One solution was found by removing wave forcing on the lateral boundaries. In this configuration longshore flow across the lateral boundaries is steered only by the convective terms and bed friction. These changes stopped the creation of large inflows across the boundary in the case of normally incident waves. However, in the case of waves with a large angle of incidence, the new boundary conditions prevented the wave generated longshore current from exiting the model correctly. This in turn lead to artificial circulation cells in the model.

Further investigation showed that wave forcing on the lateral boundaries was constantly too large because the short wave energy was not propagating properly to the lateral edges. This was solved by modifying the lateral boundary conditions for the short wave energy to include outgoing wave energy. This had previously been calculated using the wave action balance scheme. This solution allowed the longshore current to be driven out of the model domain, while still preventing large influxes of water along the lateral edges.

The resulting boundary conditions are stable and can handle the complex hydrodynamics relatively well.

B.5 Miscellaneous

During this thesis work various other changes were made to the programme structure of XBeach.

- Changes were made to the iterative stationary wave action balance solver in cooperation with Professor Roelvink of UNESCO-IHE. Lateral boundary conditions were rewritten to account for the iterative scheme, wave action advection schemes were modified and the spin-up time of the iterative solver was drastically reduced.
- The sediment transport boundary condition on the back bay boundary was modified to allow sediment to exit the model domain without causing instabilities.
- An optional module was introduced to allow users to define the type of output required. In large simulations this can save significant amounts of data space.

C Test 0

C.1 Model description

In Test 0, the capacity of XBeach to deal with varying surge and tide levels is tested. Test 0 is carried out a longshore uniform bathymetry based on the experiments carried out by Van Gent *et al*. [2006]. No waves are imposed on the offshore boundary. A sinusoidal longshore uniform tide level with a six hour period is imposed on the model domain. Morphology and sediment transport are not calculated.

C.2 Results

The XBeach model accurately replicates the imposed tide level in the entire model domain, as can be seen in Figure 14.

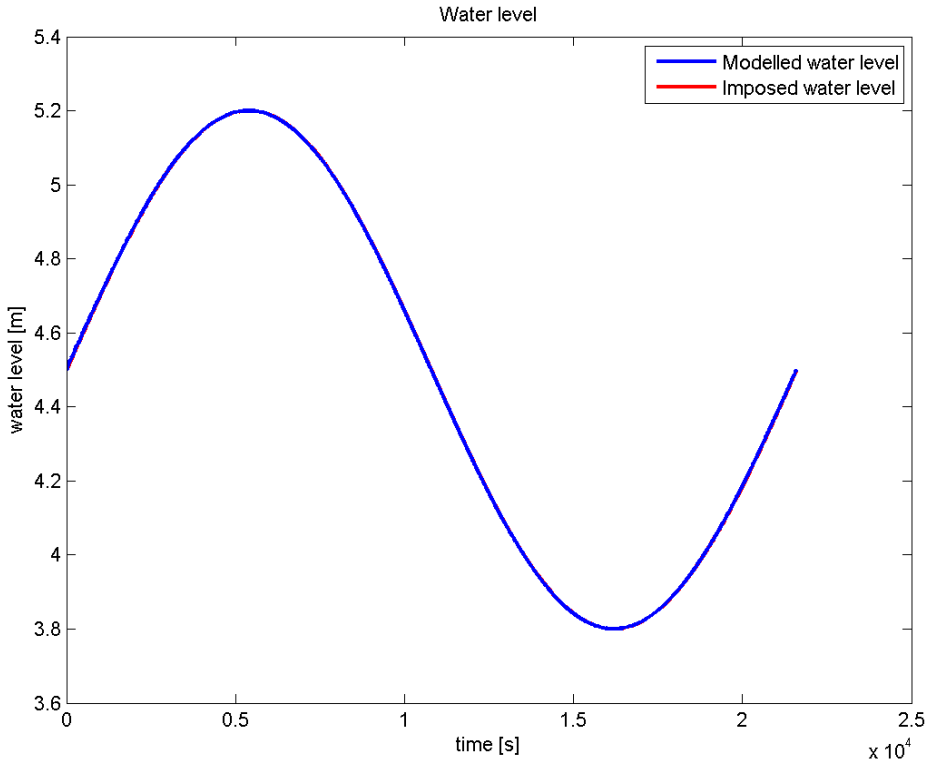


Figure 14 Modelled water level averaged over the model domain and imposed water level over time

The velocities in the model are presented in Figure 15. The mass flux related to the changing tide level is handled entirely by the cross-shore velocity gradient, which is in agreement with the assumption of longshore uniform tide.

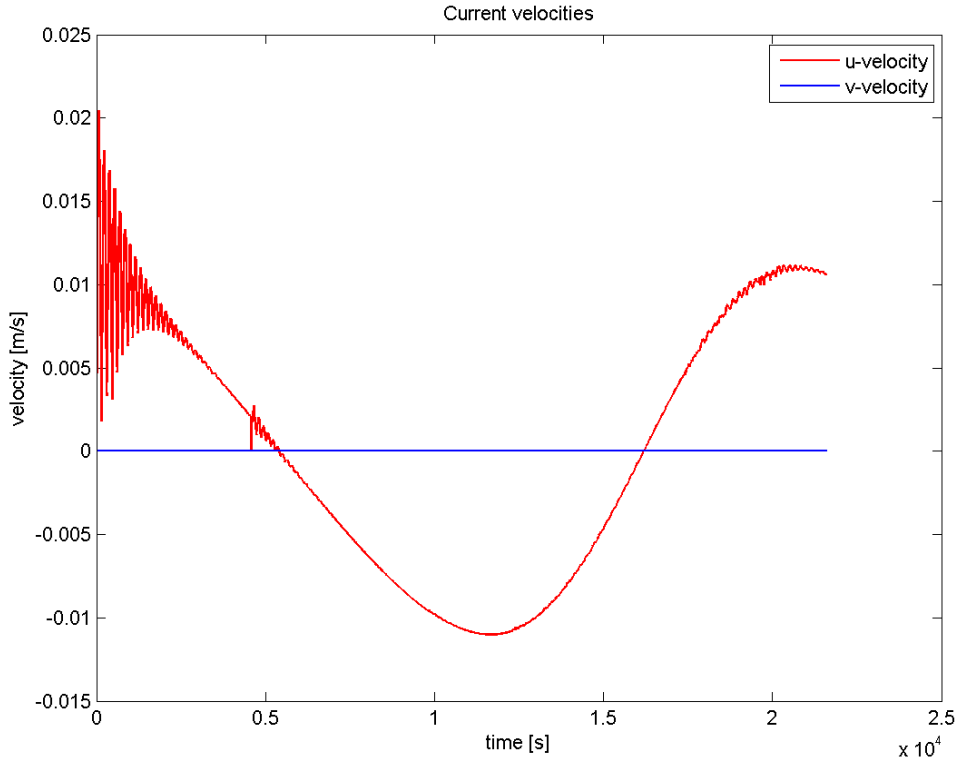


Figure 15 Average model domain cross-shore (u) and longshore (v) velocities in time

The cross-shore current velocities appear to be unstable at the start of the simulation, but gradually the instabilities decrease. This instability may be due to the fact that no spin-up time is used on the tide boundary conditions.
It is uncertain why instabilities occur again in the cross-shore velocities around 500s and 1750s. The magnitudes of these instabilities however are not large and are unlikely to affect the model results.

In order to analyse the effect of the instabilities in the cross-shore velocities, the simulation is run again with a much shorter tidal period of 6000s. As the period is shorter, the temporal water level gradient at the start of the simulation is greater. This is likely to cause greater instabilities in the cross-shore velocity.
The tide level at the start of the simulation is shown in Figure 16. As can be seen, the modelled tide level fluctuates around the imposed tide level until roughly 1500s, after which both tide levels converge. In Figure 17 it can be seen that the cross-shore velocity has even greater instabilities than in Figure 15.

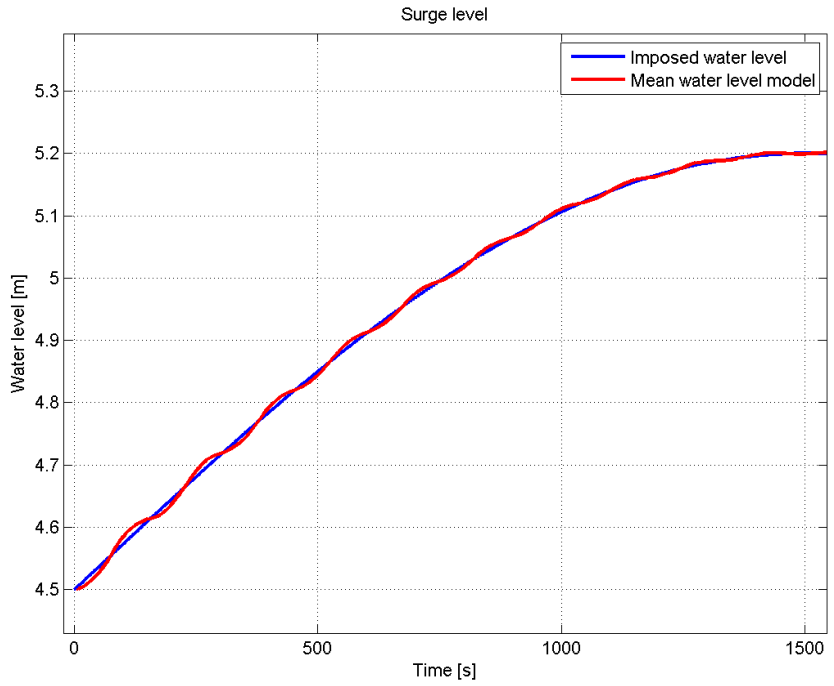


Figure 16 Modelled and imposed surge level. Surge period 6000s.

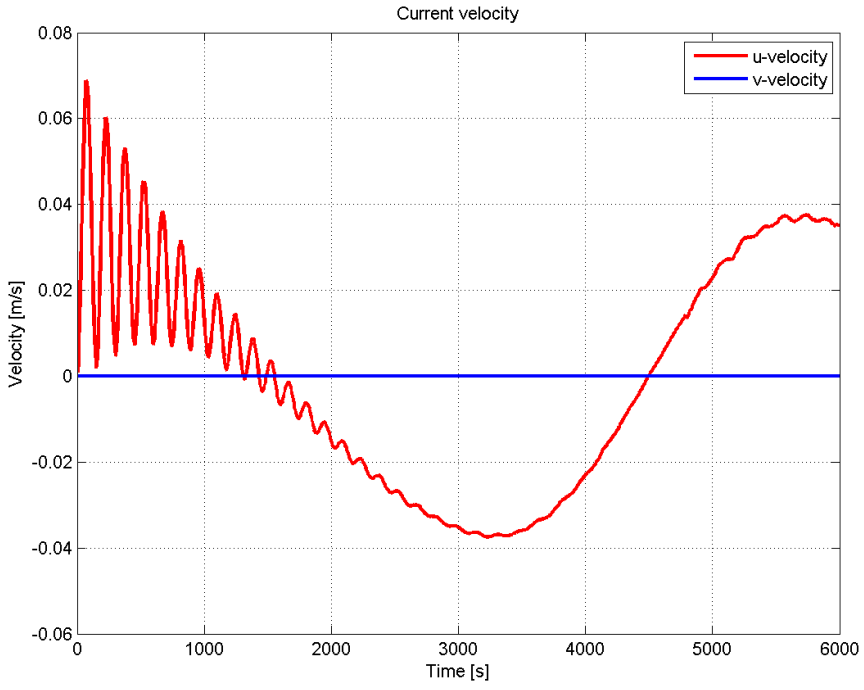


Figure 17 Average cross-shore (u) and longshore (v) velocities over time

C.3 Conclusions

It can be concluded that XBeach can adequately handle varying tide levels. However, attention must be paid to the fact that no spin-up time is used for the tide boundary conditions. If a large temporal tide or surge gradient is imposed on the model boundaries, the simulated velocities and water levels may be inaccurate at the start of the simulation. It is not expected that the model will become unstable under normal storm conditions.

D Test 1

D.1 Model description

In Test 1, the capacity of XBeach to handle short-wave shoaling and breaking and wave set-up and set-down is tested for normally incident wave conditions. Test 1 is carried out on a longshore uniform bathymetry based on the experiments carried out by Van Gent *et al.* [2006]. A stationary wave condition is imposed on the offshore boundary with short waves with a wave height of 0.5m and period of 3.5s. As there is no temporal or spatial variation in the short-wave forcing, no bound long waves are generated. The water level on the model boundary is kept constant. Morphology and sediment transport are not calculated.

D.2 Results

In order to evaluate the ability of XBeach to handle shoaling and breaking, the results of the model are compared with the results of an analytical solution for the wave height using linear wave theory. In the analytical model, see Appendix W, wave energy dissipation due to bottom friction is disregarded. Only shoaling and breaking is taken into account. As can be seen in Figure 18, XBeach is consistent with the analytical results until roughly 120m. At this point the analytical results and XBeach results diverge until wave breaking becomes dominant in both models. This is most likely due to the fact that the default Roelvink breaker relation is used in the XBeach model. The stationary wave heights across the model domain are shown in Figure 19. It can be seen that the results are longshore uniform.

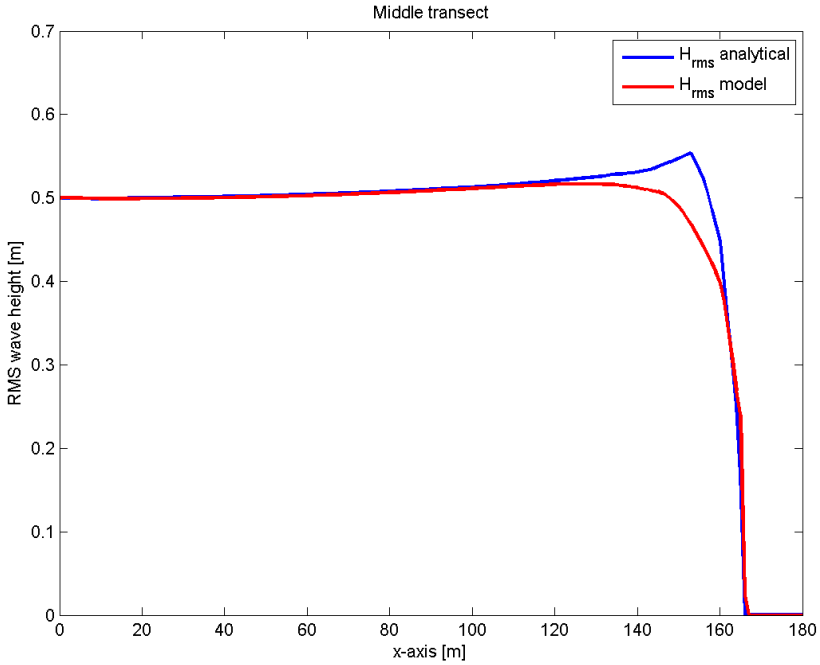


Figure 18 Wave height in middle transect in model and analytical approximation

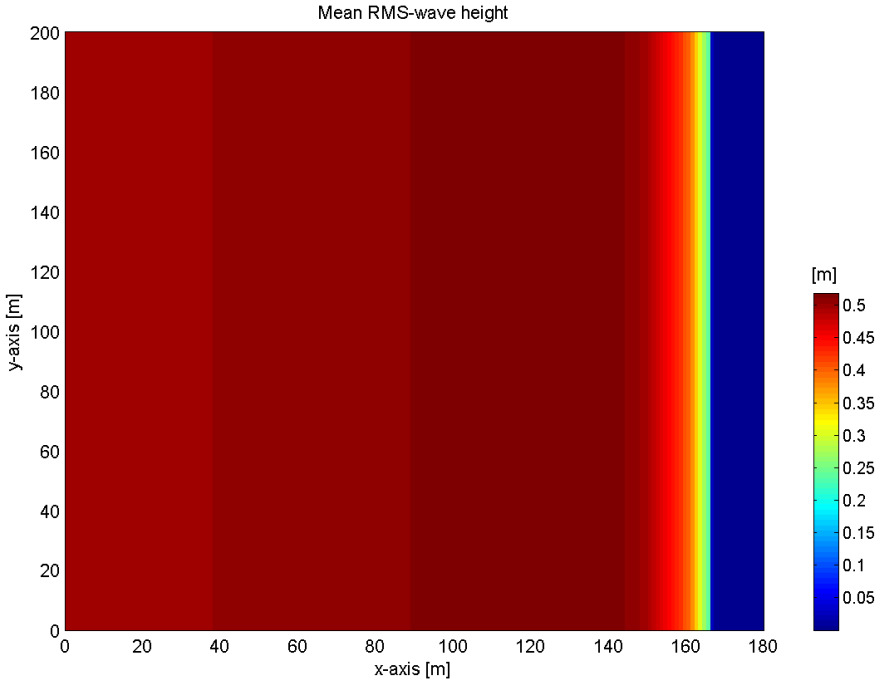


Figure 19 Time-averaged wave height over the model domain

Wave set-up and set-down is compared to a semi-analytical computation of the water level, based on a numerical integration of the cross-shore change in the radiation stress. Note that the wave energy used to calculate the radiation stress in the semi-analytical approximation is based on the wave heights from the analytical shoaling approximation, not the wave heights from the XBeach model. The comparison between the wave set-up and set-down in the XBeach model and the semi-analytical approximation can be seen in Figure 20.

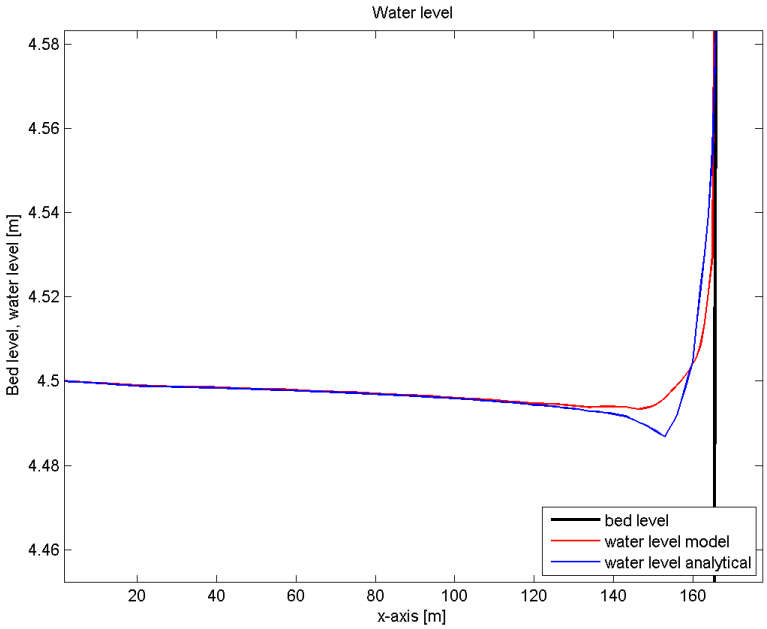


Figure 20 Water level in middle transect in model and semi-analytical approximation

The velocities in the model are examined. As the computation involves stationary waves, no wave generated cross-shore currents should occur. No wave-generated longshore currents should occur as the waves are normally incident. As can be seen in Figure 21, the spatially averaged longshore velocity is stationary and zero. The spatially averaged cross-shore velocity however is negative. Furthermore, even disregarding the spin-up effects, the cross-shore velocity is non-stationary as it oscillates around -5×10^{-4}. As can be seen in Figure 23, the cross-shore velocity is longshore uniform and cross-shore non-uniform.

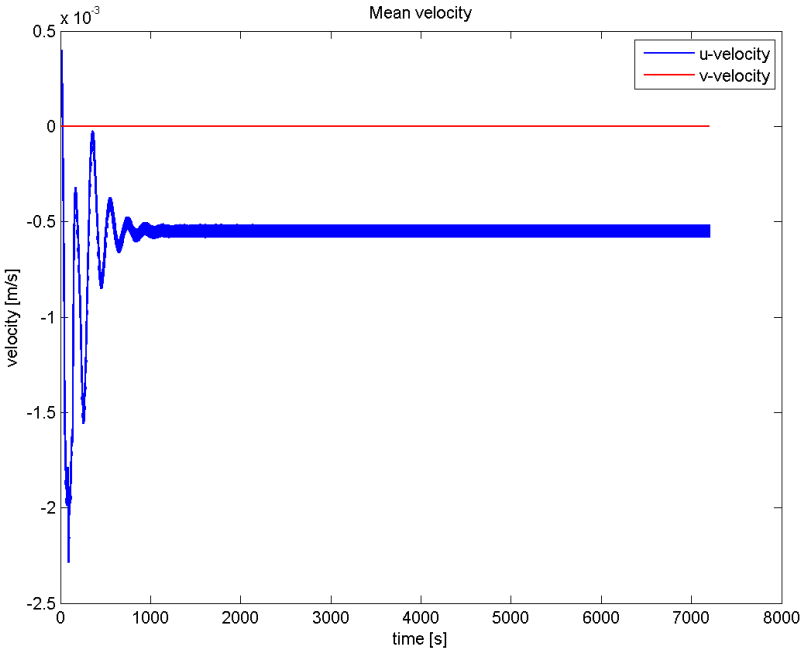


Figure 21 Spatially averaged cross-shore and longshore velocities in time

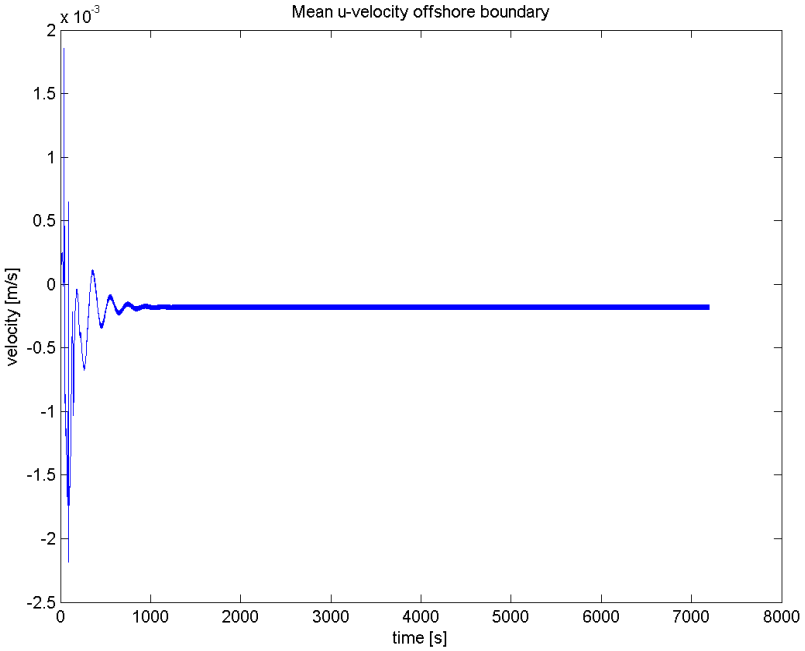


Figure 22 Longshore-averaged cross-shore velocity on the offshore boundary in time

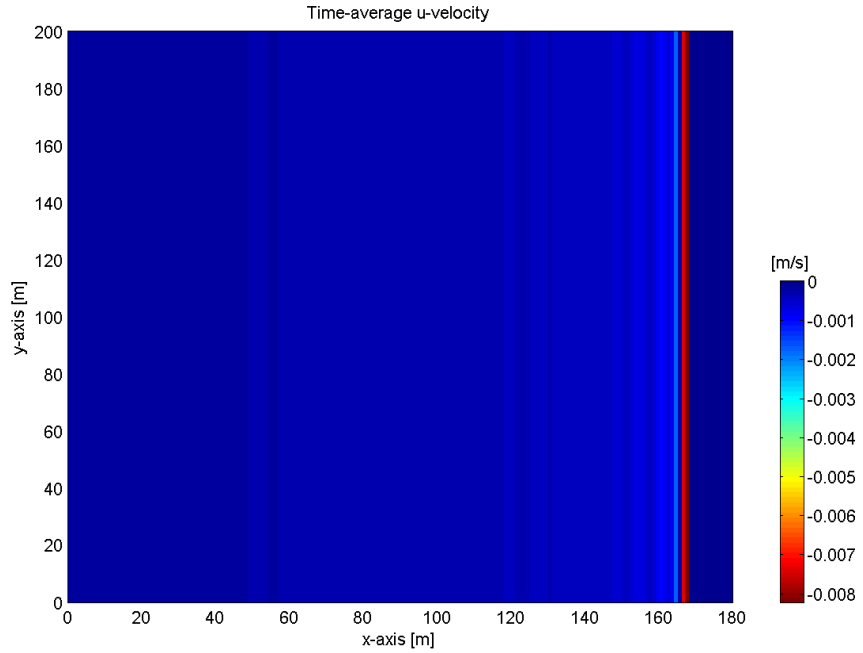


Figure 23 Time-averaged cross-shore velocity over the model domain

To examine whether mass is conserved within the model, the cross-shore and longshore velocities are multiplied by the local water depth, thus providing a discharge per unit width. As can be seen in Figure 24, the longshore component is stationary and zero, and the cross-shore component is negative and non-stationary. In Figure 25 it can be seen that the cross-shore component is longshore uniform and cross-shore non-uniform.

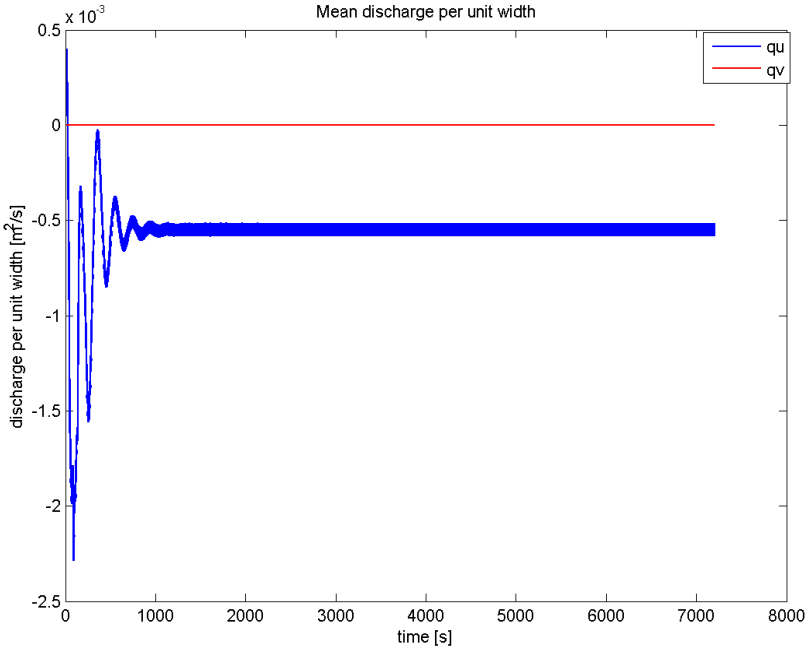


Figure 24 Spatially averaged cross-shore and longshore discharge per unit width over time

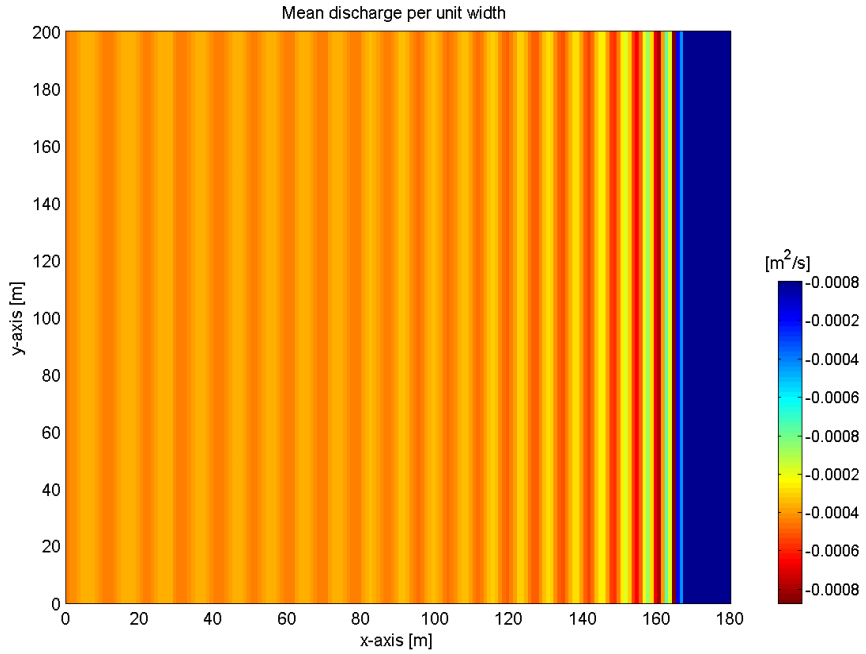


Figure 25 Time-averaged cross-shore discharge per unit width over the model domain

As the average discharge in the model is negative and the average cross-shore velocity on the offshore boundary is negative (see Figure 22), it is to be expected that the model is losing mass as generally water is flowing out of the model. To test this hypothesis, the water level averaged over all wet points is examined over time. This can be seen in Figure 26.

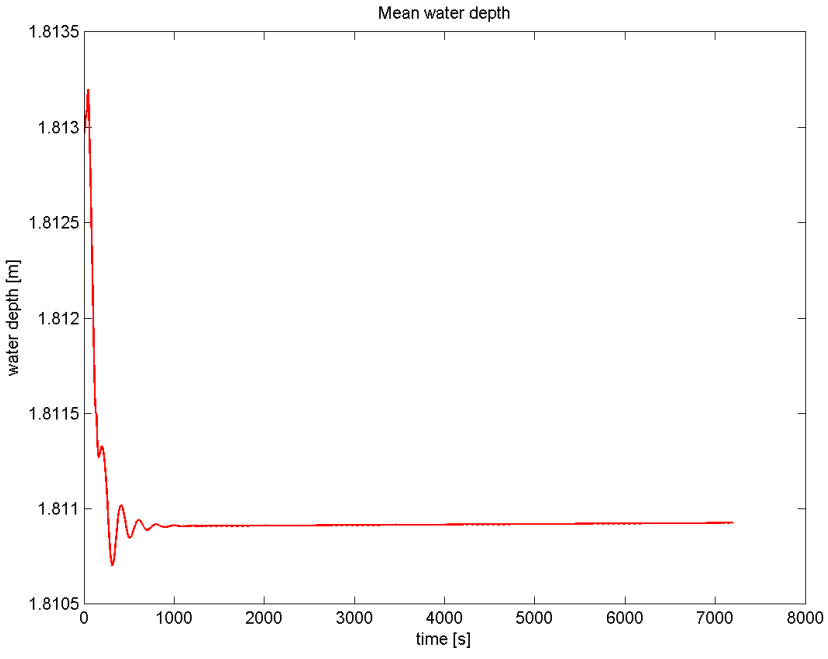


Figure 26 Average wet-point water level over time

In contrast to the hypothesis, the average water level is actually increasing in time. Mass must therefore be entering the model via another boundary. Since all longshore velocities are zero, mass must be entering via the land boundary. This is further supported by Figure

27, in which the cross-shore discharge is shown for two points in time along the middle transect. The summation of both discharges (also shown in Figure 27) clearly becomes negative at the landward boundary and remains constant on average, moving offshore.

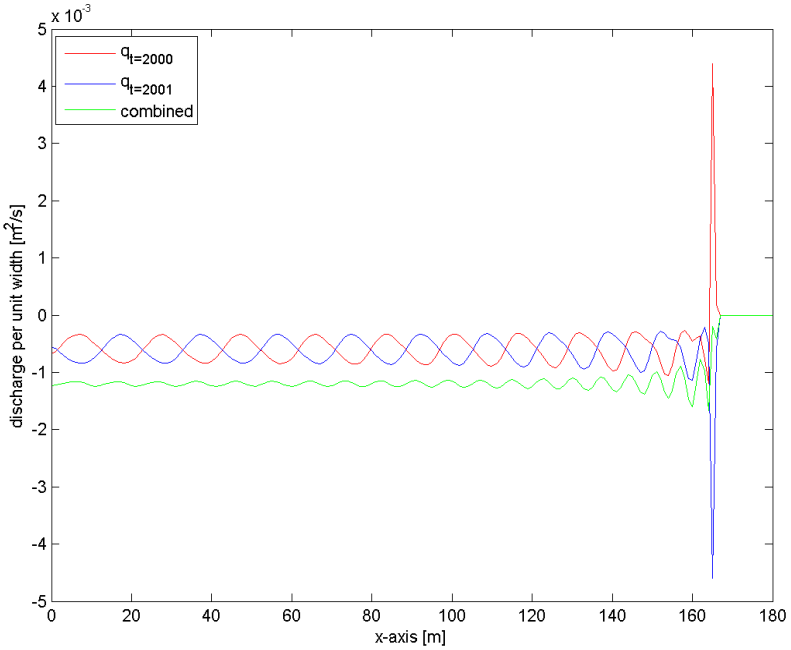


Figure 27 Cross-shore discharge per unit width in two consecutive time steps and their summation, shown for the middle transect

At first it might appear that the mass flux at the land boundary is caused by flooding-drying effects. However, the Stelling and Duijnmeyer [2003] numerical scheme is mass conservative on wet and dry points as long as the Courant condition is adhered to. It is therefore considered likely that the time stepping criterion is incorrectly applied in this version of XBeach. By improving the time-stepping procedure to take into account the Courant condition on a two-dimensional grid the mass flux problem is eliminated, as shown in Figure 28.

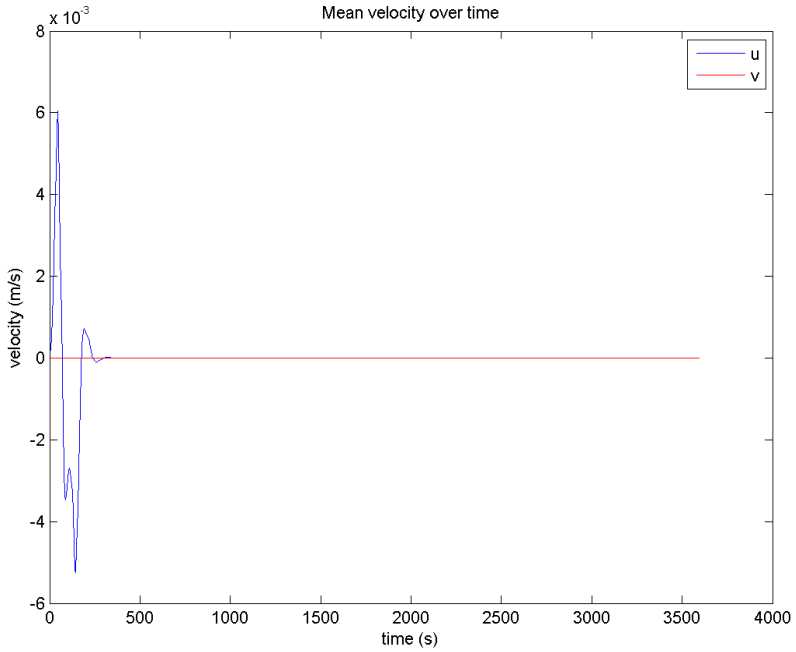


Figure 28 Spatially averaged cross-shore and longshore velocities in time, after improvement of the time stepping procedure

D.3 Conclusions

XBeach has been shown to be capable of correctly predicting shoaling and wave set-up and set-down in normally incident wave conditions. Small differences exist between the numerical results of XBeach and the (semi) analytical approximations. These differences are often due to the idealised assumptions made in the analytical approximations.

E Test 1g

E.1 Model description

In Test 1g, the influence of the grid size on the numerical result is analysed. Three simulations are run. The first simulation (Test 1g0) uses the regularly-spaced numerical grid of Test 1. The second simulation (Test 1g1) also uses a regularly-spaced grid, but with a resolution twice as large as that of Test 1. The third simulation (Test 1g2) uses an irregularly-spaced numerical grid.
A stationary wave condition is imposed on the offshore boundary with short waves with a wave height of 0.5m and period of 3.5s. The wave direction is set at 0° Cartesian convention. The water level on the model boundary is kept constant. Morphology and sediment transport are not calculated.

E.2 Results

The RMS-wave heights of the short waves calculated in Test 1g0, Test 1g1 and Test 1g2 are shown in Figure 29. The figure shows clear agreement between all three simulations. The mean water level in all three simulations is shown in Figure 30. Test 1g0 and Test 1g1 show very similar water levels. Test 1g2 differs from the other simulations by having a less linear set-down zone and less maximum set-down. The maximum set-down in Test 1g2 is in the order of 4mm less than the other simulations, or roughly 40% of the total set-down. It should be noted that this may be due to large transitions in cross shore grid size around x=80m and x=100m.

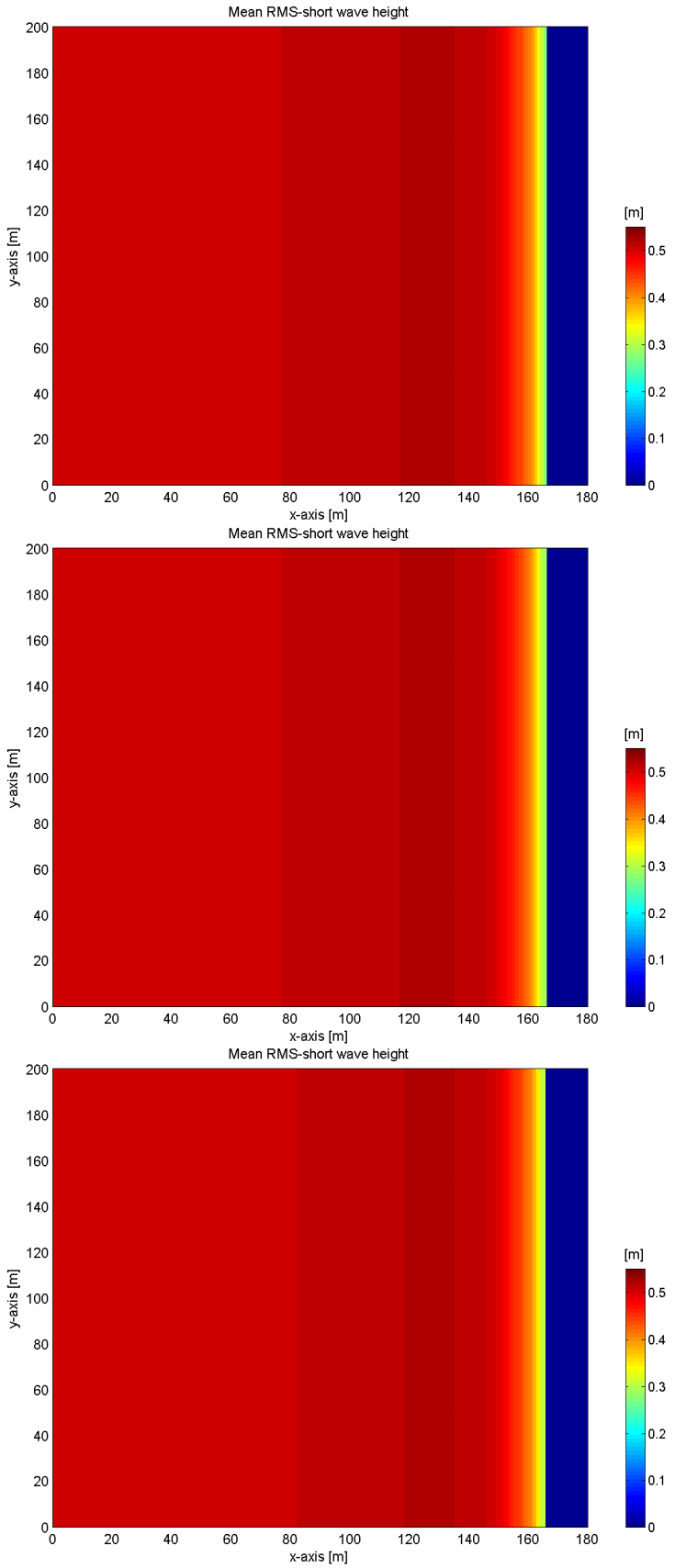


Figure 29 RMS-wave height in Test 1g0 (top), Test 1g1 (middle) and Test 1g2 (bottom)

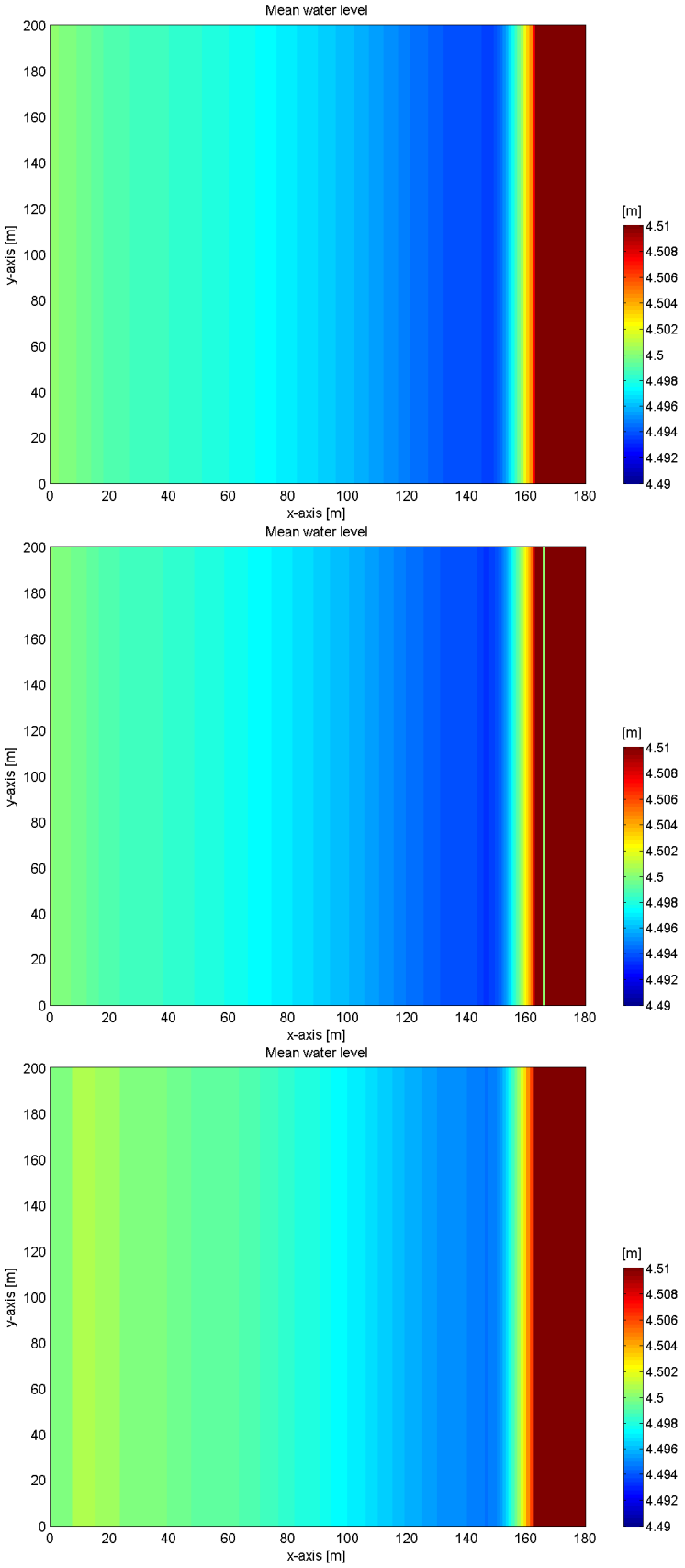


Figure 30 Time-average water level in Test 1g0 (top), Test 1g1 (middle) and Test 1g2 (bottom)

E.3 Conclusions

In general it can be stated that the short wave energy propagation scheme is unaffected by the differences between the three numerical grids. The long wave propagation scheme can be said to be stable on all three grids and unaffected by differences between the two regular grids. However, as shown by Test 1g2, care should be taken when setting up a numerical grid to ensure the transition in grid size is smooth, as this appears to affect the momentum balance. A maximum ratio between neighbouring grid cells of 1.15, as recommended for the Delft3D package [Roelvink, private correspondence], is suggested as a solution to this problem.

F Test 2

F.1 Model description

In Test 2, the capacity of XBeach to handle short-wave shoaling, refraction and breaking is tested for incident wave conditions. Additionally the wave set-up and set-down and wave-driven longshore current is tested. Test 2 is carried out a longshore uniform bathymetry based on the experiments carried out by Van Gent *et al*. [2006]. A stationary wave condition is imposed on the offshore boundary with short waves with a wave height of 0.5m and period of 3.5s. The wave direction is set at 20° Cartesian convention. As in Test 1, no bound long waves are generated on the boundary. The water level on the model boundary is kept constant. Morphology and sediment transport are not calculated.

F.2 Results

A comparison is made between the wave height calculated in XBeach and the wave height calculated by means of the analytical approximation described in Appendix W. In this case refraction is added to the analytical approximation, but no further physical processes are added. Once again, wave breaking is simulated using the Roelvink formulation. The comparison between the wave heights in the middle transect can be seen in Figure 31. As in Test 1, XBeach corresponds well with the analytical solution until about 120m. In the nearshore the results differ until breaking becomes dominant. Figure 32 shows that XBeach correctly computes longshore uniform wave heights.

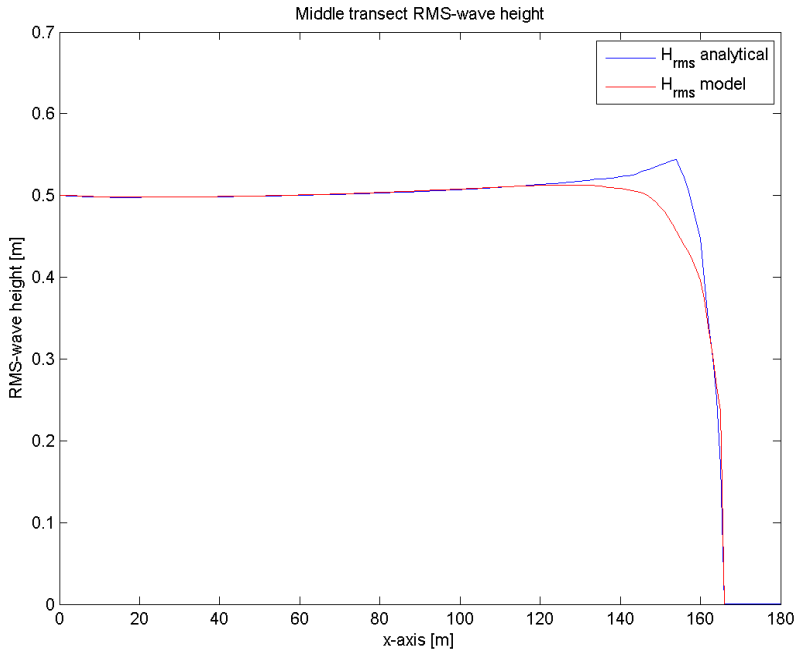


Figure 31 Wave height in middle transect in model and analytical approximation

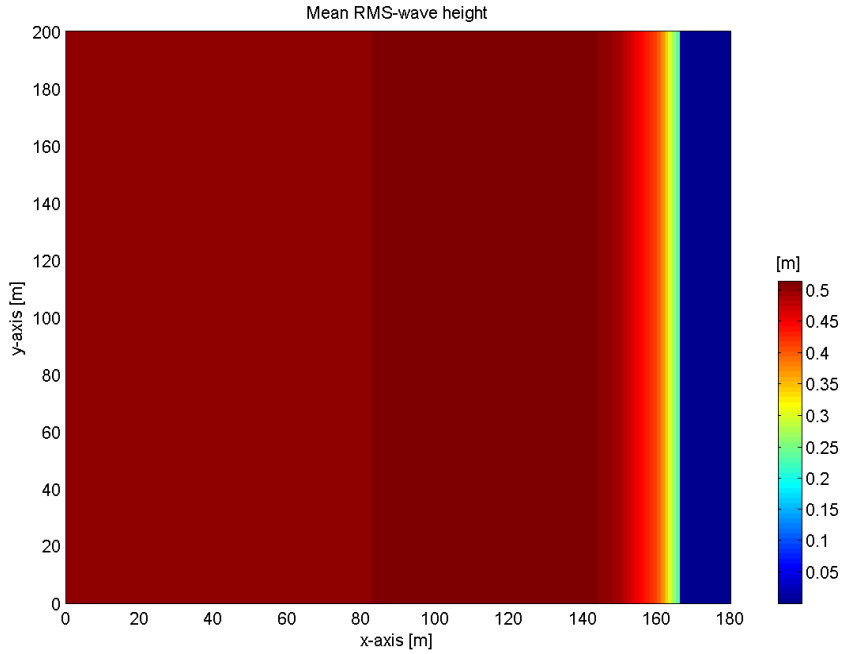


Figure 32 Time-averaged wave height over the model domain

The wave heights calculated by XBeach in Test 2 are compared to those of Test 1. The difference is shown in Figure 33 as a percentage of the wave height of Test 1. Although the wave heights of Test 2 are smaller in the entire model domain, the difference is less than would be expected using only the refraction coefficient. Referring to (A.17), the refraction coefficient is unity in Test 1. At the 140m longshore transect the refraction coefficient in Test 2 is 0.984, based on a wave angle of 14° at the 140m longshore transect. This would result in a 1.6% decrease in wave height; roughly double that shown in Figure 33. This discrepancy is most likely due to different shoaling coefficients in both models due to differing wave set-down and set-up levels and to the fact that XBeach includes non-linear dissipation of wave energy.

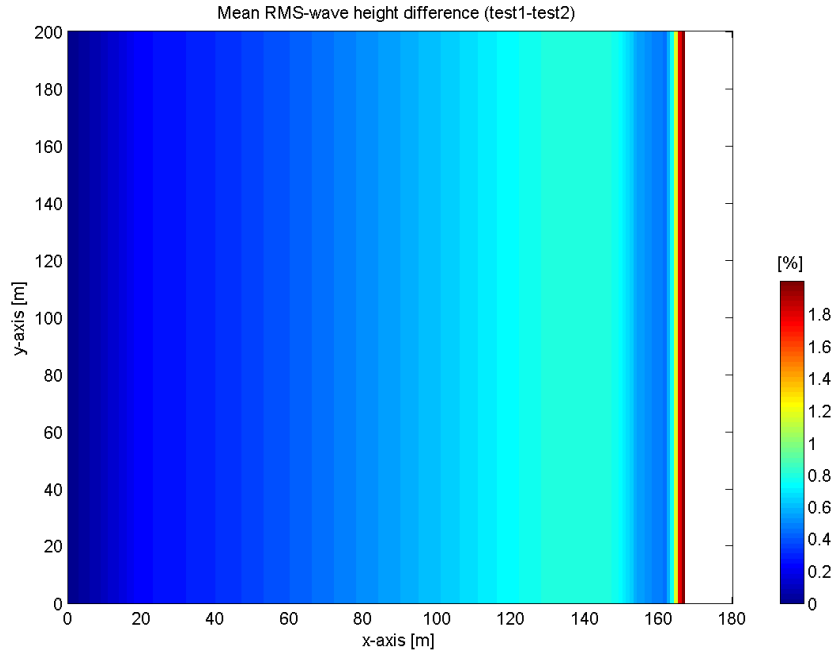


Figure 33 Time-averaged wave height difference between Test 1 and Test 2, in percentages of the wave height of Test 1

The refraction in the model is compared to the refraction calculated using the semi-analytical model described in Appendix W. The wave direction calculated by XBeach and by the semi-analytical model along the middle cross-shore transect is shown in Figure 34. Figure 35 correctly shows that the calculated refraction in XBeach is longshore uniform.

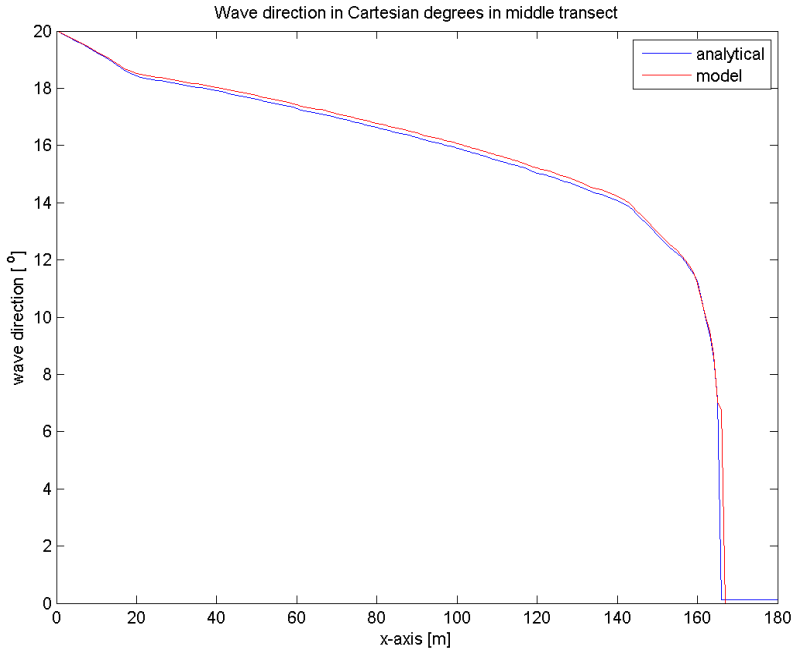


Figure 34 Wave direction along the middle transect in the model and according to the semi-analytical approximation

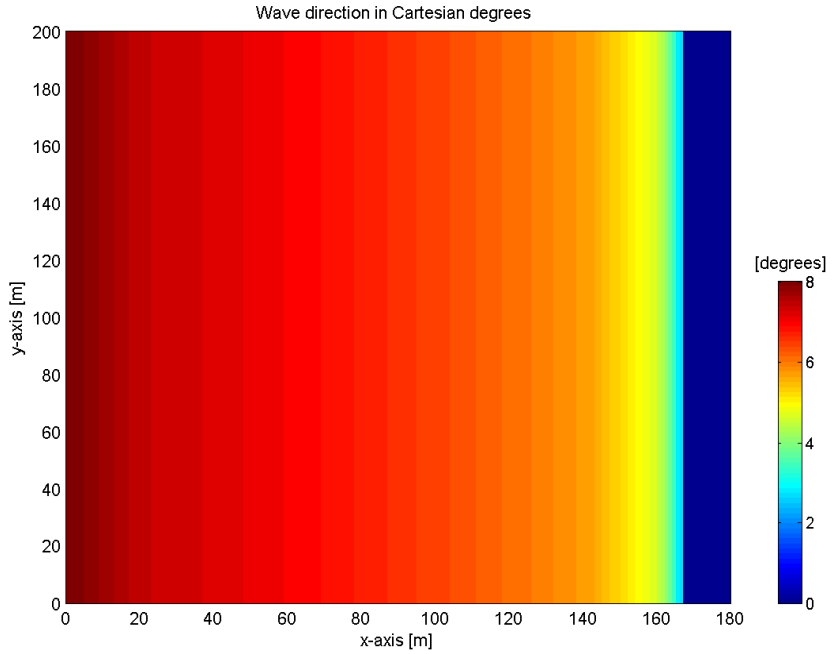


Figure 35 Wave direction across the model domain

The short-wave generated longshore current calculated by XBeach is shown in Figure 36. The maximum velocity at the shoreline is large due to the relatively high Chézy coefficient used in the model (65 $m^{½}s^{-1}$). The longshore velocity is longshore uniform.

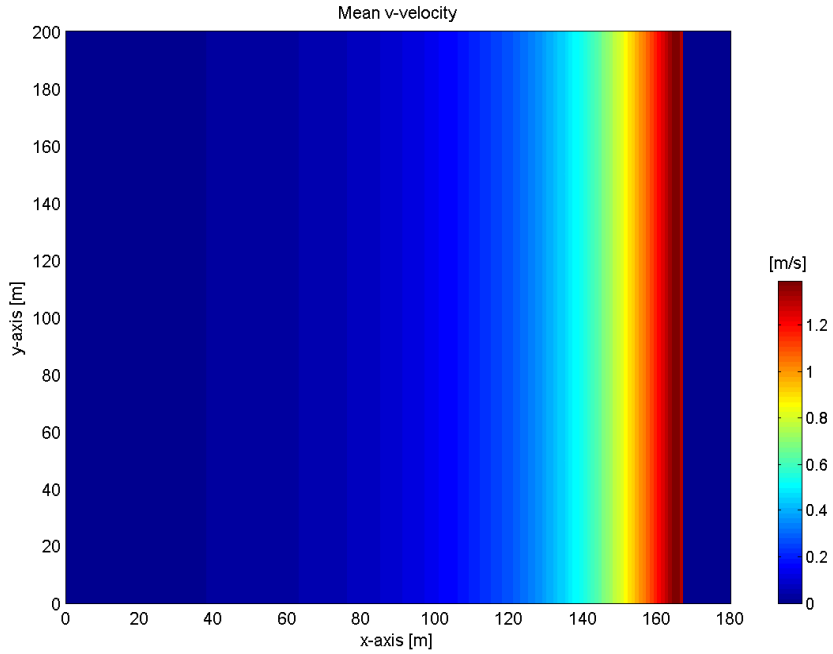


Figure 36 Short-wave generated longshore current across the model domain

The longshore velocity calculated in the XBeach model is compared to the velocity calculated using the semi-analytical model described in Appendix W. As can be seen in Figure 37, the longshore current calculated by XBeach is almost half that of the semi-analytical longshore current in the nearshore, and much larger in rest of the domain. One

major source of this discrepancy may be the use of horizontal viscosity in the XBeach model and not in the semi-analytical model. To analyse this difference, an XBeach simulation is run with horizontal viscosity turned off. The result of this run can also be seen in Figure 37. Note that the semi-analytical velocity shown in Figure 37 may not be entirely accurate due to inaccuracies in the numerical integration, see Appendix W.

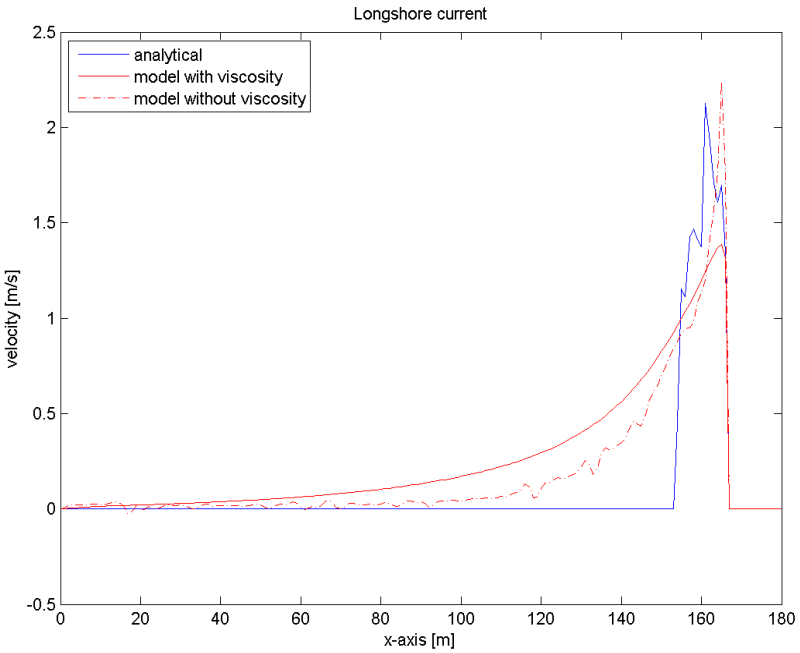


Figure 37 Short-wave generated longshore current along the middle cross-shore transect

The order of magnitude of the longshore velocity is the same between the semi-analytical calculations and the XBeach calculation without horizontal viscosity in the nearshore. Further offshore the velocity remains higher in the XBeach model. The reason for this difference is the discrepancy in the calculated radiation stress S_{yx} between the two models, see Figure 38.

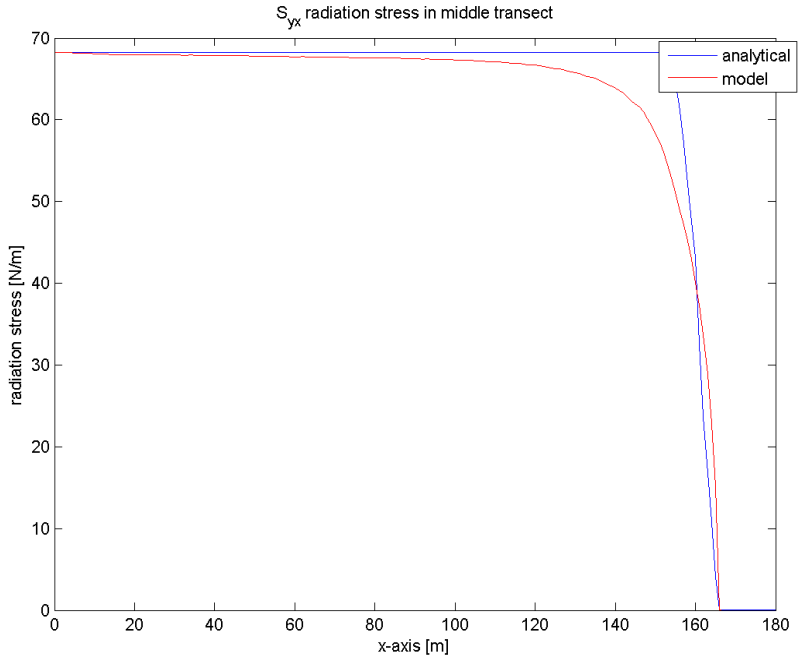


Figure 38 Short-radiation stress S_{yx} along the middle cross-shore transect

The difference between the radiation stress calculated in XBeach and the semi-analytical model is more difficult to explain. The radiation stress is determined by the wave angle, the wave energy and the ratio between the wave group velocity and wave celerity.
The wave angle has already been shown to be calculated correctly, see Figure 34. The wave group velocity – wave celerity ratio (n) is calculated correctly as shoaling is correct. This is supported by Figure 39.
The difference in wave energy, as can be seen in the different wave heights in Figure 31, may cause part of the discrepancy in radiation stress. However, this cannot be the sole explanation as the discrepancy occurs in areas where the wave height is equal.
It is suggested that the remaining difference in radiation stress may be due to the manner in which the mean wave direction is calculated from the energy density spectrum in XBeach.

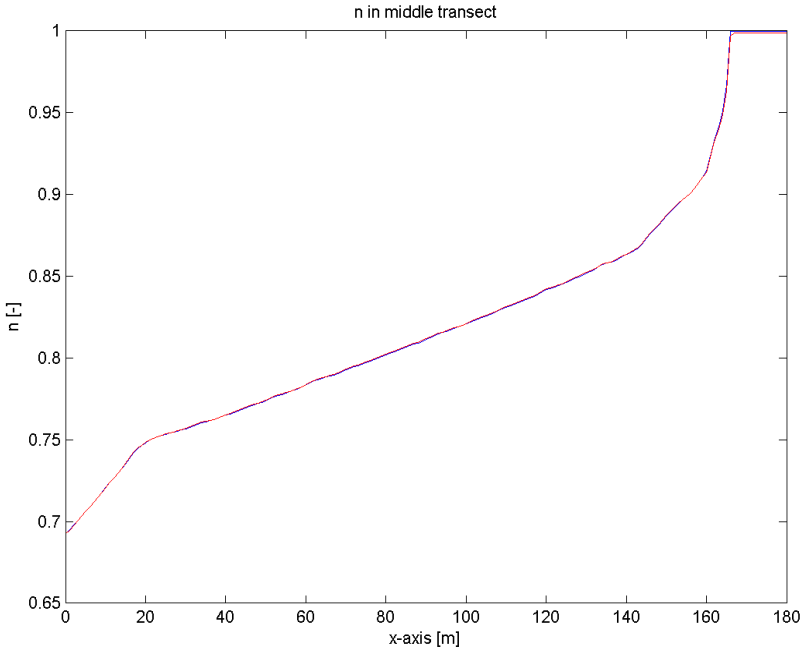


Figure 39 Ratio between wave group velocity and wave celerity along the middle cross-shore transect

F.3 Conclusions

It has been shown that XBeach handles refraction of short waves correctly, as well as shoaling of obliquely incident short waves. Very few differences exist between the results of XBeach calculations and the semi-analytical calculations.
The short-wave generated longshore current is shown to correspond well in order of magnitude to the semi-analytical current. Since the semi-analytical result is an approximation and not free of numerical errors, it is decided that the current in XBeach need not be incorrect.

G Test 3

G.1 Model description

In Test 3, the ability of XBeach to handle longshore non-uniform bathymetry is tested. The introduction of non-uniform bathymetry leads to longshore-varying short wave forcing and thus to quasi-stationary currents. The bathymetry used to carry out Test 3 is similar to the bathymetry of Test 1 and Test 2, but contains a bar in the nearshore, see Figure 40. An explanation of the bathymetry can be found in Appendix X. A stationary wave condition is imposed on the offshore boundary with short waves with a wave height of 0.5m and period of 3.5s. The wave direction is set at 0° Cartesian convention. As in Test 2, no bound long waves are generated on the boundary. The water level on the model boundary is kept constant. Morphology and sediment transport are not calculated.

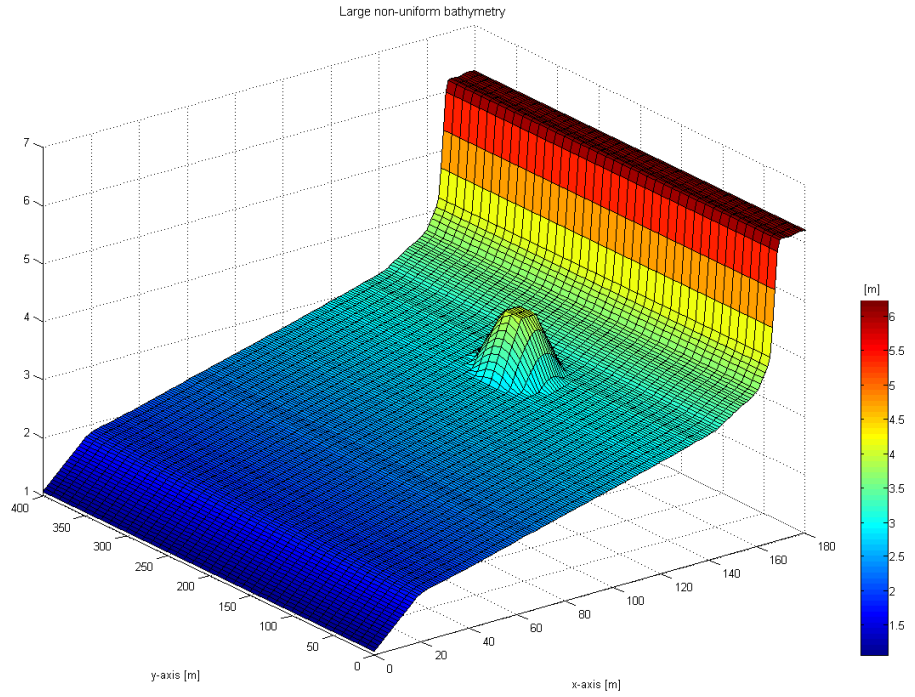


Figure 40 Bathymetry of Test 3

G.2 Results

Since no analytical solutions exist for wave hydrodynamics over longshore non-uniform bathymetries, no direct comparison can be made with the results of Test 3. Instead, the results are compared with calculations using the semi-analytical model explained in Appendix W, assuming the bathymetry of the cross section is longshore uniform. The differences are examined to see if they are plausible.

The wave height calculated in the XBeach model does not differ significantly from the semi-analytical solution, see Figure 41. In the middle cross shore transect, the wave height over the bar is lower in the XBeach calculation than in the semi-analytical, which is due to the energy dissipation term in XBeach and additional breaking due to lower water levels. At the shore face, the wave heights are equal again before breaking, despite the greater wave energy loss in XBeach over the bar. This may be due to the refraction of waves from outside the cross section. The wave height in the 270m cross shore transect does not differ significantly from the results obtained from Test 1.

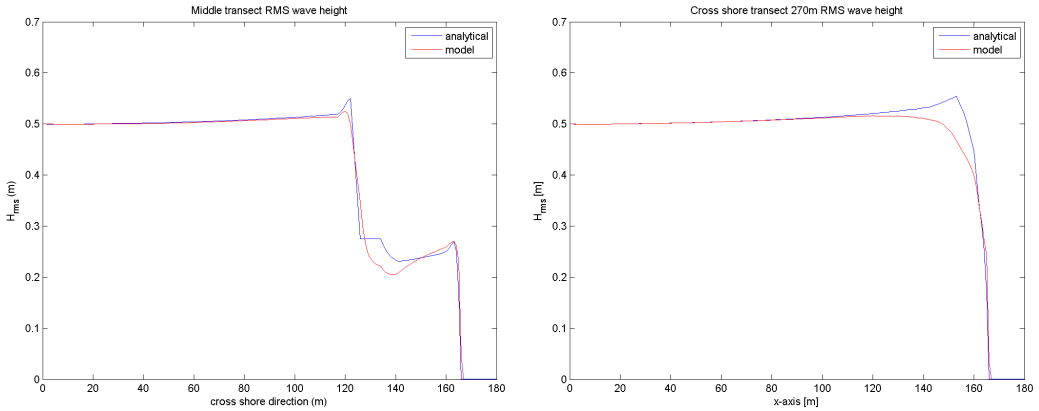


Figure 41 RMS-wave height in the middle cross-shore transect (left) and 270m cross shore transect (right) in the XBeach model and using the semi-analytical approximation

Two noticeable differences exist between the water level calculated in XBeach and those of the semi-analytical approximation. First is the water level over the bar. It can be explained that this is lower in XBeach, as the semi-analytical model assumes longshore uniformity. Therefore in the semi-analytical model the change in S_{xx} can be used to create a gradient in the water surface as the water has nowhere to go. In the XBeach model, the change in S_{xx} cannot be balanced by only a water surface gradient as the water can flow away round the bar. Instead the S_{xx} gradient is balanced by increased bed shear stress caused by higher flow velocities and a water surface gradient.

The second difference is the water level near shore in the 270m cross shore transect. In the XBeach model, the water level is slightly higher than in the semi-analytical model. This is most likely due to the influx of water from behind the bar, see Figure 46.

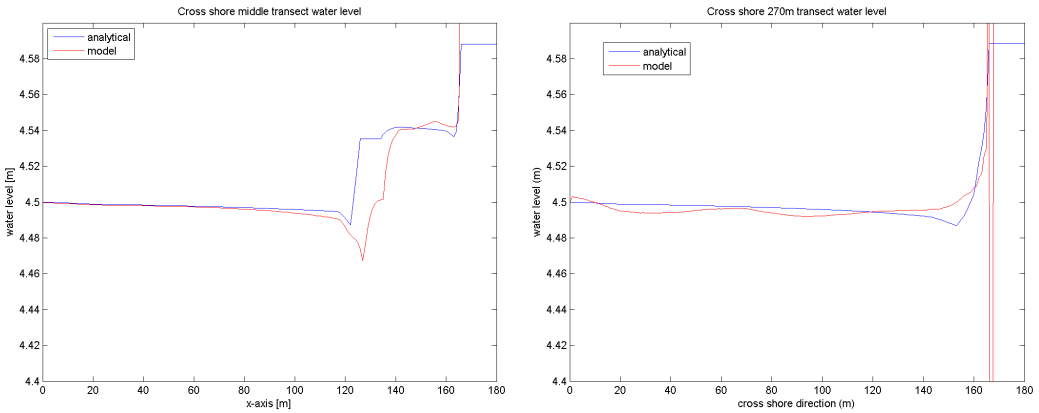


Figure 42 Water level in the middle cross-shore transect (left) and 270m cross shore transect (right) in the XBeach model and using the semi-analytical approximation

The refraction of wave energy around the bar can be seen in the contour lines of the RMS-wave height in Figure 43 and in the mean wave direction shown in Figure 44. The water surface elevation across the model domain is shown in Figure 45.

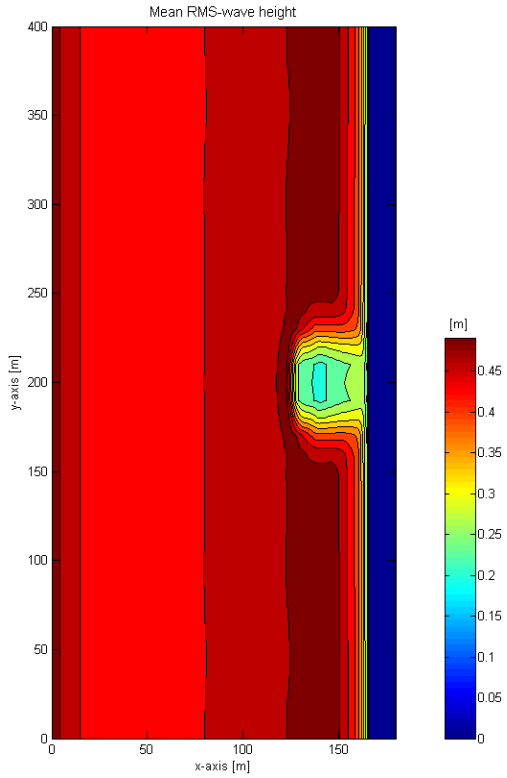


Figure 43 Stationary RMS-wave height across the model domain

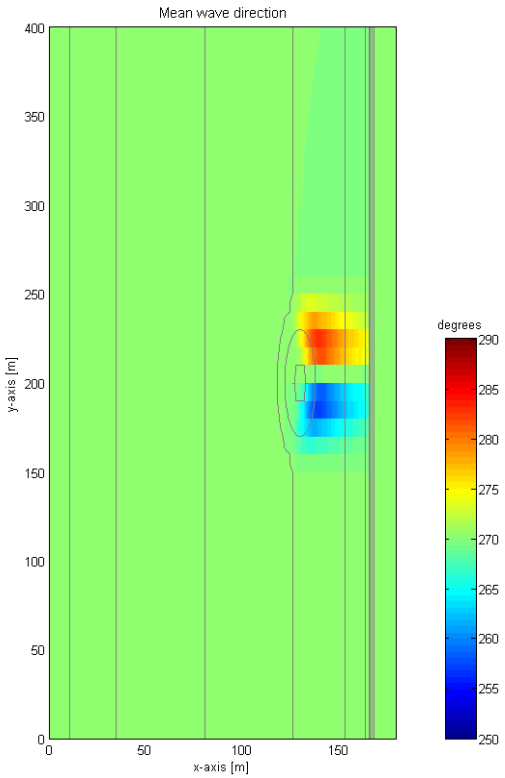


Figure 44 Stationary mean wave direction across the model domain

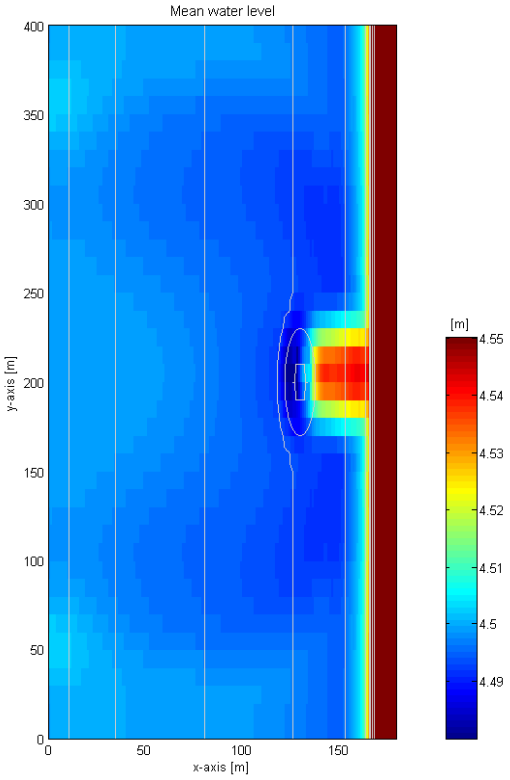


Figure 45 Stationary water surface level across the model domain

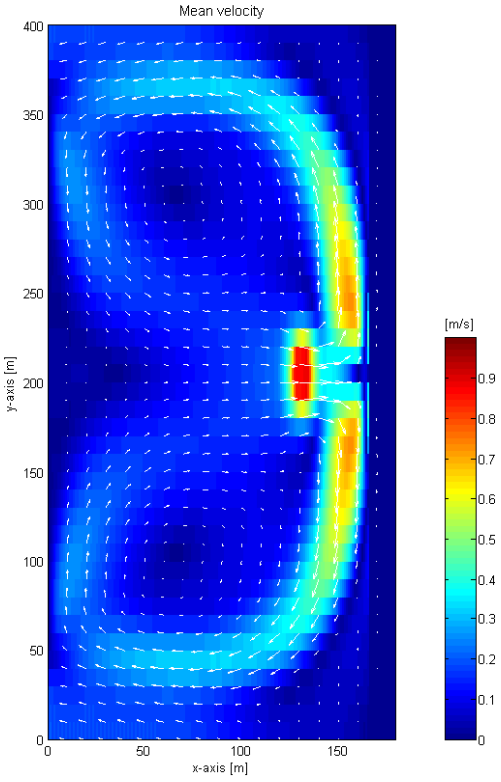


Figure 46 Stationary current velocities in the model domain

Although the results shown in Figure 43, Figure 44 and Figure 45 will not be analysed quantitatively, the results are qualitatively correct. Wave refraction will occur round a bar, leading to higher wave heights behind the bar than without refraction. In general however, the wave heights behind the bar are smaller than elsewhere due to the large energy loss due to breaking and, to a lesser degree, dissipation.
The water level behind the bar will be higher than elsewhere due to the large negative spatial gradient in S_{xx} over the bar. This gradient is compensated by high current velocities pumping water into the area behind the bar. In order for this water to flow away for conservation of mass behind the bar, a water level gradient must be formed with the adjacent areas. The water level behind the bar must therefore be higher behind the bar than in the adjacent areas.

The currents generated by the gradients in the short wave radiation stresses are shown in Figure 46. The model clearly shows two symmetrical circulation cells, transporting water from behind the bar to the front of the bar. From there water is pumped over the bar by the large gradient in S_{xx} explained earlier.

G.3 Conclusions

The hydrodynamic processes related to wave breaking over a non-longshore uniform bathymetry appear to be qualitatively well modelled in XBeach. The model shows no instabilities or unnatural behaviour during the simulations. Although the model is not

quantitatively verified, the model is assumed to be capable of modelling prototype situations with varying bathymetry.

H Test 3g

H.1 Model description

In Test 3g, the influence of the grid size on the numerical result is analysed. Three simulations are run. The first simulation (Test 3g0) uses the regularly-spaced numerical grid of Test 3. The second simulation (Test 3g1) also uses a regularly-spaced grid, but with a resolution twice as large as that of Test 3. The third simulation (Test 3g2) uses an irregularly-spaced numerical grid. All three bathymetry grids can be found in Appendix X.
A stationary wave condition is imposed on the offshore boundary with short waves with a wave height of 0.5m and period of 3.5s. The wave direction is set at 0° Cartesian convention. The water level on the model boundary is kept constant. Morphology and sediment transport are not calculated.

H.2 Results

As can be seen in Figure 47, the wave heights of the short waves in all three simulations are very similar. This shows once again how insensitive the short wave propagation scheme is to changes in numerical grid sizes.
Figure 48 shows the mean water level across the model domain. The only noticeable difference between the simulations is the level of detail of the area of wave set-up behind the shoal. In the coarse grid run, Test 3g0, the grid resolution is not great enough to fully resolve the shape of the set-up area.
The calculated velocities and current patterns, see Figure 49, are the same in all three simulations.

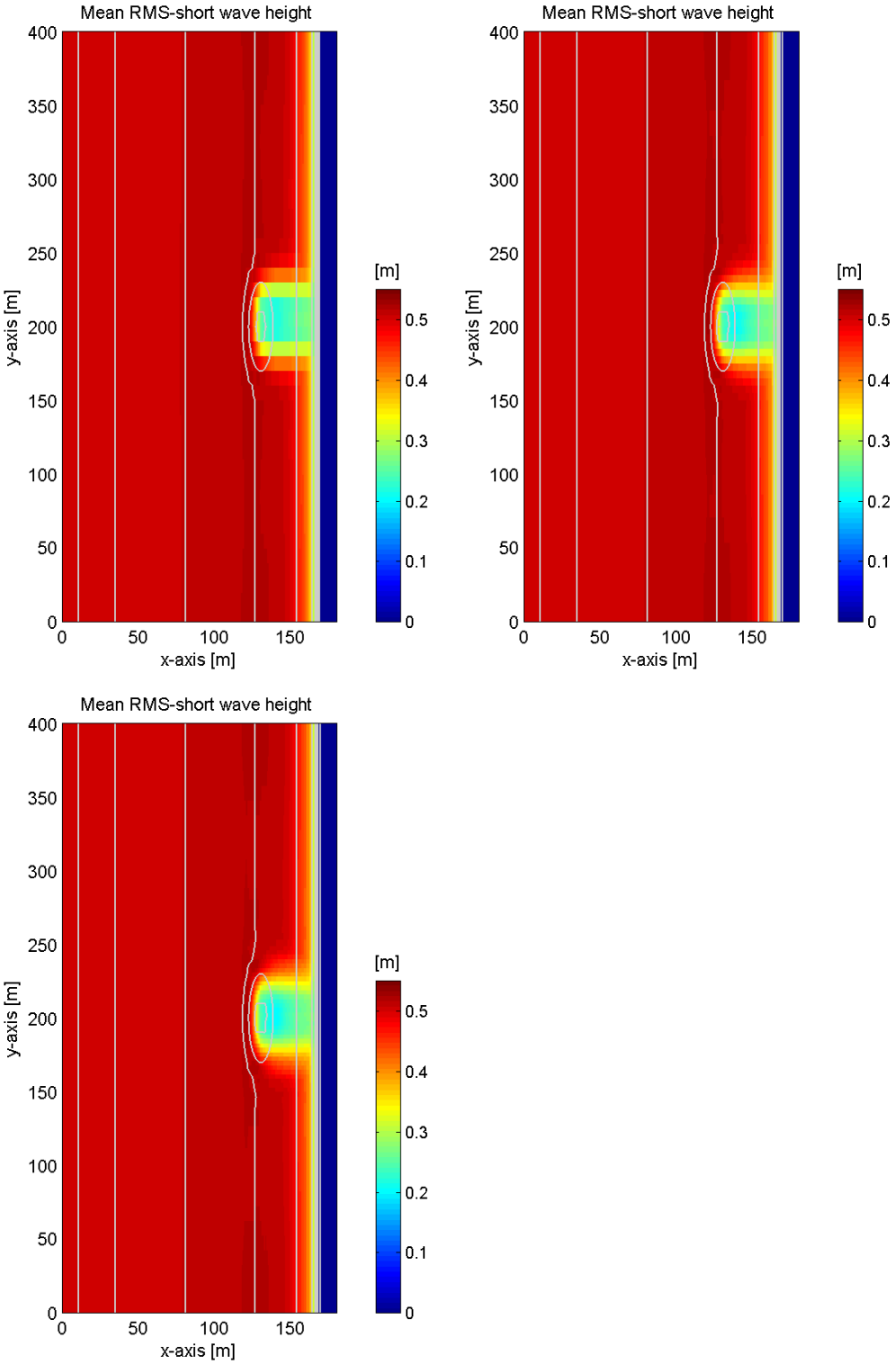


Figure 47 RMS-wave height in Test 3g0 (top left), Test 3g1 (top right) and Test 3g2 (bottom)

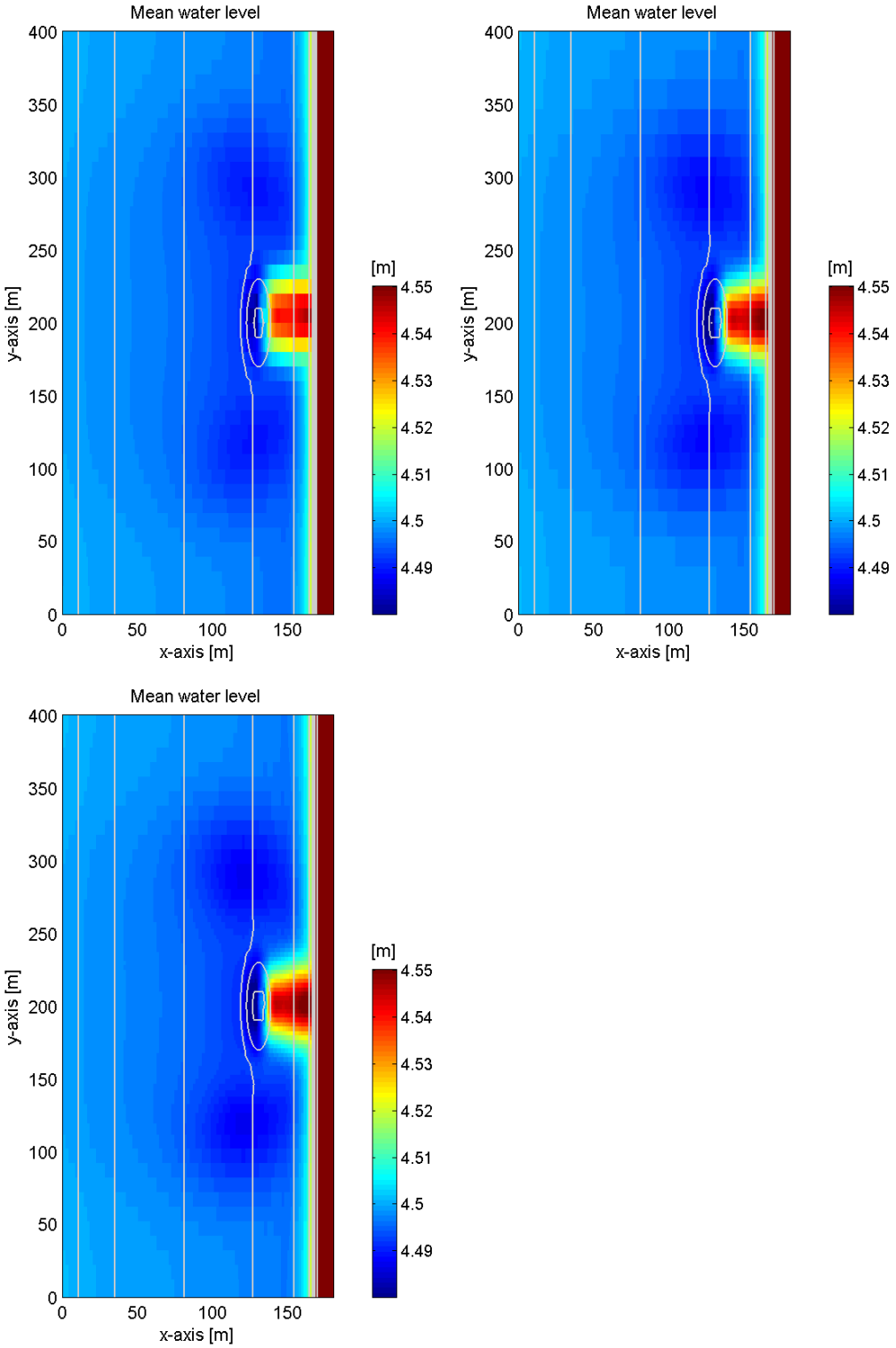


Figure 48 Water level in Test 3g0 (top left), Test 3g1 (top right) and Test 3g2 (bottom)

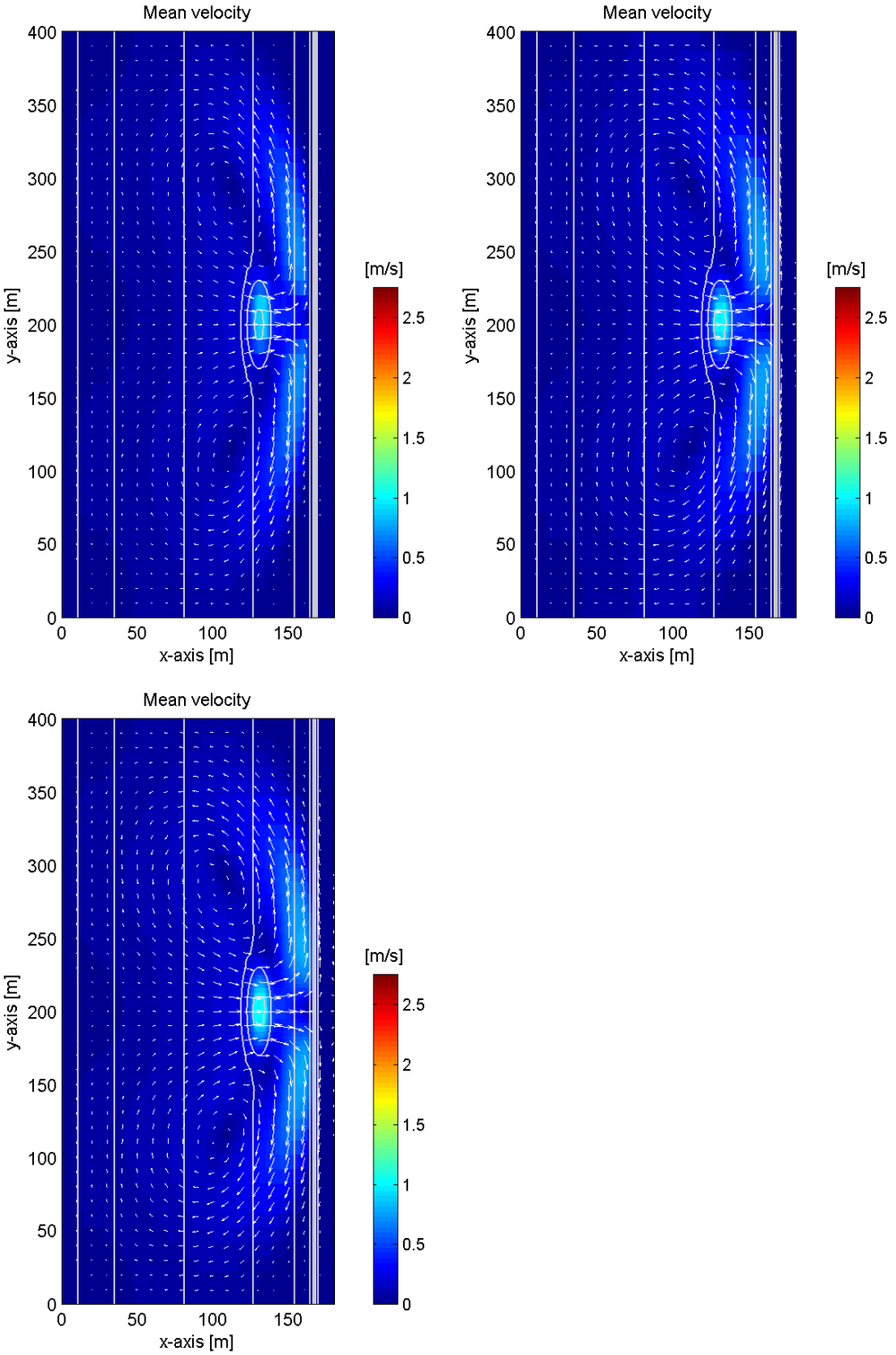


Figure 49 Lagrangian velocity in Test 3g0 (top left), Test 3g1 (top right) and Test 3g2 (bottom)

H.3 Instabilities

The results shown in section H.2 are based on the quasi-stationary conditions the models reach after the spin-up time. However, if the models are left to run for longer periods, they become unstable and start to flood. Slowly the mean water level in the model increases, see Figure 50. Flooding appears to be coming in from the lateral boundaries and leaving through the offshore boundary, see Figure 51. It is thought that this flux across the lateral boundaries may be caused by the application of the Neumann uniformity assumption in a situation in which longshore uniformity in forcing is not the case.

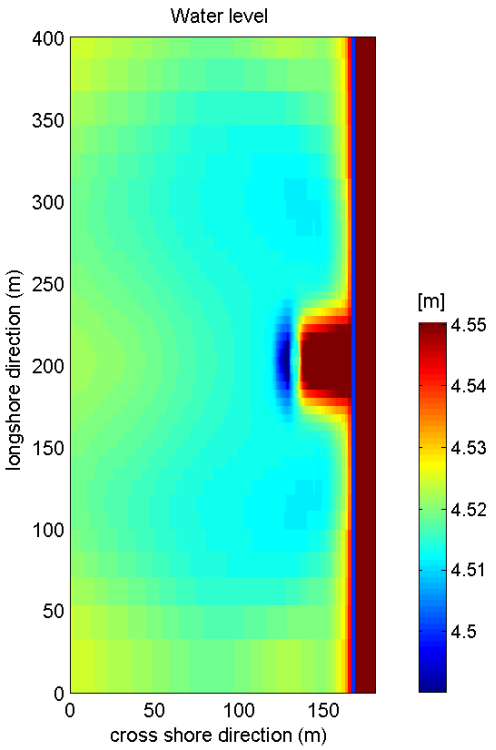


Figure 50 Water level after long calculation time, flooding is evident from the overall higher water levels, c.f. Figure 48

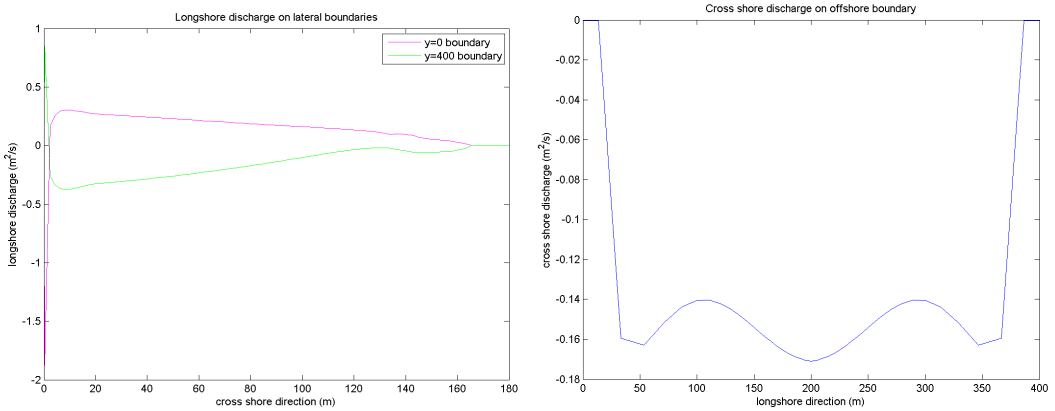


Figure 51 Mean longshore velocity on the lateral boundaries after the quasi-stationary state (left panel) and mean cross shore discharge on the offshore boundary (right panel)

H.4 Conclusions

In general Test 3g0, Test 3g1 and Test 3g2 show that XBeach is capable of handling complex hydrodynamics on varying grid resolutions. However, the tests also show that the model can become unstable after a certain period of time, possibly due to improper model assumptions on the lateral boundaries. At this stage it is unclear if the instability will affect the model in prototype usage as other processes, for instance wave driven and tidal longshore currents, may suppress the instability at the lateral boundaries.

I Test 3s

I.1 Model description

In Test 3s, the ability of XBeach to handle stationary waves and tidal surge simultaneously is analysed. This combination does not include any physical processes that have not already been tested. It does however require greater numerical stability at the model boundaries. The XBeach model will therefore be examined for the stability of the results.
A stationary wave condition is imposed on the offshore boundary with a short-wave wave height of 0.5m and period of 3.5s. The wave direction is set at 20° Cartesian convention. A sinusoidal longshore uniform tide level with a six hour period is imposed on the model domain. Morphology and sediment transport are not calculated.

I.2 Results

The water level in the XBeach model near the offshore boundary is shown relative to the imposed water level in Figure 52. Figure 53 shows the modelled RMS-wave height near the offshore boundary over time.

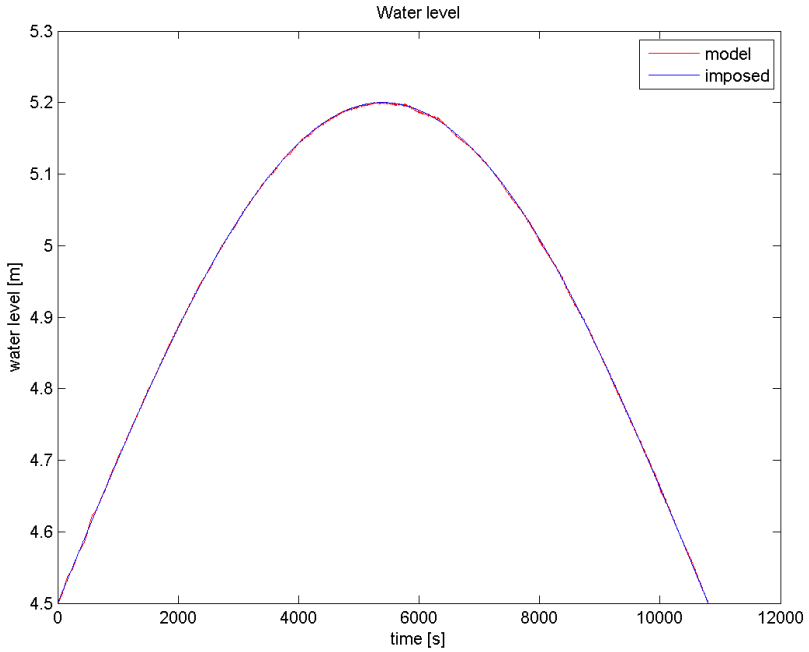


Figure 52 Modelled water level near the offshore boundary and imposed water level over time

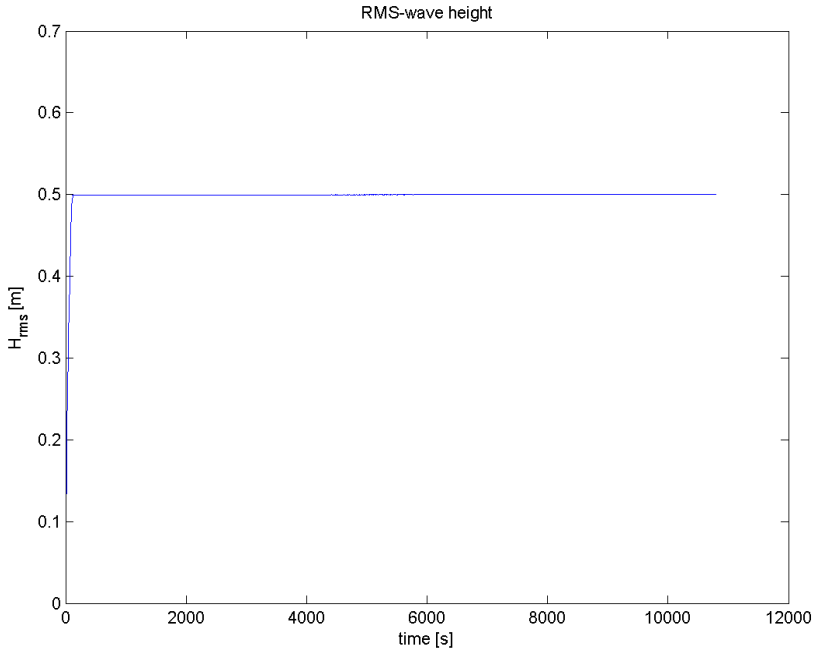


Figure 53 Modelled RMS-wave height near the offshore boundary in time

I.3 Conclusions

It can be concluded that XBeach can adequately handle varying tide levels and stationary wave conditions simultaneously.

J Test 4

J.1 Model description

In Test 4 the ability of XBeach to handle time varying short-wave forcing is examined. Due to the variation of the wave height of the short-waves on the period of incident wave groups, infragravity waves will be generated. These waves will be expressed in the model by a varying water level and additional cross-shore and longshore currents.
The model is set-up using the longshore uniform bathymetry used in Test 1. A non-stationary wave condition is imposed on the offshore boundary. The wave heights of the short-waves vary according to regular sinusoidal wave groups with a period of 24.5s. The maximum short-wave wave height is 0.5m and the short-wave wave period is 3.5s. The wave direction is set at 0° Cartesian convention. The directional spreading of the short-waves is such that the waves are long-crested. The water level on the model boundary is kept constant. Morphology and sediment transport are not calculated.

J.2 Results

The instantaneous RMS-wave height, water surface level and velocities are compared in Figure 54. Two wave groups can be seen in the top panel of the figure. One with a maximum at roughly 40m and one with a maximum at 120m cross shore distance. The wave height between these two groups varies approximately sinusoidally. Shoreward of the leading wave group, the wave height differs from the sinusoidal relation due to strong shoaling and breaking.
The water surface level in the middle panel shows a maximum between the two wave group maxima, at roughly 90m cross shore distance. As can be seen in the figure, the maximum water level is located slightly shoreward of the minimum short-wave wave height. This is likely to be the result of the interaction with a standing wave created by the infragravity waves against the shore. The standing wave envelope is shown in Figure 55. The infragravity wave height envelope at the shoreline is in the order of one decimetre, which corresponds with values found in literature; see Chapter 2 of the main report.
The bottom panel of Figure 54 shows the absolute velocities and their direction. The highest velocities occur in the nearshore, where the leading infragravity wave is starting to run-up the beach, see also Figure 55. Other velocity fields are directed towards the crest of the second infragravity wave, as to be expected considering normal wave theory.

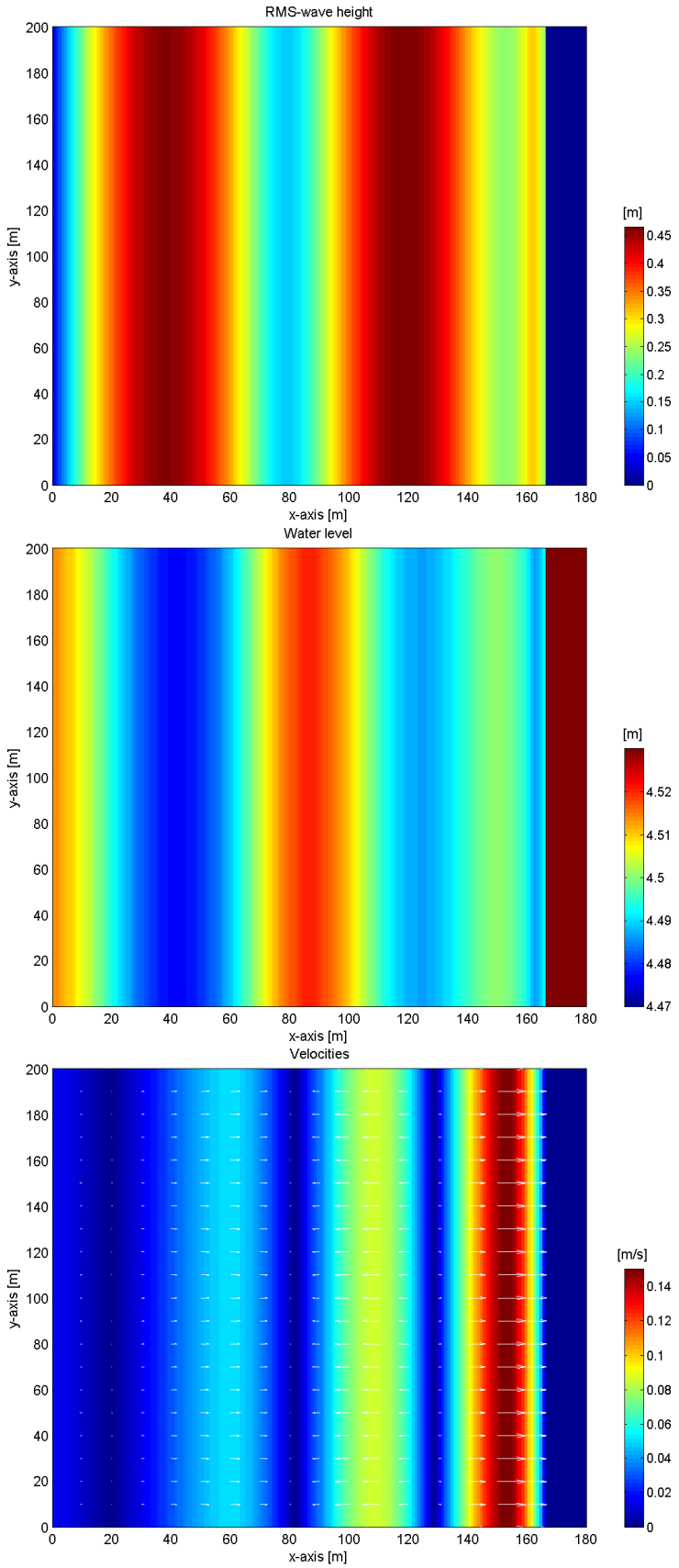


Figure 54 Snapshot of the RMS-wave height (top panel), water level (middle panel) and velocities (bottom panel)

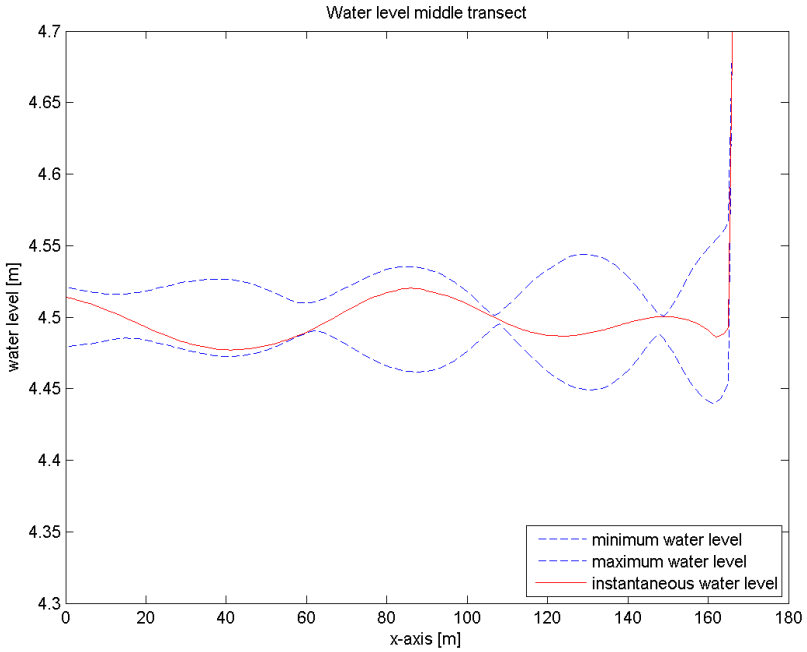


Figure 55 Water level envelope and instantaneous water level. Nodes and antinodes in the water level envelope suggest a partial standing wave on the scale of infragravity waves

The RMS-wave height, water level and velocities are examined for a period greater than one wave group period to study the average hydraulic conditions. In this case the averaging period chosen is 22 wave group periods (539s).
The average RMS-wave height over this period is shown in the top panel of Figure 56. It is immediately clear that the average wave height of the short waves on the offshore boundary is less than 0.5m. This appears to be caused by a minor error in the boundary condition routine in XBeach. The short-waves shoal to approximately 0.4m height and then start breaking at the shore face. The result is similar to that shown for the stationary conditions of Test 1, see Figure 19.

The water level in the middle panel of Figure 56 also follows a similar line to that of Test 1. In this case the point of maximum average set-down is closer to shore than in the stationary case. This is directly related to the fact that the position of the breakpoint of the short-waves is closer to shore in the non-stationary case.

The mean Lagrangian velocities, shown in the bottom panel of Figure 56, are greatest on the shore face. The velocities there are in the order of 2-5 mm/s and are directed offshore due to the dominance of the Eulerian velocity. The variations in velocities in the rest of the model correspond to the nodes and anti-nodes in the water surface level, see Figure 55. There is an apparent onshore residual velocity in the deeper areas of the model, Stokes drift. This drift is greater under the anti-nodes of the water surface level than under the nodes.

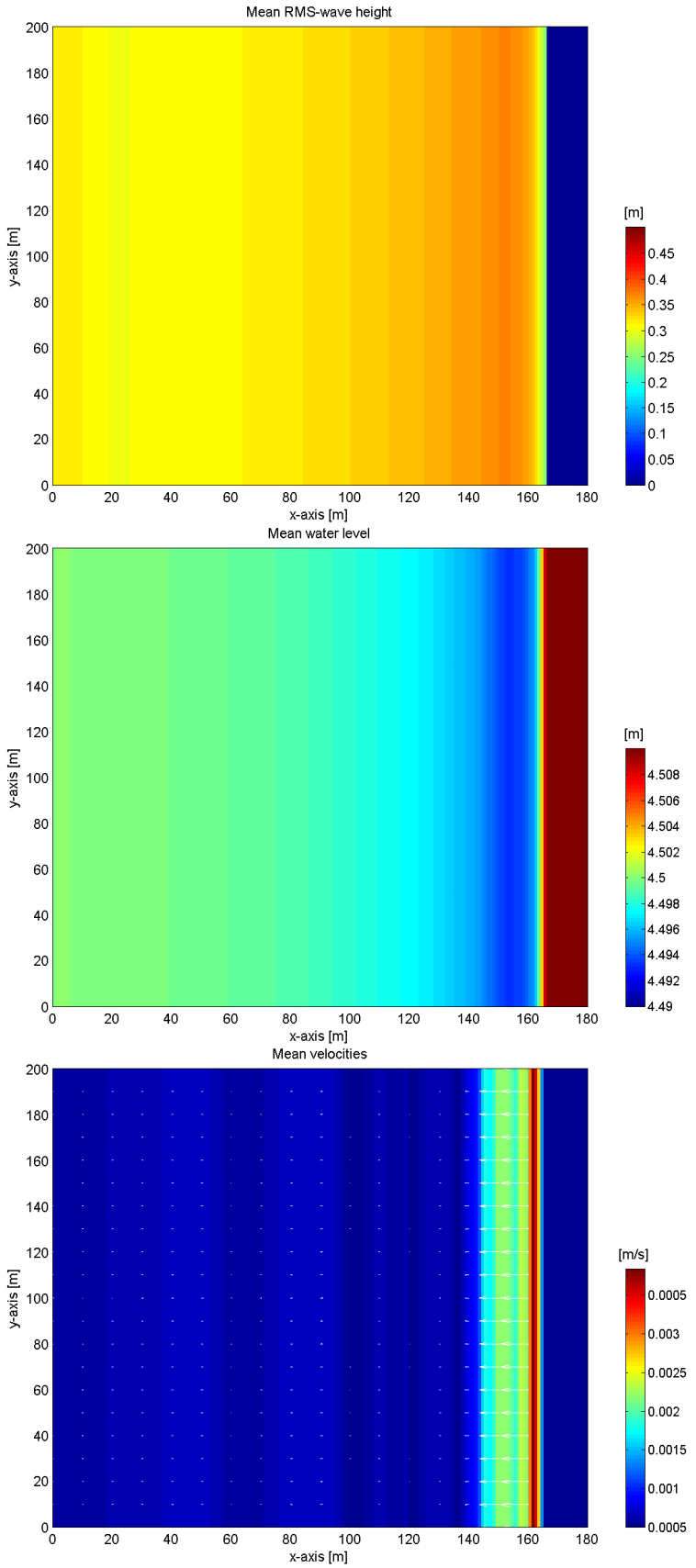


Figure 56 RMS-wave height (top panel), water level (middle panel) and velocities (bottom panel), averaged over 22 wave group periods

J.3 Conclusions

Even though no comparisons are made between the results of the XBeach simulation and analytical models or physical measurements, it can be concluded that XBeach appears to handle infragravity waves correctly. That is to say that the results of XBeach correspond with the physics of infragravity waves as known in literature. Further verification of the results must take place using laboratory or field measurements.

K Test 5

K.1 Model description

In Test 5 the ability of XBeach to handle time varying short-wave forcing in combination with non-uniform longshore bathymetry is examined. Infragravity waves will be generated by variation in short-wave forcing.
The model is set-up using the longshore non-uniform bathymetry used in Test 3. A non-stationary wave condition is imposed on the offshore boundary. The short-waves vary according to regular sinusoidal wave groups with a period of 24.5s. The maximum short-wave wave height is 0.5m and the short-wave wave period is 3.5s. The wave direction is set at 0° Cartesian convention. The directional spreading of the short-waves is such that the waves are long-crested. The water level on the model boundary is kept constant. Morphology and sediment transport are not calculated.

K.2 Results

The short-wave RMS-wave height and water surface elevation are compared for one instant in time. This is shown in Figure 57. As was the case for Test 4, the incoming short-wave envelope shows a strong negative correlation with the water surface level. The water surface level offshore of the shoal appears to have lower amplitudes than in the cross sections without the shoal. This is confirmed by Figure 58, in which the amplitude of the water surface envelope over 22 wave group periods is shown. This effect may be due to different standing wave conditions due to the presence of the shoal.

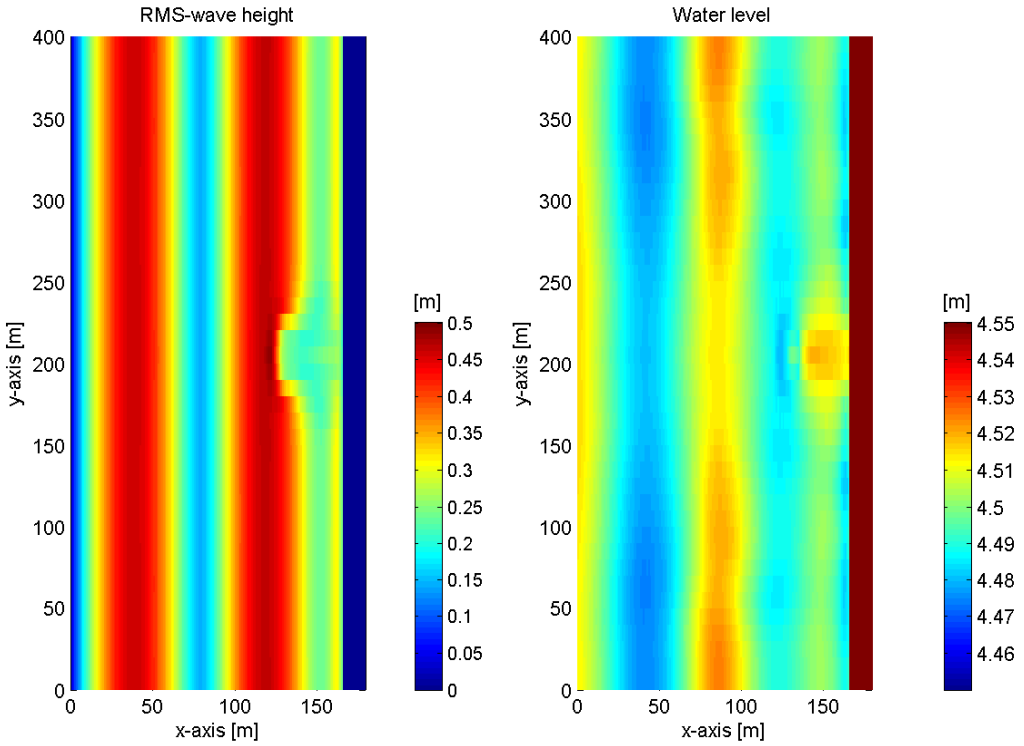


Figure 57 Instantaneous RMS-wave height (left panel), water surface level (right panel)

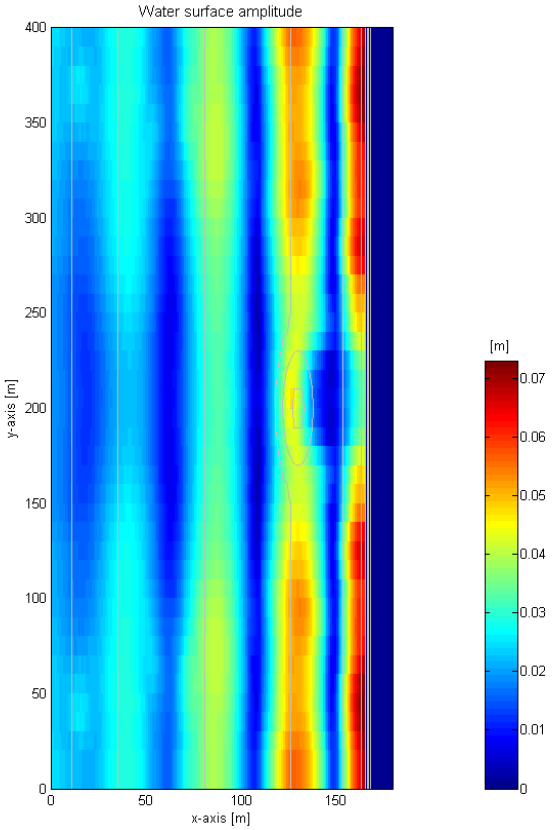


Figure 58 Water surface amplitude, calculated over 22 wave group periods

To gain more insight into the hydrodynamics in the model, several model output variables are averaged over 22 wave group periods. The results can be seen in Figure 59.
The wave height of the short waves differs little from the case of stationary waves in Test 3. The short waves break over the shoal in the same manner as in the stationary case and refract behind the shoal. A similar, but lower, wave set-up occurs behind the shoal and wave set-down occurs offshore of the shoal. The reason that the wave set-up and set-down is lower, is most likely due to lower average short-wave wave heights in the area, and thus lower wave energy density gradients. Wave refraction around the shoal is in the same order as the stationary case. The cross-shore and longshore gradients in the water surface level create circulation patterns similar to those shown in Test 3, with slightly lower velocities. Once again this difference is probably caused by lower incident short waves.

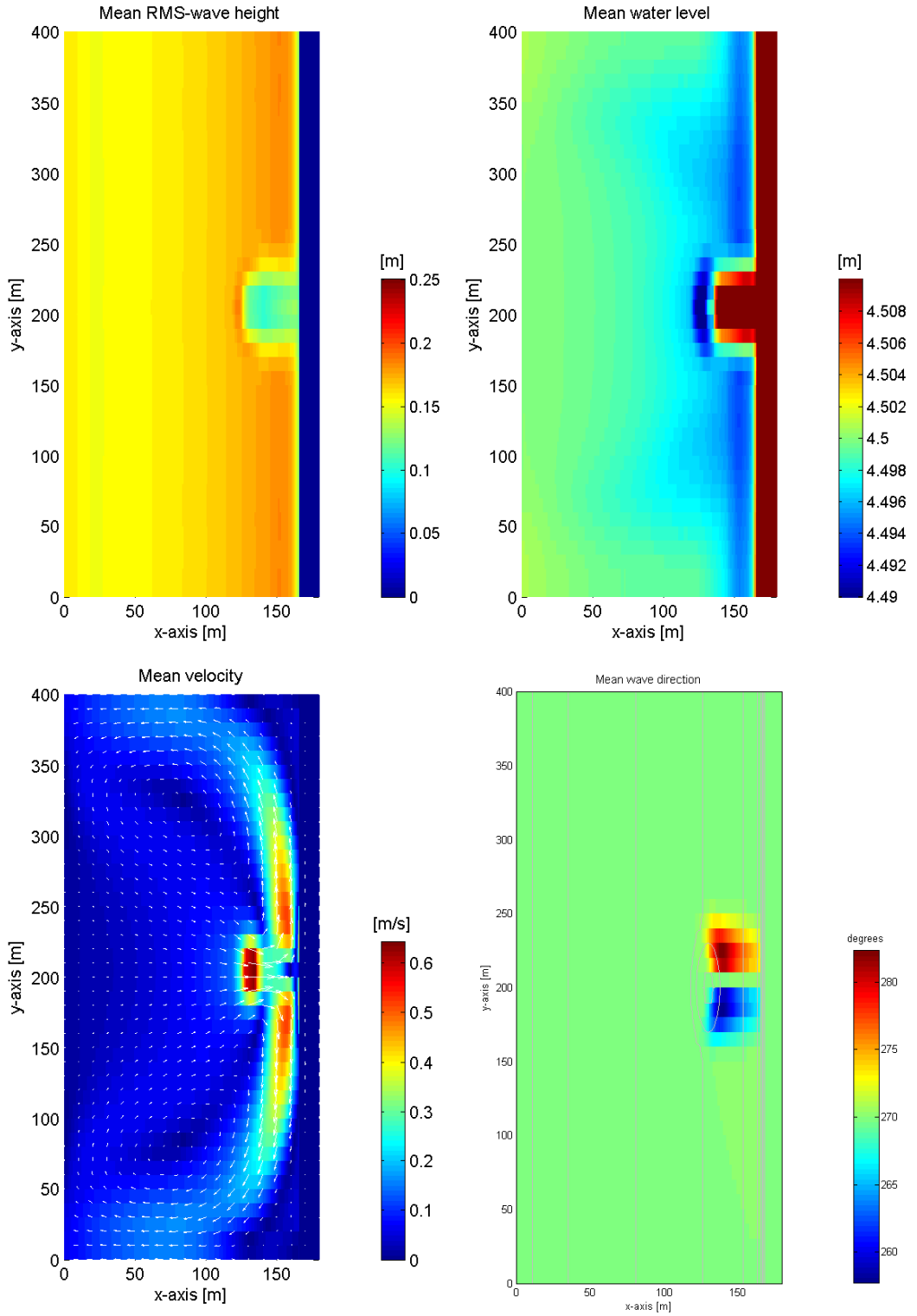


Figure 59 RMS-wave height (top left panel), water surface level (top right panel), velocities (bottom left panel) and mean wave direction, nautical convention (bottom right panel), averaged over 22 wave group periods

K.3 Conclusions

XBeach appears to produce results that are both numerically stable and physically plausible. The main problem that still remains in the XBeach model is the assumption of simple Neumann condition lateral boundaries. As can be seen in Figure 59, the longshore non-uniformity creates circulation cells, which reach all the way to the lateral edges. Such circulation is clearly not compatible with the Neumann assumption of longshore uniformity across the lateral boundaries. In this case, the use of simple Neumann boundaries for the cross-shore velocity and water level causes the circulation cell to become confined within the model domain. Depending on the amount of eddy viscosity and bed friction, this may or may not be realistic in a physical sense. The results however clearly suggest that careful consideration is needed to ensure the model domain stretches far enough beyond the region of interest.

L Test 6

L.1 Model description

XBeach has already been shown to deal with currents caused by non-uniform bathymetry. In Test 6, it is assessed whether XBeach can handle time-varying currents generated by obliquely incident short waves and wave groups.
The model is set-up using the longshore non-uniform bathymetry used in Test 3. A non-stationary wave condition is imposed on the offshore boundary. The short-waves vary according to regular sinusoidal wave groups with a period of 24.5s. The maximum short-wave wave height is 0.5m and the short-wave wave period is 3.5s. The wave direction is set at 20° Cartesian convention. The directional spreading of the short-waves is such that the waves are long-crested. The water level on the model boundary is kept constant. Morphology and sediment transport are not calculated.

L.2 Results

The incoming wave groups and the water surface elevation caused by wave forcing are shown for one instant in time in Figure 60. A small amount of numerical diffraction can be seen in the short wave RMS-wave height along the southern lateral boundary. In general however, the incoming wave groups maintain their long-crestedness well. The water surface elevation has a distinct checkerboard pattern. This pattern is caused by the interaction of incoming and reflected infragravity waves. The process is illustrated in Figure 61 in which the position and direction of two incoming infragravity wave crests and two reflected infragravity wave crests are shown. Maxima in the water surface level occur in areas where two wave crests interact, minima where two wave troughs interact. As in Test 4 and Test 5, the incoming and reflected infragravity waves create a standing wave pattern that manifests itself in regions of high and low water surface amplitude, shown in Figure 62. It is interesting to note that the standing wave pattern differs little from the wave pattern in Test 4 and Test 5. The only major difference is a greater longshore variation in the standing wave amplitudes. The nodes and antinodes however remain in roughly the same cross shore position.

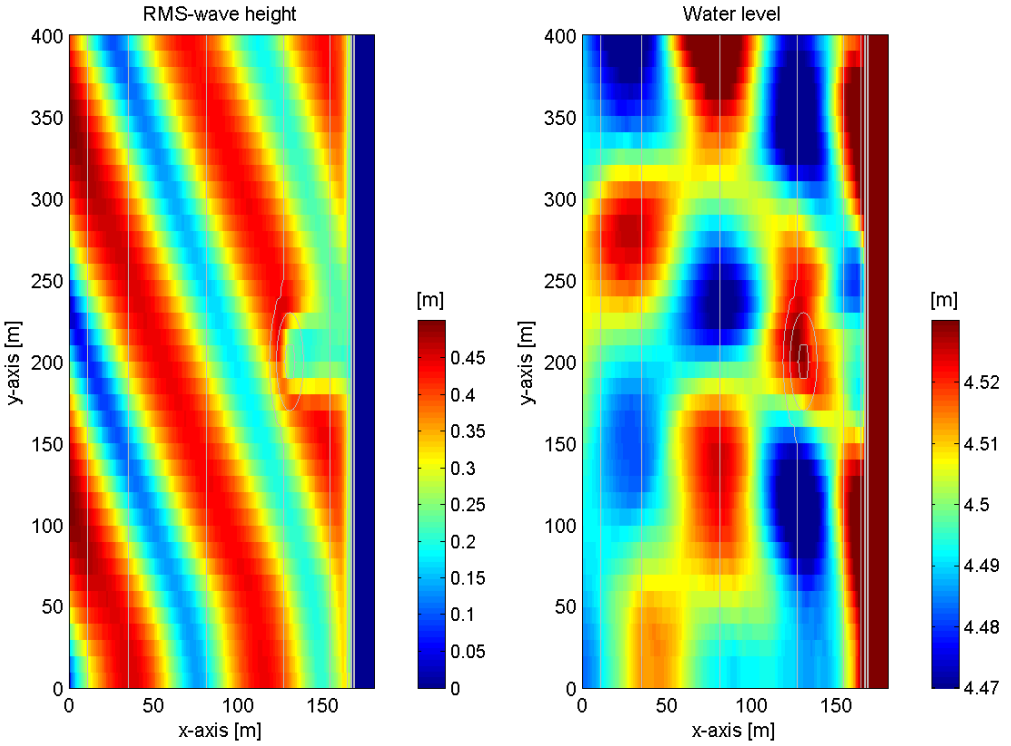


Figure 60 Instantaneous RMS-wave height (left panel), water surface level (right panel)

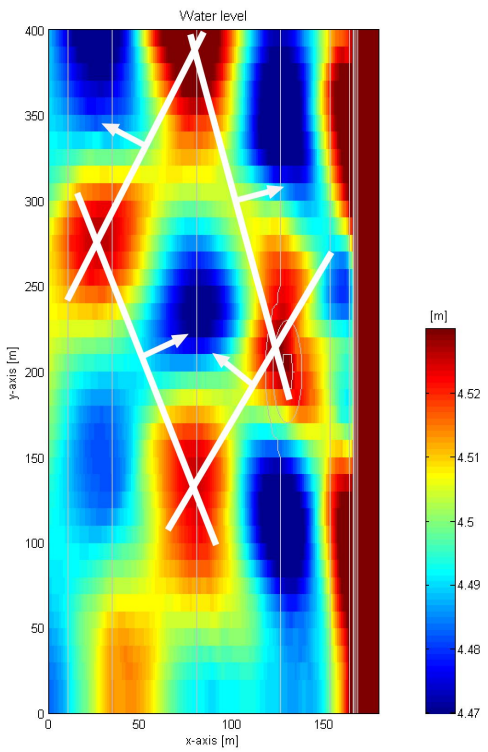


Figure 61 Incoming and reflected infragravity wave crests

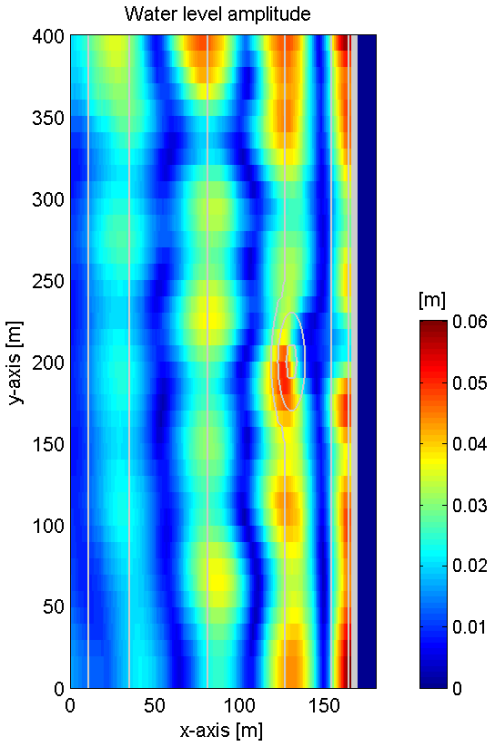


Figure 62 Water surface amplitude, calculated over 12 wave group periods

A comparison between Test 5 (Figure 59) and Test 6 (Figure 63) shows that the mean short-wave wave height is similar in both cases. As already shown for stationary cases, the short-wave wave height in the case of obliquely incident waves should be lower than for normally incident waves. This is also true for the difference between Test 5 and Test 6. The short-wave wave height is less uniform in longshore direction in Test 6 than in Test 5. This may be due to non-linear interactions between the water depth and wave height. As seen in Figure 62, the water surface amplitude is not longshore uniform in Test 6 as it is in Test 5.
It can be seen in Figure 63, that despite the variations in surface level amplitude, the mean water level over 12 wave group periods appears to be independent of the standing infragravity wave nodes and antinodes. The mean water level compares well to the mean water level of Test 5, with the exception of less wave set-down near the coast and around the shoal. The lesser set-down is likely due to lower values of S_{xx} due to obliquely incident waves.
The mean current pattern of Test 6 differs strongly from that Test 5. The main difference is of course the inclusion of a short-wave generated longshore current in the breaker zone. It can be seen however that this current disturbs the generation of two symmetrical circulation cells around the shoal. The disturbance is twofold. Up drift of the shoal, in the sense of the longshore current, there is a deficit in the longshore current. This is because behind the shoal, the cross-shore change in S_{xy} is small compared to areas not sheltered by a shoal and thus limited longshore current. Up drift of the shoal, the change in S_{xy} is large again, thus there is potential for more longshore current. The deficit is balanced by diversion of current off the shoal that would enter the up drift circulation cell in Test 5, to the longshore current up drift of the shoal. The circulation over the shoal is now entirely fed by the down drift circulation cell. This cell forces itself past the longshore current behind the shoal, thus causing an obstruction to the longshore current. As not all the longshore current can pass behind the shoal, some is diverted to the down drift circulation cell. The process described here is highly dependent on the amount of horizontal eddy viscosity. In the current simulation, the horizontal eddy viscosity coefficient is set at 0.1 m^2s^{-1}. Setting the viscosity to higher values changes the current pattern entirely, as can be seen in Figure 64, where the horizontal eddy viscosity coefficient is set at 1.0 m^2s^{-1}.
The refraction of waves in Test 6 differs little from previous tests and can be said to be satisfactory.

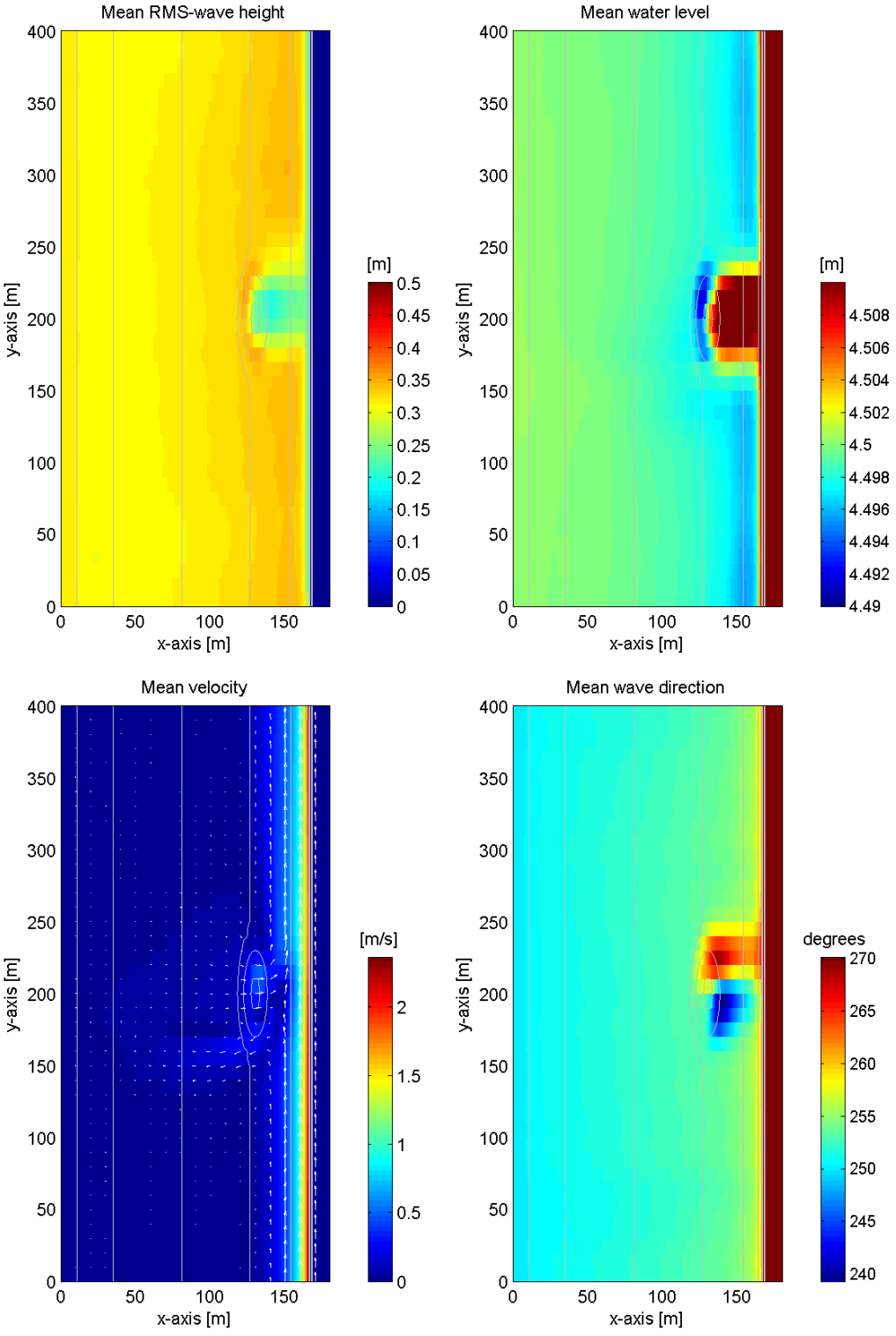


Figure 63 RMS-wave height (top left panel), water surface level (top right panel), velocities (bottom left panel) and mean wave direction, nautical convention (bottom right panel), averaged over 12 wave group periods

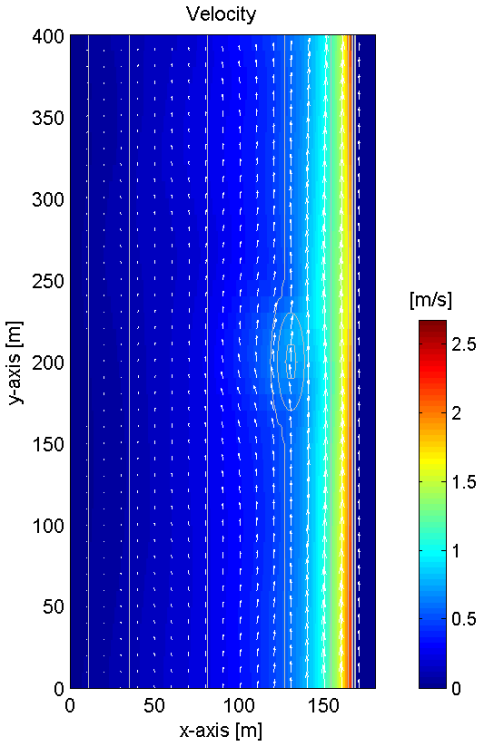


Figure 64 Velocity pattern in the case of high viscosity

L.3 Conclusions

The results of Test 6 are numerically stable and physically plausible. The results are not fully verified, as no comparison is made with measurements or analytical solutions. In general however it can be stated that XBeach has the capacity to handle time-varying short-wave forcing over non-uniform bathymetry.

One important conclusion can be made with respect to the choice of horizontal eddy viscosity. As shown in Figure 64, the current pattern round bathymetry elements can be greatly affected by the amount of eddy viscosity. Before XBeach can be used properly, more effort must be spent on finding a realistic value for the eddy viscosity coefficient. A spatially varying value would for instance be both possible and physically realistic.

M Test 6g

M.1 Model description

In Test 6g, the influence of the grid size on the numerical result is analysed. Three simulations are run. The first simulation (Test 6g0) uses the regularly-spaced numerical grid of Test 6. The second simulation (Test 6g1) also uses a regularly-spaced grid, but with a resolution twice as large as that of Test 6. The third simulation (Test 6g2) uses an irregularly-spaced numerical grid. All three bathymetry grids can be found in Appendix X.
A non-stationary wave condition is imposed on the offshore boundary. The short-waves vary according to regular sinusoidal wave groups with a period of 24.5s. The maximum short-wave wave height is 0.5m and the short-wave wave period is 3.5s. The wave direction is set at 20° Cartesian convention. The directional spreading of the short-waves is such that the waves are long-crested. The water level on the model boundary is kept constant. Morphology and sediment transport are not calculated.

M.2 Results

As was the case in Test 1g and Test 3g, the short wave RMS-wave height is almost not affected by the differences in numerical grid resolution between the three simulations. Figure 65 shows the mean water level, calculated over 60 wave group periods, for all three simulations. The figure shows a slight difference between the mean water levels, especially in the deeper areas of the model. Unlike in the Test 1g and Test 3g, the difference can also be found between the two regular grids. The difference becomes more marked if the variation in the water level is examined, see Figure 66. In this case the fine regular grid and irregular grid appear alike, while the coarser regular grid shows far greater amounts of variation. As the incoming short waves and infragravity waves are obliquely incident, point to point transfer in the longshore direction becomes more important. Such differences may therefore be caused by the resolution in longshore direction of the numerical grid.
The resulting wave-driven currents, see Figure 67, also vary between the three simulations. The difference is mainly to be found in the width of the area carrying the longshore current. In general however these differences are small and the overall current patterns remain the same.

It should be noted that the problems occurring in Test 3g to do with flooding of the model do not occur in Test 6g. This is maybe due to the strong longshore current dominating the lateral boundary calculations.

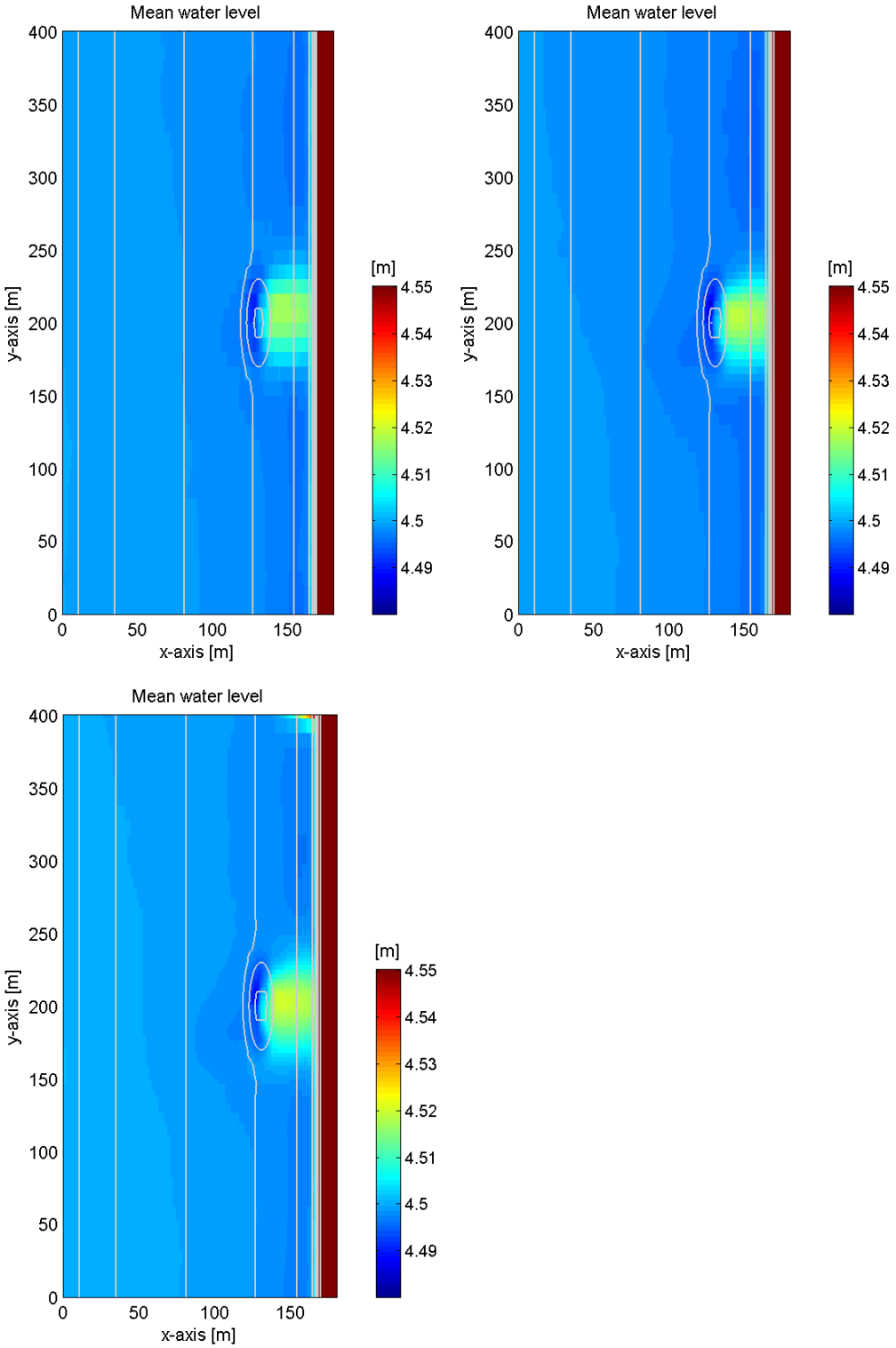


Figure 65 Mean water level in Test 6g0 (top left), Test 6g1 (top right) and Test 6g2 (bottom)

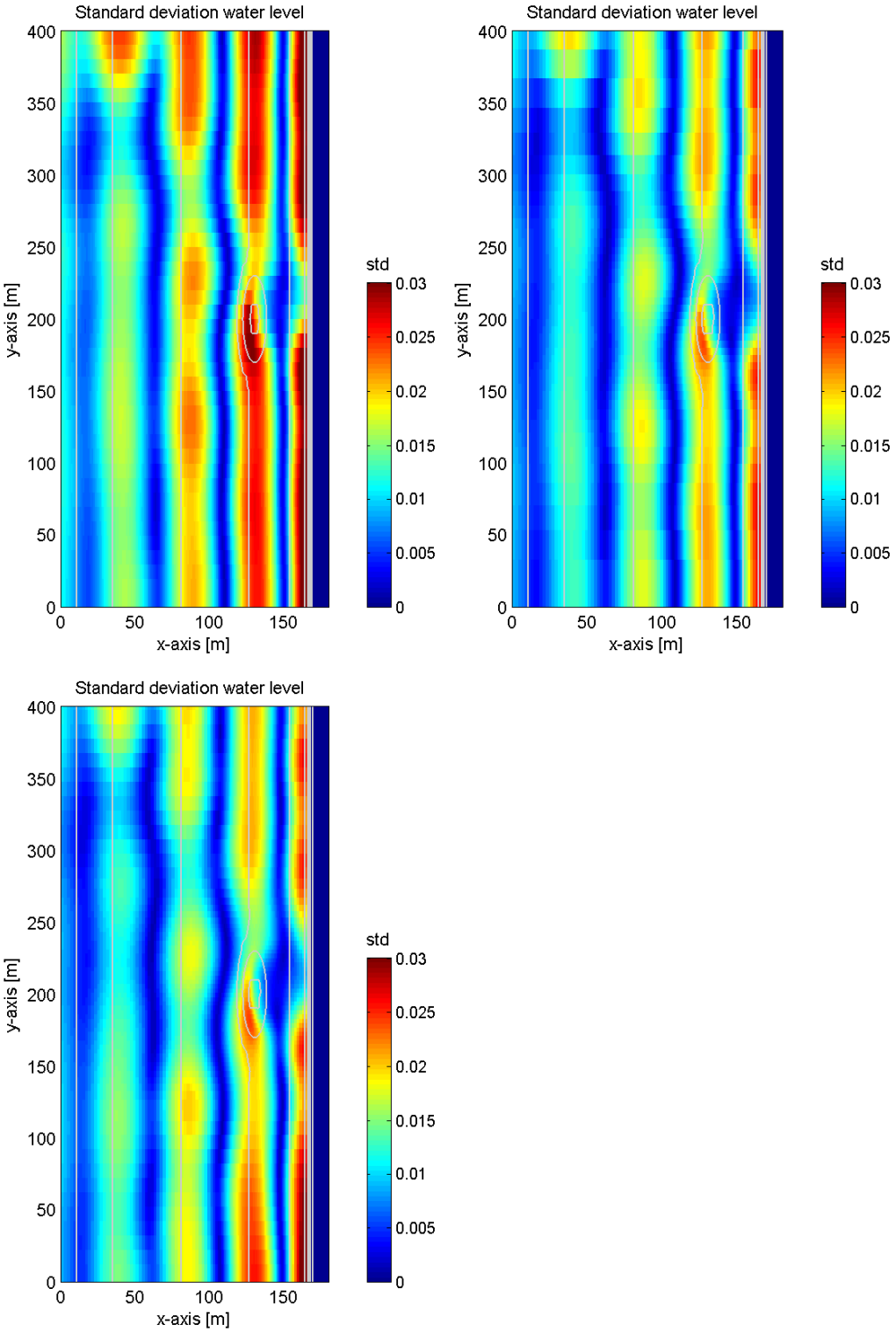


Figure 66 Standard deviation water level in Test 6g0 (top left), Test 6g1 (top right) and Test 6g2 (bottom)

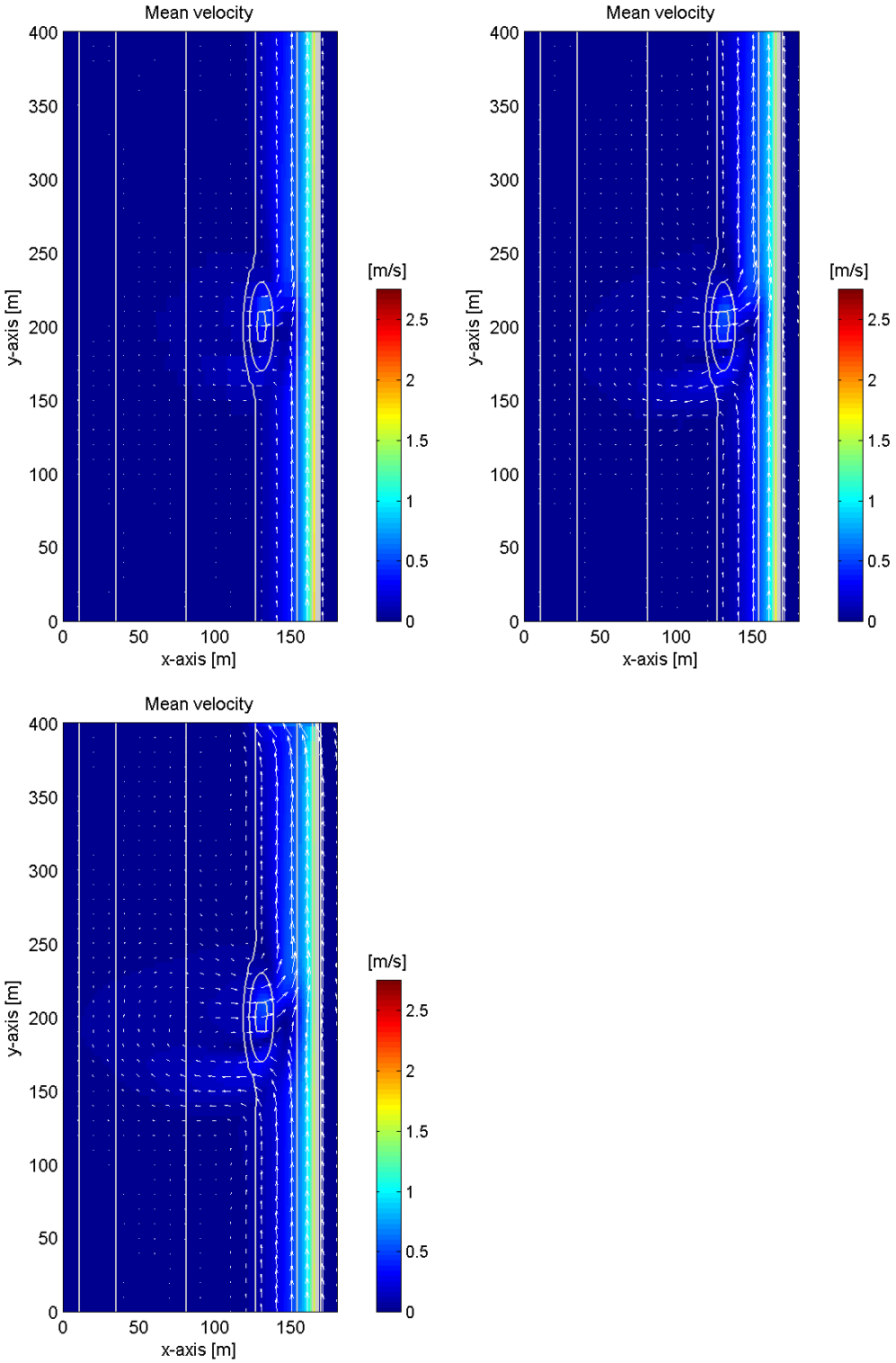


Figure 67 Mean velocity in Test 6g0 (top left), Test 6g1 (top right) and Test 6g2 (bottom)

M.3 Conclusions

With the introduction of more complex hydrodynamics, the differences between results on various numerical grids become more apparent. Without field or laboratory measurements, it is difficult to state which numerical grid is most accurate. The difference in water level variance between the three simulations may be caused by different levels of energy in the infragravity wave band.
In general it can be said that the differences between simulations on different numerical grids are small in comparison with other model uncertainties.

N Test 6s

N.1 Model description

In Test 6s, the ability of XBeach to handle non-stationary waves and tidal surge simultaneously is analysed.
The model is set-up using the longshore non-uniform bathymetry used in Test 3. A non-stationary wave condition is imposed on the offshore boundary. The short-waves vary according to regular sinusoidal wave groups with a period of 24.5s. The maximum wave height of the short waves is 0.5m and the short-wave wave period is 3.5s. The wave direction is set at 20° Cartesian convention. The directional spreading of the short-waves is such that the waves are long-crested. A sinusoidal longshore uniform tide level with a six hour period is imposed on the model domain. Morphology and sediment transport are not calculated.

N.2 Results

The imposed water level and the water level modelled at the offshore boundary are shown in Figure 68. The figure clearly shows that the modelled water level oscillates around the imposed water level with certain regularity. Since the modelled water level includes the contribution of bound and free infragravity waves, the period of the difference signal between the modelled and imposed water levels should be the same as the period of the incident wave groups. Figure 69 shows the result of a Fourier transform of the difference signal. The figure clearly shows a concentration of variance with a period of 24.5s, the period of the incident wave groups.

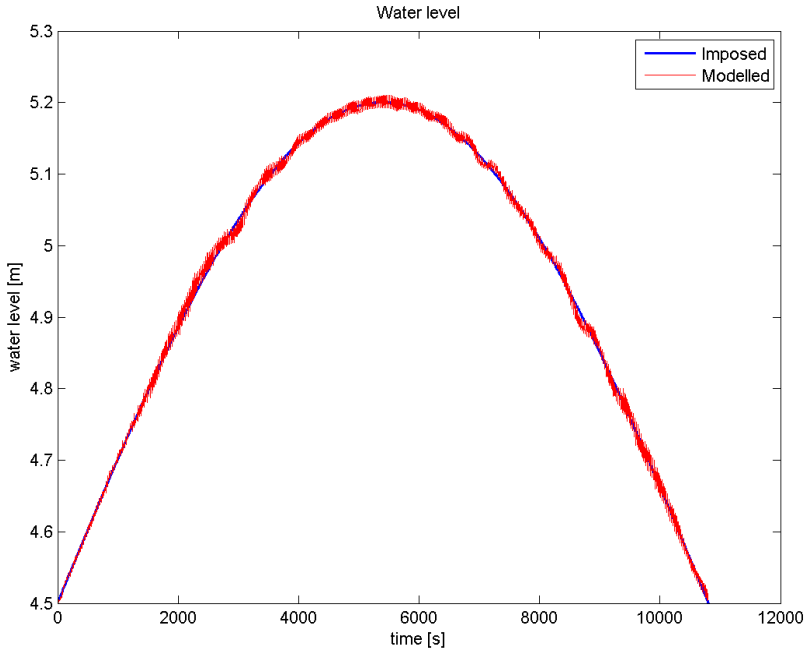


Figure 68 Water level near the offshore boundary and imposed water level

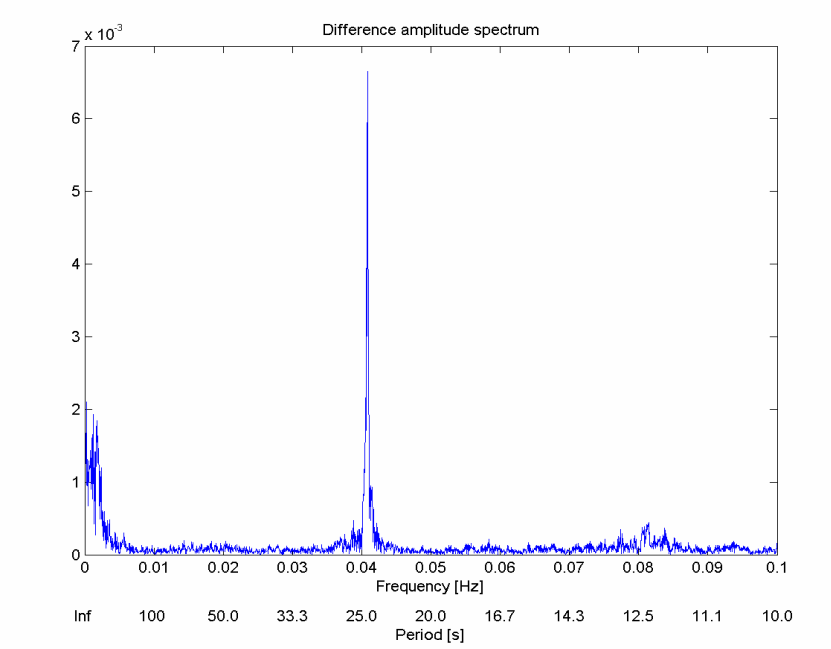


Figure 69 Amplitude density spectrum of the water level differences between the imposed water level and the modelled water level

N.3 Conclusions

The XBeach model shows no signs of instability or irregular behaviour when forced by surge and incident wave groups simultaneously. It can therefore be concluded that XBeach is capable of handling such forcing conditions.

O Test 7

O.1 Model description

In Test 7, the ability of XBeach to handle new offshore irregular wave boundary conditions is examined. The purpose of the wave boundary condition is to simulate realistic conditions in which the incoming waves are non-uniform and non-stationary.
The regular, longshore uniform bathymetry of Test 1 is used in the computation. The wave boundary condition is based on a JONSWAP spectrum, with a significant wave height of 0.5m and peak period of 3.5s. The mean wave direction is set at 0° Cartesian convention. The water level on the model boundary is kept constant. Morphology and sediment transport are not calculated.

O.2 Results

Figure 70 shows the instantaneous short wave heights, water levels and Lagrangian velocities of a certain point in time in the simulation. The figure clearly shows the presence of separate wave groups and the related bound infragravity waves in deep water (top two panels). The information that can be extracted from the data in the figure is limited due to the irregular forcing and interaction with reflected infragravity waves.
In order to gain more insight into the model results, a long term average of the short wave RMS-wave heights, water level and velocities is calculated and shown in Figure 71. The long term RMS-wave height on the offshore boundary corresponds well with the imposed *significant* wave height of 0.5m. There is a slight oscillating pattern in the contour lines of the RMS-wave height in longshore direction. It is suggested that this may be caused by the presence of an edge wave trapped between the lateral boundaries.
The long term mean water level shows much the same behaviour as in the previous tests. Due to the limited wave height of the short waves, the set-down and set-up is quite small. Additionally, the position of the mean breakpoint and thus the transition between mean set-down and set-up is closer to the shoreline.
The mean velocity in Figure 71 shows that the lateral boundaries can still generate inaccuracies in the model if the wave forcing is irregular, but normally incident.

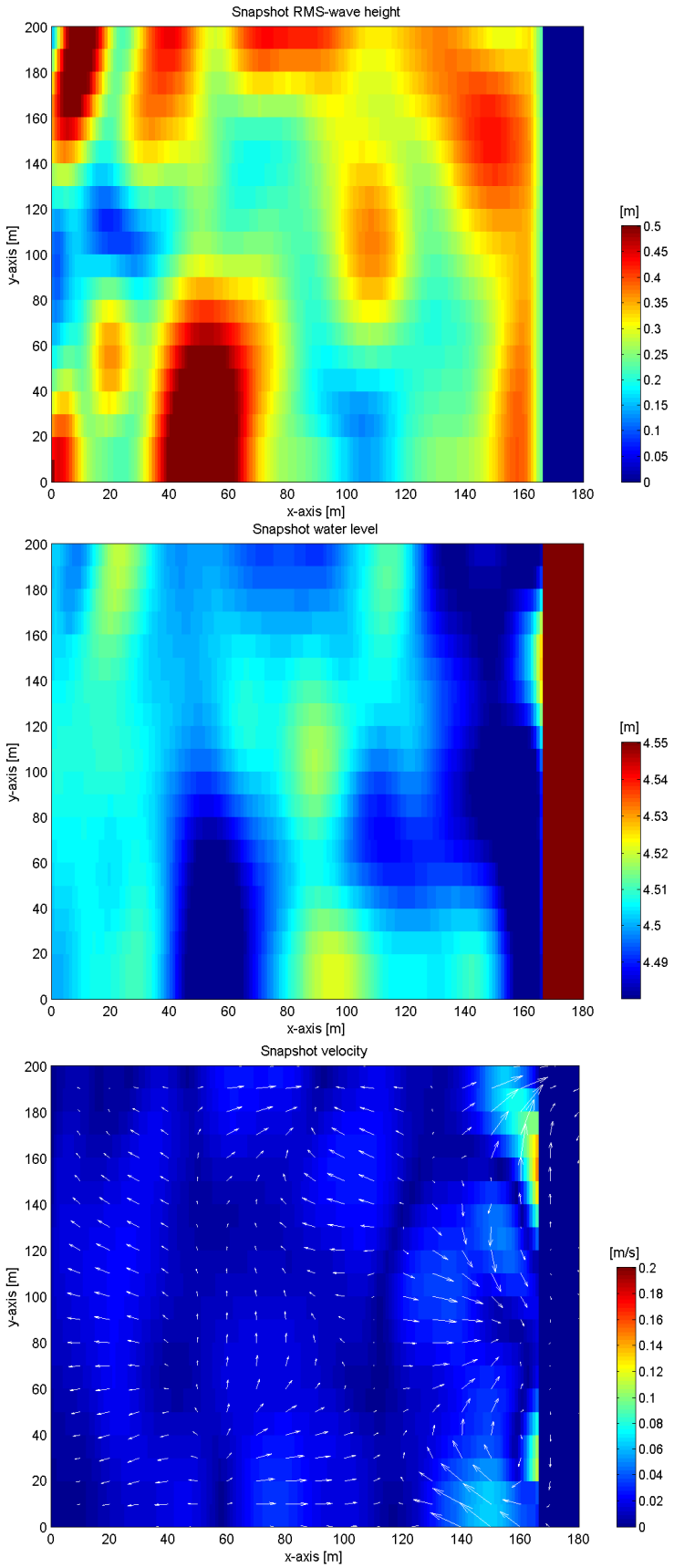


Figure 70 Snapshot of RMS-wave height (top panel), water surface level (middle panel) and velocities (bottom panel)

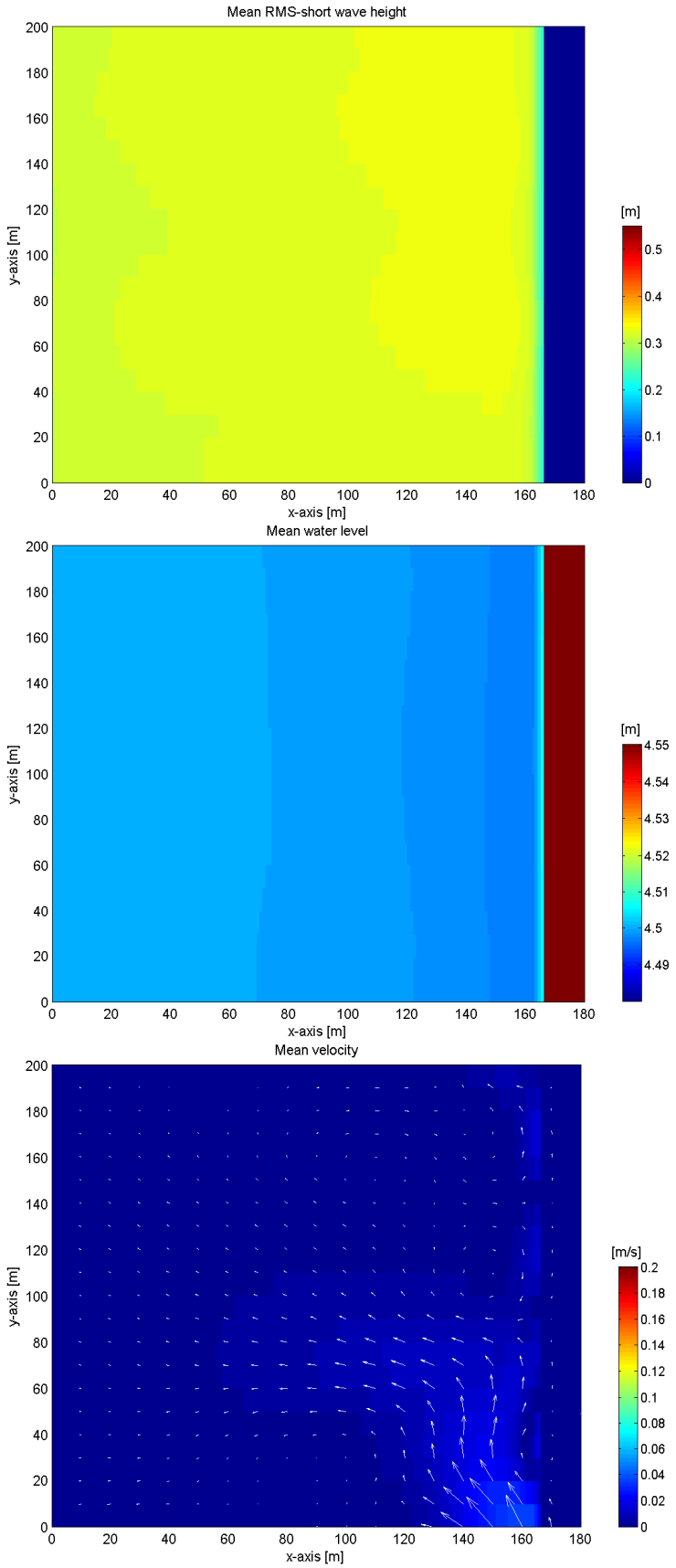


Figure 71 Mean RMS-wave height (top panel), water surface level (middle panel) and velocities (bottom panel), averaged over 2000 seconds

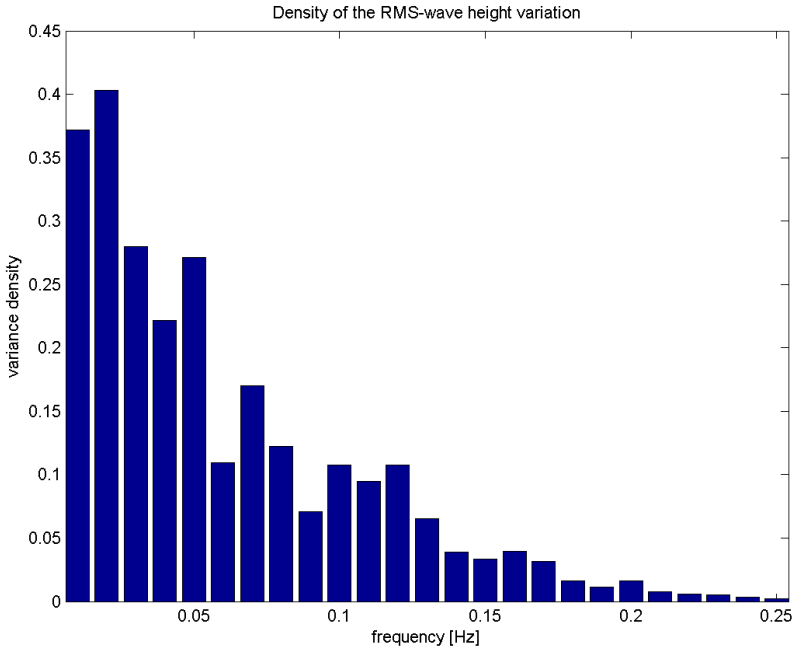


Figure 72 Distribution over frequencies of the variance in short wave RMS-wave height at the offshore boundary

The variance of the short wave RMS-wave height is examined in Figure 72. Bound infragravity wave energy is expected at roughly ¼ of the peak short wave frequency. Since on the offshore boundary the bound infragravity waves have the same time scale as the short wave groups, the maximum variation of short wave group energy should also be found at approximately ¼ of the peak frequency of the short waves. In this case the expected maximum wave group energy frequency would be 0.07Hz. It is clear from Figure 72 that the maximum short wave group variation is found at far lower frequencies.

In order to examine if the low frequency variance is caused by errors in the implementation of the boundary condition program code, a simple one-dimensional model is set up. The offshore boundary forcing for this model is a standard JONSWAP spectrum with a peak frequency of 0.125 Hz. In order to generate wave group-averaged short wave energy, the boundary condition module generates water elevation time series on the scale of individual waves. The envelope of this time series is used to calculate the wave group energy signal. The water surface elevation and envelope calculated by XBeach are shown in Figure 73. As can be seen, other than some smoothing, the wave envelope is calculated correctly. The variance density spectrum of both signals is shown in Figure 74. It can clearly be seen that the short wave spectrum centres on the peak short wave frequency of 0.125 Hz and is correct. However, once again the spectrum of the short wave envelope contains much very low frequency variance. This variance is due to the slowly modulating wave heights on the time scale of 400s – 500s. Whether this modulation is correct or incorrect, the investigation shows no abnormalities in the generation of variance on the time scale of infragravity waves.

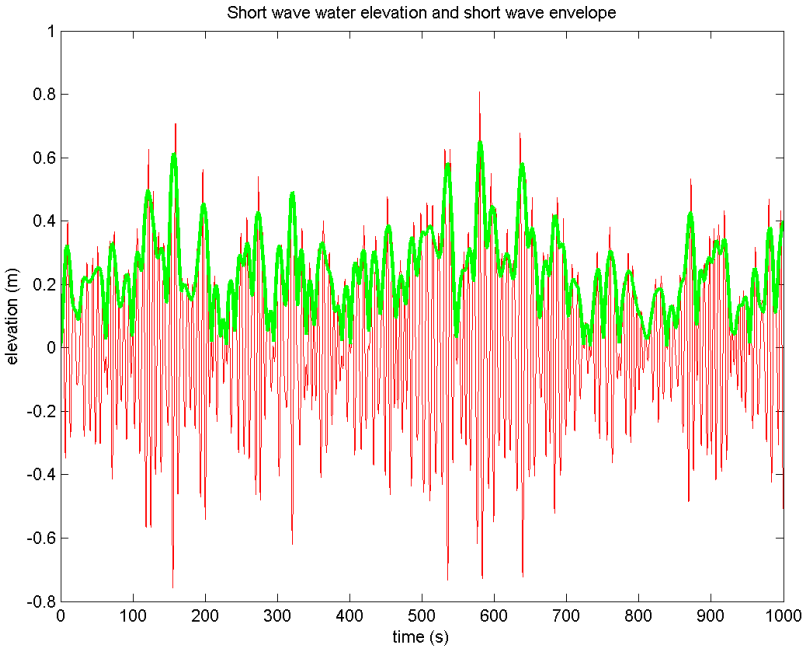


Figure 73 Short-wave resolving water surface elevation and short wave envelope imposed on the offshore boundary

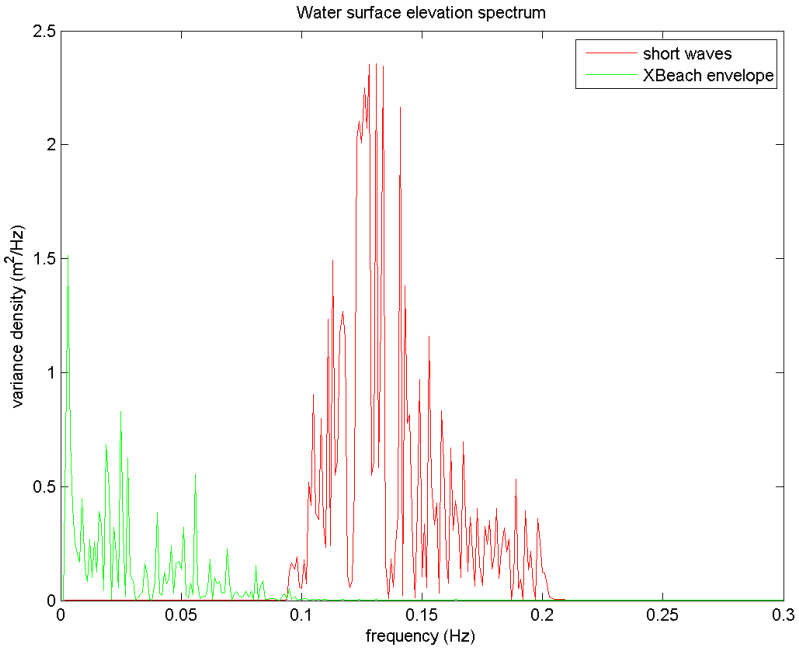


Figure 74 Variance density spectrum of the short wave signal and the short wave envelope imposed on the offshore boundary

As explained in Chapter 2 of the main report, the incident short wave envelope and associated bound long wave are negatively correlated in deep water, and slowly become positively correlated as the waves move shoreward. In order to examine if XBeach is correctly generating and propagating bound infragravity waves, a correlation plot is made of the short wave energy envelope and water level in XBeach, see Figure 75 (top panel). The result shows very little correlation in both deep water and shallow water. A similar

simulation is carried out with an incident significant wave height of 2.0m. The correlation plot of this simulation is shown in Figure 75 (bottom panel). In this case there is a clear change from negative correlation to positive correlation. The difference between these two plots may be explained by considering the amount of reflected infragravity energy compared to the incident infragravity energy. In the case of little incident short wave energy, very little bound infragravity wave energy is imposed on the offshore boundary. It is possible that most of this energy reflects off the shoreline and interferes with the correlation calculation in the model domain. In the case of high incident short wave energy, more bound infragravity wave energy is imposed on the offshore boundary. It is possible that relatively more off this energy dissipates at the shoreline and does thus not interfere so much with the correlation in the rest of the model domain. This hypothesis can be examined by decomposing the water level signal into shoreward and offshore directed components.

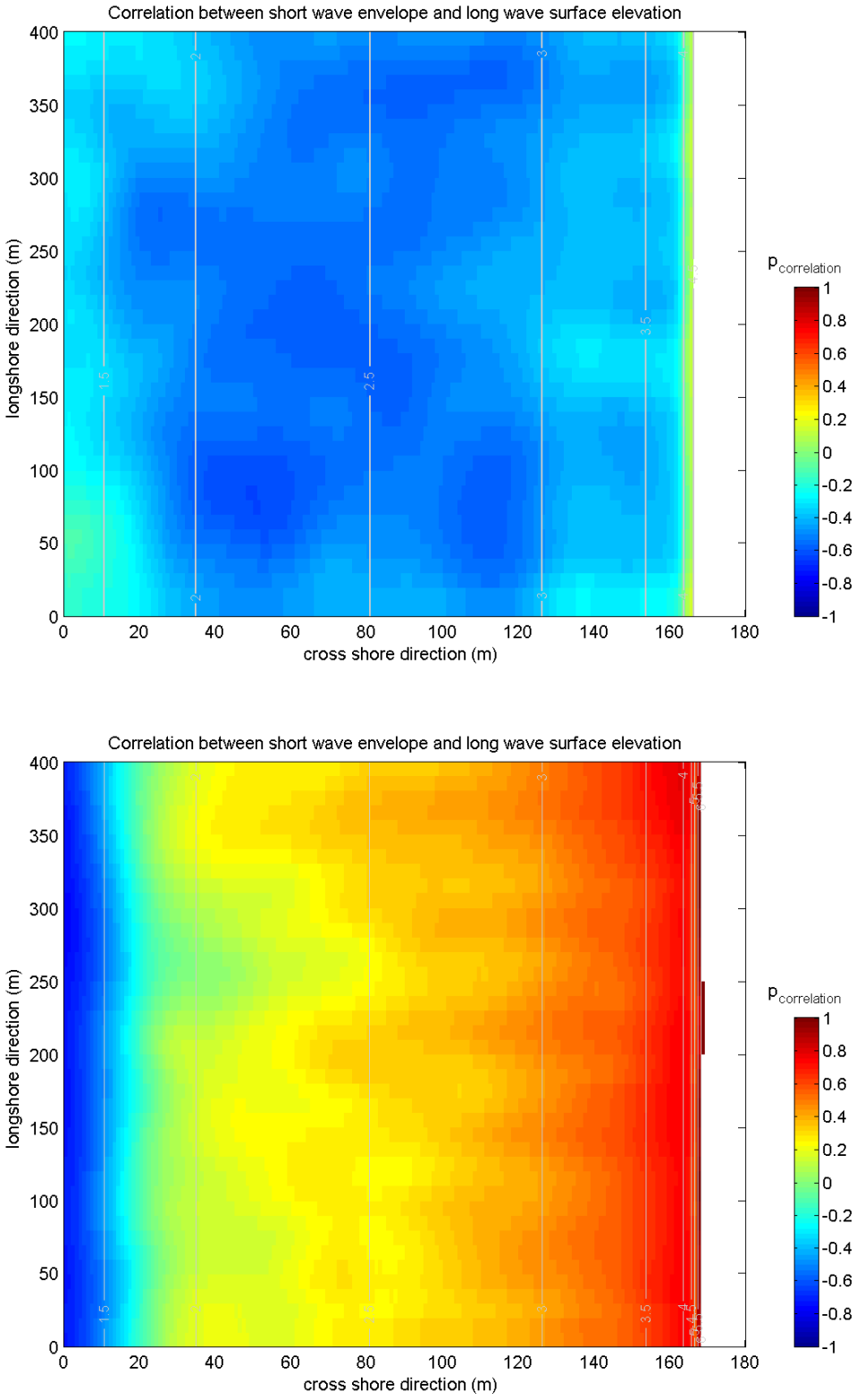


Figure 75 Correlation coefficient between the short wave envelope and water surface elevation in the case of 0.5m incident significant waves (top panel) and 2.0m incident significant waves (bottom panel)

O.3 Conclusions

Test 7 shows that XBeach is able to create fully irregular wave groups that propagate realistically through the model domain. The time-averaged wave height corresponds well with the statistical properties of the imposed wave spectrum. However, the period on which the short wave energy varies is longer than the expected period.
The model suffers from two other inaccuracies. The first is the longshore current on the lateral boundaries. As shown in Test 3g, under normally incident regular wave group forcing the lateral boundaries discharge water into or out of the model domain. This also appears to be the case for normally incident irregular wave group forcing.
The second inaccuracy is the longshore non-uniformity of the time averaged model results. At this stage it is suggested that these periodic longshore variations are caused by artificial standing edge waves in the model domain.

P Test 8

P.1 Model description

In Test 8, the ability XBeach to handle obliquely incident offshore irregular wave boundary conditions over a longshore non-uniform bathymetry is examined.
The regular, longshore non-uniform bathymetry of Test 3 is used in the computation. The wave boundary condition is based on a JONSWAP spectrum, with a significant wave height of 0.5m and peak period of 3.5s. The mean wave direction is set at 20° Cartesian convention, 250° Nautical convention. The water level on the model boundary is kept constant. Morphology and sediment transport are not calculated.

P.2 Results

Figure 76 shows the short wave RMS-wave height for one moment in time. The figure clearly shows the obliquely incident wave groups refracting towards the coast and breaking over the shoal. The figure also shows the water surface elevation and velocity field at the same point in time.
The time-averaged RMS-wave height, water level, velocity field and wave direction are shown in Figure 77. The results do not differ qualitatively much from the time-averaged results of Test 6. Due to lower incident short wave energy, the short wave RMS-wave heights are lower in Test 8 than in Test 6, leading also to less set-down and set-up. The velocity field is slightly different due to the use of a higher viscosity coefficient in Test 8.
The standard deviation of the short wave RMS-wave height, see Figure 78 (left panel), shows the effect of wave breaking over the shoal. Because there is no diffraction in XBeach, the wave heights behind the shoal remain very constant after breaking and thus the variation is practically zero. This effect can also be seen in the standard deviation of the water level, see Figure 78 (right panel). With limited short wave forcing the water level behind the shoal remains more constant than the water level in the surrounding nearshore areas.

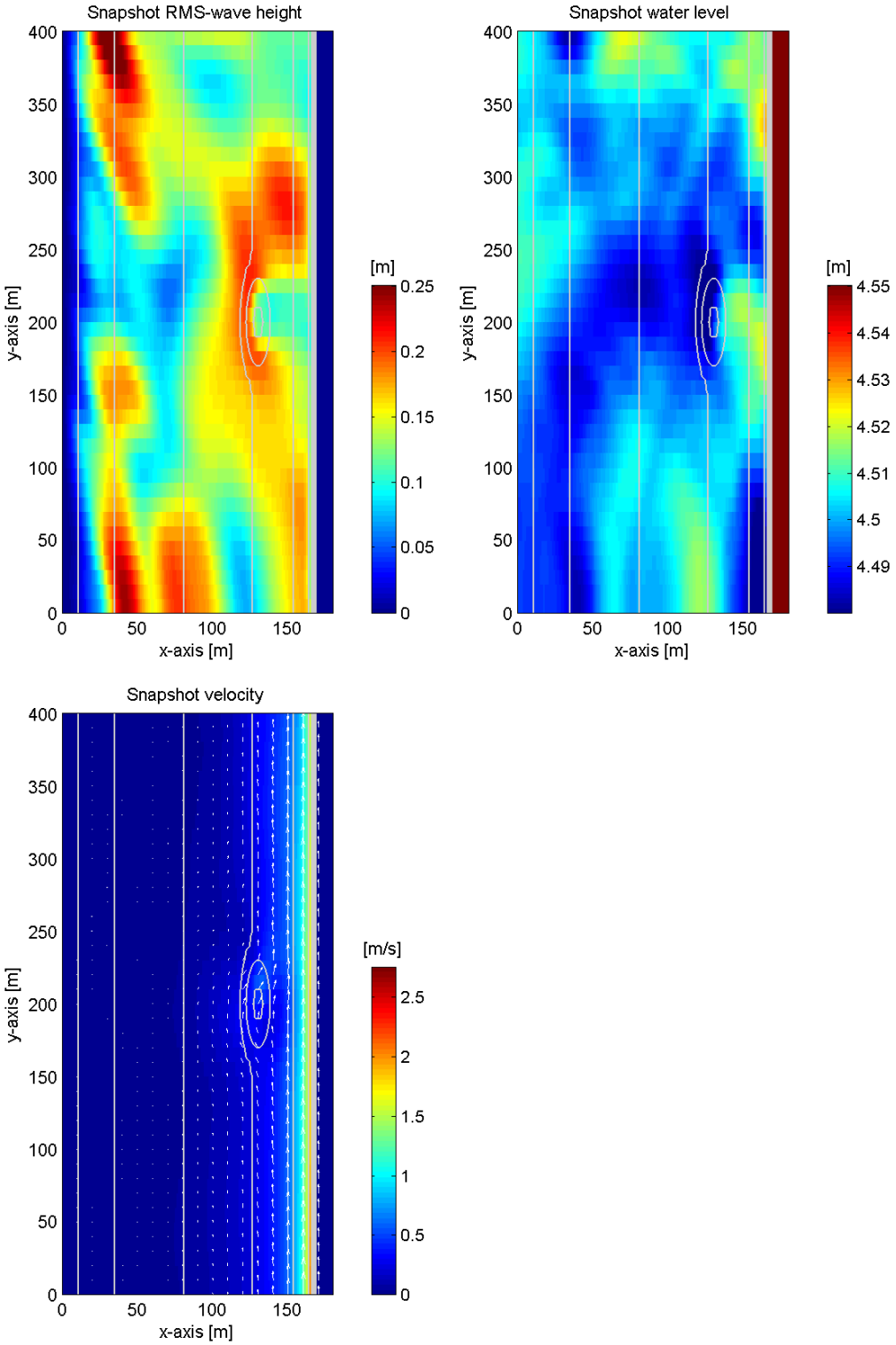


Figure 76 Snapshot of RMS-wave height (top left panel), water surface level (top right panel) and velocities (bottom left panel)

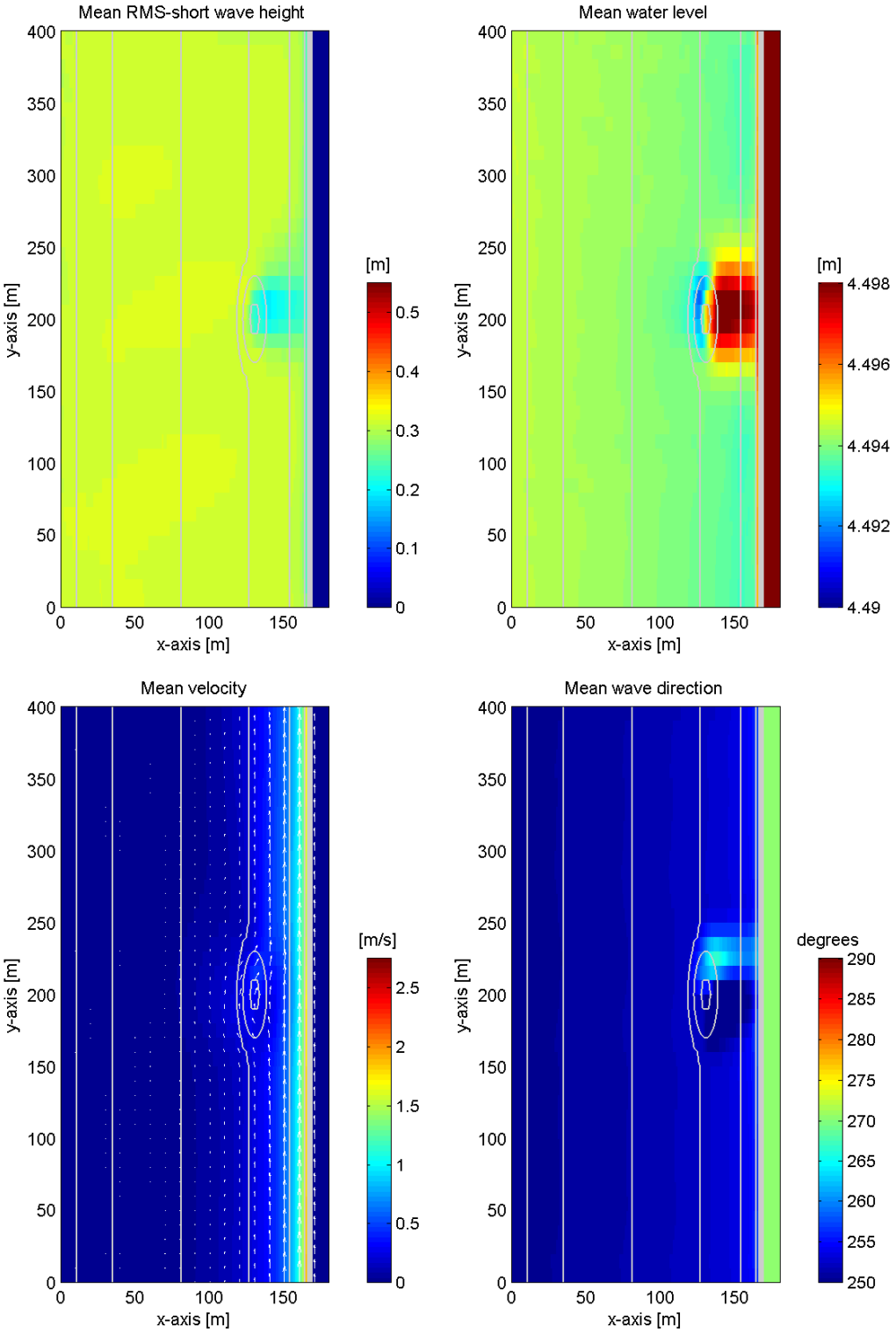


Figure 77 RMS-wave height (top left panel), water surface level (top right panel), velocities (bottom left panel) and mean wave direction, nautical convention (bottom right panel), averaged over 30 minutes

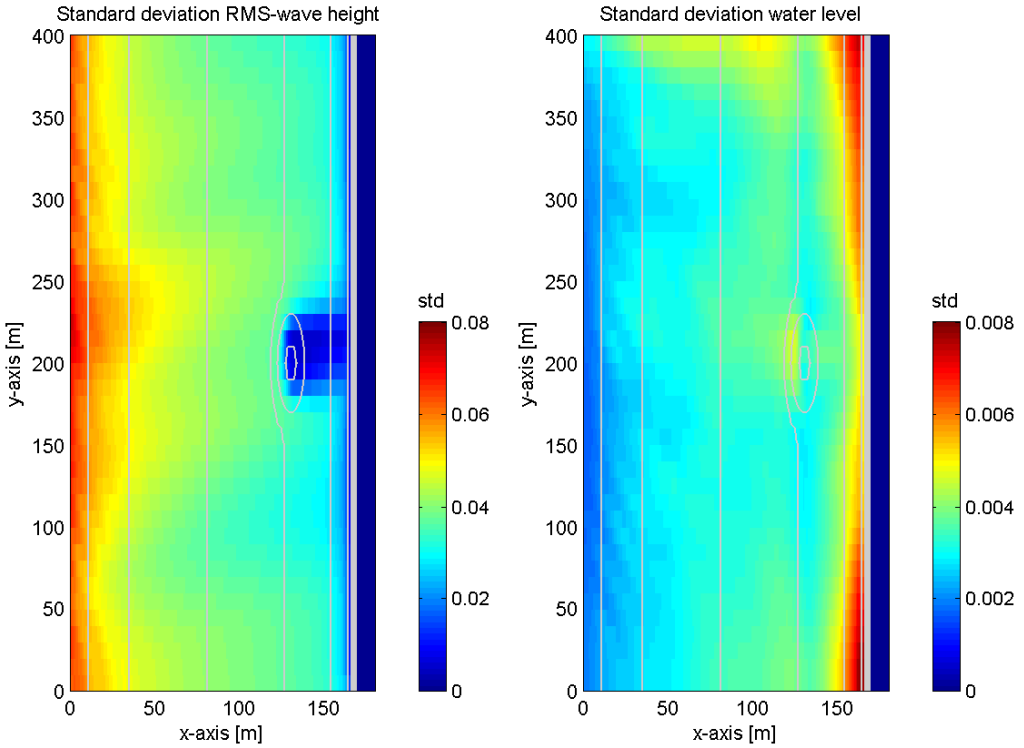


Figure 78 Standard deviation of RMS-wave height (left panel), water surface level (right panel), over 30 minutes

P.3 Conclusions

Although no comparisons are made with measured data, the results of Test 8 appear to be at least in qualitative agreement with hydrodynamic theory. Certain boundary problems still exist, mainly on the lateral boundaries. One example is the increased water level variation on the outflow (top) lateral boundary seen in Figure 78 (right panel).

Q Test 8s

Q.1 Model description

In Test 8s, the ability of XBeach to handle irregular waves and tidal surge simultaneously is analysed.
The regular, longshore non-uniform bathymetry of Test 3 is used in the computation. The wave boundary condition is based on a JONSWAP spectrum, with a significant wave height of 0.5m and peak period of 3.5s. The mean wave direction is set at 20° Cartesian convention. The directional spreading of the short-waves is such that the waves are long-crested. The water level on the model boundary is kept constant. Morphology and sediment transport are not calculated.

Q.2 Results

The modelled water level and imposed surge level on the offshore boundary are shown in Figure 79.

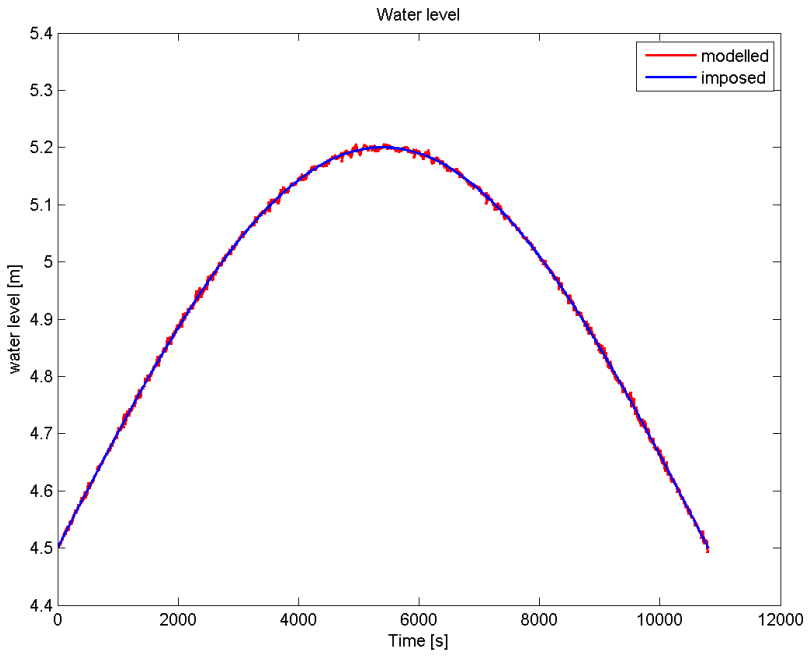


Figure 79 Water level near the offshore boundary and imposed water level

Q.3 Conclusions

Test 8s shows that XBeach is capable of handling irregular wave group forcing in combination with an imposed surge level variation on the offshore boundary.

R Test 9

R.1 Model description

Test 9 is based on the setup of the physical model tests of Berkhoff *et al* [1982]. In this study a series of experiments designed specifically to test the performance of numerical short-wave propagation models in situations with refraction and diffraction were carried out [Berkhoff, 1982; Berkhoff *et al.*, 1982]. The bathymetry of the physical model test consists of a shoal on a sloping bed, both of which are rotated 20° with respect to the wave-maker board. An illustration of the experiment setup can be seen in Figure 81.
The water depth in the deepest part of the model is 0.45m. The wave height of the regular waves was 0.046m and the wave period was 1.0s. The wave heights and phases were measured along the seven transects marked in Figure 81.

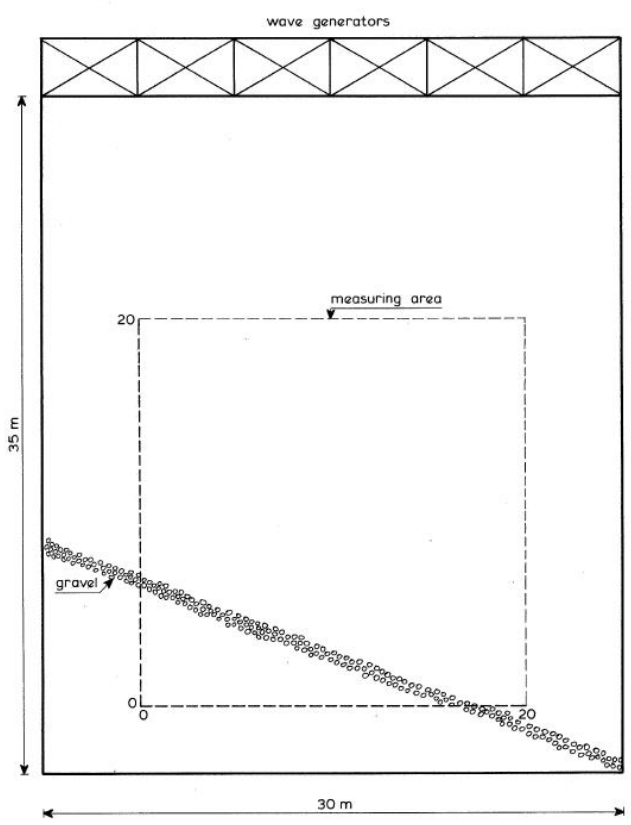


Figure 80 Plan of the physical model used by Berkhoff *et al* [Berkhoff, 1982]

By carrying out the Berkhoff test, the short-wave motions in XBeach can be verified in stationary conditions. It is to be expected that the results of the XBeach model will differ from the experimental results, as XBeach does not include diffraction and does not resolve short-wave phase.

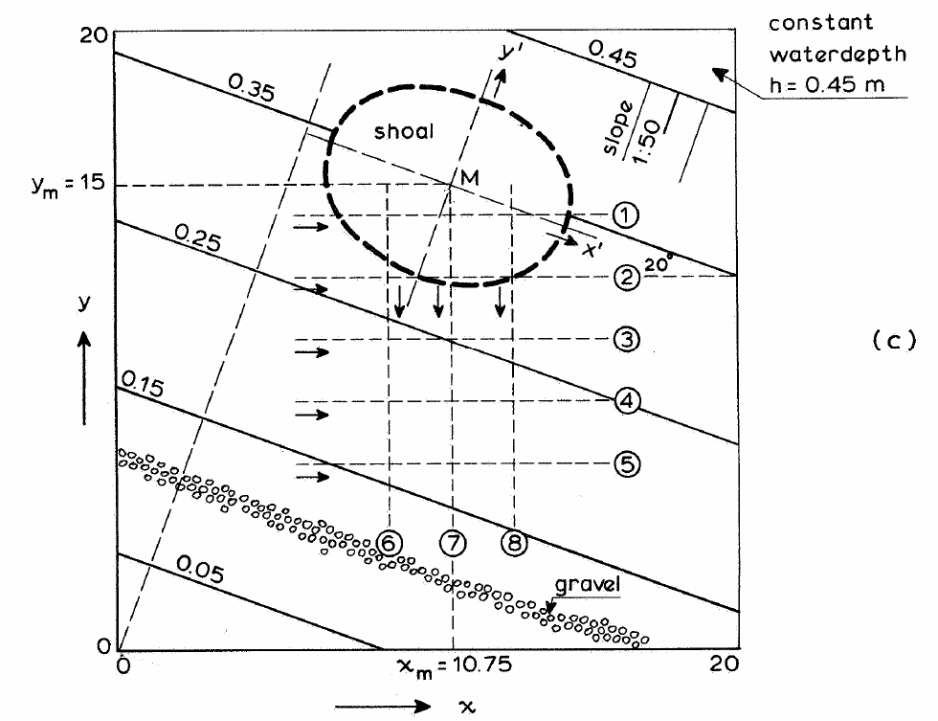


Figure 81 Bathymetry and incoming waves in the Berkhoff test [from: Berkhoff, 1982]

The model bathymetry is based on the description of the physical model by Berkhoff [1982], see Figure 80. The area from the wave generators to the back of the measuring area, from the left wall to the right wall of the wave basin, is included in the numerical model, see Figure 82.

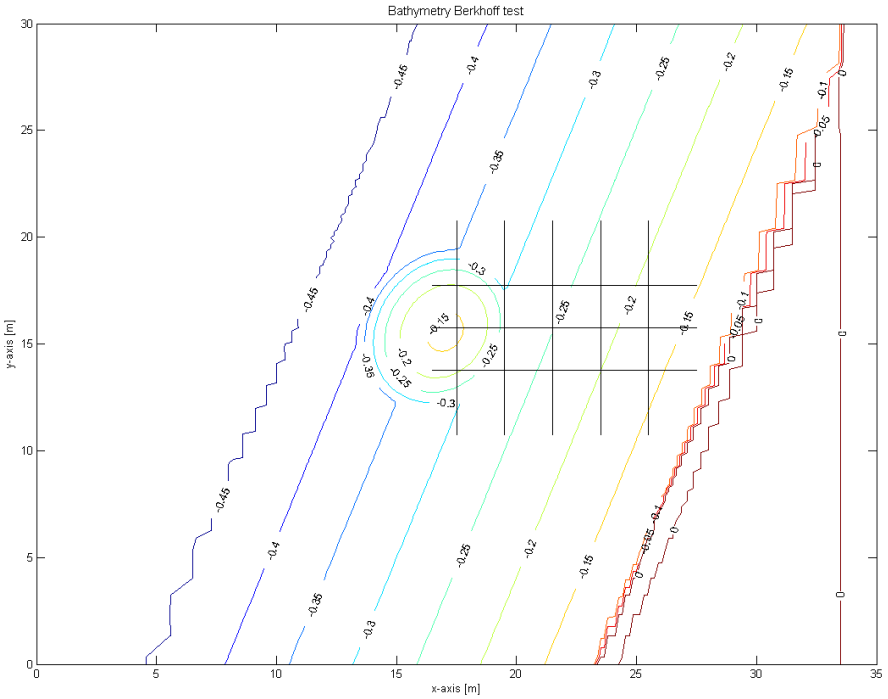


Figure 82 Berkhoff model bathymetry. Note the x- and y-axes have been switched for use in XBeach

A fine irregular calculation grid is set up for the numerical model. A grid size of 0.15m in x- and y-direction is used around the shoal and in the area of measurement, increasing to a maximum of 1.0m in x- and y-direction towards the edges of the model.

The back boundary is increased in height to form a short-wave absorbing wall. The lateral boundaries are given wall boundary conditions for long waves, but do not reflect short waves. A stationary wave condition is imposed on the offshore boundary with a short-wave wave height of 0.0464m and period of 1.0s, as used in experiment T4 [Berkhoff, 1982]. The wave direction is set at 0° Cartesian convention. The water level on the model boundary is kept constant. Morphology and sediment transport are not calculated.

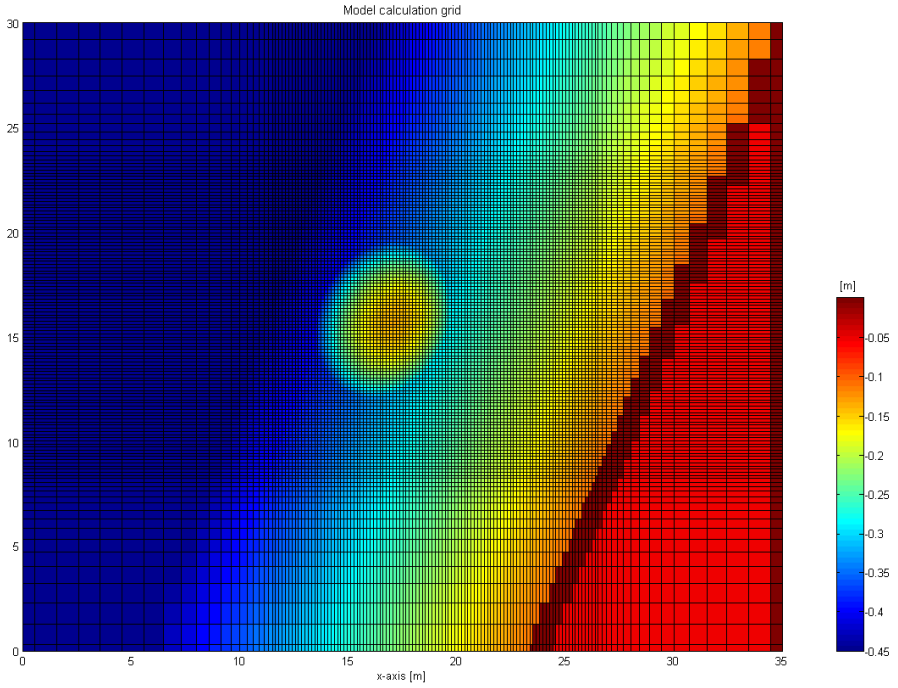


Figure 83 Model calculation grid and bathymetry data

R.2 Results

Three model parameters are varied to calibrate the model with the results of Berkhoff [1982], see Table 1. The first model parameter is the wave energy dissipation. Although it is not expected that much dissipation will occur due to the extremely small wave heights, a sensitivity test is carried out. The second parameter that is varied is the *delta*-parameter, the measure in which the height of the short waves is added to the local water depth. This parameter may play an important role in the amount of refraction and shoaling over the oblique shoal. The third parameter that is varied is the grid size in theta-space. Defining theta-step sizes that are too large may lead to significant errors in the shoaling and refraction calculation around the shoal and bed slope.

The relative wave heights calculated along the 8 sections are plotted against the measurements made by Berkhoff [1982] in Figure 84 through Figure 87.

Table 1 Berkhoff experiment variable parameters

Experiment number	Min. theta grid	Max. theta grid	Theta gridsize	Dissipation	Delta	Gamma
9.1	-27.5	+27.5	5	Roelvink	0.0	0.78
9.2	-27.5	+27.5	5	None	0.5	-
9.3	-27.5	+27.5	5	None	0.8	-
9.4	-180	180	20	None	0.5	-

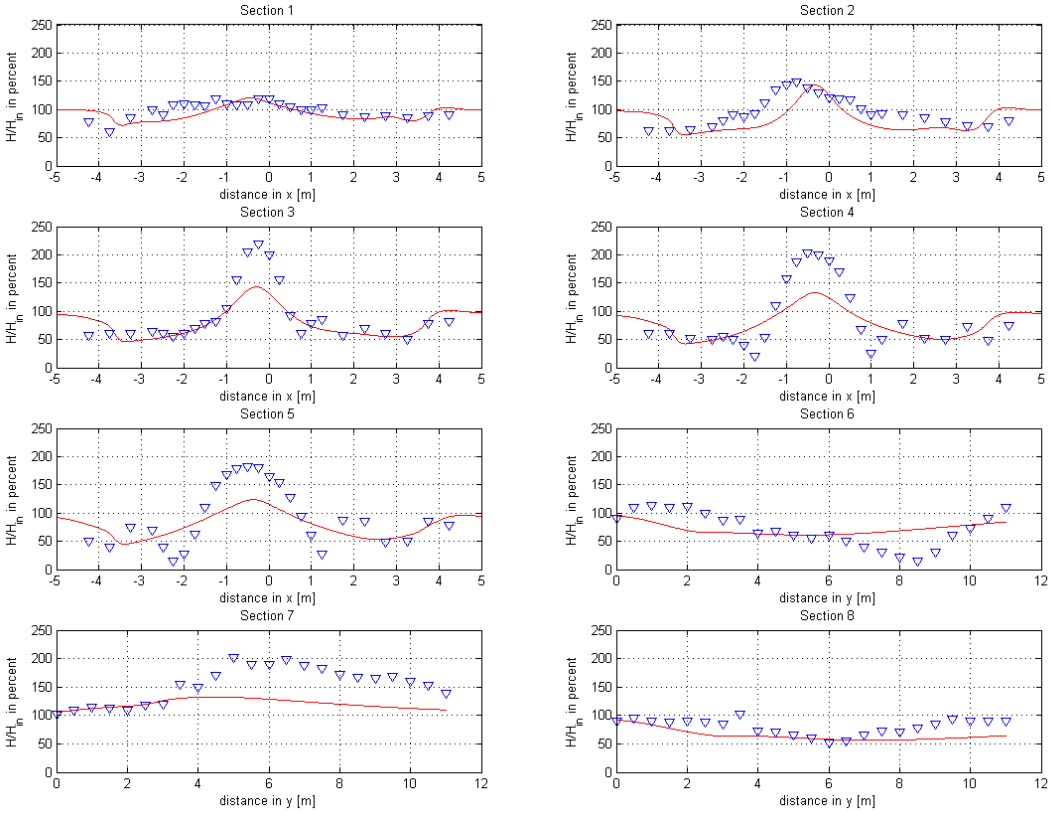


Figure 84 Results of Test 9.1: Measured (▼) and calculated (line) wave heights in sections 1-8

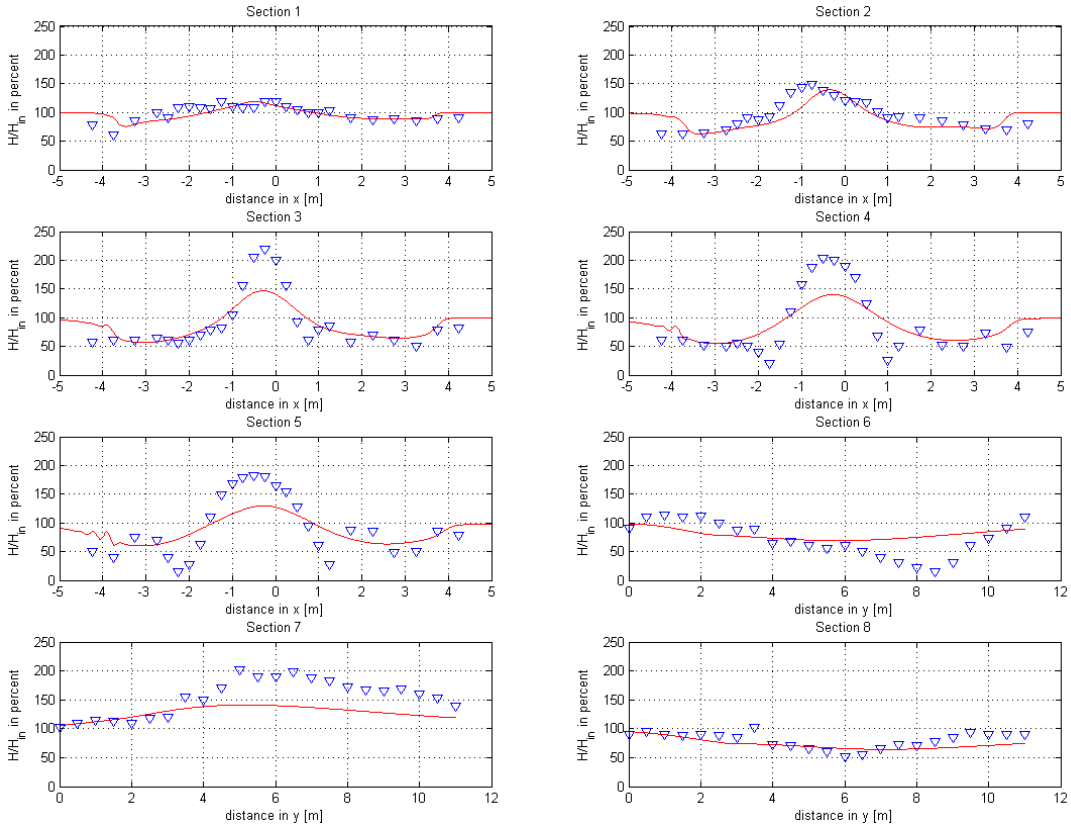


Figure 85 Results of Test 9.2: Measured (▼) and calculated (line) wave heights in sections 1-8

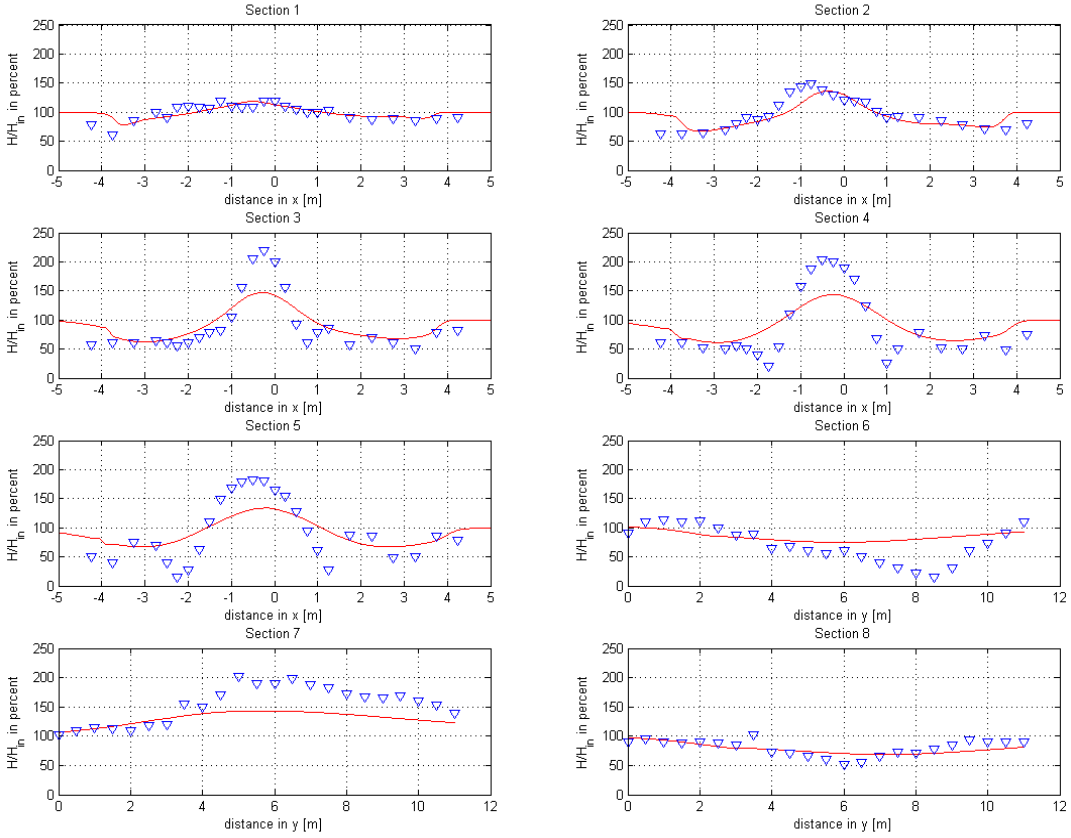


Figure 86 Results of Test 9.3: Measured (▼) and calculated (line) wave heights in sections 1-8

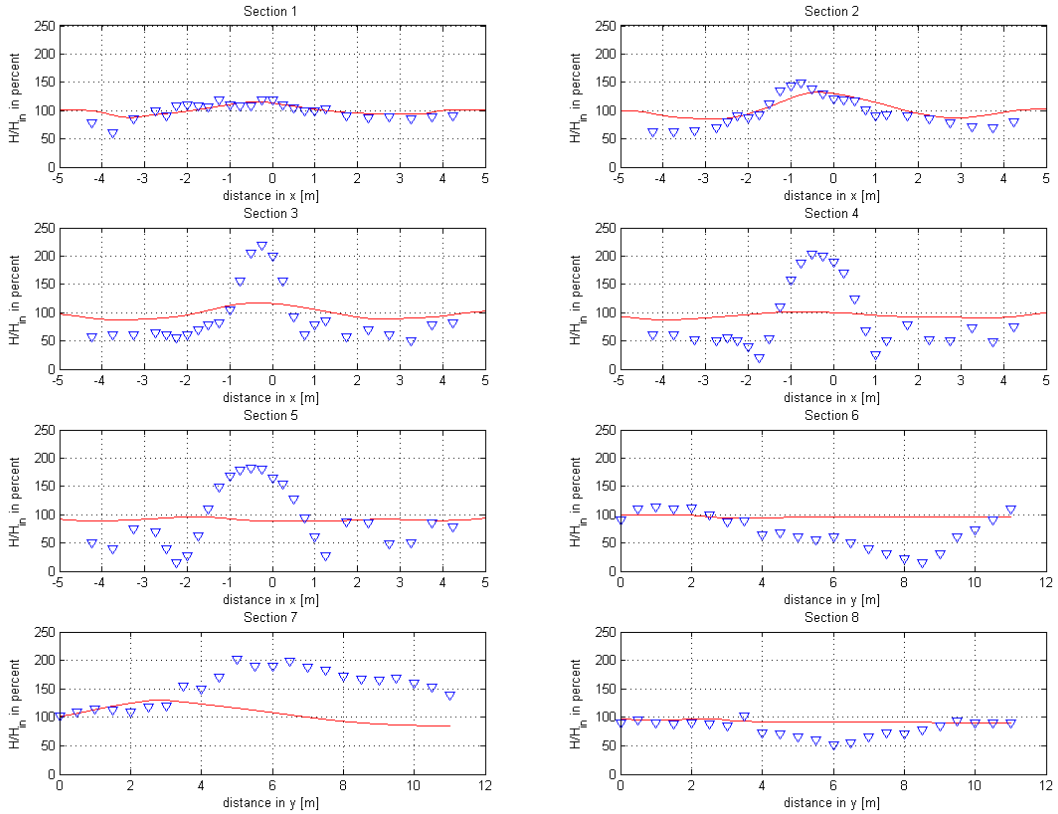


Figure 87 Results of Test 9.4: Measured (▼) and calculated (line) wave heights in sections 1-8

R.3 Conclusions

Tests 9.1 through 9.3 differ very little from each other. It would therefore be safe to conclude that in this case the wave energy dissipation and *delta*-value have little influence on the model results. The increase in theta-grid size leads to less accurate results.

In general it can be said that with sufficient resolution in theta-space, XBeach correctly models the wave heights before and on top of the shoal. Behind the shoal, the results become less accurate as wave diffraction plays and increasingly important role. The complex set of dips and humps in the wave height in longshore transects 3, 4 and 5 are not well represented. Given that XBeach resolves wave energy on the wave group time scale and does not include diffraction and phase interaction effects, the results can be considered to be reasonable.

S Test 10

S.1 Model description

Test 10 is based on the Berkhoff [1982] irregular wave data (T3). In this experiment the same bed slope and shoal configuration is used as explained in Test 9. Instead of regular waves, the wave board created irregular waves based on a JONSWAP spectrum with a significant wave height of 0.0462m and a peak period of 1.0s. In the experiment data were measured in 15 locations behind the shoal. These locations are shown and numbered in Figure 88.

In the XBeach model the wave direction is set at 0° Cartesian convention and the wave spectrum is defined such that the waves are long crested. The water level on the model boundary is kept constant. Morphology and sediment transport are not calculated. The wave settings of Test 9.2 are used in this model.

It is expected that under irregular wave group forcing, diffraction effects will play a less important role than in the regular wave case [Roelvink, private correspondence]. Therefore XBeach should be able to predict the irregular wave heights more accurately in Test 10.

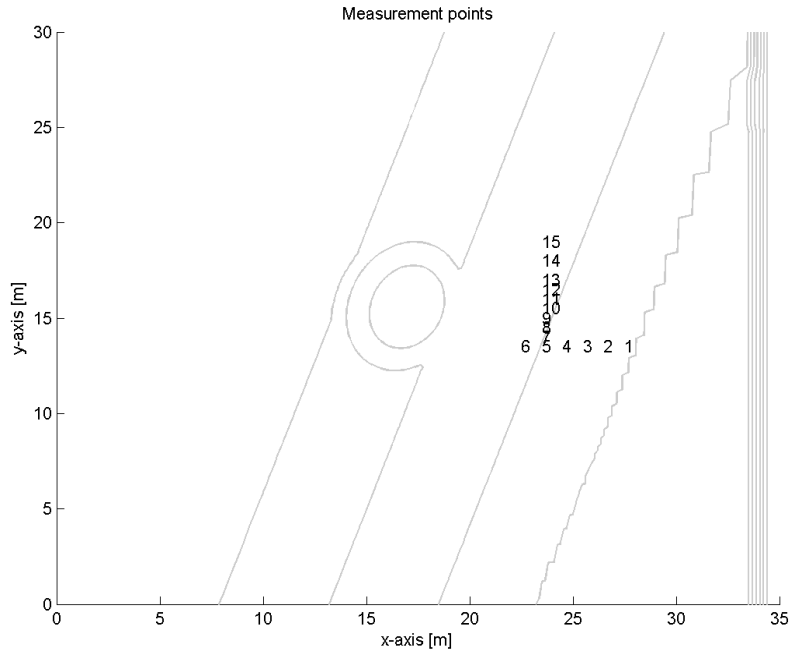


Figure 88 Position of measurement locations in the Berkhoff [1982] T3 experiment

S.2 Results

The measured RMS-wave heights and the modelled RMS-wave heights for all 15 measurement locations are shown in Figure 89. The relative RMS-wave height error in each location is shown in Figure 90.

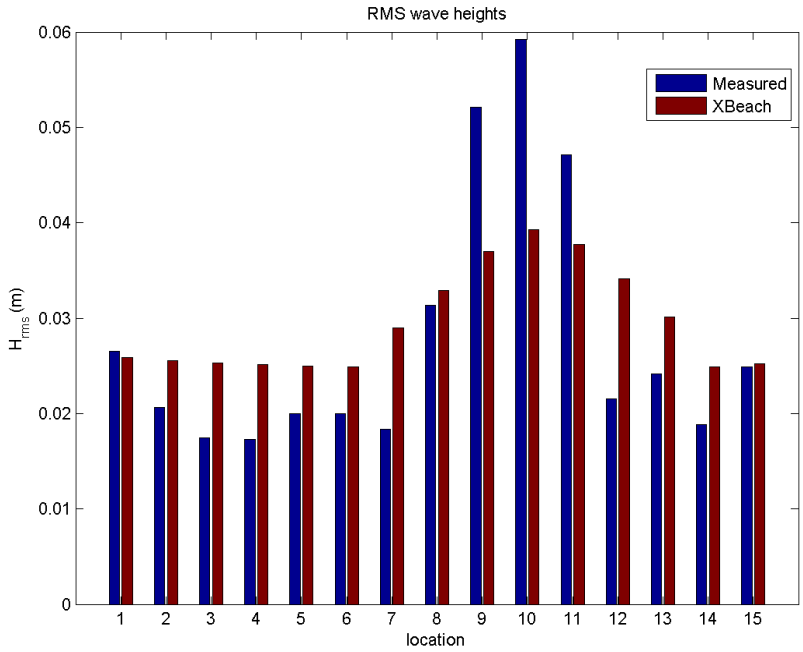


Figure 89 Measured and calculated RMS-wave heights is all measurement locations

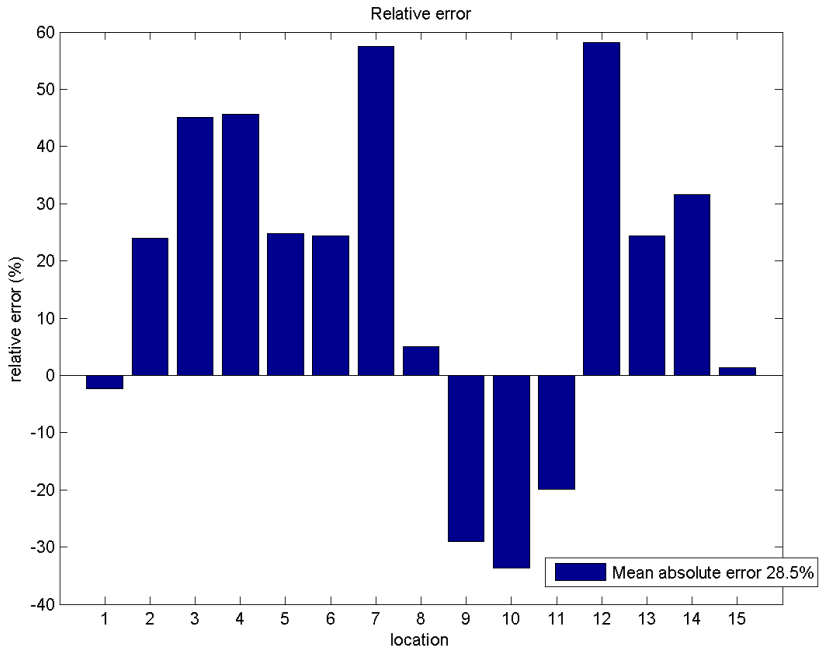


Figure 90 Relative RMS-wave height error in each measurement location

S.3 Conclusions

The inclusion of irregular wave forcing does not significantly improve the accuracy of the XBeach model. As was the case in Test 9, XBeach fails to model the peak wave heights centrally behind the shoal and does also not model the dip in the wave heights to the side and back of the shoal. The mean error in the RMS-wave height is almost 30% across the measurement locations. These results show that XBeach is not capable of very accurately modelling complex short-wave propagation in situations in which diffraction and wave focussing play an important role. It should be noted however that some improvement may still be achieved by further calibration of the model.

T Test 11

T.1 Model description

In Test 11 is designed to verify the hydrodynamics of XBeach by comparing model results to field measurements. In this case the DELILAH measurement campaign at Duck, North Carolina is selected as a suitable test location.

A simulation is set-up to model the hydrodynamic conditions at Duck on October 13th, 1990, between 10:00 and 11:00 hours. Bathymetry data and tidal water levels are respectively extracted from the daily survey data and six-minute tidal station data available on the USACE Field Research Facility online database [United States Army Corps of Engineers, 1990]. The measured short wave spectrum at the offshore edge of the model is taken from the same database. As can be seen in Figure 91, the directional spreading of the short wave field is quite large. The significant wave height at 8m water depth is 2.2m and the peak period is 10.7s. The XBeach model is forced using random wave groups based on the measured wave spectrum, see section Y.4. The numerical grid is expanded 100% in both longshore directions with a uniform bathymetry in order to minimize boundary effects in the measurement domain.

Model results are compared to measurements made in the primary cross shore array, gauge numbers 10, 20, 30, 40, 50, 60, 70, 80 and 90, see Figure 92 and Figure 93.

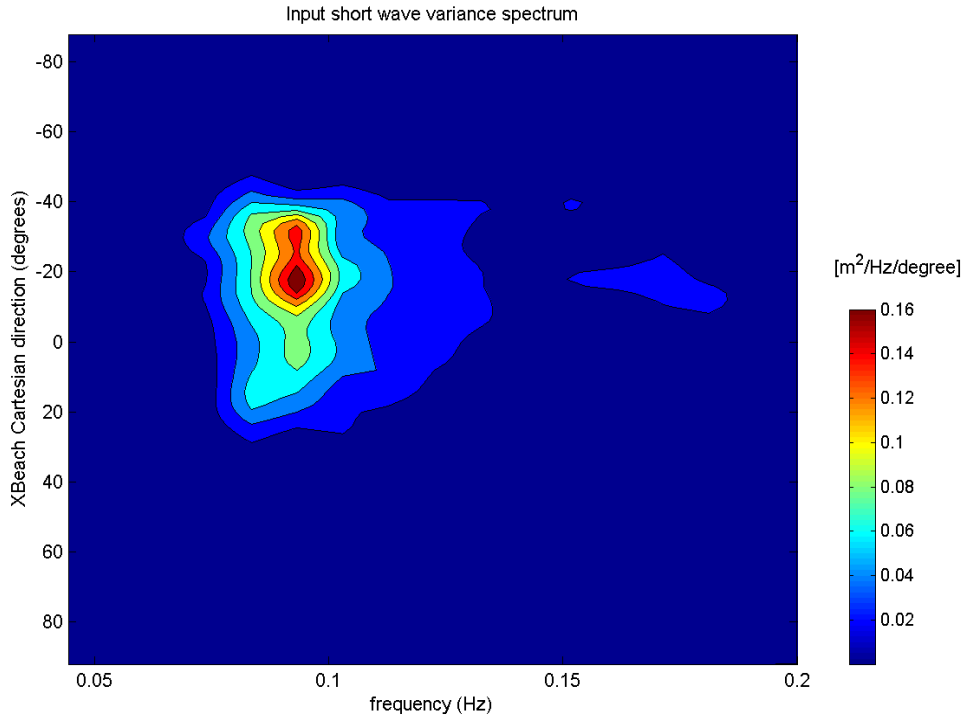


Figure 91 Short wave variance density spectrum measured at 8m water depth at the Duck FRF-8m array [United States Army Corps of Engineers, 1990]

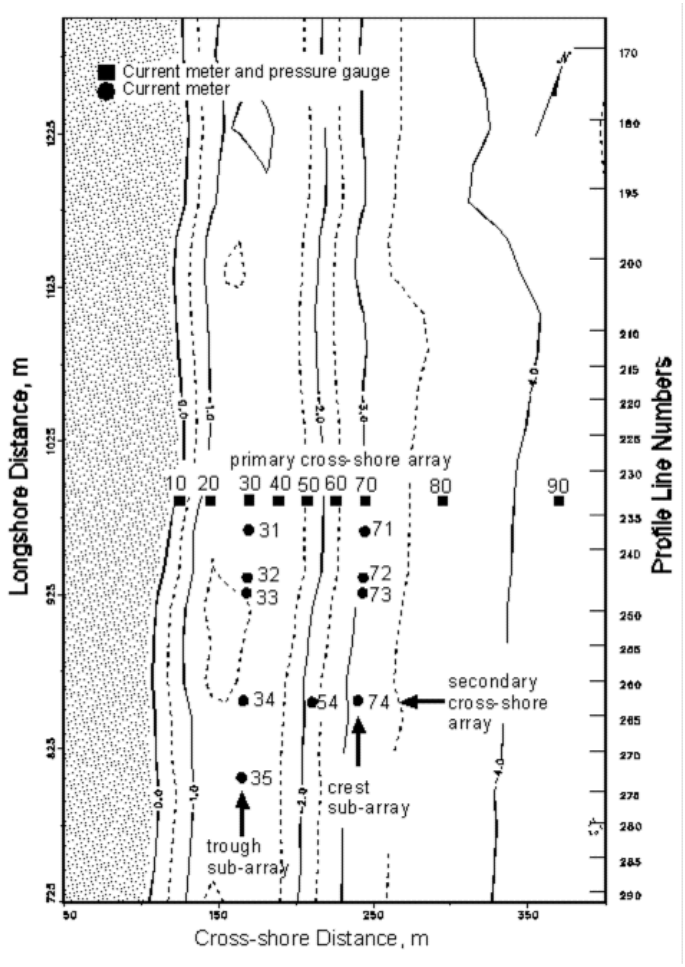


Figure 92 Name and locations of the measurement instruments used in the DELILAH campaign [United States Army Corps of Engineers, 1990]

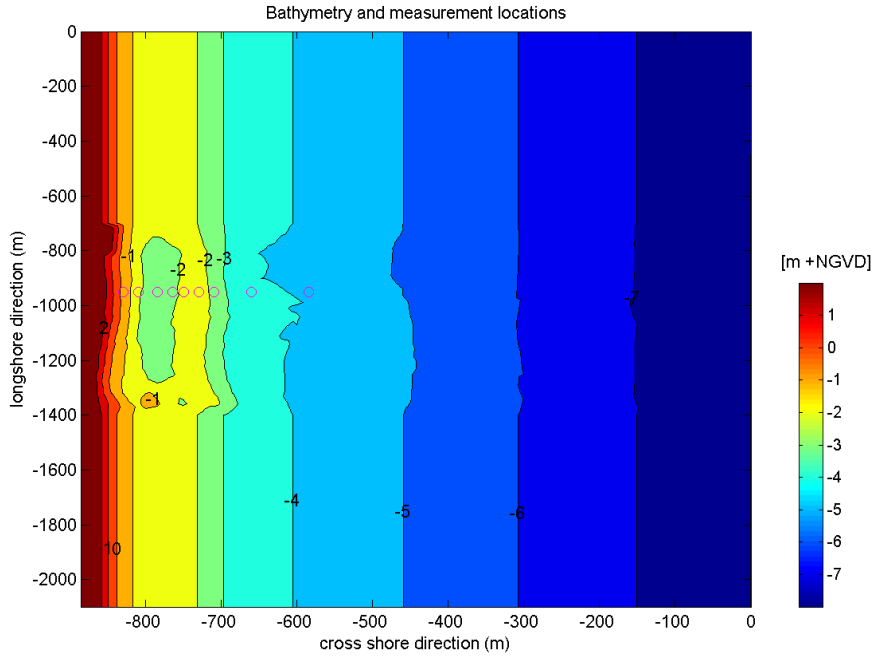


Figure 93 Model bathymetry and location of the measurement points (circles)

T.2 Results

The short wave RMS-wave heights and water levels at one point in time are shown in Figure 94. The top panel shows wave breaking occurring mainly around the -2m contour line. Landwards of this breaker zone the wave heights are more or less longshore uniform. The bottom panel shows a complex pattern of incoming and reflected infragravity waves, including waves that appear to be propagating at an angle normal to the main short wave direction. These waves may be generated by short wave interactions with very different angles, or could be the reflections of over infragravity waves off the lateral boundaries.

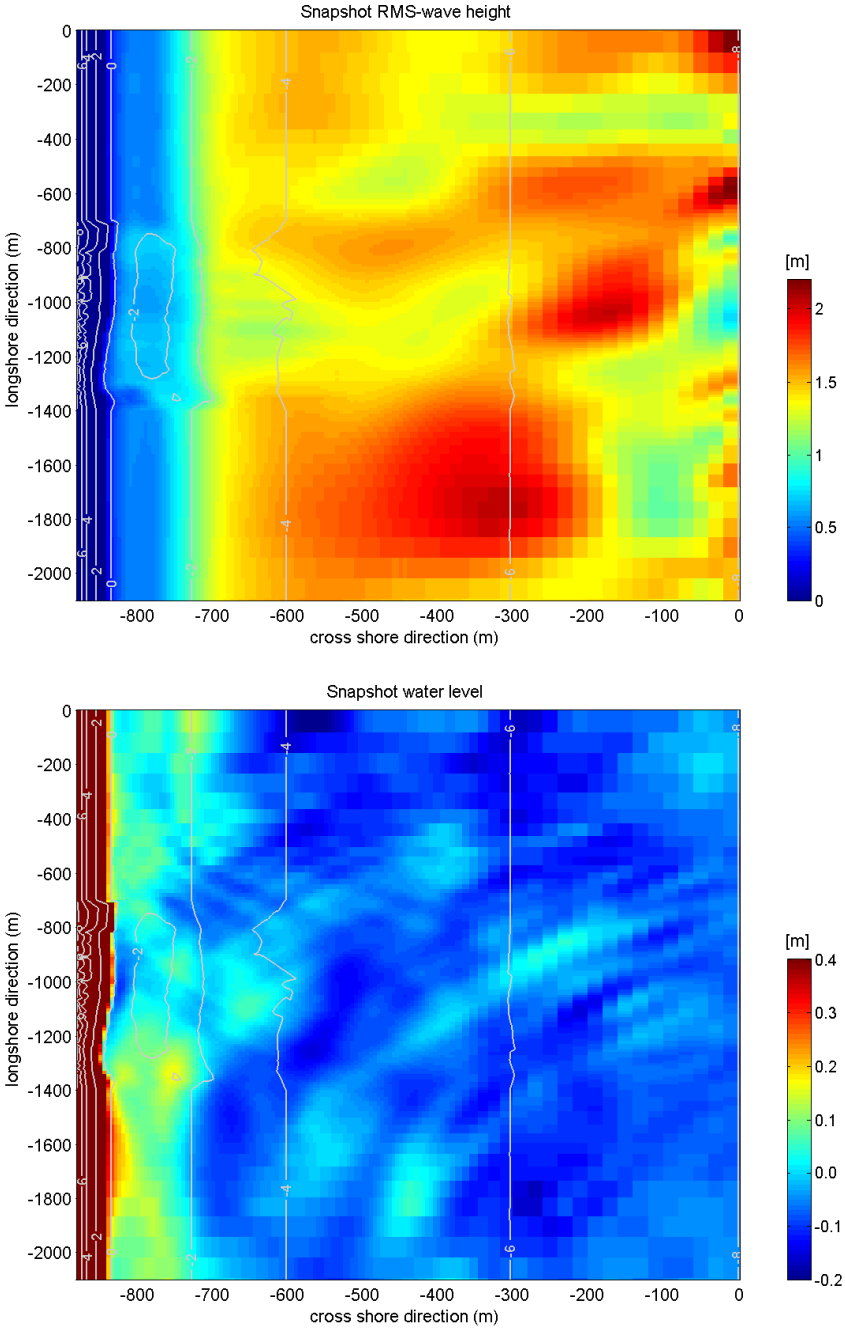


Figure 94 Snapshot of the RMS-wave heights (top panel) and water level (bottom panel)

Figure 95 shows the measured 12-minute average RMS-wave heights at the nine measurement locations in the primary cross shore array. The figure also shows the mean RMS-wave height calculated by XBeach along the same cross shore transect, as well as one standard deviation above and below the mean.
The figure shows XBeach to be quite accurate. The RMS-wave heights in locations 20, 30 and 40 are overestimated by the model. However, the difference is not great and may be improved by further calibration of the wave breaking coefficients. The measured RMS-wave heights at location 90 do not correspond with the measured offshore significant wave hight of 2.2m. It is suggested that one of the two datasets must therefore be incorrect. At this stage it assumed that the offshore wave spectrum is correct.
Figure 96 shows the mean RMS-wave height across the XBeach model domain. An area of higher average wave heights between the -4m and -6m contour lines around the -700m cross shore transect stands out in the figure. At this stage it is unclear what phenomenon is causing the local increase in wave heights. One hypothesis that is supported by Figure 97 is that the time-averaged water level may be lower in this area, thus leading to more shoaling. Complex infragravity wave interactions may be the cause of the water level lowering, although numerical errors also cannot be ignored as possible causes.

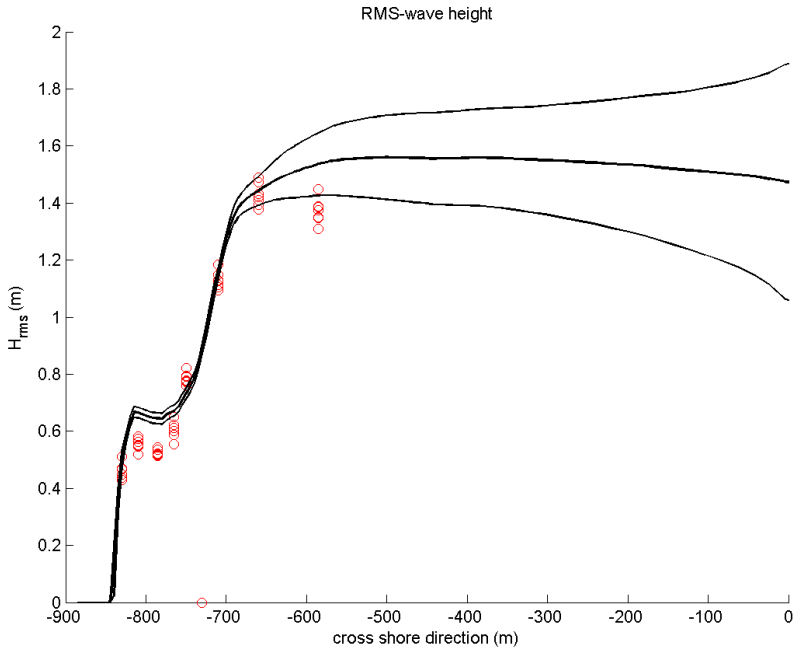


Figure 95 Measured 12-minute average RMS-wave heights (circles) and the mean and one standard deviation above and below the mean RMS-wave height in the XBeach model

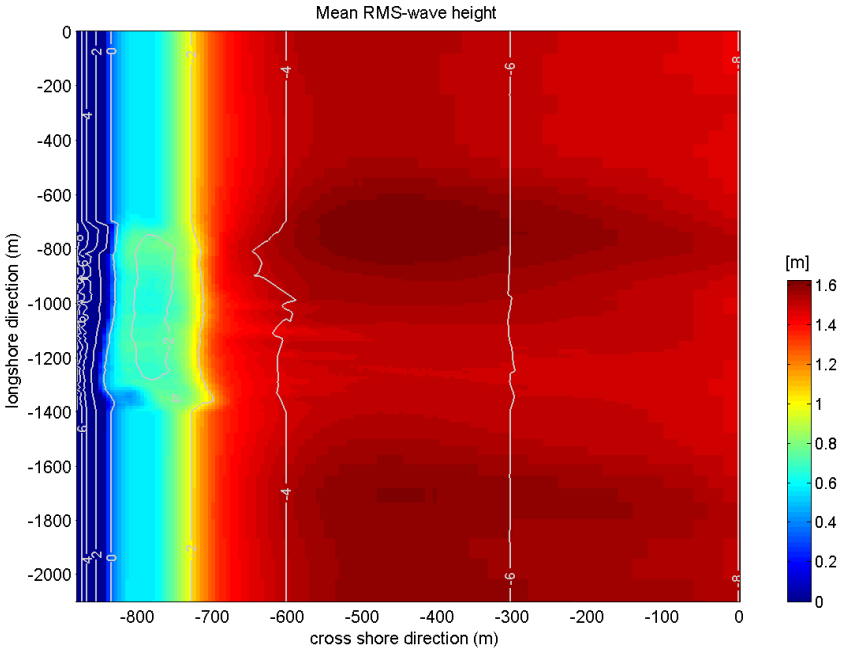


Figure 96 Mean short wave RMS-wave height in the XBeach model

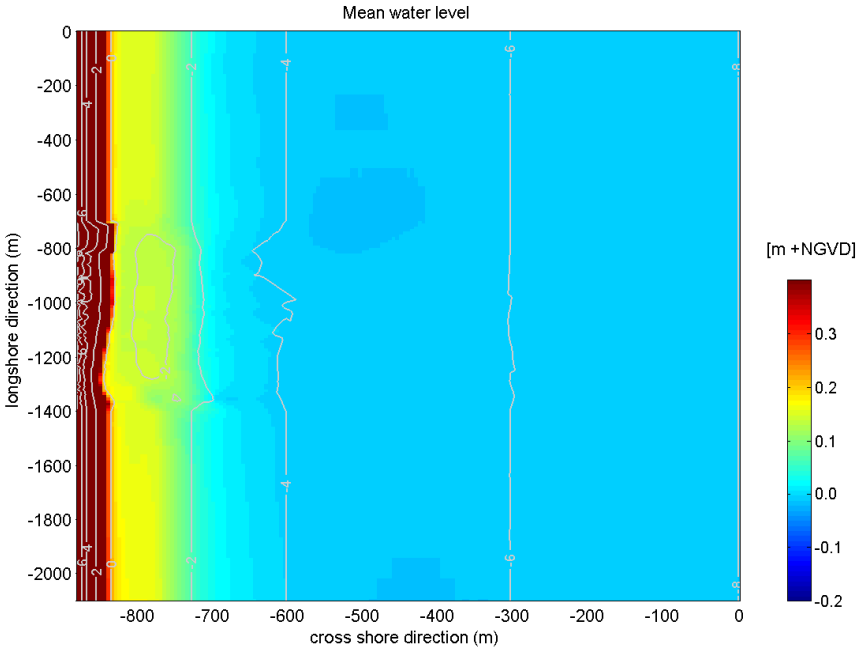


Figure 97 Mean water level in the XBeach model

As shown in Figure 98, the longshore and cross shore velocities are also fairly well represented in the XBeach model. The magnitude of the longshore Eulerian velocity corresponds well with the measured velocities. However, the XBeach results show two peaks in the longshore velocity, with one dip between the two. This cannot be found in the measured velocities. The modelled longshore velocities in locations 80 and 90 are also too low. In order to spread the longshore velocity around the peak it may be necessary to increase the horizontal viscosity term due to the cross shore gradient in the longshore current in the longshore momentum balance [Van Dongeren, private correspondence].

At this stage it is unknown why the longshore current measurements differ so greatly at location 70. It is suggested that the longshore current at this location may be varying on the timescale of a longshore current meander or shear instability. However, it is surprising that the fluctuation does not affect the neighbouring measurement locations or the cross shore velocity measurements in the same location.

The cross shore Eulerian velocity corresponds better with the measurement data. However, the magnitude of the modelled offshore current at location 10 may be too large.

Figure 99 shows the mean Eulerian velocity in the XBeach model. The figure shows an excessively strong longshore current generated on the southern lateral boundary. However, by the time the measurement domain is reached, this boundary problem has been corrected.

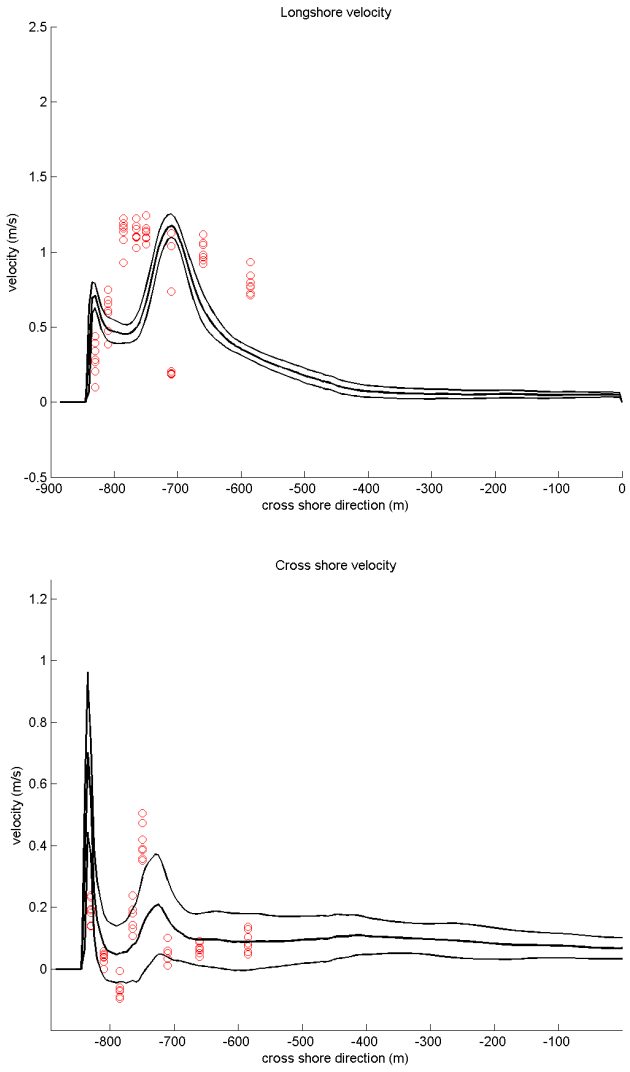


Figure 98 Measured 12-minute depth-average longshore velocity (top panel, circles) and cross shore velocity (bottom panel, circles) and the mean and one standard deviation above and below the mean longshore and cross shore Eulerian velocity in the XBeach model

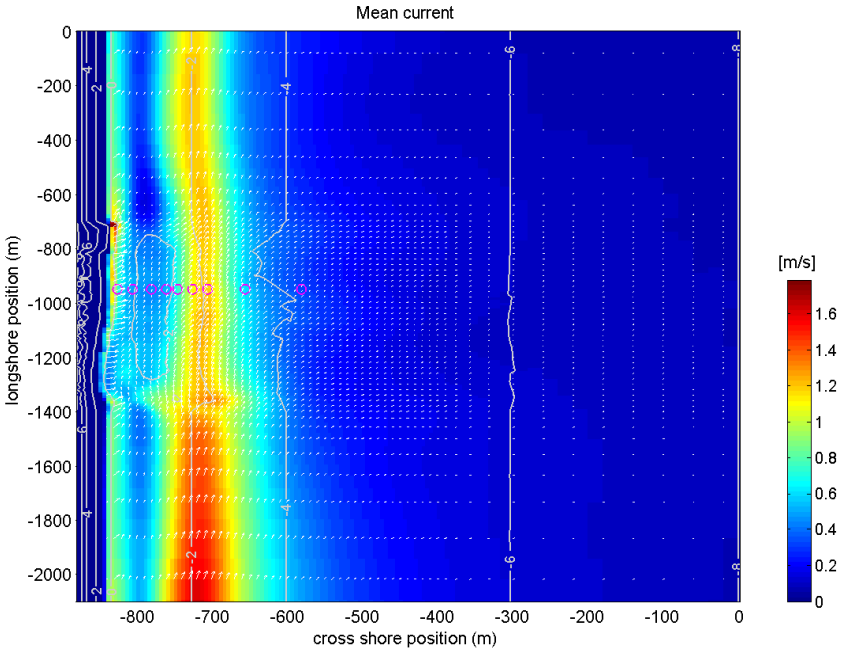


Figure 99 Mean Eulerian velocity in the XBeach model and location of the measurement points (circles)

In order to verify the infragravity wave generation and propagation in XBeach, an analysis is made of the water surface elevation in the 9 measurement locations. A similar analysis was used to verify the SHORCIRC-model using DELILAH data [Van Dongeren *et al*, 2003].

Figure 100 shows the variance density spectrum of the modelled and measured water surface elevation in measurement locations 90, 50 and 10. With an incoming short wave peak period of 10.7s, the infragravity wave band is expected to start at roughly 0.045 Hz and peak at 0.023 Hz. The measured variance density spectrum in Figure 100 shows a clear transition from wave energy in the short wave band in location 90 to the infragravity and very low frequency bands in location 10. This trend is also followed by the XBeach model. However, the variance density in the XBeach model is clearly less than the measured variance density. Furthermore, the XBeach model seems to contain more variance in the very low frequency band than in the infragravity wave band. It is suggested that this is because the variance in the very low frequency band is generated by other mechanisms, for instance longshore current instabilities.

Using the method suggested by Van Dongeren *et al* [2003], the RMS-wave height of the infragravity waves is calculated:

$$H_{rms,ifg} = \sqrt{8 \int_{0.005\,Hz}^{0.05\,Hz} Sdf} \qquad \text{(T.1)}$$

The RMS-wave heights of the measured and modelled infragravity waves for all nine measurement locations are shown in Figure 101. Following the example of Van Dongeren *et al* [2003], a second simulation is carried out without directional spreading of the short waves. The RMS-wave heights of the infragravity waves generated in this simulation are also shown in Figure 101.

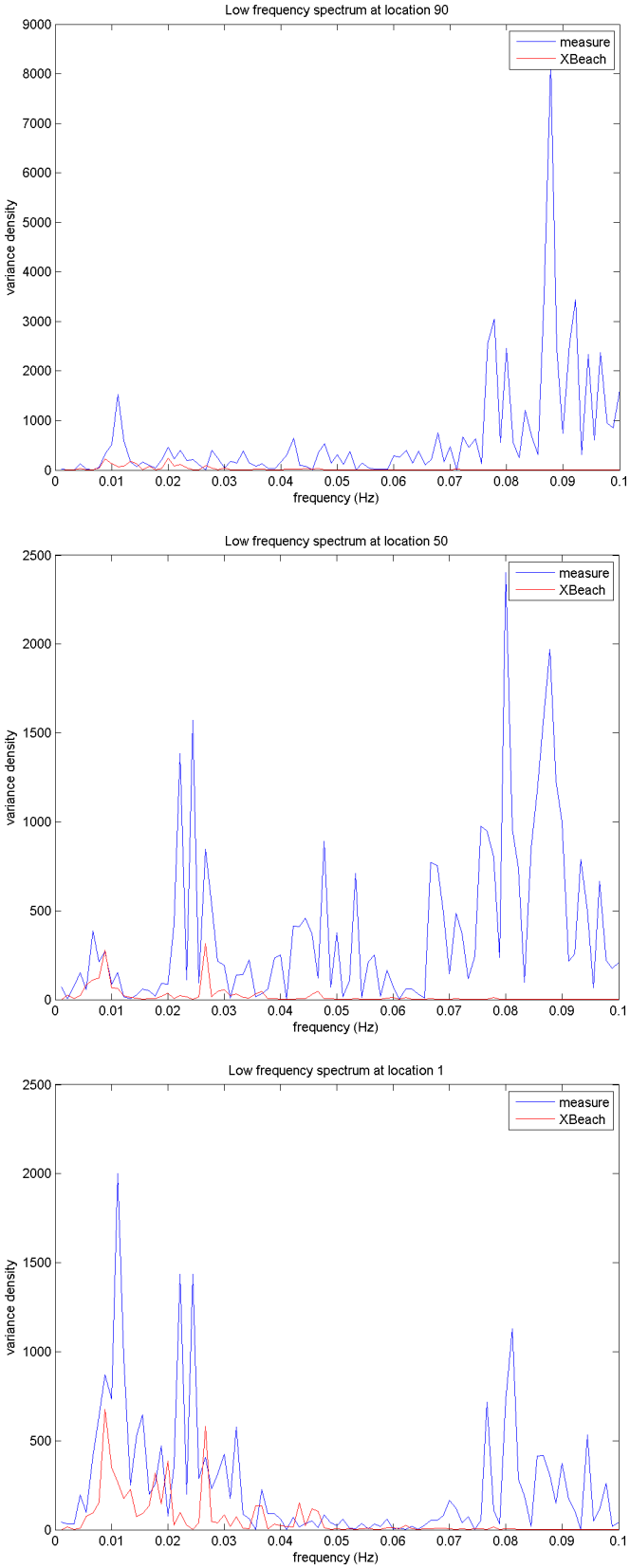


Figure 100 Measured and modelled water surface elevation variance in the low frequency band in measurement location 90 (top panel), 50 (middle panel) and 10 (bottom panel).

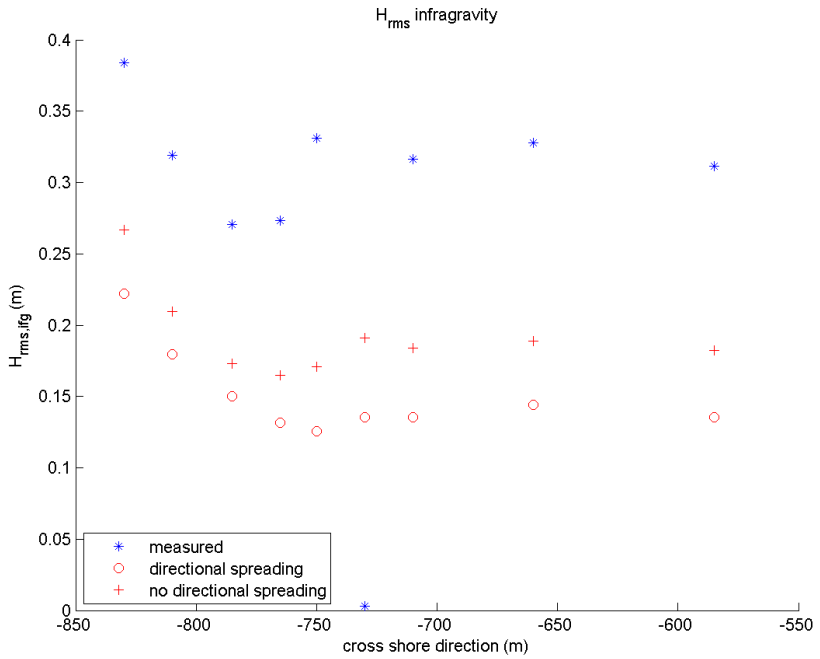


Figure 101 RMS-wave height of the measured and modelled infragravity waves

Figure 101 clearly shows that the infragravity wave height is underestimated by a factor of two in the regular XBeach model. Unlike in the results of Van Dongeren *et al* [2003], the simulation with no direction spreading in the short wave field does not overestimate the infragravity wave height, but instead remains significantly lower.

T.3 Conclusions

Test 11 shows that in general the short wave propagation and longshore and cross shore current generation are reasonably well represented in the XBeach model. It is expected that the inaccuracies in these processes can be improved by further calibration and the introduction of more complex horizontal eddy viscosity.

Test 11 also shows that the infragravity wave energy is significantly underestimated. There are three possible explanations for this.

The first is that the measurement data are incorrect. It is considered to be very unlikely that at all nine measurement locations would produce erroneous data. However, the possibility exists that the offshore wave spectrum data are incorrect, thus leading to too little forcing on the offshore boundary. In order to examine this, the measured short wave variance density is multiplied by 1.5 and used in a new calculation. As can be seen in Figure 102 the effect of this increase is not great. Therefore this cause can be disregarded in further analysis.

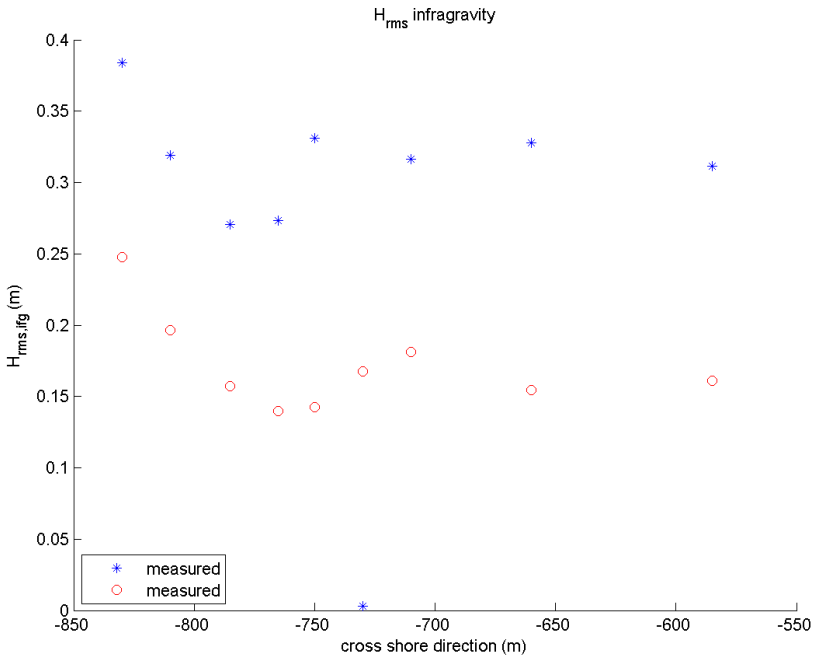


Figure 102 RMS-wave height of the measured and modelled infragravity waves in the case of increased short wave variance density on the offshore boundary

The second explanation is that not enough infragravity wave energy is imposed on the offshore boundary by the internal boundary condition generator. The third explanation is that the model does not transfer sufficient amounts of energy from the short waves to the infragravity waves in the shoaling zone or dissipates too much infragravity wave energy. The second and third explanations are discussed below.

T.3.1 Insufficient infragravity wave energy generated on the boundary

Figure 100 shows a clear lack of infragravity wave energy in the most offshore measurement point. This may suggest that not enough infragravity wave energy is imposed on the offshore boundary in the first place. In order to examine this, a simulation is carried out in which the cross shore flux imposed on the offshore boundary is increased tenfold prior to being used in the XBeach simulation. This enhanced flux should increase the variance in the infragravity frequency band. The resulting infragravity wave heights are shown in Figure 103.

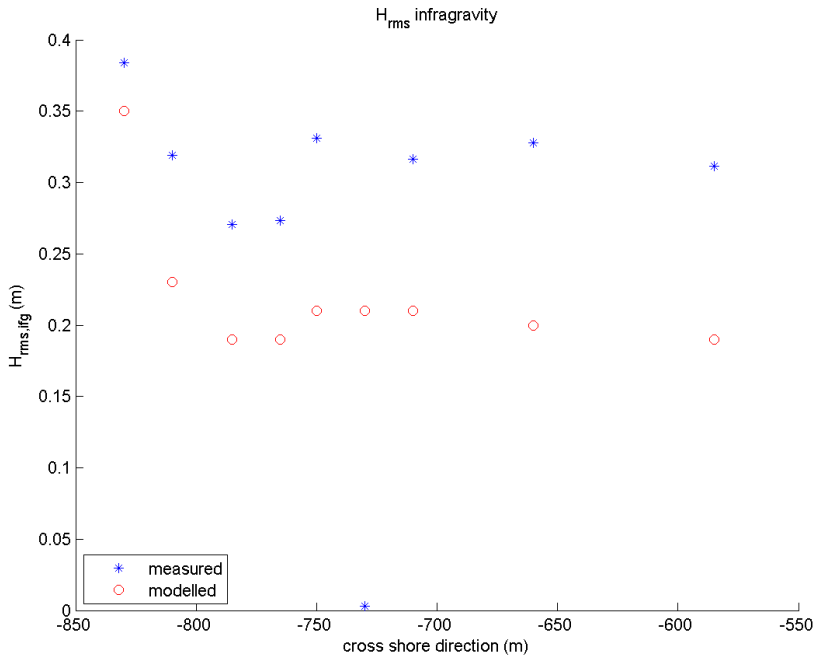


Figure 103 RMS-wave height of the measured and modelled infragravity waves in the case of ten times more infragravity flux on the offshore boundary

As Figure 103 shows, the effect of an increased imposed flux is merely a slight increase in infragravity wave height in deep water and an enormous increase in shallow water. It should be noted however that the increased infragravity energy in the shallow areas is mainly due to increased energy levels in the very low frequency band. Therefore simply increasing the amount of infragravity energy on the offshore boundary is unlikely to improve the model.

T.3.2 Internal infragravity wave issues

As shown in Test 6g, the variance in the water level can be dependent on the numerical grid size. In order to determine if this is the problem, a new simulation should be carried out on a different numerical grid size.
Numerical or physical dissipation of infragravity wave energy is one possible explanation of the reduced wave heights in the model. However, other studies, e.g. Van Thiel de Vries *et al.* [2006], show that in one-dimensional mode this is not an issue. It seems unlikely therefore that dissipation can be the problem given the fact that long-wave propagation is correct using other boundary conditions in 2DH-mode. Similarly, comparisons with 1D-models show that the transfer of energy from the short waves to the infragravity waves works correctly.

T.3.3 Discussion

The most likely cause for the limited infragravity wave height in the XBeach model is that too little variance in the forcing on the offshore boundary is generated in the infragravity wave band. Instead variance is generated in lower frequencies. As shown by Battjes *et al.* [2004], low frequency bound waves shoal according to Green's law. Since the measured infragravity waves shoal faster, approaching the theory of Longuet-Higgins and Stewart

[1962b], they will exceed the wave heights of the infragravity waves in the XBeach model. Another explanation is that the group velocity of the incoming short waves is defined using the mean period of the waves. This leads to a group velocity that may be too low to transfer energy to the bound long waves. Both mechanisms are currently being investigated.

U Test 12

U.1 Model description

In order to examine if XBeach will remain stable and produce realistic results under overwash conditions, a one-dimensional test is set up. A simple Gaussian curve is used to represent the bed level of a schematic barrier island. A constant water level is imposed on the offshore boundary, one meter lower than the top of the barrier island. The offshore boundary is forced by irregular waves with a significant wave height of 3.0m. The simulation is first carried out without morphological development to ensure the hydrodynamics are stable. A second test is carried out with morphological development to ensure the morphodynamics are stable.

U.2 Results

Figure 104 shows the hydrodynamics around the barrier island at a certain point in time in the non-morphodynamic calculation. The figure shows one infragravity wave front about to cross the crest of the island. On the lee side of the island, the remains of an earlier overwashing infragravity wave propagates toward the back barrier boundary. The short wave envelope decreases enormously across the island due to breaking. Very little short wave energy remains in the back barrier bay. The Eulerian cross shore velocity shows that the back barrier is covered by a thin layer of water moving rapidly toward the back barrier bay. The Froude number of this flow is in the order of 2.

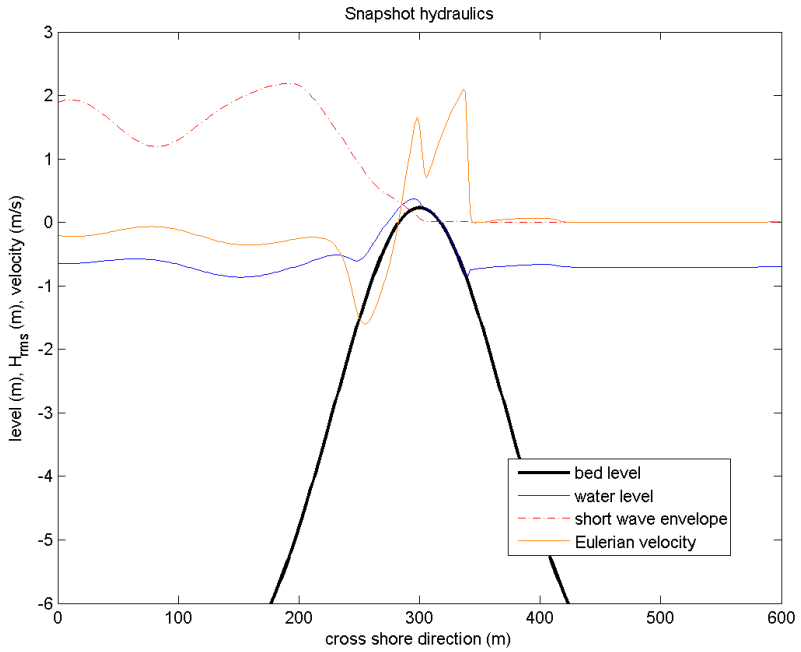


Figure 104 Hydrodynamics of runup overwash without morphological development

Some results of the morphological development of the barrier island in the second simulation are shown in Figure 105. The three plots show clearly that the back barrier slope erodes first, creating a washover delta-type feature. The figure also shows that the back barrier develops ripples before becoming completely smooth (Figure 105, bottom panel). These features may be physical, i.e. anti-dunes due to the supercritical flow, or numerical artefacts due to the cut-off depth used in the sediment transport calculations.

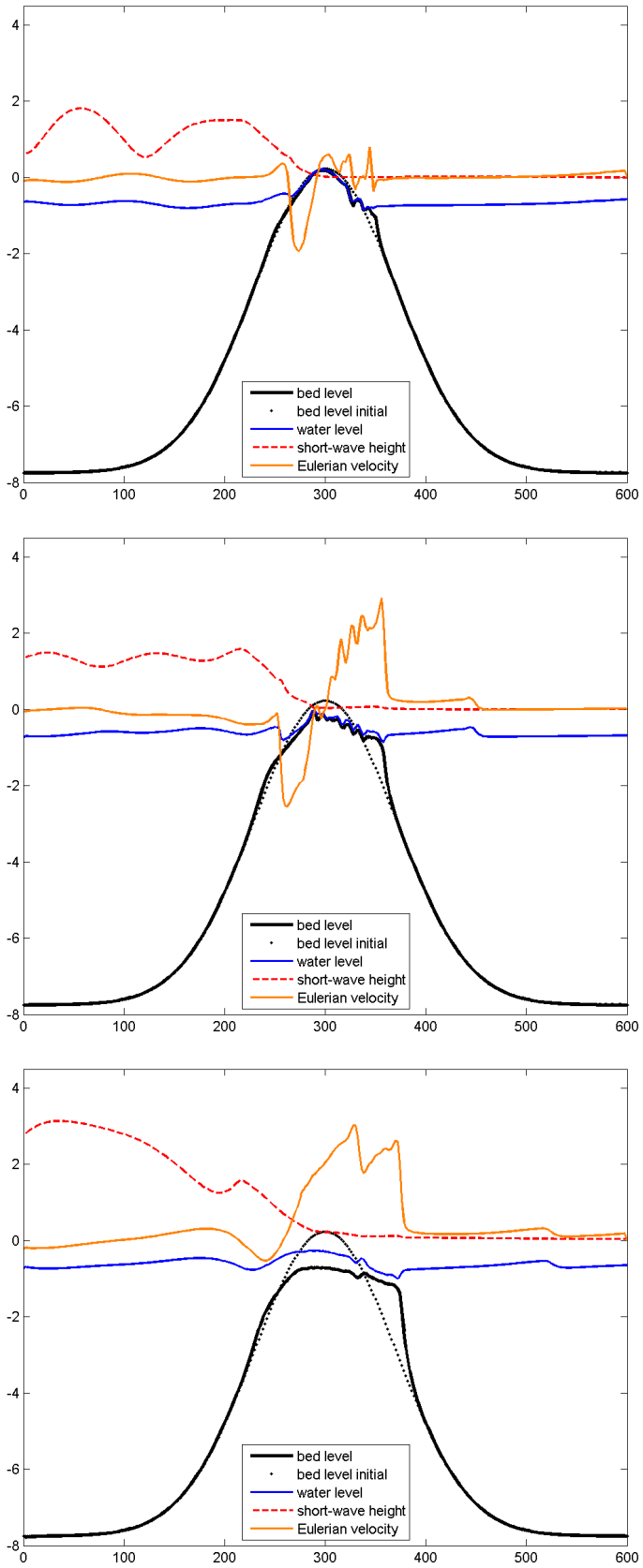


Figure 105 Hydrodynamics and morphological development after 300 seconds (top panel), 1200 seconds (middle panel) and 2500 seconds (bottom panel)

U.3 Conclusions

In one-dimensional mode XBeach remains stable during overwash conditions. The hydrodynamic development across the barrier island appears to be physically sound. The morphological development appears to be physically plausible, but possibly too fast. The development of ripples on the back barrier is not confirmed to be physically correct.

V Test 13

V.1 Model description

In order to examine if XBeach will remain stable and produce realistic results under overwash conditions in a two-dimensional model, a second overwash model is set up. The Gaussian curve bed used in Test 12 is used. The crest height of the barrier island is varied sinusoidally in longshore direction to produce to depressions. A constant water level is imposed on the offshore boundary, one meter lower than the top of the barrier island. The offshore boundary is forced by irregular waves with a significant wave height of 3.0m. The simulation is first carried out without morphological development to ensure the hydrodynamics are stable. A second test is carried out with morphological development to ensure the morphodynamics are stable.

V.2 Results

Figure 106 shows the water surface elevation at one point in time in the simulation without morphological development. The incoming waves are slightly obliquely incident, which can be seen in the lag between the two overwash tongues. Overwash takes place almost exclusively in the two depressions.

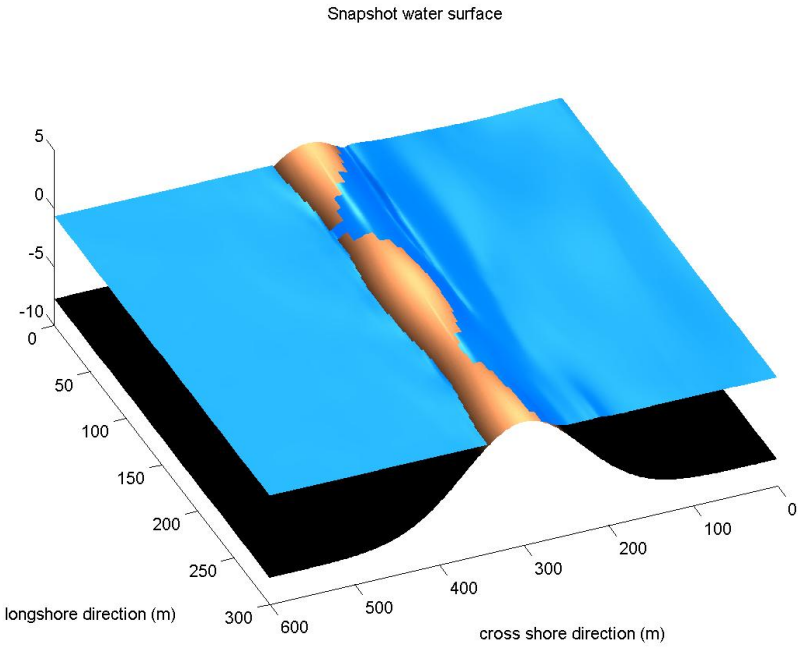


Figure 106 Water level at one moment in time without morphological development. Waves entering from the right hand side.

The morphological development of the barrier island is shown in Figure 107. Some erosion takes place in the depressions, leading to more concentration of overwash in these locations. The washover locations develop the same ripples found in Test 12. Both washover locations develop washover fans.

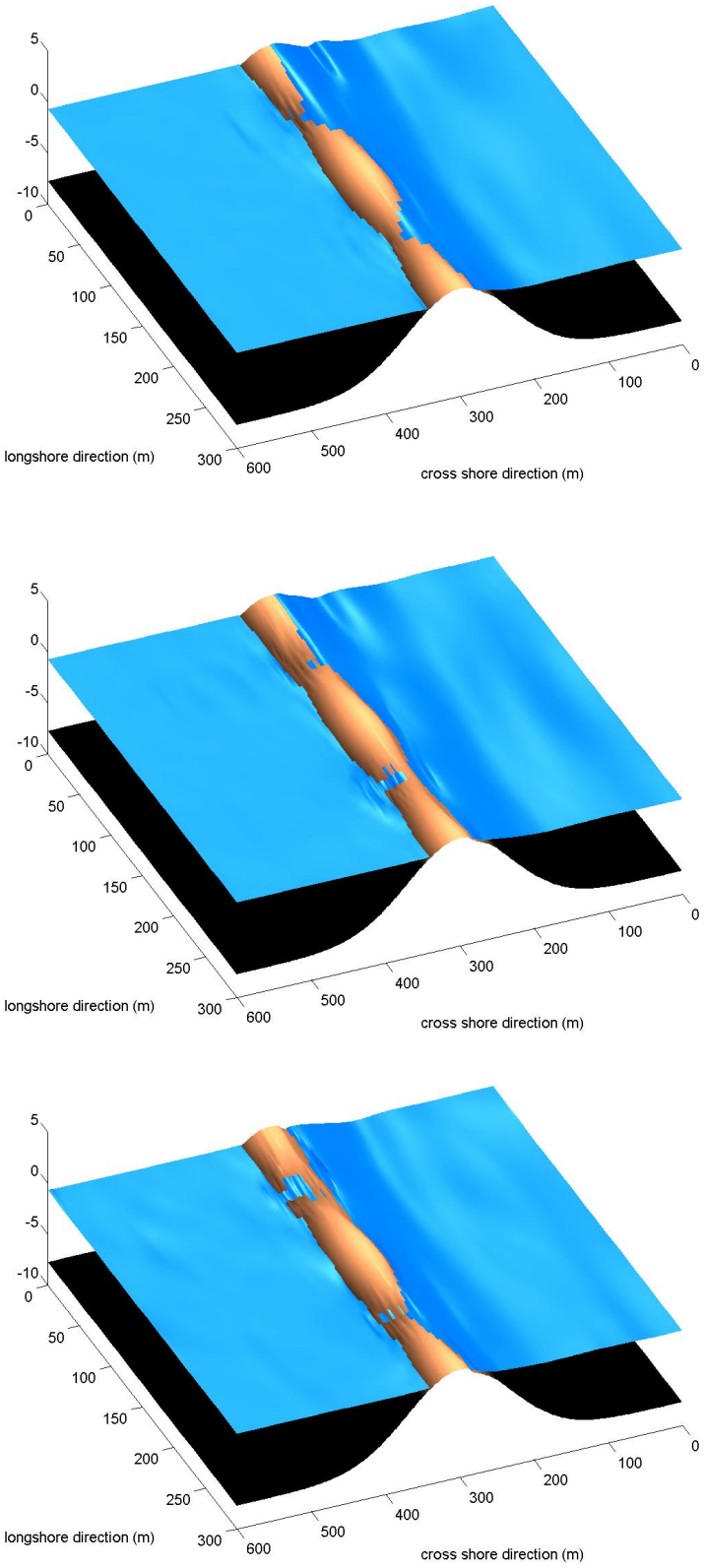


Figure 107 Water surface and morphological development after 300 seconds (top panel), 600 seconds (middle panel) and 1000 seconds (bottom panel)

V.3 Conclusions

Test 13 shows that XBeach remains stable under overwash conditions in two-dimensional mode. At this stage it is unclear whether the amount of morphological change is accurate. The simulation without morphological development shows an important difference between 1D- and 2D-hydrodynamic calculations. In Test 12, a lot of infragravity waves overwashed the barrier island. In Test 13 the waves generally only overwash the depressions, which are lower than the crest of the barrier island in Test 12. This can be explained by the fact that in the 2D-simulation the infragravity waves have the possibility to extend laterally, rather than being confined by numerical walls in the 1D-simulation. XBeach may therefore overestimate natural overwash in the 1D-case. The 1D-simulations can still be used however to model overwash in wave flume experiments.

W Semi-analytical linear wave model

In order to compare the results of XBeach with linear wave theory, a simple model is set up to compute several wave parameters. The model is described in this appendix. A description of the theory used in this model can be found in Appendix A. The model can only be applied to stationary longshore uniform wave and bathymetry conditions. Wave breaking is taken into account locally, but energy loss is only advected forwards. Therefore offshore bars may not be modelled properly.

The model is designed to calculate wave parameters along a cross-shore transect. The user supplies the bathymetry data and various starting conditions. The model then calculates output at every point given in the bathymetry data.
First the local wave length is calculated by iteration of the following relation until the wave length error is less than 5mm:

$$L = L_0 \tanh\left(\frac{2\pi h}{L}\right) \tag{W.1}$$

With this, the wave number can be calculated and the wave celerity and wave group velocity:

$$c = c_0 \tanh\left(\frac{2\pi h}{L}\right) \tag{W.2}$$

$$c_g = c\left(\frac{1}{2} + \frac{kh}{\sinh(2kh)}\right) \tag{W.3}$$

The wave direction is calculated using Snell's law:

$$\sin\theta = \sin\theta_0 \frac{c}{c_0} \tag{W.4}$$

No dissipation is included in the model, therefore:

$$\frac{H}{H_0} = \sqrt{\frac{c_{g_0}}{c_g}}\sqrt{\frac{\cos(\theta_0)}{\cos(\theta)}} \tag{W.5}$$

Breaking is included by ensuring the wave height is never greater than the local depth multiplied by the breaker coefficient:

$$H = \max(H, \gamma h) \tag{W.6}$$

The advection of energy loss due to breaking is taken into account by stating that the wave energy flux cannot grow in shoreward direction, thereby limiting wave height behind an offshore bar:

$$F = \frac{1}{8}\rho g H^2 c_g \tag{W.7}$$

$$\frac{dF}{dx} = \min\left(\frac{dF}{dx}, 0\right) \tag{W.8}$$

The radiation stresses are calculated next. As the model assumes longshore uniformity, S_{yy} is not calculated.

$$\begin{aligned} S_{xx} &= \left(n - \frac{1}{2} + n\cos^2(\theta)\right)E \\ S_{yx} &= \left(n\cos(\theta)\sin(\theta)\right)E \end{aligned} \tag{W.9}$$

From this point onwards the numerical approximations are introduced into the model. The wave set-up and set-down is calculated by forward numerical differentiation of the radiation stress:

$$\begin{aligned} dz &= \frac{-\left(S_{xx}(i) - S_{xx}(i-1)\right)}{\rho g \frac{1}{2}\left(h(i) + h(i-1)\right)} \\ z(i) &= z(i-1) + dz \end{aligned} \tag{W.10}$$

The longshore velocity is calculated by assuming a balance between the forward numerical radiation stress gradient and the bottom friction generated by the longshore current:

$$v(i) = \sqrt{\frac{-C^2}{\rho g}\frac{S_{yx}(i) - S_{yx}(i-1)}{x(i) - x(i-1)}} \tag{W.11}$$

Note that this model does not include viscosity, so the longshore velocity will include unrealistically large cross-shore gradients.

The model is programmed in MathWorks Matlab language. The code is given below.

```
function [L,k,c,cg,n,H,phi,z,Sxx,Syx,v] = &
          anashoaling(x,zb,Hstart,Tstart,phistart,zstart,chezy)

L = zeros(length(zb),1);
k = zeros(length(zb),1);
c = zeros(length(zb),1);
cg = zeros(length(zb),1);
n = zeros(length(zb),1);
a = zeros(length(zb),1);
H = zeros(length(zb),1);
phi = zeros(length(zb),1);
z = zeros(length(zb),1);
Sxx = zeros(length(zb),1);
Syx = zeros(length(zb),1);
v = zeros(length(zb),1);

g=9.81;
rho=1000;
gamma=0.55;
a(1)=0.5*Hstart;
H(1)=Hstart;
L0=g*Tstart^2/(2*pi);
c0=g*Tstart/(2*pi);
z(1)=zstart;
v(1)=0;
h=zstart-zb;
phi(1)=phistart;
h=max(h,0.0001);

for i=1:length(h)
    % iterate L
    L1=L0;
    L2=0;
    m=0;
    while (m<1)
        L2=L0*tanh(2*pi*h(i)/L1);
        if ((abs(L1-L2))<0.005)
            m=m+1;
        end
        L1=L2;
    end
    L(i)=L2;
    k(i)=2*pi/L(i);
    kh=k(i)*h(i);

    c(i)=c0*tanh(2*pi*h(i)/L(i));
    n(i)=0.5+(kh/sinh(2*kh));
    cg(i)=c(i)*n(i);
    sinphi=sind(phistart)*c(i)/c(1);
    phi(i)=asind(sinphi);
    a(i)=a(1)*sqrt(cg(1)/cg(i))*sqrt(cosd(phistart)/cosd(phi(i)));
    H(i)=2*a(i);

    H(i)=max(H(i),0);
    H(i)=min(H(i),gamma*h(i));
    E(i)=1/8*rho*g*H(i)^2;
    F(i)=E(i)*cg(i);
```

```
    if i>1
        F(i)=min(F(i-1),F(i));
        E(i)=F(i)/cg(i);
        H(i)=sqrt(E(i)*8/(rho*g));
    end


    % Wave setup / set down
    Sxx(i)=(n(i)-0.5+n(i)*cosd(phi(i))^2)*E(i);
    Syx(i)=(n(i)*sind(phi(i))*cosd(phi(i)))*E(i);



    % Wave setup / set down
    Sxx(i)=(n(i)-0.5+n(i)*cosd(phi(i))^2)*1/8*rho*g*H(i)^2;
    Syx(i)=(n(i)*sind(phi(i))*cosd(phi(i)))*1/8*rho*g*H(i)^2;

    if i>1
        deta=(Sxx(i)-Sxx(i-1))/(-1*rho*g*0.5*(h(i)+h(i-1)));
        z(i)=z(i-1)+deta;
        v(i)=sqrt((-1*chezy^2/(rho*g))*&
             (Syx(i)-Syx(i-1))/((x(i)-x(i-1))));
    end
end
```

X Bathymetry data

X.1 Longshore uniform bathymetry

This bathymetry is based on the experiments carried out by Van Gent *et al*. [2006]. The profile of this wave flume test is extended in longshore direction. The numerical grid size is 1 meter in cross shore direction and 10 meters in longshore direction.

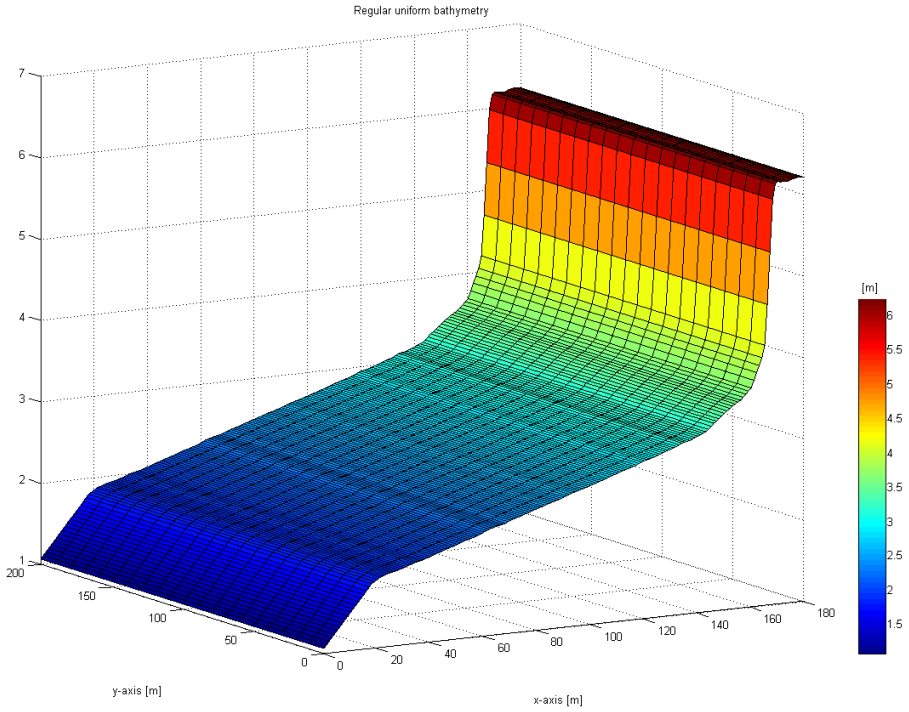


Figure 108 Regular longshore uniform bathymetry

X.2 Longshore non-uniform bathymetry

A longshore bar is formed in the bathymetry of the longshore uniform case. However, a submerged bar is added to the foreshore. The height of the bar is calculated from:

$$Z_{bar}(x,y) = 4.5 - \sqrt{\left(\frac{(x-130)}{8}\right)^2 + \left(\frac{(y-100)}{30}\right)^2} \qquad \text{(X.1)}$$

The height of the bar is limited to 4m:

$$Z_{bar}(x,y) = \min\left(Z_{bar}(x,y), 4\right) \qquad \text{(X.2)}$$

The bathymetry data are found by taking the maximum value of the regular longshore uniform bathymetry and the bar bathymetry:

$$Z_{non-uniform}(x,y) = \max\left(Z_{uniform}(x,y), Z_{bar}(x,y)\right) \quad \text{(X.3)}$$

In order to keep lateral boundary problems from the study area, the non-uniform bathymetry is extended using uniform bathymetry in longshore direction by 50% in each direction.

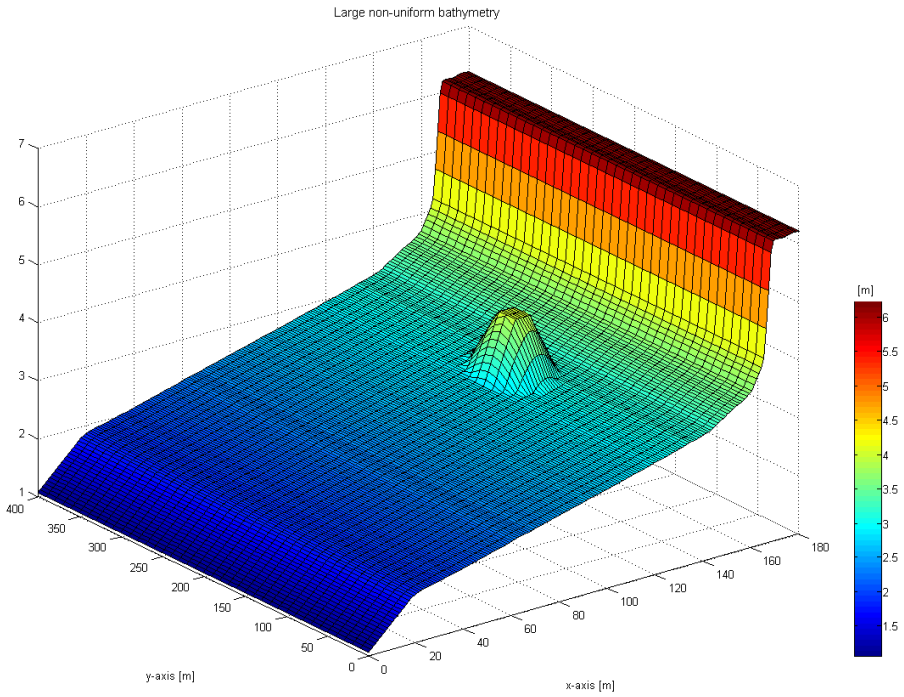


Figure 109 Large longshore non-uniform bathymetry

X.3 Irregular non-uniform bathymetry

The irregular numerical grid is made by focussing around the bar in the non-uniform bathymetry. Three areas are specified in the longshore direction; on left of the bar, one right and one centred on the bar. Similarly three areas are specified in the cross shore direction; one in deep water, one in intermediate water depths and one in shallow water. The properties of these areas can be found in Table 2.

Table 2 Definition of calculation areas

	Bounds in longshore or cross shore direction	**Grid size in longshore or cross shore direction**
Longshore area 1	0m – 140m	10m
Longshore area 2	140m – 260m	5m
Longshore area 3	260m – 400m	10m
Cross shore area 1	0m – 80m	5m
Cross shore area 2	80m – 100m	2.5m
Cross shore area 3	100m – 180m	1m

Y User guide spectrum-based boundary conditions

This user guide was written for the release of XBeach version 9.0. The guide was added to the main user manual. The purpose of the guide is to familiarise the user with the new wave boundary condition options incorporated in XBeach version 9.0 and higher.

Y.1 Spectrum-based non-stationary wave boundary conditions

XBeach has been modified to handle non-stationary wave boundary conditions. An internal module computes the incoming short-wave energy and bound long-wave mass flux from a user-specified wave variance-density table or standard JONSWAP parameters. This memo describes the use of these boundary conditions in XBeach.
User input
The user input options now include instat = 4, 5, 6 or 7 in *params.txt*. The meaning of each is summarised below:
Instat 4: Standard JONSWAP spectrum, based on user-input spectrum coefficients
Instat 5: Unmodified SWAN 2D spectrum output file
Instat 6: Formatted variance-density spectrum file
Instat 7: Reuse boundary condition files from an earlier XBeach simulation

The new module in XBeach converts the input spectral data into boundary condition time series that can be read by the main XBeach program. Boundary condition time series that are created from input spectral data are non-stationary. Due to the randomness used to generate the time series, see *Theory*, no two time series generated from the same input data will be identical. They will however share the same statistical properties. The user can avoid random variations between simulations by reusing the boundary condition time series of an earlier XBeach simulation.

The user has the option to carry out the simulation using one wave spectrum during the entire simulation period. In this case the spectral properties of the generated waves will be constant in time. Alternatively, the user may choose to vary the spectral properties of the boundary conditions in time. In this case the spectral properties of the generated waves depend on a time series of input spectral data.

The steps that should be taken for an XBeach simulation using the new wave boundary conditions are explained in the following sections. The reader is advised to consult Figure 1 to determine which sections are relevant to the simulation.

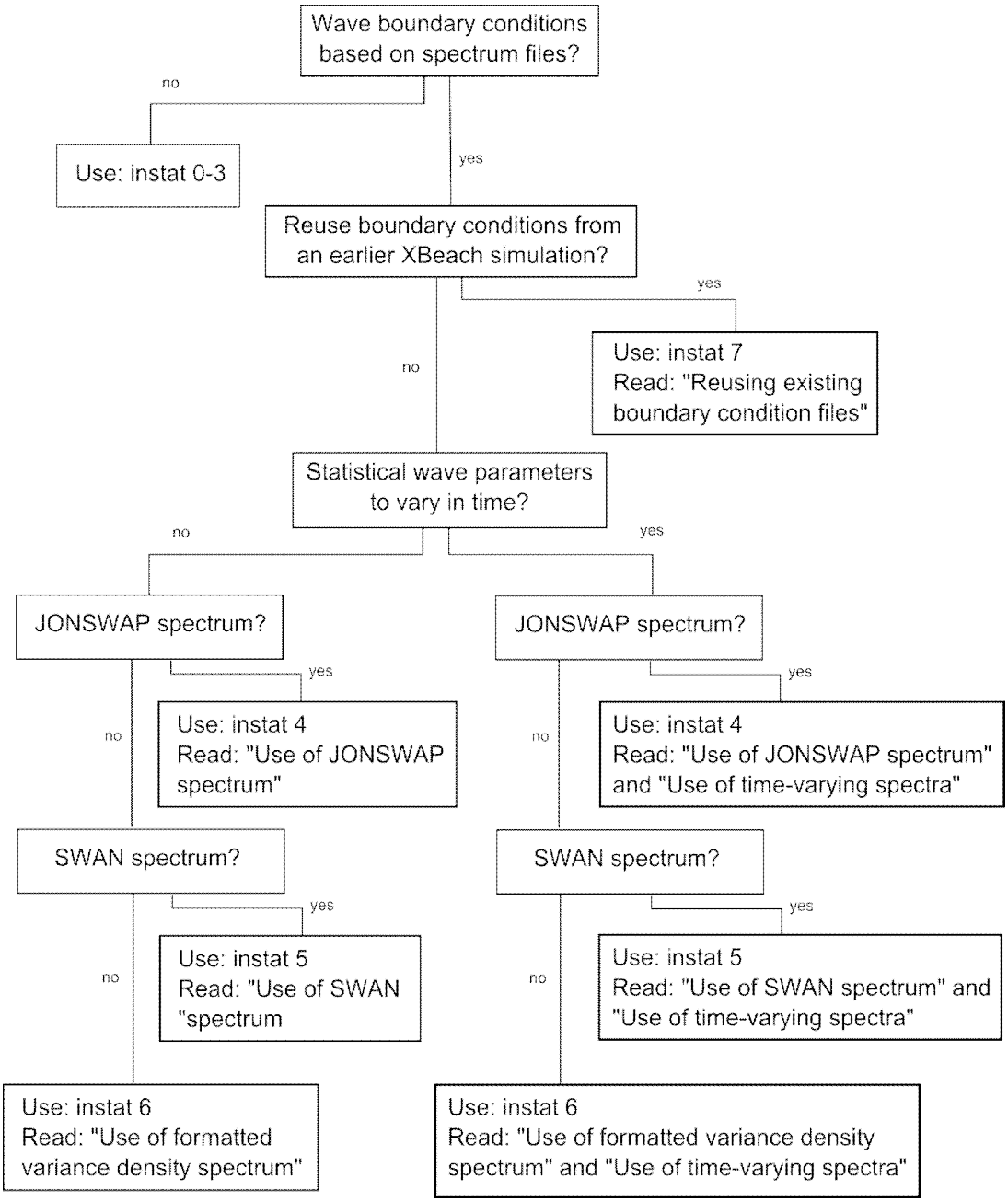


Figure 110 Reading guide

Y.2 Use of JONSWAP spectrum

The new XBeach module allows the user to provide JONSWAP parameters from which XBeach computes a spectrum.

To make use of this option, the user must specify 'instat = 4' in *params.txt*. XBeach will then attempt to read JONSWAP parameters from a separate file specified by '*bcfile* =' in *params.txt*. The user must also state in *params.txt* the required record length for the boundary condition file and the boundary condition file time step (keywords '*rt* = ' and '*dtbc* = ' respectively). If the record length (*rt*) is less than the total simulation time, XBeach will reuse the boundary condition file until the simulation is completed. The boundary

condition file time step should be small enough to accurately represent the bound long wave, but need not be as small as the time step used in XBeach, see *Explanation of input/output*.

The contents of the file specified by '*bcfile* =' in *params.txt* is a list of keyword = value combinations which determine the JONSWAP spectrum. These keywords are:

Keyword	Type	Description	Default	Minimum	Maximum
'Hm0 = '	real	H_{m0} of the wave spectrum, significant wave height [m]	0.0	0.0	5.0
'fp = '	real	Peak frequency of the wave spectrum [s^{-1}]	0.08	0.0625	0.4
'gammajsp = '	real	Peak enhancement factor in the JONSWAP expression [-]	3.3	1.0	5.0
's = '	real	Directional spreading coefficient, cosine law [-]	10.	1.0	1000.
'mainang = '	real	Main wave angle (in nautical terms) [°]	270.	180.	360.
'fnyq = '	real	Highest frequency used to create JONSWAP spectrum [s^{-1}]	0.3	0.2	1.0
'dfj = '	real	Step size frequency used to create JONSWAP spectrum [s^{-1}]	fnyq/200	fnyq/1000	fnyq/20

All variables are optional. If no value is given, the default value is used. It is advised not to specify *dfj* and allow XBeach to calculate the default value.

A typical input file contains the following:

```
Hm0       = 0.8
fp        = 0.125
mainang   = 285.
gammajsp  = 3.3
s         = 10.
fnyq      = 0.3
```

Y.3 Use of SWAN spectrum

The new XBeach module has been programmed to read standard SWAN 2D variance density or energy density output files (*.sp2* files), as specified in the SWAN v40.51 manual.

To make use of this option, the user must specify '*instat* = 5' in *params.txt*. XBeach will then attempt to read the SWAN output spectrum from a separate file specified by '*bcfile* =' in *params.txt*. The user must also state in *params.txt* the required record length for the boundary condition file and the boundary condition file time step (keywords '*rt* = ' and '*dtbc* = ' respectively). If the record length (*rt*) is less than the total simulation time, XBeach will reuse the boundary condition file until the simulation is completed. The boundary condition file time step should be small enough to accurately represent the bound long wave, but need not be as small as the time step used in XBeach, see *Explanation of input/output*.
XBeach assumes the output of the SWAN file is in nautical terms. If the file is in Cartesian angles, the user must specify the angle in degrees to rotate the x-axis in SWAN to the x-axis in XBeach (in Cartesian terms). This value is specified in *params.txt* after the keyword '*dthetaS_XB* ='.

An example of a SWAN 2D output file is given below:

```
SWAN   1                                Swan standard spectral file, version
$ Data produced by SWAN version 40.51
$ Project:'projname'     ;   run number:'runnum'
LOCATIONS                               locations in x-y-space
     1                                  number of locations
    22222.22        0.00
RFREQ                                   relative frequencies in Hz
    23                                  number of frequencies
    0.0545
    0.0622
    0.0710
    0.0810
    0.0924
    0.1055
    0.1204
    0.1375
    0.1569
    0.1791
    0.2045
    0.2334
    0.2664
    0.3040
    0.3470
    0.3961
    0.4522
    0.5161
    0.5891
    0.6724
    0.7675
    0.8761
    1.0000
CDIR                                    spectral Cartesian directions in degr
    12                                  number of directions
   30.0000
   60.0000
   90.0000
  120.0000
  150.0000
  180.0000
  210.0000
  240.0000
  270.0000
  300.0000
  330.0000
  360.0000
QUANT
     1                                  number of quantities in table
VaDens                                  variance densities in m2/Hz/degr
m2/Hz/degr                              unit
   -0.9900E+02                          exception value
FACTOR
    0.675611E-06
      51    242    574    956   1288   1482   1481   1286    957    579    244     51
     129    610   1443   2402   3238   3725   3724   3234   2406   1454    613    128
     273   1287   3054   5084   6846   7872   7869   6837   5091   3076   1295    271
     665   3152   7463  12402  16712  19229  19221  16690  12419   7518   3172    662
    1302   6159  14608  24275  32688  37618  37603  32644  24309  14716   6198   1296
    2328  10989  26020  43341  58358  67109  67080  58281  43401  26213  11058   2317
    3365  15922  37712  62733  84492  97150  97110  84380  62820  37991  16021   3349
    3426  16230  38440  63939  86109  99010  98969  85995  64027  38724  16331   3410
    2027   9612  22730  37790  50909  58529  58505  50841  37843  22898   9672   2018
     672   3178   7538  12535  16892  19440  19432  16870  12552   7594   3198    669
     101    479   1135   1890   2542   2924   2923   2539   1892   1144    482    101
       2     11     26     43     57     66     66     57     43     26     11      2
       0      0      0      0      0      0      0      0      0      0      0      0
       0      0      0      0      0      0      0      0      0      0      0      0
       0      0      0      0      0      0      0      0      0      0      0      0
       0      0      0      0      0      0      0      0      0      0      0      0
       0      0      0      0      0      0      0      0      0      0      0      0
       0      0      0      0      0      0      0      0      0      0      0      0
       0      0      0      0      0      0      0      0      0      0      0      0
       0      0      0      0      0      0      0      0      0      0      0      0
       0      0      0      0      0      0      0      0      0      0      0      0
       0      0      0      0      0      0      0      0      0      0      0      0
       0      0      0      0      0      0      0      0      0      0      0      0
```

Y.4 Use of formatted variance density spectrum

If the user has 2D spectrum information, but not in SWAN or JONSWAP form, the user can create a formatted spectrum file which can be read by XBeach.
To make use of this option, the user must specify '*instat* = 6' in *params.txt*. XBeach will then attempt to read the formatted output spectrum from a separate file specified by '*bcfile* =' in *params.txt*. The user must also state in *params.txt* the required record length for the boundary condition file and the boundary condition file time step (keywords '*rt* = ' and '*dtbc* = ' respectively). If the record length (*rt*) is less than the total simulation time, XBeach will reuse the boundary condition file until the simulation is completed. The boundary condition file time step should be small enough to accurately represent the bound long wave, but need not be as small as the time step used in XBeach, see *Explanation of input/output*.

The contents of the file specified by '*bcfile* =' in *params.txt* must follow a specified format. The information should be as follows:
First line: number of frequencies (integer)
Second line onwards: column with frequencies in Hz (each on a new line)
Then: number of angles (integer)
Then onwards: column with angles in degrees (each on a new line)
Then per line: row of variance density in each direction, per frequency (i.e. first row corresponds to variance density per direction in the first frequency band, second row of the second frequency band, etc.).

Note that the angles in the input file must be in the calculation coordinate system of XBeach, i.e. 0° is in the direction of the x-axis, 90° is in the direction of the y-axis. Also, the angles must be increasing.

An example of a formatted variance density file is given below:

```
    15
    0.0418
    0.0477
    0.0545
    0.0622
    0.0710
    0.0810
    0.0924
    0.1055
    0.1204
    0.1375
    0.1569
    0.1791
    0.2045
    0.2334
    0.2664
    13
-180.0000
-150.0000
-120.0000
 -90.0000
 -60.0000
 -30.0000
   0.0000
  30.0000
  60.0000
  90.0000
 120.0000
 150.0000
 180.0000
    0     0     0     0     0     0     0     0     0     0     0     0
   51   242   574   956  1288  1482  1481  1286   957   579   244    51
  129   610  1443  2402  3238  3725  3724  3234  2406  1454   613   128
  273  1287  3054  5084  6846  7872  7869  6837  5091  3076  1295   271
  665  3152  7463 12402 16712 19229 19221 16690 12419  7518  3172   662
 1302  6159 14608 24275 32688 37618 37603 32644 24309 14716  6198  1296
 2328 10989 26020 43341 58358 67109 67080 58281 43401 26213 11058  2317
 3365 15922 37712 62733 84492 97150 97110 84380 62820 37991 16021  3349
 3426 16230 38440 63939 86109 99010 98969 85995 64027 38724 16331  3410
 2027  9612 22730 37790 50909 58529 58505 50841 37843 22898  9672  2018
  672  3178  7538 12535 16892 19440 19432 16870 12552  7594  3198   669
  101   479  1135  1890  2542  2924  2923  2539  1892  1144   482   101
    2    11    26    43    57    66    66    57    43    26    11     2
    0     0     0     1     1     1     1     1     1     0     0     0
    0     0     0     0     0     0     0     0     0     0     0     0
    0     0     0     0     0     0     0     0     0     0     0     0
```

Y.5 Reusing existing boundary condition files

If the user does not wish to recalculate boundary condition files or specifically wants to reuse the boundary condition files of another XBeach simulation, it is possible to do so. In this case the user should select '*instat* = 7' in *params.txt*. No further wave boundary condition data need be given in *params.txt*. Obviously, the calculation grid should remain the same between runs, as the angles and number of grid points are embedded in the boundary condition files.

In order to use instat 7, the user should copy *ebcflist.bcf* and *qbcflist.bcf* to the current directory. Additionally, the user should also copy all files listed in *ebcflist.bcf* and *qbcflist.bcf*. Generally, these files have *E_* and *q_* prefixes.

Y.6 Use of time-varying spectra

The new XBeach module allows the user to specify time-varying wave spectra on the offshore boundary. This is done by feeding in several input data files such as those used for instat 4, 5 or 6, and specifying the duration for which these spectra should occur.
To make use of this option, the user must specify the instat value (4, 5 or 6) associated with the input data type for the wave boundary conditions. XBeach will then attempt to read a list of input data filenames from a separate file specified by '*bcfile* =' in *params.txt*. This keyword is the same keyword as used for non-time-varying spectra. In order for XBeach to differentiate between time-varying and non-time-varying wave spectra, the file must have the following format.
The first word in the file must be the keyword '*FILELIST'*. In the following lines, each line contains the duration of this wave spectrum condition in seconds (similar to '*rt'* in *params.txt*), the required time step in this boundary condition file in seconds (similar to '*dtbf*' in *params.txt*) and the name of the input data file used to generate these boundary conditions. The duration and boundary condition time step in this file overrules *'rt'* and *'dtbf'* in *params.txt*. XBeach will now not reuse any boundary condition time series, so the user must ensure that the total record length is greater than or equal to the simulation time.

A typical input file contains the following:

```
FILELIST
1800 0.2 jonswap1.inp
1800 0.2 jonswap1.inp
1350 0.2 jonswap2.inp
1500 0.2 jonswap3.inp
1200 0.2 jonswap2.inp
3600 0.2 jonswap4.inp
```

Note: It is not possible to use a mix of JONSWAP, SWAN and Variance Density files. It is also not possible to vary *dthetaS_XB* between files in case of non-nautical SWAN output.

Y.7 Examples

In order to clarify the instructions given above, a number of examples are given. In the first example, the user wishes to use a constant JONSWAP spectrum. In order to save calculation time and memory use, the user decides to recycle the boundary condition file every 30 minutes. Wave input parameters in the *params.txt* file are given below:

```
Boundary condition options
instat   = 4

Required for instat 4,5,6
bcfile   = jonswap.inp

if file is reused, else this information in file-list:
rt       = 1800
dtbc     = 0.2
```

The file jonswap.inp contains information as described in the section "use of one JONSWAP input file". As the user has only one input file, *rt* and *dtbc* must be specified in *params.txt*.

In the second example the user wishes to use a constant JONSWAP spectrum, but does not want to reuse the same boundary condition file as in the previous example. This can be achieved by using the multiple files option, but only using one JONSWAP data file. For instance in *params.txt*:

```
Boundary condition options
instat   = 4

Required for instat 4,5,6
bcfile   = jonswaplist.txt
```

And in the file *jonswaplist.txt*:

```
FILELIST
1800 0.2 jonswap.inp
1800 0.2 jonswap.inp
1800 0.2 jonswap.inp
1800 0.2 jonswap.inp
1800 0.2 jonswap.inp
1800 0.2 jonswap.inp
```

Note that in this case if the simulation time is greater than 3 hours (10800 seconds), XBeach will abort due to lack of input data.

In the third example the user wishes to use one SWAN 2D spectrum file. The output of the SWAN model is in nautical degrees, so *dthetaS_XB* does not need to be specified. Wave input parameters in the *params.txt* file are given below:

```
Boundary condition options
instat   = 5

Required for instat 4,5,6
bcfile   = swan14a.sp2

if file is reused, else this information in file-list:
rt       = 3600
dtbc     = 0.5
```

The file *swan14a.sp2* contains information as described in the section "use of one SWAN input file". As the user has only one input file, *rt* and *dtbc* must be specified in *params.txt*. If the simulation time is more than one hour (3600 seconds), the boundary condition file is reused.

In the final example, the user wishes to reuse the exact boundary conditions of the simulation in the previous example. In this case the user copies the files *ebcflist.bcf* and *qbcflist.bcf* and *E_reuse.bcf* and *q_reuse.bcf* to the current directory (the directory with the XBeach executable). The *params.txt* would now contain the following options for the wave boundary conditions:

```
Boundary condition options
instat   = 7
```

Y.8 Theory

The method in which the boundary wave conditions are generated is explained in [van Dongeren *et al.*, 2003]. A brief summary is given in the following.
First a wave variance density table is either read from a file or generated from JONSWAP-spectrum parameters. From this spectrum, *K* frequencies are selected, which contain more than 8% of the maximum variance. These frequencies are used to generate short waves at the offshore boundary.
Each of the *K* wave-frequency combinations is given a direction that is drawn randomly from a directional probability function. The variance density related to each of the *K* wave-frequency-direction combinations is interpolated from the original variance-density spectrum.
Fourier components are generated for every calculation point on the offshore boundary (*ny+1* points on *x=1*) for the entire time series required in the boundary condition file, using the variance density. The amplitude of the short wave envelope at every calculation point, at every point in time, and in every direction is calculated using a Hilbert transform of the Fourier components. The short-wave energy follows from this amplitude.
For all *K-1* pairs of wave-frequency-direction combinations, the interaction wave is calculated. The mass flux for all interaction components combined is set to the offshore boundary and rotated to include only the boundary-normal component of the mass flux at every calculation point, at every point in time.

Y.9 Explanation of input/output

At the start of the XBeach simulation, XBeach checks whether non-stationary varying wave boundary conditions are to be used. If this is the case, it next checks whether the wave spectrum of the wave boundary conditions is to change over time, or remain constant. If the wave spectrum is to remain constant, XBeach will only read from one input file to generate wave boundary conditions. If the wave spectrum is to vary in time, XBeach reads from multiple files.

Whether or not the wave spectrum of the boundary conditions changes over time, the XBeach module requires a record length during which the current wave spectral parameters are to apply.
For the duration of the record length, boundary conditions are calculated at every boundary condition file time step. These time steps are not required to be the same as the time steps in the XBeach main program; XBeach will interpolate where necessary. The boundary condition time steps should therefore only be small enough to accurately describe the incoming bound long waves.
The statistical data for the generation of the wave boundary conditions is read from user-specified files. At this stage the XBeach module can interpret SWAN 2D variance density output files and JONSWAP parameters.

The beginning and end of the boundary condition file is tapered by the XBeach module. This is done to ensure smooth transitions from one boundary condition file to the next.

The combination of a large record length and a small time step lead to large demands on the system memory. If the memory requirement is too large, the user must choose to either enlarge the boundary condition time step, or to reduce the record length. In case of the latter, several boundary condition files can be generated and read sequentially. It is unwise however to reduce the record length too much, as then the transitions between the boundary condition files start to play an important role.

Every time the XBeach wave boundary condition module is run, it outputs data to the local directory. Metadata about the wave boundary conditions are stored in list files: *ebcflist.bcf* and *qbcflist.bcf*. The main XBeach program uses the list files to know how and when to read and generate boundary condition files.
The actual incoming short-wave energy and long-wave mass flux data is stored in other files. These files have *E_* and *q_* prefixes. The main XBeach program uses these files for the actual forcing along the offshore edge.

Y.10 Params.txt file

The new options for the wave boundary conditions are summarised in the *params.txt* file below:

```
-----------------------------------------------------
Grid input

nx       = 104
ny       = 124
xori     = 0.
yori     = 0.
alfa     = 0.
thetamin = -90.
thetamax = 90.
dtheta   = 20
depfile  = depth.grd
posdwn   = -1
vardx    = 1

Required if vardx 1
xfile    = x.grd
yfile    = y.grd

Required if vardx 0
dx       = 1.
dy       = 1.

-----------------------------------------------------
Numerics input
CFL      = 0.2
eps      = 0.01

-----------------------------------------------------
Time input
tstart   = 0
tint     = 1.
tstop    = 1800
taper    = 20

-----------------------------------------------------
General constants
rho      = 1000
g        = 9.81

-----------------------------------------------------
Wind boundary conditions
rhoa     = 1.25
Cd       = 0.002
windv    = 0.
windth   = 90.

-----------------------------------------------------
Water level boundary conditions
tideloc  = 1

Required if tideloc > 0
zs0file  = zs0input.bcf
tidelen  = 2
paulrevere = 1

Required if tideloc 0
zs0      = 4.

-----------------------------------------------------
Boundary wave conditions absorbing
front    = 1
left     = 0
right    = 0
back     = 0

-----------------------------------------------------
```

Continued on next page …

```
--------------------------------------------------
Boundary wave conditions generating
instat   = 4
ARC      = 1

Required for instat 0,1,2,3
dir0     = 270.

Required for instat 0,1,2,3
Hrms     = 0.4
Tm01     = 6.0
m        = 200

Required for instat 0
waveint    = 1

Required for instat 1
Tlong    = 31.2

Required for instat 5 (if SWAN is Cartesian):
Angle in Cartesian degrees to rotate the x-axis in SWAN to the x-axis in XBeach
dthetaS_XB  = 0.

Required for instat 4,5,6:
Name of boundary condition file
bcfile   = jonswap.inp

Required for instat 4,5,6 if spectra are not time-varying:
Record length for the boundary condition file
rt       = 1800.
Boundary condition file time step
dtbc     = 0.2

--------------------------------------------------
Wave calculation options
break    = 1
wci      = 0
roller   = 1
beta     = 0.1
gamma    = 0.55
gammax   = 5.
alpha    = 1.
delta    = 0.0
n        = 10.
order    = 2

--------------------------------------------------
Flow calculation options
nuh      = 0.1
nuhfac   = 0.
hmin     = 0.1
C        = 65.
umin     = 0.01

--------------------------------------------------
Sediment transport calculation options
dico     = 1.
D50      = 0.0002
D90      = 0.0003
rhos     = 2650
z0       = 0.006

--------------------------------------------------
Morphological calculation options
morfac   = 10
morstart = 0
```

Z Numerical dissipation wave action balance

To further understand the possible effects of numerical dissipation and its relation with the short wave height decay, the wave action balance in XBeach is examined [Roelvink *et al.*, 2007].

$$\frac{\delta A}{\delta t}+\frac{\delta c_x A}{\delta x}+\frac{\delta c_y A}{\delta y}+\frac{\delta c_\theta A}{\delta \theta}=-\frac{D}{\sigma} \tag{Z.1}$$

Supposing a simple one dimensional model, without dissipation and currents, equation (Z.1) can be reduced:

$$\frac{\delta A}{\delta t}+\frac{\delta c_g A}{\delta x}=0 \tag{Z.2}$$

Assuming positive wave action flux, equation (Z.2) would be solved in XBeach in the following manner:

$$\frac{A_j^{m+1}-A_j^m}{\Delta t}+\frac{\left[Ac_g\right]_j^m-\left[Ac_g\right]_{j-1}^m}{\Delta x}=0 \tag{Z.3}$$

The following Taylor expansions can be made:

$$A_j^{m+1}=A_j^m+\Delta t\frac{dA}{dt}+\frac{1}{2}\Delta t^2\frac{d^2A}{dt^2}-O\left(\Delta t^3\right) \tag{Z.4}$$

$$\left[Ac_g\right]_{j-1}^m=\left[Ac_g\right]_j^m-\Delta x\frac{d\left[Ac_g\right]}{dx}+\frac{1}{2}\Delta x^2\frac{d^2\left[Ac_g\right]}{dx^2}-O\left(\Delta x^3\right) \tag{Z.5}$$

Substituting (Z.4) and (Z.5) in (Z.3) leads to:

$$\frac{A_j^m}{dt}+\frac{d\left[Ac_g\right]_j^m}{dx}+\frac{1}{2}\Delta t\frac{d^2A}{dt^2}-\frac{1}{2}\Delta x\frac{d^2\left[Ac_g\right]}{dx^2}+O\left(\Delta t^2\right)+O\left(\Delta x^2\right)=0 \tag{Z.6}$$

The first two terms correspond with the true solution. The rest is numerical truncation error:

$$E_j^m=\frac{1}{2}\Delta t\frac{d^2A}{dt^2}-\frac{1}{2}\Delta x\frac{d^2\left[Ac_g\right]}{dx^2}+O\left(\Delta t^2\right)+O\left(\Delta x^2\right) \tag{Z.7}$$

All error terms should be zero in the case of stationary waves as the temporal and spatial gradients of the wave action and wave action flux respectively are zero. Therefore, numerical truncation error is zero in the case of stationary waves without dissipation.

To examine numerical diffusion, the modified equation approach is taken. It is assumed that:

$$\begin{aligned} &D(A) = D_{\Delta x,\Delta t}(A) - E(A) \\ &\text{in which:} \\ &D(A) = 0 \quad : \quad \text{true equation} \\ &D_{\Delta x,\Delta t}(A) = 0 \quad : \quad \text{numerical equation} \end{aligned} \tag{Z.8}$$

Equation (Z.8) can also be written as [Stelling and Booij, 1999]:

$$D_{\Delta x,\Delta t}(\bar{A}) = D(\bar{A}) + E(\bar{A}) \tag{Z.9}$$

The objective is to find the differential equation $\bar{c}$ that is solved by (Z.9).

For matters of simplification, the bathymetry is assumed uniform in cross shore direction. This allows the group velocity to be independent of *x*, thus (Z.2) and (Z.7) become:

$$\frac{\delta A}{\delta t} + c_g \frac{\delta A}{\delta x} = 0 \tag{Z.10}$$

$$E_j^m = \frac{1}{2}\Delta t \frac{d^2 A}{dt^2} - \frac{1}{2}\Delta x c_g \frac{d^2 A}{dx^2} + O(\Delta t^2) + O(\Delta x^2) \tag{Z.11}$$

Assuming the following relation for the second derivatives [Stelling and Booij, 1999]:

$$\frac{d^2 A}{dt^2} = c_g{}^2 \frac{d^2 A}{dx^2} \tag{Z.12}$$

The error term can be rewritten to:

$$E_j^m = -\frac{1}{2} c_g (c_g \Delta t - \Delta x) \frac{d^2 A}{dx^2} \tag{Z.13}$$

Substitution in (Z.9) leads to:

$$D_{\Delta x,\Delta t}(\bar{A}) = \frac{d\bar{A}}{dt} + c_g \frac{d\bar{A}}{dx} + \frac{1}{2} c_g (c_g \Delta t - \Delta x) \frac{d^2 \bar{A}}{dx^2} \tag{Z.14}$$

Thus it appears the numerical solution introduces an additional diffusion term with a diffusion coefficient:

$$K = -\frac{1}{2} c_g (c_g \Delta t - \Delta x) \tag{Z.15}$$

AA Input parameters of the Santa Rosa Island model

The model inputs, as specified in the *params.txt* input file for the Santa Rosa Island model are listed below.

```
--------------------------------------------------
Grid input

nx = 499
ny = 100
xori = 502150
yori = 3357400
alfa = 101
depfile = Z.dep
thetamin = -60.
thetamax = 60.
dtheta   = 15
posdwn   = -1
vardx    = 1

Required if vardx 1
xfile    = X.grd
yfile    = Y.grd

Required if vardx 0
dx       = 1.
dy       = 1.

--------------------------------------------------
Numerics input
CFL      = 0.8
eps      = 0.01

--------------------------------------------------
Time input
tstart   = 0.
tint     = 10.
tstop    = 147600.
taper    = 100.

--------------------------------------------------
General constants
rho      = 1025
g        = 9.81

--------------------------------------------------
Wind boundary conditions
rhoa     = 1.25
Cd       = 0.002
windv    = 0.
windth   = 90.

--------------------------------------------------
Water level boundary conditions
tideloc  = 2

Required if tideloc > 0
zs0file  = surge.dat
tidelen  = 42
paulrevere = 0

Required if tideloc 0
zs0      = 4.

--------------------------------------------------
```

```
--------------------------------------------------
Boundary wave conditions generating
instat   = 4
ARC      = 1
order    = 2

Required for instat 0,1,2,3
dir0     = 270.

Required for instat 0,1,2,3
Hrms     = 0.4
Tm01     = 6.0
m        = 200

Required for instat 0
waveint    = 1

Required for instat 1
Tlong    = 31.2

Required for instat 5 (if SWAN is Cartesian):
Angle in Cartesian degrees to rotate the x-axis in SWAN to the x-axis in XBeach
dthetaS_XB  = 0.

Required for instat 4,5,6:
Name of boundary condition file
bcfile   = jonswaplist.txt

Required for instat 4,5,6 if spectra are not time-varying:
Record length for the boundary condition file
rt       = 1800.
Boundary condition file time step
dtbc     = 0.2

--------------------------------------------------
Wave calculation options
break    = 1
wci      = 0
roller   = 1
beta     = 0.1
gamma    = 0.55
gammax   = 5.
alpha    = 1.
delta    = 0.0
n        = 10.

--------------------------------------------------
Flow calculation options
nuh      = 0.1
nuhfac   = 0.
hmin     = 0.08
C        = 40.
umin     = 0.0

--------------------------------------------------
Sediment transport calculation options
dico     = 1.
D50      = 0.0002
D90      = 0.0003
rhos     = 2650
z0       = 0.006

--------------------------------------------------
Morphological calculation options
morfac   = 1.
morstart = 0.
hswitch  = 0.1
por      = 0.4
dryslp   = 1.0
wetslp   = 0.15

--------------------------------------------------
```